Dynamics of Heavy Electrons

Yoshio Kuramoto and Yoshio Kitaoka

July, 1999
(Draft of a monograph to be published by Oxford University Press)

PREFACE

The present book has twofold purposes. First, the book is intended to be a monograph on heavy electrons which have been the focus of very active experimental and theoretical studies in the last two decades. Heavy electrons are found among a number of lanthanide and actinide compounds, and are characterized by a large effective mass which becomes comparable to the mass of a muon. The heavy electrons exhibit rich phenomena such as smooth crossover to local moment behavior with increasing temperature, unconventional superconductivity, weak antiferromagnetism and pseudo-metamagnetism. Although some mysteries still remain, the authors feel that a reasonably coherent understanding is available of heavy electrons as a whole. Therefore the time is ripe to survey the properties of heavy electrons from a global and unified point of view.

The physics of heavy electrons is one of typical examples where intimate interaction between theory and experiment has disclosed step by step the origin of seemingly incredible behavior of electrons. One (Kuramoto) of the present authors has been engaged in formulating a theoretical scheme which is now widely applied to magnetic impurities and heavy electrons and, among other things, has derived dynamical response functions. The other author (Kitaoka) has been doing NMR experiment on heavy-electron systems and has found formation of metallic, insulating, superconducting and weakly magnetic phases of heavy electrons through the NMR. Thus the authors think it appropriate for them to write a book which focuses on dynamical aspect of heavy electrons. In view of the innumerable and diverse activities in the field, the authors do not try to cover every aspect on equal footing, although they do try to touch upon important thermodynamic and transport results.

The second purpose of the book is to serve as an advanced textbook on theoretical and experimental physics of strongly correlated electrons. The necessity to understand fascinating experimental results on heavy electrons has stimulated intensive theoretical efforts to go beyond existing schemes. It has turned out that many established ideas and techniques are insufficient to understand heavy electrons. On the theoretical side, enormous amount of quantum fluctuations has brought disaster to celebrated mean-field theories. On the other hand, extreme experimental condition has been required such as applying strong magnetic field and pressure at ultralow temperatures. Thus heavy-electron systems have been a target of a case study for applying and testing almost all tools in theoretical and experimental condensed-matter physics. Those graduate students and researchers who want to work on strongly correlated condensed-matter systems will find in the book many examples how the conventional concepts on solids work or do not work in heavy-electron systems. Although we try to make the book self-contained for those readers who have the knowledge of condensed matter physics in the undergraduate level, they may sometimes find the description of the book too concise. We advise consulting available textbooks on elementary many-body physics in such a case.

The book tries to build coherent picture of heavy electrons out of collection of apparently diverse experimental and theoretical results. However the authors do not intend to be exhaustive in citing papers, nor to be excessively on the alert for a report made yesterday. At any rate a monograph cannot compete with a review in scientific journals for covering newest findings. Instead the book tries to provide an entire outlook which should be especially useful to newcomers to the field of strongly correlated electrons, either experimental or theoretical, and tries to help them to initiate a new stage of investigation. Thus the book emphasizes new theoretical methods and concepts which might be effective also in other related areas. It also emphasizes the utility and limitation of dynamical information brought about by the NMR and neutron scattering. Special attention is paid to similarity to other strongly correlated systems like the copper oxide high-temperature superconductors. Since the research area of heavy electrons is vast, our treatment inevitably reflects our favorite choice of the topics, and pays unavoidable attention to our own contribution to the field. We would apologize those authors whose contributions are not touched upon, or are not treated properly. Especially we have omitted many topics on transport, thermodynamic properties, and dynamical measurements other than NMR and neutron scattering.

As an exiting monograph on Kondo effect and heavy electrons, we mention a book by A.C. Hewson (Cambridge 1993). The present book puts more emphasis on the side of periodic systems rather than magnetic impurities, and also on experimental aspects. Hence we hope that the present monograph serves complementary to Hewson's book. To make the book of reasonable size we have to omit some interesting theoretical topics like the Bethe ansatz and the conformal field theory. These topics are extensively dealt with by other monographs.

The content of the book is arranged as follows: Chapter 1 presents first the phenomena of heavy electrons from thermodynamic measurement, and then introduces the two basic pictures of electrons in

solids: itinerant and localized states. These pictures represent opposite limiting behaviors of electrons and do not reconcile with each other at the naive level. A brief account of the Fermi liquid theory is given. Basics of NMR and neutron scattering experiments are explained.

Chapter 2 deals with the single magnetic impurity problem. The Kondo effect is discussed from various viewpoints; scaling, $1/n$ expansion, local Fermi liquid, and so on. We emphasize the effective Hamiltonian approach which includes the concept of the renormalization group. The local non-Fermi liquid state is treated with emphasis on the unique excitation spectrum. Detailed experimental results are presented which can be interpreted without taking account of the intersite interactions among f-electrons.

In Chapter 3 we turn to periodic systems where heavy electrons are formed. Experimental facts on both metallic and insulating systems are presented. Although the metallic ground state is basically understood by the Fermi-liquid picture, the system shows strange behaviors in a magnetic field. We present intuitive ideas and theoretical apparatus to understand the basic features of heavy electrons. Practical methods to compute physical quantities such as the density of states and the dynamical susceptibility are explained.

These two chapters as a whole represent complementary approaches to heavy electrons from local and itinerant limits. In Chapter 4 we discuss the anomalous magnetism which emerges as a result of complicated interference between quasi-particles. The relevant phenomena include the weak antiferromagnetism with tiny ordered moments, and the orbital ordering accompanying quadrupole moments. Alternatively, the anomalous magnetism is interpreted as coming from competition between the Kondo screening and the intersite interaction, if one takes the viewpoint from high temperatures. Although there is no established understanding of these phenomena, we present a possible view which emphasizes the dual nature of electrons with strong correlations; simultaneous presence of both itinerant and localized characters.

Chapter 5 deals with superconductivity of heavy electrons. We begin with introductory treatment of anisotropic pairing in general and symmetry classification of singlet and triplet pairings. Then detailed review of experimental situation is given for representative superconducting systems. Emphasis is put on the interplay between superconductivity and anomalous magnetism, and subtle coupling to the lattice degrees of freedom.

In Chapter 6 we compare heavy-electron systems with some cuprates which show high-temperature superconductivity. The latter system also has strongly correlated electrons, but the parameters characterizing the electrons are rather different from heavy electrons. Interestingly, some dynamical properties such as the NMR relaxation rate below the superconducting transition shows similar temperature dependence if one scales the temperature by the transition temperature of each system. We discuss similarities and differences between these two systems, and pursue a picture for unified understanding of strongly correlated electrons including non-Fermi liquid states.

In Appendices, we summarize theoretical techniques frequently used in the many-body theory. They constitute a compact treatise which should be understandable independent of the content of the main text.

It took us an unexpectedly long time to finish this book. During this period we have been benefited by discussion with our colleagues and friends. We are grateful to all of them for helping our understanding on the subject, and especially to Erwin Müller-Hartmann who introduced one of the authors (Kuramoto) to the early stage of the field 20 years ago, and to Kunisuke Asayama and Hiroshi Yasuoka who introduced the other author (Kitaoka) to the field of NMR in condensed matter physics. We acknowledge fruitful cooperation with and valuable suggestions by Jacques Flouquet, Kenji Ishida, Yusuke Kato, Hiroaki Kusunose, Frank Steglich, Hideki Tou and Hisatoshi Yokoyama. Special thanks are due to Frank Steglich, Yusuke Kato and Stephen Julian who read the first manuscript and made a number of constructive remarks to improve the book.

Yoshio Kuramoto
Yoshio Kitaoka

Contents

Chapter 1

Fundamental Properties of Electrons in Solids

1.1 What are Heavy Electrons?

Electrons in metals have an effective mass m^* which is in general different from the mass $m_0 = 9.1 \times 10^{-28} g$ in vacuum. Experimentally, the effective mass can be measured by such methods as cyclotron resonance, de Haas-van Alphen (dHvA) effect, specific heat and so on. The temperature dependence of the specific heat C much below room temperature is usually fitted in the form

$$C = \gamma T + \beta T^3, \tag{1.1}$$

where the second term comes from lattice vibrations in ordinary metals. In the free electron model of metals with the spherical Fermi surface, γ is given by

$$\gamma = \frac{\pi^2}{3} k_B^2 \rho^*(\mu), \tag{1.2}$$

where k_B denotes the Boltzmann constant and $\rho^*(\mu) = m^* k_F/(\pi^2\hbar^2)$ is the density of states at the Fermi level μ. For a general shape of the Fermi surface, the effective mass in the above formula should be interpreted as the average over the Fermi surface with the same volume enclosed as that of a sphere with radius k_F. The spin part χ of the magnetic susceptibility at low temperatures is also determined by $\rho^*(\mu)$. Namely we obtain

$$\chi = (g\mu_B)^2 \rho^*(\mu), \tag{1.3}$$

where g is the g-factor close to 2 and $\mu_B = e\hbar/(2m_0 c)$ is the Bohr magneton.

In simple metals such as K or Al, γ is of the order of mJ/(K^2 mol). This means that the effective mass is of the order of m_0. However in some materials it becomes larger than m_0 by as much as three order of magnitudes. As an example, the temperature dependence of γ is shown in Fig.1.1 for $Ce_xLa_{1-x}Cu_6$ with varying Ce concentrations [1, 2]. We interpret the large γ as coming from the large effective mass, since k_F is determined by the density of conduction electrons which is of the order of $10^{22} cm^{-3}$ independent of metals. Hence these compounds are called heavy-electron (or heavy-fermion) systems. The validity of this interpretation depends on the Fermi-liquid theory to be explained later. It is remarkable that these data fall on a single curve if it is divided by x. This means that each Ce ion contributes to the enhanced specific heat rather independently. In other words, possible intersite interaction among Ce ions does not play an important role in γ. Thus the steep increase of γ below 10 K is essentially a single-site effect.

The magnetic susceptibility for various Ce concentration is shown in Fig.1.2. Like the specific heat, the susceptibility per mole Ce is almost independent of x up to 0.9 [1]. In general, thermodynamic data point to the importance of the single-ion effect. Most of apparent deviation from the single-ion behavior can be understood with account of change of the lattice parameter and other peripheral effects. As we shall discuss in detail later in this book, the origin of heavy effective masses is traced back to strong local correlations. The Kondo effect is the keyword to understand all the anomalous properties in a universal fashion, as we shall explain in detail later.

Table 1.1 summarizes the values of γ and χ for representative compounds. The average valency of Ce

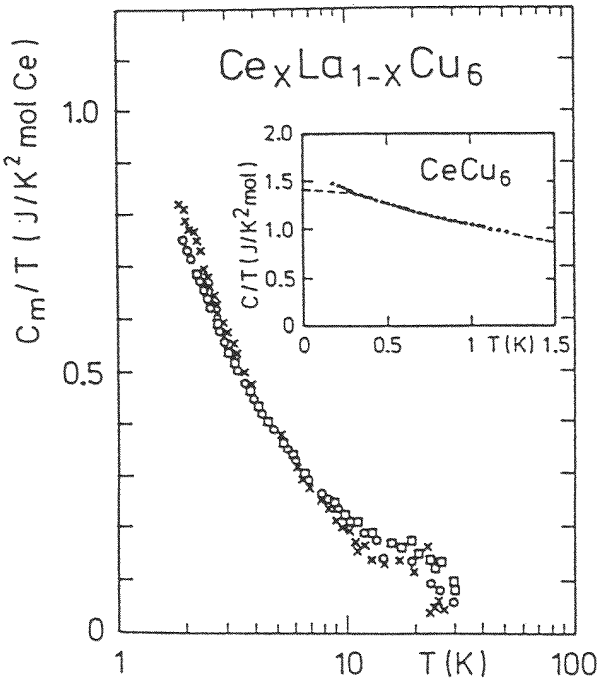

Figure 1.1: Temperature dependence of $4f$-derived specific heat per mole of Ce as C_m/T plotted against T for $Ce_xLa_{1-x}Cu_6$ with $x = 1$ (◯), 0.8 (□) and 0.5 (×)[1]. Inset indicates low-T data. Dashed curve is the calculation for an S=1/2 Kondo impurity with T_K=4.2 K.

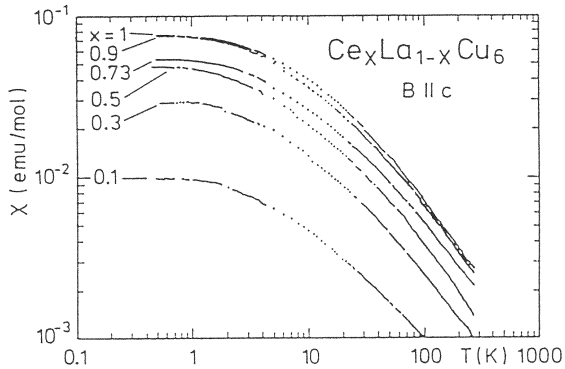

Figure 1.2: Temperature dependence of the magnetic susceptibility per mole of formula unit for $Ce_xLa_{1-x}Cu_6$ [1].

system	$\chi(10^{-3}$ emu/mol)	γ (mJ/mol K^2)
$CeCu_6$	80 (c)	1600 [1]
$CeCu_2Si_2$	8 (c), 4 (ab)	1100 [3]
$CeRu_2Si_2$	30 (c)	350 [4]
UBe_{13}	13	1100 [5]
UPt_3	4 (c), 8 (ab)	400 [6]

Table 1.1: Low-temperature susceptibility and specific heat coefficient of some heavy electron systems. The susceptibilities along the c-axis, shown as (c) in the table, and in the ab-plane shown as (a) can be different in non-cubic systems.

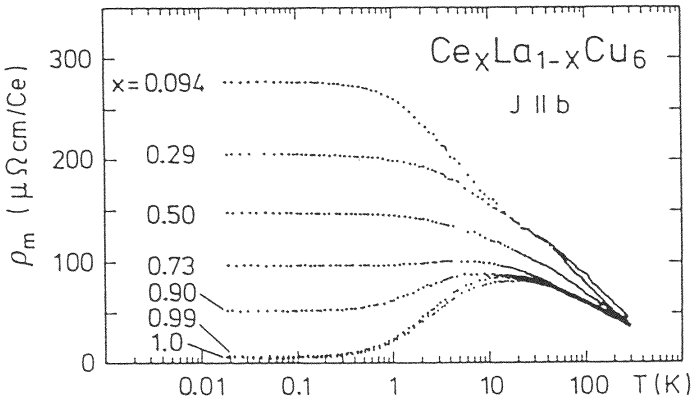

Figure 1.3: Temperature dependence of magnetic resistivity[1] per mole of formula unit for $Ce_xLa_{1-x}Cu_6$.

and Yb in heavy electron systems is very close to 3+. However in some Yb materials which have smaller values of γ of the order of 10^2mJ/(K^{2}mole), the average valency is between 2+ and 3+. These systems are called intermediate valence compounds. Since the valency fluctuates quantum mechanically between 2+ and 3+, the phenomena are also called valence fluctuation, a term with emphasis on the dynamical aspect.

Transport properties of these materials also show unusual temperature dependence. As an illustration, Fig.1.3 shows the temperature dependence of the magnetic part of the resistivity for $Ce_xLa_{1-x}Cu_6$ [1]. The magnetic part is obtained by subtracting the resistivity of $LaCu_6$ with no f electrons. In the dilute limit, nearly logarithmic increase of the resistivity is observed over more than two decades of T. This is a typical signature of the Kondo effect. On the other hand, in the pure limit of $CeCu_6$, this logarithmic dependence disappears with $T \to 0$. Instead the T^2 law of the resistivity takes place. The latter behavior is typical of itinerant electrons with strong mutual interaction. Thus the resistivity of $Ce_xLa_{1-x}Cu_6$ depends on x in a way completely different from those for the specific heat and the susceptibility.

In order to study how the heavy electrons are realized in condensed-matter systems, and how one can understand very rich properties of them, we begin in the following with fundamental consideration about electrons in solids. From this point on we take units such that $\hbar = k_B = 1$ to simplify the notation except for deriving numerical values with a dimension.

1.2 Itinerant and Localized States

Real solids are quantum many-body systems consisting of a large number of atomic nuclei and electrons. We simplify this complicated system by keeping only those degrees of freedom which are essential to

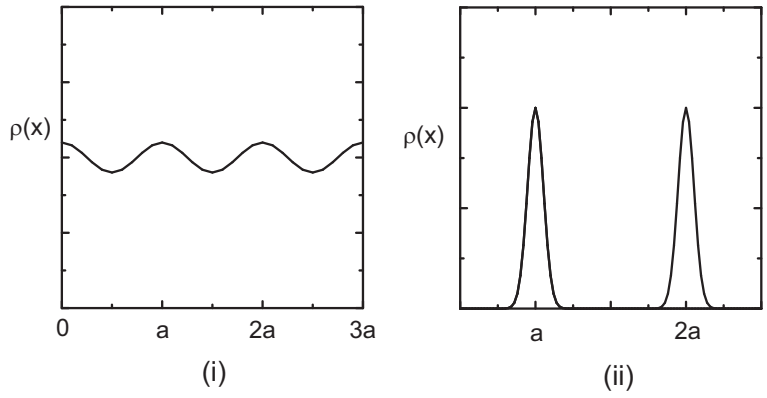

Figure 1.4: Schematic view of the charge density of electrons: (i) the case of $a \ll a_{\rm B}$, and (ii) $a \gg a_{\rm B}$.

realize the most fundamental properties of electrons in solids. In order to clarify the point step by step we begin with the simplest model that shows the essence of itinerant as well as localized natures of electrons in solids. Consider the simple cubic lattice of hydrogen atoms. We assume for simplicity that protons have no spin and are fixed at lattice points $\boldsymbol{R}_i$ with distance a from the nearest neighbors. By this simplification we neglect the effect of lattice vibrations present in real solids. The hydrogen lattice does not have incomplete atomic shells with $3d, 4f$ or $5f$ orbitals which are important for the occurrence of heavy electrons. These complications will be discussed in later chapters.

The Hamiltonian is given in the second quantization by

$$H = \sum_{\sigma} \int d\boldsymbol{r} \Psi_{\sigma}^{\dagger}(\boldsymbol{r})[-\frac{\Delta}{2m} - \sum_{i} v(\boldsymbol{r} - \boldsymbol{R}_i)]\Psi_{\sigma}(\boldsymbol{r}) + \frac{1}{2}\sum_{i \neq j} v(\boldsymbol{R}_i - \boldsymbol{R}_j) + V_C \tag{1.4}$$

where $\Psi_{\sigma}(\boldsymbol{r})$ is the field operator of electron with spin σ, $v(\boldsymbol{r}) = e^2/|\boldsymbol{r}|$ and V_C is the Coulomb interaction among electrons given by

$$V_C = \frac{1}{2}\int d\boldsymbol{r} \int d\boldsymbol{r}' v(\boldsymbol{r} - \boldsymbol{r}') \sum_{\sigma,\sigma'} \Psi_{\sigma}^{\dagger}(\boldsymbol{r})\Psi_{\sigma'}^{\dagger}(\boldsymbol{r}')\Psi_{\sigma'}(\boldsymbol{r}')\Psi_{\sigma}(\boldsymbol{r}). \tag{1.5}$$

Two extreme cases are considered: (i) a is much smaller than the Bohr radius $a_{\rm B} = 1/(me^2)$, and (ii) $a \gg a_{\rm B}$. Figure 1.4 illustrates the charge density of electrons in each case.

1.2.1 Formation of energy bands

In the case (i) the wave functions of each 1s state overlap with each other substantially. As a result, mixing with 2s, 2p and higher orbitals is so significant that the wave function is better constructed from plane waves. The kinetic energy of electrons is the most important part and the fluctuation $\langle (n_{\sigma}(\boldsymbol{r}) - \langle n_{\sigma}(\boldsymbol{r})\rangle)(n_{\sigma'}(\boldsymbol{r}') - \langle n_{\sigma'}(\boldsymbol{r}')\rangle)\rangle$ of the operator $n_{\sigma}(\boldsymbol{r}) = \Psi_{\sigma}^{\dagger}(\boldsymbol{r})\Psi_{\sigma}(\boldsymbol{r})$ becomes small as compared with $\langle n_{\sigma}(\boldsymbol{r})\rangle\langle n_{\sigma'}(\boldsymbol{r}')\rangle$. Then the simplest approximation is to replace the electron-electron interaction by a mean-field acting on $n_{\sigma}(\boldsymbol{r})$. Namely we approximate

$$\Psi_{\sigma}^{\dagger}(\boldsymbol{r})\Psi_{\sigma'}^{\dagger}(\boldsymbol{r}')\Psi_{\sigma'}(\boldsymbol{r}')\Psi_{\sigma}(\boldsymbol{r}) \sim n_{\sigma}(\boldsymbol{r})\langle n_{\sigma'}(\boldsymbol{r}')\rangle + \langle n_{\sigma}(\boldsymbol{r})\rangle n_{\sigma'}(\boldsymbol{r}') - \langle n_{\sigma}(\boldsymbol{r})\rangle\langle n_{\sigma'}(\boldsymbol{r}')\rangle. \tag{1.6}$$

This is called the Hartree approximation. Note that eq.(1.6) does not exhaust factorization into fermion bilinear operators. The rests are called exchange terms to be explained shortly. In the Hartree approximation H is approximated by

$$H_H = \int d\boldsymbol{r} \sum_{\sigma} \Psi_{\sigma}^{\dagger}(\boldsymbol{r}) h_H(\boldsymbol{r}) \Psi_{\sigma}(\boldsymbol{r}) + E_D, \tag{1.7}$$

where the constant E_D is given by

$$E_D = \frac{1}{2}\sum_{i \neq j} v(\boldsymbol{R}_i - \boldsymbol{R}_j) - \frac{1}{2}\int d\boldsymbol{r} \int d\boldsymbol{r}' v(\boldsymbol{r} - \boldsymbol{r}') \sum_{\sigma,\sigma'} \langle n_{\sigma}(\boldsymbol{r})\rangle\langle n_{\sigma'}(\boldsymbol{r}')\rangle. \tag{1.8}$$

The effective single-particle Hamiltonian $h_H(\boldsymbol{r})$ is defined as

$$h_H(\boldsymbol{r}) = -\frac{\Delta}{2m} + v_H(\boldsymbol{r}), \tag{1.9}$$

where the one-body potential $v_H(\boldsymbol{r})$ is given by

$$v_H(\boldsymbol{r}) = \int d\boldsymbol{r}' v(\boldsymbol{r}-\boldsymbol{r}')[\sum_\sigma \langle n_\sigma(\boldsymbol{r}')\rangle - \sum_j \delta(\boldsymbol{r}'-\boldsymbol{R}_j)]. \tag{1.10}$$

We notice that the electron-ion attraction alone would give divergent potential. Only with partial cancellation of it by the electron-electron repulsion does one have a finite potential as given by eq.(1.10).

Let's consider the Schrödinger equation

$$h_H(\boldsymbol{r})\phi_n(\boldsymbol{r}) = E_n\phi_n(\boldsymbol{r}). \tag{1.11}$$

where the eigenvalue E_n is indexed from the lowest one as $E_1, E_2, \ldots$. Here we take the periodic boundary condition with the dimension L of the system in each direction. Strictly speaking, the Coulomb interaction should in this case be modified in order to meet the periodic boundary condition. We neglect this modification since this does not influence the final result in the limit of large L. In terms of the complete set $\{\phi_n\}$, the field operator is expanded as

$$\Psi_\sigma(\boldsymbol{r}) = \sum_n c_{n\sigma}\phi_n(\boldsymbol{r}), \tag{1.12}$$

where $c_{n\sigma}$ is the annihilation operator. The N-body ground state $|g\rangle$ with N even is constructed from the vacuum $|vac\rangle$ by filling $N/2$ states for each spin:

$$|g\rangle = \prod_\sigma \prod_{n=1}^{N/2} c_{n\sigma}^\dagger |vac\rangle. \tag{1.13}$$

In the first quantization the state $|g\rangle$ is represented by a single Slater determinant. The electron density is given by

$$\langle n_\sigma(\boldsymbol{r}')\rangle = \sum_{n=1}^{N/2} |\phi_n(\boldsymbol{r}')|^2, \tag{1.14}$$

which in turn determines the Hartree potential $v_H(\boldsymbol{r})$ self-consistently by eq.(1.10). In the ground state the N electrons fill the lower half of the first band. The set of highest occupied $\boldsymbol{k}$ states constitutes the Fermi surface. The volume V_F enclosed by the Fermi surface is related to the electron density $n = N/L^3$ by $V_F/(2\pi)^3 = n/2$.

The Hartree approximation has a weakness that v_H gives nonzero electron-electron interaction even when there is only a single electron. This is due to neglect of the quantum nature of $n_\sigma(\boldsymbol{r})$, the proper account of which should exclude self-interaction of an electron. To remedy this, one should take account of other contributions to the mean field from

$$\Psi_\sigma^\dagger(\boldsymbol{r})\Psi_{\sigma'}^\dagger(\boldsymbol{r}')\Psi_{\sigma'}(\boldsymbol{r}')\Psi_\sigma(\boldsymbol{r}) \rightarrow \tag{1.15}$$

$$-\langle\Psi_\sigma^\dagger(\boldsymbol{r})\Psi_{\sigma'}(\boldsymbol{r}')\rangle\Psi_{\sigma'}^\dagger(\boldsymbol{r}')\Psi_\sigma(\boldsymbol{r}) - \Psi_\sigma^\dagger(\boldsymbol{r})\Psi_{\sigma'}(\boldsymbol{r}')\langle\Psi_{\sigma'}^\dagger(\boldsymbol{r}')\Psi_\sigma(\boldsymbol{r})\rangle + \langle\Psi_\sigma^\dagger(\boldsymbol{r})\Psi_{\sigma'}(\boldsymbol{r}')\rangle\langle\Psi_{\sigma'}^\dagger(\boldsymbol{r}')\Psi_\sigma(\boldsymbol{r})\rangle. \tag{1.16}$$

The approximation which keeps this contribution in addition to $v_H(\boldsymbol{r})$ is called the Hartree-Fock approximation. In this case the mean field acts not only on $n_\sigma(\boldsymbol{r})$ but on a non-local operator $\Psi_{\sigma'}^\dagger(\boldsymbol{r}')\Psi_\sigma(\boldsymbol{r})$. If a magnetic order is present, $\langle\Psi_{\sigma'}^\dagger(\boldsymbol{r}')\Psi_\sigma(\boldsymbol{r})\rangle$ may not be diagonal in spin indices. The scheme to allow for this possibility is often called the unrestricted Hartree-Fock theory.

One obtains the Hamiltonian which is bilinear in the electron fields as

$$H_{HF} = \int d\boldsymbol{r}\int d\boldsymbol{r}' \sum_{\sigma,\sigma'} \Psi_\sigma^\dagger(\boldsymbol{r}) h_{\sigma\sigma'}(\boldsymbol{r},\boldsymbol{r}')\Psi_{\sigma'}(\boldsymbol{r}') + E_{DX}, \tag{1.17}$$

where

$$h_{\sigma\sigma'}(\boldsymbol{r},\boldsymbol{r}') = h_H(\boldsymbol{r})\delta_{\sigma,\sigma'}\delta(\boldsymbol{r}-\boldsymbol{r}') - v(\boldsymbol{r}-\boldsymbol{r}')\langle\Psi_{\sigma'}^\dagger(\boldsymbol{r}')\Psi_\sigma(\boldsymbol{r})\rangle. \tag{1.18}$$

$$E_{DX} = E_D + \frac{1}{2}\int d\boldsymbol{r}\int d\boldsymbol{r}' v(\boldsymbol{r}-\boldsymbol{r}')\sum_{\sigma,\sigma'}\langle\Psi^\dagger_{\sigma'}(\boldsymbol{r}')\Psi_\sigma(\boldsymbol{r})\rangle\langle\Psi^\dagger_\sigma(\boldsymbol{r})\Psi_{\sigma'}(\boldsymbol{r}')\rangle. \tag{1.19}$$

The one-body Schrödinger equation reads

$$\int d\boldsymbol{r}' \sum_{\sigma'} h_{\sigma\sigma'}(\boldsymbol{r},\boldsymbol{r}')\psi_n(\boldsymbol{r}',\sigma') = E_{n\sigma}\psi_n(\boldsymbol{r},\sigma), \tag{1.20}$$

which takes into account a possible spin polarization in the ground state.

The Hartree-Fock Hamiltonian H_{HF} can have Bloch states as a self-consistent solution for the paramagnetic state. Then the ground-state wave function is given by a single Slater determinant as in eq.(1.13). It is noted that the self-consistent solution is not necessarily unique. Among the states given by a single Slater determinant, each self-consistent solution satisfies the variational property that the ground-state energy is stationary against small variation around the solution. The state that gives a local minimum is either the ground state or a metastable state.

The average magnitude of the electron-electron interaction is much smaller than the width of the energy band in the case (i). Thus in the zero-th approximation the Bloch picture of nearly free electrons is valid. One can naturally ask the importance of fluctuations so far neglected. Because the excitation has no gap in the band state, this may lead to singularities in the perturbation theory. In the one-dimensional system, it is known that virtual transitions across the Fermi surface make the Hartree-Fock state unstable, however weak the two-body interaction is. This is characteristic in one-dimension because the phase space available to the particle-hole excitation is particularly large in one dimension. In three dimensions, a small two-body interaction only perturbs the Hartree-Fock ground state. Thus the metallic character with the Fermi surface remains. In the presence of strong two-body interactions, the paramagnetic state may become unstable against magnetic or superconducting states. If the state remains paramagnetic, a theorem on the Fermi liquid theory shows that the volume enclosed by the Fermi surface is the same as the one determined by the mean-field theory [7]. However the excitation spectrum may be drastically affected by the correlation. In the case of high electron density the difference from the Hartree approximation is not important qualitatively. The common feature is that the ground state is a metal with a Fermi surface.

We will come back to discuss the correlation problem in detail, but for the moment let us continue on very elementary picture of electrons.

1.2.2 Localized states

In the case (ii) with $a \gg a_B$, one starts from the atomic picture of the ground state in which each proton has an electron in its 1s orbital, and the influence from other hydrogens is a small perturbation. In this case the ground state should be insulating. According to Mott [8], such insulating state can be found in actual materials, although the electronic state is much more complicated than the hydrogen lattice. In the energy band picture, the insulating state needs a long-range order of spins so that the unit cell contains even number of electrons. In reality, some materials such as NiS remains insulating even above the transition temperature to an antiferromagnetic state. If one applies pressure, or replaces some constituent atoms to cause equivalent chemical effect, systems such as V_2O_3 [8] could be changed into a metal. Such systems are often called Mott insulators.

We inspect whether the mean-field theory can deal with the case of $a \gg a_B$. If we start from the paramagnetic ground state, the many-electron wave function given by the Slater determinant of Bloch states give substantial probability of having both up- and down-spin electrons in a 1s orbital. However with $a \gg a_B$ there should be either up or down spin but not both in each 1s orbital.

Therefore we consider artificially the situation where all electrons have spin up. Also in this case the Hartree approximation cannot deal with the situation because $v_H(\boldsymbol{r})$ cannot reproduce the potential for the hydrogen atom. The exchange potential, on the other hand, cancels most of the direct Coulomb interaction from the same cell. As a result the Hartree-Fock Hamiltonian reproduces the limit of weakly coupled hydrogens as long as the spin is completely polarized.

This observation permits us to define the basis functions which are necessary to establish the localized picture [9, 10]. Suppose we have solved the Hartree-Fock equation assuming a fully polarized ground state. Then the lowest energy band, which consists dominantly of the 1s state at each site, is full. The next lowest bands separated by the energy gap consist of 2s and 2p states. In the case of (ii) the gap

should be about $0.75Ryd$. From the Bloch functions $\psi_{\boldsymbol{k}}(\boldsymbol{r})$ of the lowest band we construct the Wannier function by

$$w_i(\boldsymbol{r}) = \frac{1}{\sqrt{N}} \sum_{\boldsymbol{k}} \psi_{\boldsymbol{k}}(\boldsymbol{r}) \exp(-i\boldsymbol{k} \cdot \boldsymbol{R}_i), \tag{1.21}$$

which is similar to the 1s wave function at site $\boldsymbol{R}_i$. In contrast to the atomic wave function, the Wannier functions constitute an orthogonal set. The annihilation operator $c_{i\sigma}$ corresponding to this Wannier state is defined by

$$c_{i\sigma} = \int d\boldsymbol{r} w_i^*(\boldsymbol{r}) \Psi_\sigma(\boldsymbol{r}). \tag{1.22}$$

Furthermore the eigenenergy $E_{\boldsymbol{k}}$ of the first band is Fourier transformed to give

$$t_{ij} = \frac{1}{\sqrt{N}} \sum_{\boldsymbol{k}} E_{\boldsymbol{k}} \exp[i\boldsymbol{k} \cdot (\boldsymbol{R}_i - \boldsymbol{R}_j)]. \tag{1.23}$$

Here $t_{ii} \equiv \epsilon_a$ represents the 1s level with a possible shift, and t_{ij} with $i \neq j$ is the hopping energy between the sites i, j. Explicitly t_{ij} is given by

$$t_{ij} = \int d\boldsymbol{r} \int d\boldsymbol{r}' w_i^*(\boldsymbol{r}) h_{\uparrow\uparrow}(\boldsymbol{r}, \boldsymbol{r}') w_j(\boldsymbol{r}'). \tag{1.24}$$

We are now ready to represent the original Hamiltonian given by eq.(1.4) in terms of the Wannier basis. Since the complete set has infinitely many energy bands, the number of Wannier states is also infinite. If we are interested in the ground state and low-lying excitations, the subspace consisting of 1s states but with arbitrary spin configurations is the most important one. We introduce a projection operator P_{1s} to this subspace. Then we get

$$P_{1s} H P_{1s} = H_1 + H_2 + E_{DX}, \tag{1.25}$$

$$H_1 = \sum_{i\sigma} \epsilon_a c_{i\sigma}^\dagger c_{i\sigma} + \sum_{i \neq j, \sigma} t_{ij} c_{i\sigma}^\dagger c_{j\sigma}, \tag{1.26}$$

$$H_2 = \frac{1}{2} \sum_{ijlm} \sum_{\sigma\sigma'} \langle ij|v|ml\rangle (c_{i\sigma}^\dagger c_{j\sigma'}^\dagger c_{m\sigma'} c_{l\sigma} - c_{i\sigma}^\dagger c_{l\sigma} \delta_{jm} + c_{i\sigma}^\dagger c_{m\sigma'} \delta_{\sigma\sigma'} \delta_{jl}), \tag{1.27}$$

where

$$\langle ij|v|ml\rangle = \int d\boldsymbol{r} \int d\boldsymbol{r}' v(\boldsymbol{r} - \boldsymbol{r}') w_i^*(\boldsymbol{r}) w_j^*(\boldsymbol{r}') w_m(\boldsymbol{r}') w_l(\boldsymbol{r}). \tag{1.28}$$

Note that we use the ordering of basis in the bra as defined by $\langle ij| = |ji\rangle^\dagger$ throughout the book. The bilinear terms in H_2 compensate the mean-field contribution to t_{ij}. Without the mean-field contribution, t_{ij} would become infinite because of the long range of the Coulomb interaction. Thus the mean field is by no means a small perturbation.

The nature of $w_i(\boldsymbol{r})$ localized around $\boldsymbol{R}_i$ makes most of $\langle ij|v|ml\rangle$ small, leaving two kinds of dominant terms in H_2: first, terms of the type $\langle ij|v|ji\rangle$ remain significant even for a pair of distant sites i and j, and second the exchange terms of the type $\langle ij|v|ij\rangle$ for neighboring sites. The first type is called the Coulomb integral and is responsible for the charge fluctuations like plasma oscillation and exciton-type correlation. On the other hand the second type is called the exchange integral and favors the parallel arrangement of spins at neighboring sites.

The simplest way to see the effect of each term on the spin configuration is to take $N = 2$ with the free boundary condition, which makes possible the analogy to the hydrogen molecule. In H_2 we keep $U \equiv \langle 11|v|11\rangle$, $K \equiv \langle 12|v|21\rangle$, $J_d \equiv \langle 12|v|12\rangle$ and equivalent ones, all of which are positive. In this case exact solution of $H_1 + H_2$ is easily obtained. Of the six states in total, three of them are spin triplet with energy $E_t = 2\epsilon_a$. Of the three singlet states, the lowest one has the energy

$$E_s = 2\epsilon_a + J_d + (U - K)/2 - [(U - K)^2/4 + 4t_{12}^2]^{1/2}, \tag{1.29}$$

and the double occupation of a site tends to zero in the limit of $a \gg a_B$. In this limit U is much larger than $|t_{12}|$ and K. Then we may expand the square root to first order. It is convenient to use the projection operators P_s and P_t to the singlet and triplet pairs as given by

$$P_s = \frac{1}{4} - \boldsymbol{S}_1 \cdot \boldsymbol{S}_2, \quad P_t = \frac{3}{4} + \boldsymbol{S}_1 \cdot \boldsymbol{S}_2, \tag{1.30}$$

in terms of spin operators $\boldsymbol{S}_1$ and $\boldsymbol{S}_2$. Then we obtain the effective Hamiltonian to describe the singlet and triplet states:

$$H_{spin} = E_s P_s + E_t P_t \sim 2\epsilon_a + \frac{1}{4}J_d - \frac{t_{12}^2}{(U-K)} + \left[\frac{4t_{12}^2}{(U-K)} - J_d\right] \boldsymbol{S}_1 \cdot \boldsymbol{S}_2. \tag{1.31}$$

The coefficient of the spin-dependent term is called the exchange interaction. Two competing effects are present here. The part with the transfer favors the singlet pair. This is because the doubly occupied site can occur as the intermediate state by perturbation in terms of t_{12}. On the other hand, J_d favors the triplet pair. This gain of energy originates from the Pauli principle which discourages the overlap of wave functions with the same spin.

In the Heitler-London theory for the bonding of hydrogen molecule, the stability of the singlet state is interpreted in terms of Coulomb attraction due to accumulated electrons in between the protons. The stabilization by the kinetic exchange represents the same accumulation effect in different terms. Note that the use of orthogonal states is especially convenient in dealing with large systems. In the case of general N, the competing exchange mechanisms described above are also present. Since J_d decays faster than t_{12}^2 as a/a_B increases, the kinetic exchange wins in the case (ii). In addition, more complicated exchange involving more than two sites is possible. For general N we cannot expect the exact solution even in the 1s subspace. Instead we introduce below a version of perturbation theory for a systematic treatment.

Let us describe in general the effective Hamiltonian which acts on the restricted Hilbert space M called the model space [10, 11]. We introduce a projection operator P to the model space M by

$$P = \sum_{\alpha \in M} |\alpha\rangle\langle\alpha| \tag{1.32}$$

where $|\alpha\rangle$ denotes a state in M. From a state Ψ_i which is an eigenstate of H with eigenvalue E_i, we make a projected wave function $P\Psi_i$. We define the effective Hamiltonian H_{eff} such that the same eigenvalues are reproduced within the model space, i.e.,

$$H_{eff} P\Psi_i = E_i P\Psi_i. \tag{1.33}$$

Since the dimension of M is less than that of the original Hilbert space, some $P\Psi_i$ are actually zero. The effective Hamiltonian is useful only if the states of interest have nonzero $P\Psi_i$. If Ψ_i has a substantial weight in M, the projection can be performed accurately by lower-order perturbation theory. It should be noted, however, that in strongly correlated systems one often has to work with a model space with very small weight. This is typically the case when one deals with the Kondo effect.

The unperturbed Hamiltonian is defined as $H_0 = PHP + QHQ$ with $Q = 1 - P$. The perturbation part is then given by $V = H - H_0 = PHQ + QHP$. It is obvious that P and Q commute with H_0. The Schrödinger equation $H\Psi_i = E_i\Psi_i$ is written in the form,

$$(E_i - H_0)Q\Psi_i = QV\Psi_i. \tag{1.34}$$

In terms of the operator $R(E) = (E - H_0)^{-1}$ which is called the resolvent, we get

$$Q\Psi_i = R(E_i)QV\Psi_i. \tag{1.35}$$

This form is convenient for iteration. Namely we obtain

$$\Psi_i = P\Psi_i + Q\Psi_i = \sum_{n=0}^{\infty} [R(E_i)QV]^n P\Psi_i \equiv \Omega(E_i)P\Psi_i, \tag{1.36}$$

where the wave operator $\Omega(E)$ is introduced in the last part. Thus H_{eff} which satisfies eq.(1.33) is given by

$$H_{eff}(E_i) = PH\Omega(E_i)P, \tag{1.37}$$

where the rightmost P could equally be removed by the property $P^2 = P$. The notable feature here is that $H_{eff}(E_i)$ depends on the eigenvalue to be derived. This kind of formalism with self-consistency condition for E_i is called the Brillouin-Wigner perturbation theory. It is possible to eliminate the energy dependence in H_{eff} by a modification of the above expansion. The resultant formalism is called the

Rayleigh-Schrödinger perturbation theory, which is more commonly used in quantum mechanics. We explain the latter scheme in Appendix C in connection to the renormalization of the Kondo model. Up to second order in V, there is no difference between the two kinds of perturbation theory.

In the case of the hydrogen lattice with $a/a_B \gg 1$, it is appropriate to define the model space M as the singly occupied set of 1s Wannier orbitals. The perturbation part V consists of the hopping and the two-body interactions. In the lowest order in V, we replace E_i by the unperturbed one $N\epsilon_a$. Then we get

$$H_{eff} = H_0 + PV(N\epsilon_a - H_0)^{-1}QVP. \tag{1.38}$$

Of the two competing exchanges, J_d comes from H_0 and the kinetic exchange from the second term. If one uses the atomic 1s orbital, U is calculated to be 17 eV. However, as one goes higher in V, the parameters M_d and U are renormalized by the presence of 2s and other orbitals. In actual solids, this polarization effect reduces U drastically (to about half). It is therefore very difficult to obtain the exchange parameter from first principles. It should be emphasized that the magnitude of the exchange and other parameters in the effective Hamiltonian depends on the model space chosen. This feature is often overlooked in the literature and causes confusion in interpretation of experimental data.

Another higher order effect of V is to produce many-spin exchange terms. Estimation of the magnitude is even more difficult than the two-spin exchange. We only note here that in some cases the spin ordering experimentally observed requires significant three-spin or four-spin interactions [12, 13].

The most important feature in the case (ii) is that the energy gap of the order of 0.75 Ryd survives for any spin configuration, and that the system needs a finite threshold energy to conduct the electronic current. Thus the system behaves as an insulator at absolute zero. However, spin excitations from the ground state are gapless. In the case of magnetically ordered ground state the gapless excitation is related to the Goldstone theorem on the spontaneous breakdown of the continuous symmetry [14]. We emphasize that this insulating state is different from the band insulator where there are an even number of electrons per cell. In the latter case the energy gap is both for spin and charge excitations as exemplified by solid He with $1s^2$ configuration. The band insulator is smoothly connected to weakly interacting atoms as the lattice parameter increases in this case.

Let us summarize the two fundamental characters of electrons in the hydrogen lattice. In the case where the kinetic energy is the most important quantity as in high densities, the ground state is a metal and electrons form energy bands. In the opposite case where the Coulomb repulsion among electrons is the most important one, the ground state is insulating and the electrons are localized. Except in one dimension, the ground state has a certain kind of magnetic order.

The fundamental question to ask is what happens in the case of $a \sim a_{\rm B}$. The question was raised by Mott [8], and the effort to answer this question has opened remarkably rich outcomes in both experiment and theory. We will explore the actual examples in this book. In closing this section we introduce the simplest model that is still capable of describing both itinerant and localized features of electrons. Namely in H_2 given by eq.(1.28) we keep only the largest term in $\langle ij|v|lm\rangle$ that corresponds to the case of $i = j = l = m$. Then H_2 is replaced by

$$H_2 \to U\sum_i (n_{i\uparrow}n_{i\downarrow} - n_{i\uparrow} - n_{i\downarrow}) \equiv H_U - UN_e. \tag{1.39}$$

where $U = \langle ii|v|ii\rangle$ and $n_{i\sigma} = a^\dagger_{i\sigma}a_{i\sigma}$, and N_e is the total number of electrons which may not be equal to N. The resultant model $H_1 + H_U$ is called the Hubbard model [15, 16, 17]. Namely the Hubbard model H_{Hub} is given by

$$H_{Hub} = \sum_{i\sigma} \epsilon_a c^\dagger_{i\sigma}c_{i\sigma} + \sum_{i\neq j,\sigma} t_{ij}c^\dagger_{i\sigma}c_{j\sigma} + U\sum_i n_{i\uparrow}n_{i\downarrow} \tag{1.40}$$

We note that the fully polarized Hartree-Fock state becomes an eigenstate of the Hubbard model. However, this ferromagnetic state costs more energy in H_1 given by eq.(1.26) than the paramagnetic and antiferromagnetic states. According to available exact solution in one dimension, the ferromagnetic state is not actually the ground state [18].

In heavy-electron systems, the Hubbard model with a single energy band is actually too simplistic. The minimum elements to be included are not only a conduction band but nearly localized electrons. The simplest model with these two kinds of states is called the Anderson lattice, which will be discussed in Chapter 3.

1.3 Fundamentals of Spin Dynamics

1.3.1 Itinerant magnetic moments

In the case of a single conduction band, the magnetization $\boldsymbol{M}_i$ at site i is given by

$$\boldsymbol{M}_i = -\frac{1}{2} g\mu_B c_{i\alpha}^\dagger \boldsymbol{\sigma}_{\alpha\gamma} c_{i\gamma}, \tag{1.41}$$

where $\boldsymbol{\sigma}$ denotes the vector composed of the Pauli matrices, α and γ are spin components, and g is the g-factor. The Fourier transform $\boldsymbol{M}(\boldsymbol{q})$ of $\boldsymbol{M}_i$ is given by

$$\boldsymbol{M}(\boldsymbol{q}) = -\frac{1}{2} g\mu_B \sum_{\boldsymbol{k}\alpha\gamma} c_{\boldsymbol{k}\alpha}^\dagger \boldsymbol{\sigma}_{\alpha\gamma} c_{\boldsymbol{k}+\boldsymbol{q}\gamma}. \tag{1.42}$$

If the spin-orbit interaction is strong in the band, one should interpret the spin indices α, γ as representing a state in a Kramers doublet for each momentum. In this case the g-factor should also be replaced by a tensor. We shall encounter an important example of this case in the superconductivity of heavy electrons in Chapter 5.

The dynamical property of the magnetic moment is most conveniently characterized by the linear response against external perturbation. The linear response theory provides the dynamical magnetic susceptibility tensor $\mu_B^2 \chi_{\alpha\gamma}(\boldsymbol{q}, \omega)$ in terms of the statistical average of the commutator

$$\mu_B^2 \chi_{\alpha\gamma}(\boldsymbol{q}, \omega) = \frac{i}{V} \int_0^\infty dt \exp(i\omega t) \langle [M_\alpha(\boldsymbol{q}, t), M_\gamma(-\boldsymbol{q})] \rangle, \tag{1.43}$$

where V is the volume of the system, and $M_\alpha(\boldsymbol{q}, t) = \exp(iHt) M_\alpha(\boldsymbol{q}) \exp(-iHt)$ is the magnetization in the direction α. Here we take the Heisenberg picture with Hamiltonian H. The statistical average is taken with respect to the Boltzmann weight factor $\exp(-\beta H)/Z$ with Z being the partition function $\mathrm{Tr} \exp(-\beta H)$. We refer to Appendix A for brief review of linear response theory.

We begin with the simplest case of a free electron gas for which the dynamical magnetic susceptibility can be obtained exactly. Note that

$$M_+(\boldsymbol{q}) = M_x(\boldsymbol{q}) + iM_y(\boldsymbol{q}) = -\mu_B \sum_{\boldsymbol{k}} c_{\boldsymbol{k}\uparrow}^\dagger c_{\boldsymbol{k}+\boldsymbol{q}\downarrow}, \tag{1.44}$$

with $g = 2$, and that the time dependence is simply given by $c_{\boldsymbol{k}\sigma}(t) = \exp(-i\epsilon_{\boldsymbol{k}} t) c_{\boldsymbol{k}\sigma}$. Then we use the commutation rule

$$[c_1^\dagger c_2, c_3^\dagger c_4] = \delta_{23} c_1^\dagger c_4 - \delta_{14} c_3^\dagger c_2 \tag{1.45}$$

where the obvious set of quantum numbers have been abbreviated symbolically. The magnetic susceptibility is then given by

$$\mu_B^2 \chi_0(\boldsymbol{q}, \omega) = \frac{2\mu_B^2}{V} \sum_{\boldsymbol{k}} \frac{f(\epsilon_{\boldsymbol{k}+\boldsymbol{q}}) - f(\epsilon_{\boldsymbol{k}})}{\omega - \epsilon_{\boldsymbol{k}+\boldsymbol{q}} + \epsilon_{\boldsymbol{k}} + i\delta}, \tag{1.46}$$

which in this case is a scalar. Here $f(\epsilon) = [\exp(\beta\epsilon) + 1]^{-1}$ is the Fermi distribution function with the chemical potential being the origin of energy.

1.3.2 Localized magnetic moments

Heavy electrons are observed mainly in rare-earth and actinide compounds. These compounds have incomplete f shells which have finite magnetic moments. We summarize elementary facts about magnetic moments associated with f shells [19].

Let us consider a case of a free trivalent Ce ion with the electron configuration $(4f)^1$ on top of Xe configuration. The spin-orbit interaction splits the 14-fold degenerate level with the orbital angular momentum $L = 3$ and the spin $S = 1/2$ into two levels with $J = L + S = 7/2$ and $J = L - S = 5/2$ where J is the total angular momentum. The 6-fold degenerate level with $J = 5/2$ lies lower than the $J = 7/2$ level by about 0.3 eV.

The magnitude of the magnetic moment M associated with the $J = 5/2$ level is given by $M = -g_J \mu_B J$ where μ_B is the Bohr magneton and

$$g_J = \frac{3}{2} + \frac{S(S+1) - L(L+1)}{2J(J+1)} \tag{1.47}$$

is the Landé g-factor.

In the case of a free rare-earth ion with more f electrons, the energy levels are described by the LS-coupling (or Russel-Saunders) scheme. Here one first neglects the spin-orbit interaction and takes a multiplet with definite angular momenta $\boldsymbol{S}$ and $\boldsymbol{L}$. The effect of spin-orbit interaction is approximated by the term $H_{LS} = \lambda \boldsymbol{L} \cdot \boldsymbol{S}$ where λ gives the strength of the interaction. According to an empirical rule called the Hund rule, the ground state of the atom takes the largest possible S and the largest L allowed for the S. The effective Hamiltonian H_{LS} should work if the magnitude of λ is much smaller than the splitting of multiplets with different L and S. The sign of λ is positive for a less-than-half filled shell, i.e. less than seven $4f$ electrons, and favors antiparallel $\boldsymbol{L}$ and $\boldsymbol{S}$. On the other hand, λ is negative for a more-than-half filled shell. Thus in the case of trivalent Yb with 13 electrons in the $4f$ shell, the spin-orbit interaction favors parallel $\boldsymbol{L}$ and $\boldsymbol{S}$, leading to the ground level with $J = 7/2$. The spin-orbit splitting is larger than the Ce case, and amounts to 0.8 eV.

The actinides have even larger spin-orbit interaction, and the LS-coupling scheme for describing levels within a multiplet is not so accurate as in rare-earths. However at least for light actinides like U, the scheme is still practical for discussion of energy levels.

A rare-earth or an actinide ion in a crystal feels the potential of the environment. The relevant point group symmetry is lower than the spherical one. As a result the degeneracy $2J + 1$ for a spin-orbit level with the angular momentum J is split into sublevels. This splitting as well as associated physical effects are called crystalline-electric-field (CEF) effects. In the case of Ce^{3+} in a cubic CEF, for example, the $J = 5/2$ level is split into a doublet called Γ_7 and a quartet called Γ_8. The CEF eigenstates are given for the Γ_7 by

$$\psi_{7,\pm} = \sqrt{\frac{1}{6}} |\pm \frac{5}{2}\rangle - \sqrt{\frac{5}{6}} |\mp \frac{3}{2}\rangle, \tag{1.48}$$

in terms of the eigenstates of J_z. The eigenstates for Γ_8 are given by

$$\psi_{8A,\pm} = \sqrt{\frac{5}{6}} |\pm \frac{5}{2}\rangle + \sqrt{\frac{1}{6}} |\mp \frac{3}{2}\rangle, \quad \psi_{8B,\pm} = |\pm \frac{1}{2}\rangle \tag{1.49}$$

The magnetic moment operator M_z has nonvanishing matrix elements only within a CEF level. However the M_x and M_y components have finite elements both within the CEF levels and between different levels.

In order to describe the localized levels and transitions between them, it is convenient to introduce an operator $X_{\mu\nu} \equiv |\mu\rangle\langle\nu|$ which describes a transition from a localized multi-electron state $|\nu\rangle$ to another state $|\mu\rangle$. In the case of $\nu = \mu$, $X_{\mu\mu} \equiv |\mu\rangle\langle\mu|$ becomes a projection operator onto $|\mu\rangle$. The set of localized levels $\{E_\mu\}$ with inclusion of the spin-orbit interaction and CEF effects is summarized by the Hamiltonian H_l as

$$H_l = \sum_\mu E_\mu X_{\mu\mu}. \tag{1.50}$$

The magnetic moment in the z-direction is expressed as

$$M_z = \sum_{\mu\nu} \langle\mu|M_z|\nu\rangle X_{\mu\nu}, \tag{1.51}$$

The Lande g-factor is included in the matrix element $\langle\mu|M_z|\nu\rangle$.

It is sometimes convenient to associate a pseudo spin 1/2 with the doublet CEF. We derive the effective g-factor taking as an example the tetragonal CEF. The basis functions of the lowest doublet $|\pm\rangle$ are given by

$$|\pm\rangle = a|\pm 5/2\rangle - b|\mp 3/2\rangle, \tag{1.52}$$

where a, b are real parameters with the constraint $a^2 + b^2 = 1$. We calculate a matrix element

$$\frac{1}{\mu_B}\langle +|M_z|+\rangle = \left(\frac{5}{2}a^2 - \frac{3}{2}b^2\right) g_J \equiv -\frac{1}{2} g_z, \tag{1.53}$$

where we introduce the effective g-factor g_z along the z-direction. Similarly we introduce the perpendicular component $g_\perp = g_x = g_y$ by

$$\langle +|M_x + iM_y|-\rangle = -g_\perp \mu_B. \tag{1.54}$$

Then a simple calculation gives

$$g_z = -\frac{6}{7}(1 + 4\cos 2\theta),\ g_\perp = \frac{6\sqrt{5}}{7}\sin 2\theta, \tag{1.55}$$

with $a = \cos\theta$, and we have put $g_J = -6/7$. In the special case of cubic symmetry, we get $g_z = g_\perp = 10/7$ with $\cos\theta = 1/\sqrt{6}$. Figure 1.5 shows each component as functions of θ. It should be noted that the effective g-factor can be very anisotropic depending on the CEF; it is Ising-like with $\theta = 0, \pi$ and XY-like with $\tan^2\theta = 5/3$. In reality θ is determined as a function of the CEF parameters as explained in ref.[19] for example. The implication of the anisotropic g factor for superconductivity seems to be an important problem, but has not yet been discussed in the literature.

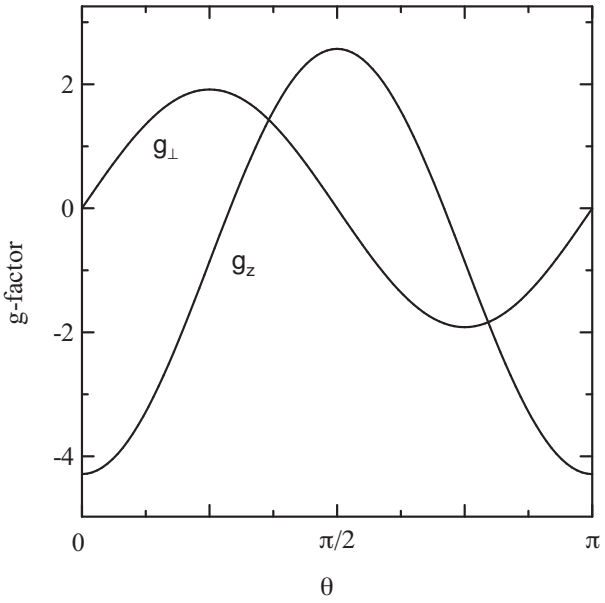

Figure 1.5: The effective g-tensor as a function of the parameter θ. See text for details.

The origin of the CEF is not only the Coulomb potential of the environment, but also includes the overlap of wave function of the ligands. The latter is called hybridization. If the perturbation energy due to hybridization is smaller than the splitting of spin-orbit split levels, one can still keep the localized picture of f electrons. In the opposite limit, $4f$ electrons can be better treated as itinerant electrons. The degree of hybridization depends on each material, but the general tendency is that $4f$ electrons are more strongly localized than 5f electrons. In particular, U ions often have hybridization strength for which neither the localized picture nor the itinerant picture applies well.

In a hypothetical case of localized electrons with no interaction with the environment, one can obtain the dynamical susceptibility exactly. With use of the X-operators the linear response formula can be evaluated directly. There is no dependence on the wave number. The result for the susceptibility $\chi_{zz}(\omega)$ at a site of localized electrons is

$$\mu_B^2 \chi_{zz}(\omega) = \sum_{\mu\nu} |\langle\mu|M_z|\nu\rangle|^2 \frac{\langle X_{\nu\nu}\rangle - \langle X_{\mu\mu}\rangle}{\omega - E_\nu + E_\mu + i\delta}. \tag{1.56}$$

The factor δ is required to make the integral converge and is related to causality.

If the external field is static the susceptibility is obtained from the formula

$$\mu_B^2 \chi_{\alpha\gamma} = \int_0^\beta d\lambda \langle e^{\lambda H} M_\gamma e^{-\lambda H} M_\alpha\rangle = \mu_B^2 \chi_{\gamma\alpha}, \tag{1.57}$$

which corresponds to the isothermal susceptibility. On the other hand, the static limit of eq.(1.56) corresponds to the adiabatic susceptibility. In the system without hybridization the result is given by

$$\chi_{zz} = \chi_{zz}(\omega \to 0) + \frac{1}{\mu_B T} \sum_{\mu\nu} |\langle \mu | M_z | \nu \rangle|^2 \langle X_{\mu\mu} \rangle, \tag{1.58}$$

where the sum in the second term is only over degenerate states μ, ν which do not contribute to the first term. The second term gives the Curie law while the first term is called the van Vleck term. Thus if the ground state of the system is degenerate the adiabatic and isothermal static susceptibilities differ by the second term. In reality, localized electrons interact with conduction electrons by hybridization, or with themselves at different sites by higher order interactions. These effects remove the degeneracy of the ground state. Then the time average becomes equivalent to the statistical average which is referred to as ergodicity. Accordingly the adiabatic and isothermal susceptibilities become the same.

1.3.3 Random phase approximation

In realistic systems, the electrons are neither free nor strictly localized. The difficulty to take reliable account of the interaction effects stimulated various theories for the dynamical response. Let us explain the simplest account of the interaction effect. To do this we write the interaction H_U given by eq.(1.39) as

$$H_U = \frac{U}{4} \sum_i (n_i^2 - m_i^2 - 4n_i) \tag{1.59}$$

where $n_i = n_{i\uparrow} + n_{i\downarrow}$ and $m_i = n_{i\uparrow} - n_{i\downarrow}$. We focus attention on the term $-m_i^2$, and decompose it as

$$m_i^2 = (\langle m_i \rangle + \delta m_i)^2 = \langle m_i \rangle^2 + 2\langle m_i \rangle \delta m_i + (\delta m_i)^2, \tag{1.60}$$

where $\delta m_i = m_i - \langle m_i \rangle$ and $\langle m_i \rangle$ means a certain average to be determined self-consistently. The approximation we make is to neglect the last term in eq.(1.60). This is a kind of mean field approximation, and is often called the random phase approximation (RPA). This is equivalent to replacing H_U in the Heisenberg picture by

$$H_{eff} = -\sum_i \phi_i(t) m_i(t) = -\sum_{\boldsymbol{q}} \int_{-\infty}^{\infty} d\omega \exp(i\boldsymbol{q} \cdot \boldsymbol{R}_i) \phi(\boldsymbol{q}, \omega) m(-\boldsymbol{q}, \omega), \tag{1.61}$$

with $\phi_i(t) = U\langle m_i(t) \rangle / 2$ being the dynamic effective field, and

$$m(-\boldsymbol{q}, \omega) = \sum_i \int_{-\infty}^{\infty} dt \exp(-i\boldsymbol{q} \cdot \boldsymbol{R}_i + i\omega t) m_i(t), \tag{1.62}$$

$$\phi(\boldsymbol{q}, \omega) = \frac{U}{2} \langle m(\boldsymbol{q}, \omega) \rangle. \tag{1.63}$$

In the presence of a space- and time-dependent external magnetic field $H \exp(i\boldsymbol{q} \cdot \boldsymbol{R}_i - i\omega t)$ along the z direction, the linear response of the system with H_{eff} is given by

$$\langle m(\boldsymbol{q}, \omega) \rangle \equiv \chi(\boldsymbol{q}, \omega) h = \chi_0(\boldsymbol{q}, \omega)[h + \phi(\boldsymbol{q}, \omega)], \tag{1.64}$$

where $h = \mu_B H$ and $\chi_0(\boldsymbol{q}, \omega)$ is given by eq.(1.46). By substituting eq.(1.63) for $\phi(\boldsymbol{q}, \omega)$ the dynamical spin susceptibility $\chi(\boldsymbol{q}, \omega)$ of the system is derived as

$$\chi(\boldsymbol{q}, \omega)^{-1} = \chi_0(\boldsymbol{q}, \omega)^{-1} - \frac{U}{2}. \tag{1.65}$$

We make two remarks about eq.(1.65). First, in the static and homogeneous limit we obtain from eq.(1.46)

$$\chi_0(\boldsymbol{0}, 0) = \frac{2}{V} \sum_k \delta(\epsilon_{\boldsymbol{k}}) \equiv \rho(\mu). \tag{1.66}$$

The RPA is a good approximation if $\alpha \equiv \rho(\mu)U/2 \ll 1$. As α increases toward unity, the contribution of fluctuations becomes important. Thus the divergence of $\chi(\boldsymbol{0}, 0)$ at $\alpha = 1$ should not be taken literally. In fact one of the most important problems in heavy electrons is to explain the stability of the paramagnetic state although the opposite limit $\alpha \gg 1$ is realized. Secondly, since the system has rotational invariance with respect to the spin direction, $\chi(\boldsymbol{q}, \omega)$ is a scalar, i.e., it is independent of the direction of the magnetic field.

1.3.4 Fermi liquid theory

If the state near absolute zero of temperature T is a paramagnetic metal, the Fermi liquid theory of Landau provides a very successful description. Let us briefly review the basic idea of the Fermi-liquid theory [20, 21]. The starting point is the assumption that the low-lying excitations of interacting fermions are in one-to-one correspondence with those in a non-interacting counterpart. The assumption is equivalent to adiabatic continuity when turning on the interaction. Provided the perturbation expansion with respect to the interaction converges, the continuity should be satisfied no matter how strong the interaction is. Then any excited state can be characterized by the distribution $\{n_{\boldsymbol{p}\sigma}\}$ of quasi-particles. The quasi-particle is a concept to characterize the one-to-one correspondence, and reduces to the original particle in the noninteracting limit. We consider a change of the distribution function of a quasi-particle from that of the ground state. For momentum $\boldsymbol{p}$, spin $s_z(=\sigma/2=\pm 1/2)$ the change is written as $\delta n_{\boldsymbol{p}\sigma}$. Then the excitation energy δE is expanded as

$$\delta E = \sum_{\boldsymbol{p}\sigma} \epsilon_{\boldsymbol{p}} \delta n_{\boldsymbol{p}\sigma} + \frac{1}{2} \sum_{\boldsymbol{p}\sigma} \sum_{\boldsymbol{p}'\sigma'} f(\boldsymbol{p}\sigma, \boldsymbol{p}'\sigma') \delta n_{\boldsymbol{p}\sigma} \delta n_{\boldsymbol{p}'\sigma'} + O(\delta n_{\boldsymbol{p}\sigma}^3), \tag{1.67}$$

where $\epsilon_{\boldsymbol{p}}$ is the quasi-particle energy measured from the Fermi level, and $f(\boldsymbol{p}\sigma, \boldsymbol{p}'\sigma')$ describes the interaction between quasi-particles. Since $\epsilon_{\boldsymbol{p}}$ is a small quantity, the first and second terms in the right hand side are of the same order of magnitude. It is possible to neglect terms of higher order with respect to $\delta n_{\boldsymbol{p}\sigma}$.

Let us assume spherical symmetry in the system. Then we can regard the absolute value of the momenta $\boldsymbol{p}, \boldsymbol{p}'$ of quasi-particles equal to the Fermi momentum p_F. In terms of the angle $\theta_{\boldsymbol{p}\boldsymbol{p}'}$ between $\boldsymbol{p}, \boldsymbol{p}'$ we decompose

$$\rho^*(\mu) f(\boldsymbol{p}\sigma, \boldsymbol{p}'\sigma') = \sum_{l=0}^{\infty} (F_l + \sigma\sigma' Z_l) P_l(\cos\theta_{\boldsymbol{p}\boldsymbol{p}'}), \tag{1.68}$$

where $\rho^*(\mu)$ is the density of states of quasi-particles at the Fermi level. It is given by

$$\rho^*(\mu) = \frac{1}{V} \sum_{\boldsymbol{p}\sigma} \delta(\epsilon_{\boldsymbol{p}}) = \frac{m^* p_F}{\pi^2} \tag{1.69}$$

with m^* being the effective mass of a quasi-particle. The dimensionless quantities F_l, Z_l are called Landau parameters. A similar decomposition for $\delta n_{\boldsymbol{p}\sigma}$ is given in terms of spherical harmonics by

$$\delta n_{\boldsymbol{p}\sigma} = \sum_{\ell m} \delta n_{\ell m\sigma} Y_{\ell m}(\hat{p}), \tag{1.70}$$

where $\hat{p}$ denotes the solid angle of $\boldsymbol{p}$. Then the second term of eq.(1.67) can be written as

$$\frac{1}{2\rho^*(\mu)} \sum_{\ell m} \sum_{\sigma\sigma'} (F_l + \sigma\sigma' Z_l) \delta n_{\ell m\sigma} \delta n_{\ell m\sigma'} \tag{1.71}$$

The observables at low excitation energies are described quantitatively in terms of a small number of Landau parameters. Thus by comparison with measurement these parameters can be determined experimentally. This is the most advantageous aspect of the Fermi-liquid theory. The interaction between quasi-particles plays no role for the specific heat C at low T. Namely we obtain

$$C = \frac{\pi^2}{3} \rho^*(\mu) T, \tag{1.72}$$

which takes the same form as the free electron gas. The interaction effect appears only in the effective mass.

Next we derive the static spin susceptibility χ. If the Landau parameters are all zero, the susceptibility would be given by $\chi_0^* = \rho^*(\mu)$. This is regarded as the static and small $\boldsymbol{q}$ limit of the free quasi-particle susceptibility analogous to eq.(1.46). As the next simplest case we assume the presence of homogeneous polarization density $M = V^{-1} \sum_{\boldsymbol{p}} (n_{\boldsymbol{p}\uparrow} - n_{\boldsymbol{p}\downarrow})$. Then eq.(1.67) is rewritten as

$$\frac{\delta E}{V} = \frac{1}{2\chi_0^*} M^2 + \frac{1}{2\rho^*(\mu)} Z_0 M^2 \equiv \frac{1}{2\chi} M^2. \tag{1.73}$$

Taking the second derivative of eq.(1.73) with respect to M we obtain

$$\chi = \chi_0^*/(1+Z_0), \tag{1.74}$$

where we have used the relation $\chi_0^* = \rho^*(\mu)$.

One can regard eq.(1.67) as an effective Hamiltonian for the quasi-particles. Then it should be possible to derive the dynamical properties of the system as well. This is done by Landau in the form of the transport equation. We here follow an alternative approach which is easier to compare with perturbation theory. Let us consider the situation where an external magnetic field H along the z-axis has a single Fourier component $\boldsymbol{q}$. Namely we assume

$$H_{ex}(t) = -m(-\boldsymbol{q},t)h\exp(-i\omega t) \tag{1.75}$$

with $h = \mu_B H$. The dynamical susceptibility of non-interacting quasi-particles is written as $\chi_0^*(\boldsymbol{q},\omega)$ and can be calculated as in eq.(1.46). From the static result we anticipate that the dynamical response is given by

$$\langle m(\boldsymbol{q},\omega)\rangle = \chi_0^*(\boldsymbol{q},\omega)[h + h_{eff}(\boldsymbol{q},\omega)] \tag{1.76}$$

where $h_{eff}(\boldsymbol{q},\omega)$ is the self-consistent field. If we neglect Landau parameters other than Z_0, we obtain

$$h_{eff}(\boldsymbol{q},\omega) = -Z_0\chi_0^*(\boldsymbol{q},\omega)\langle m(\boldsymbol{q},\omega)\rangle. \tag{1.77}$$

Thus the full susceptibility $\chi(\boldsymbol{q},\omega) = \langle m(\boldsymbol{q},\omega)\rangle/h$ is given by

$$\chi(\boldsymbol{q},\omega)^{-1} = \chi_0^*(\boldsymbol{q},\omega)^{-1} + Z_0/\rho^*(\mu). \tag{1.78}$$

Since there are many nonzero Landau parameters in general, eq.(1.78) constitutes an approximation which may be called the quasi-particle RPA [22]. In the original RPA for bare particles in the Hubbard model, $\chi_0(\boldsymbol{q},\omega)$ includes the bare spectrum and $Z_0/\rho^*(\mu)$ is replaced by $-U/2$. We emphasize that eq.(1.78) is meaningful only for excitations with small ω and $\boldsymbol{q}$.

In concluding this subsection we note the complication in real materials. In the presence of multiple energy bands, the magnetic susceptibility consists of both the spin susceptibility as discussed above and the inter-band contribution which corresponds to the van Vleck term in the local moment case. It is not at all trivial to separate two contributions from the measured susceptibility in heavy electrons. In fact the inter-band term is often large and requires careful analysis in NMR and neutron scattering [23].

1.3.5 Parametrization of the dynamical susceptibility

For practical purposes it is useful to parametrize the dynamical susceptibility approximately. Assuming $q/k_F \ll 1$ and $\omega/v_F q < 1$ with v_F being the Fermi velocity, we obtain from eq.(1.46)

$$\chi_0^*(\boldsymbol{q},\omega) = \rho^*(\mu)[1 - b^2q^2 + i\frac{\pi\omega}{2v_Fq}], \tag{1.79}$$

where b is a constant of $O(k_F^{-1})$. In the case of the parabolic spectrum we have $b^{-2} = 12k_F^2$. To extrapolate to larger q and ω we modify eq.(1.79) as follows:

$$\chi_0^*(\boldsymbol{q},\omega) = \rho^*(\mu)[1 + b^2q^2 - i\frac{\pi\omega}{2v_Fq}]^{-1}. \tag{1.80}$$

By this approximation the original cut singularity in $\chi_0^*(\boldsymbol{q},\omega)$ as a function of ω is replaced by the pole singularity. Then using eq.(1.78) we obtain

$$\chi(\boldsymbol{q},\omega) = \frac{\rho^*(\mu)}{1 + Z_0 + b^2\boldsymbol{q}^2 - i\pi\omega/(2v_Fq)}. \tag{1.81}$$

The imaginary part can be written in the form:

$$\mathrm{Im}\chi(\boldsymbol{q},\omega) = \frac{\chi}{1+\xi^2q^2}\frac{\omega\Gamma_q}{\omega^2+\Gamma_q}, \tag{1.82}$$

where $\xi^2 = b^2/(1+Z_0)$ and

$$\Gamma_q = 2v_F(1+Z_0)q(1+\xi^2q^2). \tag{1.83}$$

This "double Lorentzian" form is often used for fitting experimental results of neutron scattering. The correlation length ξ of magnetic fluctuation becomes divergent at the ferromagnetic instability $Z_0 = -1$. The relaxation rate Γ_q is proportional to q for small wave number which is a feature specific to itinerant magnetism. The characteristic energy of the ferromagnetic spin fluctuation is given by $(1 + Z_0)v_F k_F$, and becomes much smaller than the Fermi energy near the ferromagnetic instability $1 + Z_0 = 0$.

Let us now consider the case where the antiferromagnetic (AF) correlation is dominant. The relevant wave number is near the ordering vector $\boldsymbol{Q}$. The relaxation rate $\Gamma(\boldsymbol{q})$ in the AF case remains finite at $\boldsymbol{q} = \boldsymbol{Q}$. The difference from eq.(1.83) comes from the absence of conservation law for the staggered magnetization. Let us assume that the dissipation in the system occurs dominantly through local processes. Then the dynamical susceptibility can be parametrized in the form

$$\chi(\boldsymbol{q}, \omega) = \frac{\chi_L(\omega)}{1 - J(\boldsymbol{q})\chi_L(\omega)}, \tag{1.84}$$

where $J(\boldsymbol{q})$ is the Fourier transform of the intersite exchange interaction. Note that the local susceptibility $\chi_L(\omega)$ describes the dissipation process. Antiferromagnetic order takes place when the denominator of eq.(1.84) becomes zero at $\boldsymbol{q} = \boldsymbol{Q}$. We postulate the Lorentzian form

$$\chi_L(\omega) = \frac{\chi_L \Gamma}{\Gamma - i\omega}, \tag{1.85}$$

where Γ is the local relaxation rate. Then we may write eq.(1.84) as

$$\chi(\boldsymbol{q}, \omega) = \frac{\chi(\boldsymbol{q})\Gamma(\boldsymbol{q})}{\Gamma(\boldsymbol{q}) - i\omega}, \tag{1.86}$$

where $\Gamma(\boldsymbol{q}) = [1 - J(\boldsymbol{q})\chi_L]\Gamma$ and $\chi(\boldsymbol{q}) = \chi(\boldsymbol{q}, 0)$. From this equation we learn that the $\boldsymbol{q}$-dependent relaxation rate $\Gamma(\boldsymbol{q})$ becomes small near the AF instability. In fact we have the relation [24]

$$\chi(\boldsymbol{q})\Gamma(\boldsymbol{q}) = \chi_L \Gamma. \tag{1.87}$$

In order to study the $\boldsymbol{q}$ dependence of the relaxation we expand $J(\boldsymbol{q})$ around $\boldsymbol{q} = \boldsymbol{Q}$ as

$$J(\boldsymbol{Q} + \boldsymbol{q}) = J(\boldsymbol{Q}) - Aq^2 + \ldots, \tag{1.88}$$

where we assume isotropic $\boldsymbol{q}$-dependence of $J(\boldsymbol{Q} + \boldsymbol{q})$ and $A = -J''(\boldsymbol{Q})/2$. Then we get

$$\chi(\boldsymbol{Q} + \boldsymbol{q}) = \frac{\chi(\boldsymbol{Q})}{1 + q^2\xi^2}, \tag{1.89}$$

$$\Gamma(\boldsymbol{Q} + \boldsymbol{q}) = \Gamma(\boldsymbol{Q})(1 + q^2\xi^2), \tag{1.90}$$

where $\xi^2 = A\chi(\boldsymbol{Q})$. Note that ξ represents the correlation length of the AF fluctuation. In the itinerant AF system one can use the same parametrization as given by eqs.(1.86), (1.89) and (1.90) even though one does not rely on the RKKY interaction and the local nature of relaxation.

As we have seen the relaxation of magnetic moments depends strongly whether or not magnetization is a conserved quantity at the relevant wave number. If it is conserved the magnetic relaxation is suppressed for small wave numbers. We now turn to another phenomenological description which is useful in the presence of disorder in itinerant systems or in local-moment systems. We follow Kadanoff and Martin in deriving $\chi(\boldsymbol{q}, \omega)$ in the hydrodynamic regime [25]. One starts with the continuity equation for the magnetization density $M(\boldsymbol{r}, t)$ along the z-direction:

$$\frac{\partial}{\partial t} M(\boldsymbol{r}, t) + \nabla \cdot \boldsymbol{j}(\boldsymbol{r}, t) = 0 \tag{1.91}$$

where $\boldsymbol{j}(\boldsymbol{r}, t)$ is the magnetization current. It is understood that direction of the magnetization is always along the z-axis, and that $M(\boldsymbol{r}, t)$ and $\boldsymbol{j}(\boldsymbol{r}, t)$ are c-numbers. In terms of a parameter D called the spin diffusion coefficient, the current is given by

$$\boldsymbol{j}(\boldsymbol{r}, t) = -D\nabla M(\boldsymbol{r}, t). \tag{1.92}$$

Substituting this into the continuity equation, we get a diffusion equation for the magnetization,

$$\frac{\partial}{\partial t}M(\boldsymbol{r},t) = D\nabla^2 M(\boldsymbol{r},t). \tag{1.93}$$

We note that this equation is valid only when the magnetic field is absent. In order to make connection with the linear response we take the Laplace transform of eq.(1.93). Then we obtain

$$M(\boldsymbol{q},z) = \frac{M(\boldsymbol{q},t=0)}{-iz+Dq^2}, \tag{1.94}$$

where

$$M(\boldsymbol{q},z) = \int_0^\infty dt M(\boldsymbol{q},t)\exp(izt). \tag{1.95}$$

Here the complex variable z has a positive imaginary part. Equation(1.94) gives the Laplace transform of the relaxation function, since $M(\boldsymbol{q},t=0)$ is determined by the static magnetic field present up to $t=0$. Then using the relation to the retarded Green function as given by eq.(B.10) in Appendix B we obtain the dynamical susceptibility as

$$\chi(\boldsymbol{q},\omega) = \frac{\chi(\boldsymbol{q},0)Dq^2}{-i\omega+Dq^2}. \tag{1.96}$$

The form (1.96) is often used in analyzing experimental results at small $\boldsymbol{q}$ for systems with conserved local moments. In the case of pure itinerant ferromagnetism, the diffusion equation eq.(1.93) does not hold since there is no hydrodynamic regime.

1.3.6 Mode-coupling picture of spin fluctuations

To account for the spin fluctuations going one step beyond the RPA, one can use the Hartree approximation for the coupling of spin fluctuations [26, 27, 28]. In this section we critically survey fundamental ideas of this mode-coupling theory. For simplicity we take the Hubbard model with the paramagnetic ground state, and consider the Helmholtz free energy F per site under the condition that homogeneous spin polarization $m = \langle n_{i\uparrow} - n_{i\downarrow}\rangle$ is present. The magnetic susceptibility χ in units of μ_B^2, which is the homogeneous and static limit of the dynamical susceptibility $\chi(\boldsymbol{q},\omega)$, is given by the thermodynamic derivative

$$\chi^{-1} = \frac{\partial^2 F}{\partial m^2}. \tag{1.97}$$

The task is to account for the interaction effect in F. We rewrite H_U as

$$H_U = -\frac{U}{2}\sum_i \{S_i^+, S_i^-\} + \frac{U}{2}N \tag{1.98}$$

in terms of spin flip operators at each site i. The free energy of the system with the coupling strength gU $(0<g<1)$ is given by

$$F(g) = -T\ln \mathrm{Tr}\exp[-(\beta H_1 + gH_U)], \tag{1.99}$$

where H_1 is given by eq.(1.26) and the trace is over all states with fixed number of particles. Then we obtain

$$g\frac{\partial}{\partial g}F(g) = \langle H_{gU}\rangle_g. \tag{1.100}$$

where the average is taken for the system with the interaction gU. In the non-interacting state the average of the anticommutator can be derived easily as

$$\langle\{S_i^+, S_i^-\}\rangle_0 = n + \frac{1}{2}(n^2 - m^2). \tag{1.101}$$

Thus we obtain

$$F = F_0 + \frac{1}{2\chi_0}m^2 - \frac{1}{4}Um^2 + \Delta F, \tag{1.102}$$

where F_0 is the free energy of the non-interacting system with $m = 0$, and ΔF accounts for the correlation effect. The latter is given by

$$\Delta F = \int_0^1 dg[\langle\{S_i^+, S_i^-\}\rangle_g - \langle\{S_i^+, S_i^-\}\rangle_0]. \tag{1.103}$$

Neglect of ΔF in eq.(1.97) leads to the Hartree-Fock susceptibility, which corresponds to the static and homogeneous limit of the dynamical susceptibility in the RPA. In computing ΔF we notice that the average in eq.(1.103) is given by

$$\langle\{S_i^+, S_i^-\}\rangle_g = \int_{-\infty}^{\infty} \frac{d\omega}{2\pi} \coth(\frac{1}{2}\beta\omega)\mathrm{Im}\chi^{\perp}_{m,gU}(\omega) = T\sum_n \chi^{\perp}_{m,gU}(i\nu_n) \tag{1.104}$$

where $\chi^{\perp}_{m,gU}(\omega) = -\langle[S_i^+, S_i^-]\rangle_g(\omega)$ is the local transverse susceptibility in the presence of magnetization m. This is an example of the fluctuation-dissipation theorem explained in Appendix B. In the second equality $i\nu_n$ denotes the Matsubara frequency (see Appendix B).

In the RPA, the dynamical susceptibility is given by

$$\chi^{\perp}_{m,gU}(\boldsymbol{q},\omega)^{-1} = \chi^{\perp}_{m,0}(\boldsymbol{q},\omega)^{-1} - gU. \tag{1.105}$$

Then one can easily derive the correlation part in the RPA as

$$\Delta F_{RPA} = T\sum_n \sum_{\boldsymbol{q}} \left\{\ln[1 - \frac{U}{2}\chi^{\perp}_{m,0}(\boldsymbol{q}, i\nu_n)] + \frac{U}{2}\chi^{\perp}_{m,0}(\boldsymbol{q}, i\nu_n)\right\}. \tag{1.106}$$

The RPA theory has an obvious inconsistency [27] : The static and homogeneous limit of eq.(1.105) with $g = 1$ does not agree with the one derived with use of eq.(1.106) and eq.(1.97). This discrepancy becomes serious if one wants to calculate the Curie temperature T_c by the condition $\chi^{-1} = 0$, since the RPA susceptibility diverges at T_c^{HF} which is different from T_c to be calculated from eq.(1.97).

The simplest way to remedy this drawback is to introduce a parameter λ by

$$\chi^{-1} = (1 + \lambda)\chi_0^{-1} - \frac{1}{2}U. \tag{1.107}$$

The correlation effect represented by λ is related to ΔF as

$$\lambda\chi_0^{-1} = \left.\frac{\partial^2 \Delta F}{\partial m^2}\right|_{m=0}. \tag{1.108}$$

One then modifies eq.(1.106) in the following manner [27]

$$\Delta F_{SCR} = T\sum_n \sum_{\boldsymbol{q}} \left\{\ln[1 + \lambda - \frac{U}{2}\chi^{\perp}_{m,0}(\boldsymbol{q}, i\nu_n)] + \frac{U}{2}\chi^{\perp}_{m,0}(\boldsymbol{q}, i\nu_n)\right\}. \tag{1.109}$$

Provided that takes maximum at $\boldsymbol{q} = 0$ and $m = 0$, a singularity in ΔF_{SCR} occurs at T_c as the ferromagnetic instability. This instability at T_c is consistent with the divergence of χ given by eq.(1.107). Thus the inconsistency of the RPA has been removed.

Equation (1.109) is of central importance in the so-called self-consistent renormalization (SCR) theory of Moriya and Kawabata [27]. Since $\chi^{\perp}_{m,0}(\boldsymbol{q}, i\nu_n)$ can be derived explicitly for a given spectrum of electrons, it is possible to set up a self-consistency equation for λ at each temperature. One obtains $\lambda(T) - \lambda(0) \propto T^{4/3}$ since the local susceptibility with $m = 0$ in eq.(1.104) behaves as $\omega^{1/3}$ for small ω. This power-law behavior will be derived shortly. The second derivative of $\chi^{\perp}_{m,0}(\boldsymbol{q}, i\nu_n)$ with respect to m does not change this leading behavior at $m = 0$. We emphasize that the T-dependence of $\lambda(T)$ is controlled by spectrum of the ferromagnetic spin fluctuation and is independent of details of the band structure. In the case of antiferromagnetic metals, the different q-dependence of spin fluctuations leads to $\mathrm{Im}\chi(\omega) \propto \omega^{1/2}$ and $\lambda(T) - \lambda(0) \propto T^{3/2}$.

The temperature dependence of λ leads to an approximate Curie-Weiss-like behavior of the susceptibility, which is the most remarkable effect of the mode coupling. The SCR theory has been widely used in explaining temperature dependence of physical quantities in transition metals and some of their

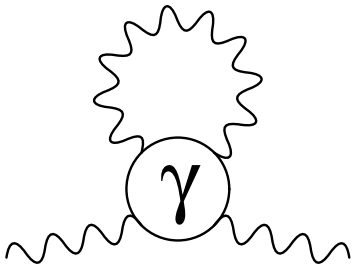

Figure 1.6: The dominant fluctuation contribution to the susceptibility.

compounds. The temperature dependence deviate from the RPA theory significantly near the magnetic transition. The most appealing feature of the SCR theory is that the mode-coupling effect is taken into account in a simple and practical manner. However, eq.(1.109) cannot be justified microscopically near the magnetic transition. Since the SCR theory relies on $\chi^{\perp}_{m,0}(\boldsymbol{q},\omega)$ as the basic ingredient like the RPA, the parameter λ should be small to justify the SCR as a weak-coupling theory. However λ becomes actually of the order of unity by the self-consistency requirement. This is simply because ΔF_{SCR} does not vanish even with $\lambda = 0$, and therefore $\lambda \ll 1$ cannot be a self-consistent solution of eq.(1.108) near the magnetic instability. By this reason one should regard the SCR theory as a semi-phenomenological scheme to deal with the mode coupling among spin fluctuations, rather than a microscopic theory for the Hubbard model. The original Moriya-Kawabata theory as presented above was later modified in a few different ways. We refer to Moriya's book [29] for comprehensive account of the SCR theory.

An alternative approach to take account of the mode-coupling effect has been proposed by Dzyaloshinskii and Kondratenko [28] by the use of the Fermi liquid theory. Let us assume again the paramagnetic Fermi liquid ground state. We consider the leading finite temperature correction to the dynamical susceptibility $\chi(\boldsymbol{q},\omega;T)$ at low temperature T. According to the Matsubara Green function formalism the leading correction is obtained by the following procedure: From a Feynman diagram for $\chi(\boldsymbol{q},i\omega;T)$ we pick up a part $\Gamma(i\nu;T)$ with low frequency ν flowing from and to the rest of the diagram. Then we replace the frequency summation in this part by

$$\left(T\sum_{\nu} - \int_{-\infty}^{\infty}\frac{d\omega}{2\pi}\right)\Gamma(i\nu;T), \tag{1.110}$$

and integration is performed over all the remaining frequencies.

In the case of a weak ferromagnet, the dominant contribution to $\Gamma(i\nu;T)$ comes from a spin fluctuation with small wave number and frequency. Particle-hole excitations have the energy scale of the Fermi energy and can safely be neglected. Thus the relevant diagram is represented by Fig.1.6 and constitutes the self-energy like correction to the susceptibility. Namely we obtain

$$\chi(0,0;0)^{-1} - \chi(0,0;T)^{-1} = -\gamma\int_0^{\infty}\frac{d\omega}{2\pi}\int\frac{d\boldsymbol{q}}{(2\pi)^3}\frac{1}{\exp(\omega/T)-1}\mathrm{Im}\chi(\boldsymbol{q},\omega;T) \equiv -\gamma\beta(T), \tag{1.111}$$

where γ is a parameter for the mode-coupling, and the Bose distribution function emerges from the analytic continuation of eq.(1.110). One can regard γ as a constant since dependence on wave number, frequency, and temperature is on the much larger scale of one-particle excitations.

The temperature-dependent correction given by eq.(1.111) corresponds to $\lambda(T) - \lambda(0)$ in the SCR theory. The magnitude of γ cannot be evaluated by perturbation theory since higher order terms are equally important in general. In the nearly ferromagnetic ground state, $1 + Z_0 \equiv \alpha$ is much smaller than unity. Then the characteristic temperature $T_{SF} = \alpha v_F k_F$ of spin fluctuations is much lower than the Fermi temperature $T_F = v_F k_F/2$. In doing the integration in eq.(1.111) for the temperature range $T_{SF} \ll T \ll T_F$, one may use the parametrized form eq.(1.81) for $\chi(\boldsymbol{q},\omega;T)$. This is firstly because only the small q/k_F becomes important, and secondly the detailed analytic structure with respect to ω is not important for small T_{SF}/T. We scale the integration variables as $q = \omega^{1/3}\bar{q}$, and then $\omega = T\bar{\omega}$. Integrations with respect to $\bar{q}$ and $\bar{\omega}$ in eq.(1.111) give rise to the factor

$$\beta(T) \sim T^{4/3}. \tag{1.112}$$

With the nearly ferromagnetic ground state the magnetic susceptibility follows $\chi(T) \sim T^{-4/3}$. Thus the same temperature dependence as that of the SCR theory [27] has been obtained. This agreement is not accidental as is clear from the above derivation.

1.4 Nuclear Magnetic Resonance (NMR)

For understanding specific properties of heavy-electron systems, it is important to investigate and describe low energy excitations. In this context, both nuclear magnetic resonance (NMR) and neutron scattering experiments play central roles in obtaining information about the dynamical response of heavy-electron systems. Whereas the NMR probes the local environment of one particular nucleus and, therefore, a wave-vector average of the dynamical response function with a small energy transfer comparable to the nuclear Zeeman energy ($10^{-6} \sim 10^{-8}$ meV), neutron scattering experiments can scan wider energies and wave vectors corresponding to the whole Brillouin zone. In real situations the energy transfer is usually limited below about 100 meV with use of thermal neutrons. Thus, both experiments are complementary. The advantage of NMR is that it can extract the lowest energy excitation and detect a magnetic instability with a tiny moment if it appears. Furthermore in the superconducting state, NMR can provide a detailed structure of response function reliably. In this section, we begin with the description of experimental aspects of NMR. For more detailed descriptions on NMR, we refer to standard textbooks [30].

1.4.1 Phenomenology

A nucleus with spin I has a magnetic moment $\boldsymbol{\mu}_n = \gamma_n \boldsymbol{I}$ where γ_n is the nuclear gyromagnetic ratio. If an isolated nucleus is placed in external magnetic field $\boldsymbol{H}_0$, the nuclear spin levels are split into $2I+1$ levels with an equal energy separation:

$$\Delta E = \gamma_n H_0. \tag{1.113}$$

According to the quantum-mechanical selection rule, the magnetic dipole transitions are induced only between adjacent levels. Thus the nuclear spin system undergoes resonance absorption if the perturbing oscillatory magnetic field $\boldsymbol{H}_1$ is applied perpendicularly to $\boldsymbol{H}_0$ with the condition $\omega_n = \gamma_n H_0$. Actually a nucleus in a nonmagnetic solid experiences a magnetic field which is different from the external field; the correction ΔH contains contributions from dipolar fields of other nuclei, atomic diamagnetism and the chemical shift. The correction is proportional to the induced electronic moment, and gives rise to frequency shift and linewidth of NMR absorption spectrum. On the other hand, in a magnetically ordered solid a nuclear spin experiences a dominant internal magnetic field associated with the spontaneous magnetization of the electrons.

Let $\boldsymbol{H}_0$ be applied along the z axis, and $\boldsymbol{M}(t)$ be the nuclear magnetization averaged over the sample at time t. In most cases the z-component $M_z(t)$ will recover to the equilibrium value M_0 exponentially. The equation of motion for $\boldsymbol{M}(t)$ is then described by

$$\frac{dM_z(t)}{dt} = \gamma_n (\boldsymbol{M}(t) \times \boldsymbol{H})_z + \frac{1}{T_1}(M_0 - M_z(t)), \tag{1.114}$$

where T_1 is the nuclear spin-lattice relaxation time and characterizes the rate at which energy is transferred from the nuclear spin system to the electron spin system. In heavy-electron systems, the spin fluctuations resulting from exchange couplings among localized electron spins and/or with conduction electron spins are responsible for the nuclear-spin lattice relaxation process. The magnetic field $\boldsymbol{H}$ is in general different from $\boldsymbol{H}_0$ because of polarization of the medium.

In addition to T_1, there is another relaxation time T_2 which is related to the component $\boldsymbol{M}_\perp(t)$ of the magnetization perpendicular to the external field. The transverse magnetization is associated with forced precession of the nuclear moment caused by the perturbing oscillation field H_1. The equation of motion for $\boldsymbol{M}_\perp(t)$ is described by

$$\frac{d\boldsymbol{M}_\perp(t)}{dt} = \gamma_n (\boldsymbol{M}(t) \times \boldsymbol{H}) - \frac{\boldsymbol{M}_\perp(t)}{T_2^*}. \tag{1.115}$$

Note that $\boldsymbol{M}_\perp$ is zero in thermal equilibrium. The characteristic time T_2^* does not directly reflect the relaxation of the nuclear spin since possible inhomogeneity of the external field over the sample and/or a static distribution of hyperfine fields at nuclear sites in the magnetic substance contribute to T_2^*.

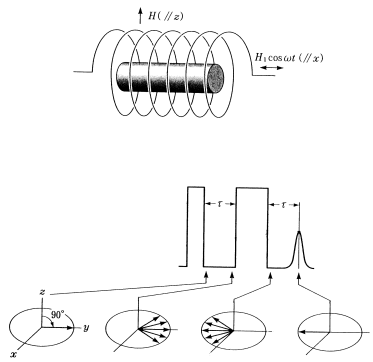

Figure 1.7: Illustration of the spin-echo NMR method.

In order to determine the intrinsic transverse relaxation time T_2, one typically uses the spin-echo method which is illustrated in Figure 1.7. The experiment goes as follows: Under the external field H_0 along the z-axis, one applies an alternating field H_1 with the resonance frequency ω_n for a short time $\delta t = \pi/(2\gamma_n H_1)$ ($\ll T_1$) along the x-axis. This pulse causes $\boldsymbol{M}$ to rotate toward the y-axis by the angle $\pi/2$, and hence is called a $\pi/2$-pulse. After the pulse is turned off, each nuclear spin contributing to $M_\perp(t)$ begins to precess in the x-y plane. Because of the nuclear spin-spin interaction and the inhomogeneous field, the precession frequency of each spin is different. Then the free induction signal, which comes from the sum total of $M_\perp(t)$ from all portions of the sample, decays exponentially with a time constant T_2^*. Waiting for a time τ ($> T_2^*$) after the first $\pi/2$-pulse, one applies the second pulse for a time duration $\delta t' = \pi/(\gamma_n H_1)$, which generates rotation of each nuclear spin by the angle π around the x-axis. The nuclear spins, which are pointing toward various directions in the x-y plane under the inhomogeneous field, resume precession and finally refocus along the $-y$-direction after a time 2τ from the first $\pi/2$-pulse. This refocusing results in the recovery of $M_\perp(t)$, which is probed as a peak in the free induction signal like an echo. Hence the phenomenon is called the spin-echo.

The amplitude $M_s(2\tau)$ of the spin-echo usually decays exponentially as a function of 2τ as

$$M_s(2\tau) = M_\perp(0) \exp\left(-\frac{2\tau}{T_2}\right). \tag{1.116}$$

The refocusing occurs only when the spins precessing under the inhomogeneous field keep the memory of their phase. Then the condition $\tau \ll T_1, T_2$ is required in the spin-echo. In the case of $T_2 \ll T_1$, decay of the spin-echo is caused by the nuclear spin-spin interaction without any influence of the inhomogeneous field distribution. Hence T_2 provides information about intrinsic properties of the system. We will discuss T_1 and T_2 in greater detail later for nuclei embedded in a magnetic solid.

1.4.2 Magnetic hyperfine interaction

Most NMR experiments in heavy-electron systems have been carried out for nuclei of non-lanthanide constituents. As an exception, Yb NMR has been observed in the valence fluctuating compounds $YbAl_2$ and $YbAl_3$ [31]. In these materials the average valency of Yb is between 2+ and 3+ and the valency fluctuates quantum mechanically. One can discuss directly the magnetic relaxation rate of f electrons which is related to the linewidth of quasi-elastic neutron scattering intensity. This discussion of course requires a reliable knowledge of the hyperfine field. On the other hand, the hyperfine interaction between non-lanthanide nuclei and f electrons is caused by mixing between f electrons and conduction electrons which in turn interact with the nuclei. This transferred hyperfine interaction dominates the magnetic hyperfine interaction between non-lanthanide nuclei and f electrons in most of heavy-electron compounds. The interaction is mediated by the Fermi contact interaction, the spin-dipolar, and the orbital hyperfine interactions with nuclei at non-Lanthanide sites. The Fermi contact interaction acts only for s electrons and the latter two act only for non-s electrons as explained below.

Let us first discuss the Fermi contact interaction between a nucleus and an electron in an s-orbital. Provided the magnetization density $\boldsymbol{M}_n = \gamma_n \boldsymbol{I}/v_n$ of the nucleus is uniform inside the nuclear volume

v_n, the magnetic field $\boldsymbol{B}$ produced by $\boldsymbol{M}_n$ is given by $\boldsymbol{B} = (8\pi/3)\boldsymbol{M}_n$. On the other hand the electronic magnetization $\boldsymbol{M}_e$ at the nucleus position is given by $\boldsymbol{M}_e = -g\mu_B \boldsymbol{s}|\phi_s(0)|^2$. Here $|\phi_s(0)|^2$ is the probability density of the electron at the nucleus position, and $\boldsymbol{s}$ is the spin operator of the s electron. The interaction between $\boldsymbol{M}_e$ and $\boldsymbol{B}$ is described by the Hamiltonian $H_c = -\boldsymbol{B}\cdot\boldsymbol{M}_e v_n$ which is rewritten as follows:

$$H_c = \frac{8\pi}{3}\gamma_n g\mu_B |\phi_s(0)|^2 \boldsymbol{I}\cdot\boldsymbol{s}. \tag{1.117}$$

We emphasize that this Fermi contact interaction remains finite only for s electrons with nonvanishing values of $|\phi_s(0)|^2$.

On the other hand, an electron in a non-s orbital has zero amplitude at the nucleus position. It has instead the spin-dipolar interaction H_d and the orbital hyperfine interaction H_l of the form:

$$H_d = -\gamma_n g\mu_B \frac{1}{r^3}\left[\boldsymbol{I}\cdot\boldsymbol{s} - \frac{3(\boldsymbol{I}\cdot\boldsymbol{r})(\boldsymbol{s}\cdot\boldsymbol{r})}{r^2}\right], \tag{1.118}$$

$$H_l = \gamma_n \mu_B \frac{2}{r^3}\boldsymbol{I}\cdot\boldsymbol{l}, \tag{1.119}$$

where $\boldsymbol{l}$ is the orbital angular momentum of the non-s electron. In actual metals the orbital motion appears as the orbital Knight shift which is usually independent of temperature.

Furthermore we mention the inner core polarization which is due to unpaired non-s electrons. These electrons have vanishing amplitude at the nucleus, but can induce an unbalanced spin density of paired inner s electrons. In contrast with the Fermi contact interaction, the sign of the hyperfine field due to the core polarization is negative.

We now proceed to the many-body description of the hyperfine interaction. In heavy-electron systems like Ce and U compounds, the spin-orbit interaction is so strong that the electronic state of an ion is characterized by the total angular momentum as $\boldsymbol{J} = \boldsymbol{L} + \boldsymbol{S}$ and the magnetic moment $-g_J\mu_B\boldsymbol{J}$. The lowest J manifold is furthermore split into several sublevels by the crystal electric field (CEF). We take for simplicity a nucleus at the origin. The nuclear spin $\boldsymbol{I}$ and f electrons at site $\boldsymbol{R}_j$ interact through the hyperfine interaction as

$$H_{hyper} = \sum_j \boldsymbol{I}\cdot\boldsymbol{A}(\boldsymbol{R}_j)\cdot\boldsymbol{J}(\boldsymbol{R}_j), \tag{1.120}$$

where the sum is taken over all nearest-neighbor ions of lanthanides or actinides. The tensor $\boldsymbol{A}(\boldsymbol{R}_j)$ consists of the orbital and the spin parts projected onto the total angular momentum $\boldsymbol{J}(\boldsymbol{R}_j)$. This is in contrast to transition metals where spin and orbital parts survive separately because of much weaker spin-orbit interaction. In the hyperfine coupling tensor $\boldsymbol{A}(\boldsymbol{R}_j)$ in heavy-electron systems, the transferred (indirect) hyperfine interaction plays a main role for the magnetic interaction for non-lanthanide nuclei. The dipole-dipole interaction between f-electron spin and nuclear spin is unimportant and is neglected in the following.

The hyperfine interaction causes the magnetic field at the nucleus to deviate from the external one H_0 by an amount ΔH. Here we take the direction α of H to be one of the principal axes of the crystal to avoid complexity. The shift satisfies the relation

$$\gamma_n \Delta H = A_\alpha \langle J_\alpha\rangle, \tag{1.121}$$

where $\langle J_\alpha\rangle$ is the average of $\boldsymbol{J}(\boldsymbol{R}_j)$ in the α-direction, and

$$A_\alpha = \mathop{\mathrm{Av}}_j [\boldsymbol{A}(\boldsymbol{R}_j)]_{\alpha\alpha},$$

is the spatial average of the diagonal element of the hyperfine interaction. Let the number of f electrons per unit volume be n. By definition of the static susceptibility χ_α we have

$$n g_J \mu_B \langle J_\alpha\rangle = \chi_\alpha H_0.$$

Then the Knight shift K_α defined by $K = \Delta H/H_0$ is expressed as

$$K_\alpha = \frac{A_\alpha}{n\gamma_n g_J \mu_B}\chi_\alpha. \tag{1.122}$$

On can extract the transferred hyperfine field by plotting the Knight shift vs the susceptibility with temperature as an implicit parameter, i.e.

$$A_\alpha = n\gamma_n g_J \mu_B \left(dK_\alpha/d\chi_\alpha\right).$$

It often happens that the K vs χ plot is not linear in the whole temperature range. A straight line in the high T range goes over to another one below a certain crossover temperature. This means that A_α in the low T range is no longer the same as that in the high T range. This change occurs possibly because the conduction electron spin polarized by the *c-f* mixing varies with temperature, which reflects the change of the character of f electrons from localized to itinerant. In the NMR investigation for non-lanthanide nuclei, the knowledge of the transferred hyperfine tensor enables us to extract a dynamical response function from the nuclear-spin-lattice relaxation measurements. This leads to a quantitative comparison with that derived by neutron scattering experiments.

1.4.3 Electric quadrupolar interaction

We now describe the electric quadrupolar interaction between electrons and nuclei with $I > 1/2$. These nuclei have an aspherical charge distribution $\rho(\boldsymbol{r})$, and therefore have an electric quadrupole moment $Q'_{jk} = \int \rho(\boldsymbol{r}) x_j x_k d\boldsymbol{r}$. Let $V(\boldsymbol{r})$ denote the electrostatic potential due to surrounding charges around the nucleus, and $V_{jk} = \partial^2 V(\boldsymbol{r})/\left(\partial x_j \partial x_k\right)_{r=0}$ be the field gradient tensor at the nucleus. Then the interaction Hamiltonian H_Q of the quadrupole moment of a nucleus with the field gradient is given by

$$H_Q = \frac{1}{2}\sum_{j,k} Q'_{jk} V_{jk} + \cdots. \tag{1.123}$$

We can express the traceless tensor $Q_{jk} = 3Q'_{jk} - \delta_{jk}\sum_i Q'_{ii}$ in terms of the nuclear spin $\boldsymbol{I}$ as

$$Q_{jk} = \frac{eQ}{I(2I-1)}\left[\frac{3}{2}(I_j I_k + I_k I_j) - \delta_{jk}\boldsymbol{I}^2\right]. \tag{1.124}$$

For an axially symmetric electric field gradient we define eq by

$$eq = \left(\frac{\partial^2 V}{\partial z^2}\right)_{r=0} = -e\int d\boldsymbol{r}\frac{3z^2 - r^2}{r^5} n(\boldsymbol{r}), \tag{1.125}$$

where $n(\boldsymbol{r})$ denotes the electronic density. Then H_Q is given by

$$H_Q = \frac{e^2 qQ}{4I(2I-1)}\left[3I_z^2 - I(I+1)\right] \tag{1.126}$$

with

$$eQ = Q_{zz} = 3Q'_{zz} - \sum_i Q'_{ii} = \int \rho(\boldsymbol{r})(3z^2 - r^2) d\boldsymbol{r}. \tag{1.127}$$

If the $V(\boldsymbol{r})$ has no uniaxial symmetry, an additional term $\eta(I_x^2 - I_y^2)$ enters into H_Q with an asymmetry parameter $\eta = (V_{xx} - V_{yy})/V_{zz}$. Here x, y, z are taken to be the principal axes of the field gradient. This electric interaction splits the nuclear spin levels into several multiplets, and the transition between them causes a resonant absorption of radio-frequency. This is called the nuclear quadrupole resonance (NQR). The important feature of the NQR is that the experiment does not need an external magnetic field. For example, the NQR of ^{63}Cu was observed at 3.91 and 3.43 MHz for $CeCu_6$ and $CeCu_2Si_2$, respectively. The NQR experiment is particularly advantageous in investigating low energy excitations in the superconducting state at zero magnetic field. We note that the coupling of the nuclear quadrupole moment with the lattice vibration opens another relaxation channel mediated by the charge fluctuation in ionic or metallic crystals including nuclei with a large quadrupole moment. However in heavy electron systems the magnetic relaxation channel prevails in most cases.

1.4.4 Nuclear spin-lattice relaxation time T_1

Nuclear spin-lattice relaxation in heavy-electron systems is mostly caused by f-electron spin fluctuations through the transferred hyperfine interaction given by eq.(1.120). The relaxation rate $1/T_1$ defined by eq.(1.114) corresponds to that of the nuclear magnetic susceptibility. In Appendix D we have given necessary formulae to derive the relaxation rate by perturbation theory. The dynamics of the z-component I_z of the nuclear spin is described by

$$\frac{\partial I_z}{\partial t} = i[H_{hyper}, I_z] = \sum_j [-A_x(\boldsymbol{R}_j)J_x(\boldsymbol{R}_j)I_y + A_y(\boldsymbol{R}_j)J_y(\boldsymbol{R}_j)I_x]. \tag{1.128}$$

In the case where the hyperfine interaction can be treated in the lowest order, we obtain from eq.(D.12)

$$\frac{1}{T_1} = \frac{T}{2}\sum_{\boldsymbol{q}} \left[|A_x(\boldsymbol{q})|^2\langle J_x(\boldsymbol{q})|\delta(\omega_n - \mathcal{L}_0)|J_x(\boldsymbol{q})\rangle + |A_y(\boldsymbol{q})|^2\langle J_y(\boldsymbol{q})|\delta(\omega_n - \mathcal{L}_0)|J_y(\boldsymbol{q})\rangle\right], \tag{1.129}$$

where $\mathcal{L}_0$ is the unperturbed Liouville operator, and ω_n is the frequency at the resonance which is much smaller than the characteristic frequency of the electrons. The factor T in the right-hand side of eq.(1.129) comes from $\langle I_z|I_z\rangle = \beta I(I+1)/3$ in the denominator. The quantity $\langle \ldots \rangle$ is related to the dynamical susceptibility of the f electrons. Namely with use of eq.(B.10) we have

$$\langle J_x(\boldsymbol{q})|\delta(\omega - \mathcal{L}_0)|J_x(\boldsymbol{q})\rangle = (g_J\mu_B)^2 \mathrm{Im}\chi_{xx}(\boldsymbol{q},\omega)/\omega. \tag{1.130}$$

From eq.(1.130) we see that $1/T_1$ reflects sensitively the low-energy magnetic excitations. If the dynamical response is dominated around a special wave vector $\boldsymbol{Q}$, $1/T_1T$ is directly connected to the slope at the low energy tail around $\omega \sim 0$ of $\mathrm{Im}\chi(\boldsymbol{Q},\omega)$. Below we take typical examples of local moment and itinerant electron systems and discuss the temperature dependence of $1/T_1$ for each case.

local moment system

We first consider the case of localized f electrons, the dynamics of which is described by the Heisenberg model with the exchange interaction J_{ex}. According to the formalism in Appendix D, the spectral shape becomes of the Gaussian type if the short-time relaxation behavior dominates the spectrum. This is the case in the paramagnetic state of the system. Then we have from eqs.(D.18) –(D.21)

$$\langle M(t)|M\rangle = (g_J\mu_B)^2 \frac{J(J+1)}{3} \exp\left[-\frac{1}{2}\langle\omega^2\rangle_c t^2\right], \tag{1.131}$$

where $\langle\omega^2\rangle_c = J_{ex}^2 z_n J(J+1)$ with z_n being the number of nearest neighbors of interacting local moments. From the eq.(1.129), we get

$$\frac{1}{T_1} = \sqrt{2\pi}\frac{C|A_{hf}|^2}{\sqrt{\langle\omega^2\rangle_c}}, \tag{1.132}$$

where the $\boldsymbol{q}$-dependent hyperfine coupling eq.(1.129) is replaced by the average A_{hf} over $\boldsymbol{q}$. We note that $1/T_1$ is independent of temperature in the present case.

On the other hand if the relaxation of local moments is caused by the exchange interaction J_{cf} with conduction electrons, the relaxation function is dominated by the long-time behavior. Then the spectrum undergoes motional narrowing with the linewidth of the order of J_{cf}^2/D where D is the bandwidth of the conduction electrons. The relaxation function is given by

$$\langle M(t)|M\rangle = (\mu_B g_J)^2 \frac{J(J+1)}{3} \exp\left[-\Gamma_{cf}t\right]. \tag{1.133}$$

for large time t. Since the long time behavior given above determines the spectrum, we can parametrize the dynamical susceptibility as

$$\chi(\omega) = \frac{C\Gamma_{cf}}{T(\Gamma_{cf} - i\omega)}. \tag{1.134}$$

From eqs.(1.129) and (1.130) we obtain

$$\frac{1}{T_1} = \frac{C|A_{hf}|^2}{\Gamma_{cf}}. \tag{1.135}$$

As will be discussed in the next section, Γ_{cf} has a linear T-dependence if f spins decay through coupling with conduction electrons. Thus $1/T_1$ decreases as $1/T$ upon heating.

itinerant electron system

For itinerant electrons at low temperatures, the Fermi liquid theory provides a reliable description as presented in the previous section. We discuss $1/T_1$ on the basis of the quasi-particle RPA given by eq.(1.78). In terms of the quasi-particle susceptibility $\chi_0^*(\boldsymbol{q},\omega)$ we obtain

$$\mathrm{Im}\chi(\boldsymbol{q},\omega) = \left|\frac{\chi(\boldsymbol{q},\omega)}{\chi_0^*(\boldsymbol{q},\omega)}\right|^2 \mathrm{Im}\chi_0^*(\boldsymbol{q},\omega). \tag{1.136}$$

Since $\mathrm{Im}\chi(\boldsymbol{q},\omega)$ is much smaller than $\mathrm{Re}\chi(\boldsymbol{q},\omega)$ in the relevant frequency range, we can approximate

$$\left|\frac{\chi(\boldsymbol{q},\omega)}{\chi_0^*(\boldsymbol{q},\omega)}\right|^2 \sim \left(\frac{1}{1+\chi_0^*(\boldsymbol{q},0)Z_0/\rho^*(\mu)}\right)^2, \tag{1.137}$$

which acts as an enhancement factor in $1/T_1$.

We get the imaginary part of $\chi_0^*(\boldsymbol{q},\omega)$ near the Fermi energy μ as

$$\mathrm{Im}\chi_0^*(\boldsymbol{q},\omega) = \pi\omega \sum_{\boldsymbol{k}} \left(-\frac{\partial f}{\partial \epsilon_{\boldsymbol{k}}}\right) \delta(\omega - \epsilon_{\boldsymbol{k}+\boldsymbol{q}} + \epsilon_{\boldsymbol{k}}) \tag{1.138}$$

Furthermore we replace the enhancement factor by its average. Then we get

$$\frac{1}{T_1} = \pi A_{hf}^2 \rho^*(\mu)^2 T \langle \left(\frac{1}{1+\chi_0^*(\boldsymbol{q},0)Z_0/\rho^*(\mu)}\right)^2 \rangle_{FS}. \tag{1.139}$$

where $\langle\cdots\rangle_{FS}$ means the average over the Fermi surface. If the enhancement factor is the same as that for the $\boldsymbol{q}=0$ case, we have the so-called Korringa relation:

$$\frac{1}{T_1 T} = \pi (\frac{\gamma_n}{\mu_B})^2 K^2, \tag{1.140}$$

where K is the Knight shift. Note that the result obtained above neglects the presence of anisotropy. In reality, although magnetic properties in most heavy-electron systems are very anisotropic, there are cases where the Korringa relation is valid for the actinide heavy-electron compounds. Since the Landau parameters provide a quantitative description only in the isotropic case, due care is necessary in interpreting experimental data.

As long as the temperature is much smaller than the Fermi energy, the quantity $1/(T_1T)$ is independent of T. This property holds as long as the Fermi liquid is realized. We often call the constancy of $1/(T_1T)$ the Korringa law even though the stronger relation given by eq.(1.140) is not confirmed.

1.4.5 Nuclear spin-spin relaxation time T_2

In heavy-electron systems, the indirect nuclear spin-spin interaction plays a primary role in the decay of the transverse nuclear magnetization [32]. A nuclear spin at site $\boldsymbol{R}$ interacts with other nuclear spins indirectly. First it interacts with the spin of a conduction electron at $\boldsymbol{r}$ through the hyperfine interaction tensor $\boldsymbol{A}(\boldsymbol{r}-\boldsymbol{R})$. The conduction electron propagates to another nuclear site and interacts with the second nucleus via the hyperfine interaction. This indirect interaction is called the Ruderman-Kittel-Kasuya-Yosida (RKKY) interaction. The interaction Hamiltonian H_{ij} between two nuclear spins $\boldsymbol{I}_i$ and $\boldsymbol{I}_j$ is expressed as

$$H_{ij} = -I_i \hat{\Phi}(\boldsymbol{R}_{ij}) I_j \tag{1.141}$$

where

$$\hat{\Phi}(\boldsymbol{R}_{ij}) = \int d\boldsymbol{r} \int d\boldsymbol{r}' \boldsymbol{A}(\boldsymbol{R}_i - \boldsymbol{r}) \hat{\chi}(\boldsymbol{r}-\boldsymbol{r}') \boldsymbol{A}(\boldsymbol{r}' - \boldsymbol{R}_j), \tag{1.142}$$

with $\hat{\chi}(\boldsymbol{r}-\boldsymbol{r}')$ being the susceptibility tensor of the conduction electrons. Consequently, the calculation of the indirect nuclear spin coupling is reduced to that of magnetic susceptibility $\hat{\chi}(\boldsymbol{r})$ or its Fourier transform $\hat{\chi}(\boldsymbol{q})$. If we assume a contact hyperfine interaction given by $\boldsymbol{A}(\boldsymbol{R}_i - \boldsymbol{r}) = \boldsymbol{A}_s \delta(\boldsymbol{R}_i - \boldsymbol{r})$, the

range of the interaction is simply determined by $\hat{\chi}(\boldsymbol{r})$. In this case, the indirect interaction is written as

$$\hat{\Phi}(\boldsymbol{R}_{ij}) = \frac{1}{N}\sum_{\boldsymbol{q}} \boldsymbol{A}_s \hat{\chi}(\boldsymbol{q}) \boldsymbol{A}_s \exp(i\boldsymbol{q}\cdot\boldsymbol{R}_{ij}). \tag{1.143}$$

For the free electron gas model, the above formula leads to the Ruderman-Kittel form for the indirect nuclear spin-spin interaction. On the other hand in magnetically ordered states at temperatures well below the transition temperature, $\hat{\chi}(\boldsymbol{q})$ can be calculated by a spin wave approximation.

In the case where $\Phi(\boldsymbol{R}_{ij})_{zz}$ dominates over all the other components, the transverse relaxation spectrum becomes of the Gaussian shape. Namely in the spin-echo experiment one has

$$M_{\perp}(2\tau) = M_{\perp}(0)\exp\left[-\frac{1}{2}\left(\frac{2\tau}{T_{2G}}\right)^2\right], \tag{1.144}$$

where the relaxation rate $1/T_{2G}$ is given by $(1/T_{2G})^2 = \langle\omega^2\rangle$ with $\langle\omega^2\rangle$ being defined by eq.(D.21) in Appendix D. In the lowest-order perturbation theory we assume for simplicity that the anisotropy of $\hat{\Phi}(\boldsymbol{R}_{ij})$ comes from large A_{zz} and that $\hat{\chi}(\boldsymbol{q})$ is isotropic. Then we have

$$\left(\frac{1}{T_{2G}}\right)^2 = \frac{3I(I+1)}{4}\sum_{i\neq j} \mid \Phi_{zz}(\boldsymbol{R}_{ij}) \mid^2 = A_{zz}^4 \frac{3I(I+1)}{4}\left[\mathrm{Av}_{\boldsymbol{q}}\,\chi(\boldsymbol{q})^2 - \left(\mathrm{Av}_{\boldsymbol{q}}\,\chi(\boldsymbol{q})\right)^2\right], \tag{1.145}$$

where $\mathrm{Av}_{\boldsymbol{q}}$ means the average over $\boldsymbol{q}$. On the other hand, possible exchange interaction causes the correlation function of the hyperfine field to decay with a time constant τ_C. If the exchange interaction is strong, one has $1/\tau_C^2 \gg \langle\omega^2\rangle$ where $\langle\omega^2\rangle$ is the second moment of the local field. In this case the nuclear spin cannot feel the full magnitude of the local field and the NMR spectrum is narrowed. This is called exchange narrowing. As a result the spin-echo has the simple exponential law with the decay rate $1/T_{2L}$, which is roughly given by $1/T_{2L} \sim \tau_C\langle\omega^2\rangle$.

In heavy-electron systems such as $CeCu_2Si_2$ the AF spin correlation develops at low temperatures even though no magnetic order takes place. Then the enhancement of the susceptibility at the corresponding $\boldsymbol{Q}$ vector should be reflected in the temperature dependence of T_2. To show the characteristic behavior we use the parametrization of the $\boldsymbol{q}$-dependent susceptibility as given by eq.(1.89). Then we obtain

$$\left(\frac{1}{T_2}\right)^2 \sim \int \left(\frac{\chi(\boldsymbol{Q})}{1+q^2\xi^2}\right)^2 d\boldsymbol{q} \sim \frac{\chi(\boldsymbol{Q})^2}{\xi^3}. \tag{1.146}$$

In the typical case of $\chi(\boldsymbol{Q}) \sim \xi^2(T)$, we infer that $(1/T_2)^2 \sim \xi(T)$. Therefore, $1/T_2$ is strongly enhanced as the magnetic correlation length $\xi(T)$ grows up.

To summarize, important physical quantities to be obtained by the NMR in magnetic solids are the Knight shift, the nuclear-spin-lattice relaxation time (T_1), the nuclear spin-spin relaxation time (T_2). For the nuclear electric quadrupole (NQR) resonance, which does not need a magnetic field, the NQR frequency and the relaxation time are relevant quantities. The internal field probed by the NMR in the ordered state also provides valuable information on the dispersion relation of the spin-wave excitations.

1.5 Neutron Scattering

1.5.1 Characteristics and utility

Low energy neutrons with typical energy of 30-500 K and with wavelength in a range of 1- 5 $\mathring{A}$ interact with nuclei and magnetic moments of electrons in solids. The corresponding scattering length is of the order of 10^{-13} cm for the nuclear scattering, and of $e^2/mc^2 = 2.8\times10^{-13}$ cm for the magnetic scattering. For magnetic materials, both cross sections are comparable. The magnetic Bragg scattering, i.e. elastic scattering, provides information about the orientation and length of the magnetic moments in the ordered state, and the shape of spin density of magnetic ions. Inelastic scattering in the ordered state may determine the spectrum of elementary excitations like spin-waves. In the paramagnetic state, on the other hand, study of wave-number dependence and the energy distribution of scattering neutrons provides information about the magnetic correlation length and a characteristic energy scale in the spin system.

Neutron scattering experiment is a powerful tool to investigate the spin dynamics in the heavy-electron system since the magnetic neutron scattering cross-section is proportional to the dynamical structure factor $S(\boldsymbol{q},\omega)$, and to $\mathrm{Im}\chi(\boldsymbol{q},\omega)$. For magnetically ordered heavy-electron systems with tiny moments, the elastic scattering profile often shows diffuse scattering instead of the true Bragg one. This shows that the correlation length is finite in contrast to the case of true long-range order. This raises a fundamental problem about the nature of heavy-electron magnetism, which is not yet resolved. In the following we describe very briefly the basics of neutron scattering by magnetic moments. For more details of neutron scattering we refer to standard monographs[33, 34].

1.5.2 Magnetic scattering

The interaction between a neutron (n) at the origin and an electron (e) at $\boldsymbol{r}$ is given by

$$\boldsymbol{V}_e = -\boldsymbol{\mu}_e \cdot \boldsymbol{H}_n(\boldsymbol{r}) \tag{1.147}$$

where $\boldsymbol{\mu}_e$ is the magnetic moment of the electron, and $\boldsymbol{H}_n(\boldsymbol{r})$ is the magnetic field due to the neutron. The latter is given by

$$\boldsymbol{H}_n = \nabla \times \left[\nabla \times (\frac{\boldsymbol{\mu}_n}{r})\right], \tag{1.148}$$

where $\boldsymbol{\mu}_n$ is the magnetic moment of the neutron. In the momentum space, the interaction is simply written as

$$\int d\boldsymbol{r} \exp(-i\boldsymbol{q}\cdot\boldsymbol{r}) V_e(\boldsymbol{r}) = -4\pi\left[\boldsymbol{\mu}_n\cdot\boldsymbol{\mu}_e - (\boldsymbol{\mu}_n\cdot\boldsymbol{e}_q)(\boldsymbol{\mu}_e\cdot\boldsymbol{e}_q)\right] = -4\pi\left(\boldsymbol{\mu}_n\cdot\boldsymbol{\mu}_{e\perp}\right), \tag{1.149}$$

where $\boldsymbol{e}_q$ is the unit vector along $\boldsymbol{q}$, and $\boldsymbol{\mu}_{e\perp}$ denotes the moment of an electron perpendicular to $\boldsymbol{q}$. In deriving this result we use the fact that the Fourier transform of $1/r$ is given by $4\pi/q^2$, and that of ∇ by $i\boldsymbol{q}$.

We consider a collision where the incoming neutron with momentum $\boldsymbol{k}_0$ and energy $k_0^2/2M$ is scattered by the potential $\boldsymbol{H}_s = \sum_j \boldsymbol{V}_e(\boldsymbol{r}_j)$ due to many electrons in the solid. The outgoing neutron loses momentum $\boldsymbol{q}$ and energy ω. The resultant momentum $\boldsymbol{k}_1$ and energy $k_1^2/2M$ should then satisfy

$$\boldsymbol{k}_0 = \boldsymbol{k}_1 - \boldsymbol{q}, \qquad\qquad \frac{k_1^2}{2M} = \frac{k_0^2}{2M} - \omega. \tag{1.150}$$

The differential cross section $d^2\sigma/d\Omega d\omega$ which represents the number of outgoing neutrons in the solid angle $d\Omega$ and in the energy range $d\omega$ around the average value defined by $\boldsymbol{k}_1$ is the central quantity. We specify the spin state of the neutron by σ, and the state of the scattering system by n. Then we obtain

$$\frac{d^2\sigma}{d\Omega d\omega} = \left(\frac{M}{2\pi}\right)^2 \left|\frac{\boldsymbol{k}_1}{\boldsymbol{k}_0}\right| \sum_{\sigma,\sigma'}\sum_{n,n'} P_\sigma P_n \mid \langle \boldsymbol{k}_0\sigma n \mid H_s \mid \boldsymbol{k}_1\sigma' n'\rangle \mid^2 \delta(E_n - E_{n'} + \omega), \tag{1.151}$$

in the Born approximation. The Born approximation is justified since, with R the ionic radius, the magnitude of the interaction is of order $\mu_e\mu_n/R^3$ which is much smaller than the kinetic energy of neutrons $1/(2MR^2)$. In eq.(1.151), $P_n = (1/Z)\exp(-E_n/T)$ is the probability of finding the scattering system in the initial state n, and P_σ is the probability of finding the neutron spin in the initial state σ.

In order to derive the matrix element in eq.(1.151) we assume that only the spin part of the electronic wave function is relevant to the collision, and that the spatial part remains the same before and after the collision. In such a case we have

$$H_s = -4\pi \sum_{\boldsymbol{q}} F(\boldsymbol{q}) \boldsymbol{M}_\perp(\boldsymbol{q}) \cdot \boldsymbol{\mu}_n, \tag{1.152}$$

where we introduce the form factor $F(\boldsymbol{q})$ which represents the spin density in momentum space, and the transverse magnetization $\boldsymbol{M}_\perp(\boldsymbol{q})$ which is defined only inside the Brillouin zone. Namely we have

$$F(\boldsymbol{q})\boldsymbol{M}_\perp(\boldsymbol{q}) = \sum_j \boldsymbol{\mu}_{e\perp} \exp(-i\boldsymbol{q}\cdot\boldsymbol{r}_j).$$

The matrix element is then written as

$$\left(\frac{M}{2\pi}\right)\langle \boldsymbol{k}_0\sigma n \mid H_s \mid \boldsymbol{k}_1\sigma' n'\rangle = \frac{A}{2\mu_B}F(\boldsymbol{q})\langle \sigma n \mid \sigma\cdot\boldsymbol{M}_\perp(\boldsymbol{q}) \mid \sigma' n'\rangle \tag{1.153}$$

where $A=-g_n e/(2Mc\hbar)=0.537\times10^{-12}$ cm with $g_n=-1.91$ being the g-factor of the neutron.

With these notations we obtain the compact formula

$$\frac{d^2\sigma}{d\Omega d\omega}=\left(\frac{A}{2\mu_B}\right)^2\left|\frac{\boldsymbol{k}_1}{\boldsymbol{k}_0}\right| \mid F(\boldsymbol{q}) \mid^2 \sum_{\alpha,\beta}\langle\sigma_\alpha\sigma_\beta\rangle\int\frac{dt}{2\pi}e^{-i\omega t}\langle M_\perp^\alpha(\boldsymbol{q},0)M_\perp^\beta(-\boldsymbol{q},t)\rangle \tag{1.154}$$

where the symbol $\langle\ldots\rangle$ denotes the statistical average. In the case where neutrons are unpolarized, i.e. $\langle\sigma_\alpha\sigma_\beta\rangle=\delta_{\alpha\beta}$, the cross section is reduced to

$$\frac{d^2\sigma}{d\Omega d\omega}=A^2\left|\frac{\boldsymbol{k}_1}{\boldsymbol{k}_0}\right| \mid F(\boldsymbol{q}) \mid^2 \sum_{\alpha,\beta}(\delta_{\alpha\beta}-\boldsymbol{e}_q^\alpha\boldsymbol{e}_q^\beta)S^{\alpha\beta}(\boldsymbol{q},\omega), \tag{1.155}$$

where the tensor $S^{\alpha\beta}(\boldsymbol{q},\omega)$ is called the dynamical structure factor. This quantity is related to the imaginary part of the dynamical susceptibility tensor $\chi^{\alpha\beta}(\boldsymbol{q},\omega)$ via the fluctuation-dissipation theorem:

$$S^{\alpha\beta}(\boldsymbol{q},\omega)=\frac{1}{4\pi}\frac{\mathrm{Im}\chi^{\alpha\beta}(\boldsymbol{q},\omega)}{1-\exp(-\omega/T)}. \tag{1.156}$$

Here the factor 1/4 comes from the definition of $\chi^{\alpha\beta}(\boldsymbol{q},\omega)$ according to eq.(1.56). The fluctuation-dissipation theorem and its background is explained in Appendix B.

Since the correlation between $M_\perp^\alpha(\boldsymbol{q},0)$ and $M_\perp^\beta(\boldsymbol{q},t)$ disappears for $t\to\infty$,

$$\lim_{t\to\infty}\langle M_\perp^\alpha(\boldsymbol{q},0)M_\perp^\beta(-\boldsymbol{q},t)\rangle=\langle M_\perp^\alpha(\boldsymbol{q})\rangle\langle M_\perp^\beta(-\boldsymbol{q})\rangle \tag{1.157}$$

is valid. Accordingly, the result of eq.(1.154) is divided into two parts,

$$\frac{d^2\sigma}{d\Omega d\omega}=\left(\frac{d^2\sigma}{d\Omega d\omega}\right)_{elastic}+\left(\frac{d^2\sigma}{d\Omega d\omega}\right)_{inelastic} \tag{1.158}$$

$$\begin{aligned}\left(\frac{d^2\sigma}{d\Omega d\omega}\right)_{elastic} &= \left(\frac{A}{2\mu_B}\right)^2\left|\frac{\boldsymbol{k}_1}{\boldsymbol{k}_0}\right| \mid F(\boldsymbol{q}) \mid^2 \sum_{\alpha,\beta}\langle\sigma_\alpha\sigma_\beta\rangle\langle M_\perp^\alpha(\boldsymbol{q})\rangle\langle M_\perp^\beta(-\boldsymbol{q})\rangle\delta(\omega)\\ \left(\frac{d^2\sigma}{d\Omega d\omega}\right)_{inelastic} &= \left(\frac{A}{2\mu_B}\right)^2\left|\frac{\boldsymbol{k}_1}{\boldsymbol{k}_0}\right| \mid F(\boldsymbol{q}) \mid^2 \sum_{\alpha,\beta}\langle\sigma_\alpha\sigma_\beta\rangle\\ &\quad\times\int\frac{dt}{2\pi}e^{-i\omega t}\left[\langle M_\perp^\alpha(\boldsymbol{q},0)M_\perp^\beta(-\boldsymbol{q},t)\rangle-\langle M_\perp^\alpha(\boldsymbol{q})\rangle\langle M_\perp^\beta(-\boldsymbol{q})\rangle\right]\end{aligned} \tag{1.159}$$

The first elastic part is referred to as the magnetic Bragg scattering and is nonzero only for a discrete set of $\boldsymbol{q}$ values. If the magnetization density is periodic with some well-defined magnetic unit cell, the average value of $\langle\boldsymbol{M}(\boldsymbol{q})\rangle$ remains nonzero only for $\boldsymbol{q}=\pm\boldsymbol{Q}+\boldsymbol{K}_n$ where $\boldsymbol{Q}$ is associated with the magnetic order and $\boldsymbol{K}_n$ is the reciprocal lattice vector. Due to this selection rule of the Bragg scattering, the detailed spin structure is determined even for complex spin arrangement such as helixes or spin density waves.

The second inelastic part has no strong selection rules on $\boldsymbol{q}$ and ω, and gives the diffuse scattering. The magnetic inelastic cross section in the paramagnetic state where $\langle\boldsymbol{M}(\boldsymbol{q})\rangle$=0 is proportional to the Fourier component of the spin correlation function of $\boldsymbol{S}(\boldsymbol{q})$. The integration of eq.(1.159) over ω is derived with eq.(1.155) and eq.(1.156) as

$$\frac{d\sigma}{d\Omega}=A^2\left|\frac{\boldsymbol{k}_1}{\boldsymbol{k}_0}\right| \mid F(\boldsymbol{q}) \mid^2 T\sum_{\alpha,\beta}(\delta_{\alpha\beta}-\boldsymbol{e}_q^\alpha\boldsymbol{e}_q^\beta)\chi^{\alpha\beta}(\boldsymbol{q}), \tag{1.160}$$

which is proportional to the static susceptibility, $\chi(\boldsymbol{q})$. Therefore, the scattering intensity is significantly increased upon cooling towards the ordering temperature $T_{\boldsymbol{Q}}$, since $\chi_{\boldsymbol{Q}}$ diverges at $T_{\boldsymbol{Q}}$. This is the

so-called critical scattering. In the ordered state, the magnetic inelastic scattering can probe spin-wave excitations, leading to a direct measure of the dispersion relation.

The essential feature of the magnetic scattering profile in heavy-electron compounds is that it consists of a superposition of two contributions at low temperatures: (i) $\boldsymbol{q}$-independent (single-site) quasi-elastic contribution which is of the Lorentzian shape, (ii) a strongly peaked inelastic contribution at finite wave vector $\boldsymbol{Q}$ associated with intersite spin correlations. Furthermore there is a case where the most relevant wavevector $\boldsymbol{Q}$ for the low-energy response changes as the temperature decreases. The same happens also as a function of the energy transfer at low temperature. Thus, the neutron scattering experiment provides a direct way to obtain detailed information on the wave-number and energy dependences of the dynamical response function in heavy-electron systems.

By combining both NMR and neutron scattering experiments, we can study dynamical properties of heavy-electron systems with different types of ground states. This is a central issue to be addressed below in detail from both experimental and theoretical points of view.

Bibliography

[1] Y.Onuki and T.Komatsubara, J. Magn. Magn. Mater. **63-64**, 281 (1987).

[2] F.Steglich, U.Rauchschwalbe, U.Gottwick, H.M. Mayer, G.Sparn, N.Grewe, and U.Poppe, J. Appl. Phys. **57**, 3054 (1985) .

[3] W. Assmus, M. Herrman, U.Rauchschwalbe, S. Riegel, W. Lieke, H. Spille, S. Horn, G. Weber and F.Steglich, Phys. Rev. Lett. **52**, 469 (1984).

[4] J.-M. Mignot, J. Flouquet, P. Haen, F. Lapierre, L. Puech and J. Voiron, J. Magn. Magn. Mater. **76-77**, 97 (1988).

[5] H.R. Ott, H. Rudigier, T.M. Rice, K. Ueda, Z. Fisk and J.L. Smith, Phys. Rev. Lett.**52**, 1915 (1984).

[6] L. Taillefer, J. Flouquet and G.G. Lonzarich, Physica B **169**, 257 (1991).

[7] J.M. Luttinger, Phys. Rev. **121**, 942 (1961)

[8] N.F. Mott, *Metal Insulator Transitions* (Taylor and Francis, London 1990).

[9] P.W. Anderson, *Solid State Physics* Vol.14 (Academic Press, New York, 1963), p.14.

[10] B. Brandow, Adv. Phys, **26**, 651 (1977).

[11] I. Lindgren and J. Morrison, *Atomic Many-Body Theory*, (Springer Verlag, Berlin, 1986).

[12] S. Inagaki and K. Yosida, J. Phys. Soc. Jpn. **50**, 3268 (1981).

[13] M. Roger, J.H. Hetherington and J.M. Delrieu, Rev. Mod. Phys. **55**, 1 (1983).

[14] J. Zinn-Justin, *Quantum Field Theory and Critical Phenomena* (Oxford University Press, Oxford, 1993).

[15] J. Hubbard, Proc. Roy. Soc. **A276**, 238 (1963).

[16] J. Kanamori, Prog. Theor. Phys. **30**, 275 (1963).

[17] M. Gutzwiller, Phys. Rev. Lett. **10**, 159 (1963).

[18] E.H. Lieb and F.Y. Wu, Phys. Rev. Lett. **20**, 1445 (1968).

[19] P. Fulde in *Handbook on the Physics and Chemistry of Rare Earths, Vol.II* (Eds., K.A. Gschneider Jr. and L. Eyring, North-Holland, Amsterdam, 1978), ch.17.

[20] L.D. Landau, Sov. Phys. JETP **3**, 920; ibid., **5**, 101 (1957).

[21] D. Pines and P. Nozieres, *The Theory of Quantum Liquids* (W.A. Benjamin, New York, 1966).

[22] J.W. Serene and D. Rainer, Phys. Reports **101**, 222 (1983).

[23] N. R. Bernhoeft and G. C. Lonzarich, J. Phys. C **7**, 7325 (1995).

[24] Y. Kuramoto, Solid State Commun. **63**, 467 (1987).

[25] L.P. Kadanoff and P.C. Martin, Ann. Phys. **24**, 419 (1963).

[26] K.K. Murata and Doniach, Phys. Rev. Lett. **29**, 85 (1972).

[27] T. Moriya and A. Kawabata, J. Phys. Soc. Jpn. **34**, 639 (1973).

[28] I. E. Dzyaloshinskii and P.S. Kondratenko, Sov. Phys. JETP **43**, 1036 (1976).

[29] T. Moriya, *Spin Fluctuations in Itinerant Electron Magnetism*, (Springer, Berlin, 1985).

[30] A. Abragam, *the Principles of Nuclear Magnetism* (Oxford Press, London, 1961); C.P. Slichter, *Principles of Magnetic Resonance, 2nd Edition* (Springer Series in Solid State Sciences, New York, 1978); J. Winter, *Magnetic Resonance in Metals* (Oxford Press, New York,1967).

[31] T.Shimizu, M.Takigawa, H.Yasuoka and J.H. Wernick, J. Magn. Magn. Mat. **52**, 187 (1985).

[32] T.Moriya, Prog. Theor. Phys. **28** (1962) 371.

[33] S. W. Lovesey, *Theory of Neutron Scattering from Condensed Matter Vols.1 & 2*, (Clarendon Press, Oxford 1984).

[34] G.L. Squires, *Introduction to the Theory of Thermal Neutron Scattering*, (Cambridge University Press, Cambridge, 1978).

Chapter 2

Crossover from Localized Moment to Local Fermi or Non-Fermi Liquid

2.1 Description of Singlet Formation

2.1.1 Renormalization of the exchange interaction

A fundamental theoretical model that can deal with the Kondo effect is called the Anderson model [1]. In the simplest version of the model, one considers an impurity with a nondegenerate localized orbital in a metallic environment which has a single conduction band with the spectrum $\epsilon_{\boldsymbol{k}}$. The localized orbital has the on-site Coulomb repulsion U, and the electron with spin σ is annihilated by the operator f_σ. The model is given by

$$H_A = \sum_{\boldsymbol{k}\sigma}[\epsilon_{\boldsymbol{k}} c^\dagger_{\boldsymbol{k}\sigma} c_{\boldsymbol{k}\sigma} + \frac{1}{\sqrt{N}} V_{\boldsymbol{k}}(c^\dagger_{\boldsymbol{k}\sigma} f_\sigma + f^\dagger_\sigma c_{\boldsymbol{k}\sigma})] + \sum_\sigma \epsilon_f f^\dagger_\sigma f_\sigma + \frac{1}{2} U \sum_{\sigma\neq\sigma'} n_{f\sigma} n_{f\sigma'} \tag{2.1}$$

where $V_{\boldsymbol{k}}$ is the strength of the hybridization, and N the number of lattice sites. It is straightforward to generalize the Anderson model so that more realistic structures of the f shell and the conduction bands are taken into account.

In spite of its simple appearance, the Anderson model has a remarkably rich physics including the Kondo effect. There are already an enormous number of treatises on the Kondo effect in general [2, 3, 4], and in particular on the exact solution with use of the Bethe ansatz [4, 5, 6]. In view of this situation we avoid in this book a repetition of such treatment. Instead we emphasize the effective Hamiltonian approach which naturally includes the concepts of scaling and the renormalization group.

As the first step to construct the effective Hamiltonian we consider the situation where the average occupation of the f state is unity, and the charge fluctuation of the f state can be neglected. This situation is realized when the f level ϵ_f is deep below the Fermi level (taken to be zero), and $\epsilon_f + U$ is far above the Fermi level. Thus we work with the model space where f states are neither vacant nor doubly occupied. The hybridization part H_{hyb} in H_A connects the model space and the other states to be projected out. According to eq.(1.38) the effective interaction in the lowest order is given by

$$H_{int} = P H_{hyb} (E_i - H_c - H_f)^{-1} Q H_{hyb} P. \tag{2.2}$$

Here the energy E_i can be taken as the zero-th order value. The intermediate $f$states orthogonal to P are either vacant or double occupied. Only a singlet pair consisting of an incoming conduction electron and an $f$electron change into the doubly occupied state, which decays again by hybridization. In the latter process we have two possibilities: either the spin of the conduction electron remains the same as the incoming one or not. The resultant effective model is given by

$$H_{eff} = H_c + \frac{1}{N} \sum_{\boldsymbol{k}\alpha} \sum_{\boldsymbol{k}'\beta} [\frac{1}{2} J_{\boldsymbol{k}\boldsymbol{k}'} \boldsymbol{S} \cdot \boldsymbol{\sigma}_{\beta\alpha} c^\dagger_{\boldsymbol{k}'\beta} c_{\boldsymbol{k}\alpha} + K_{\boldsymbol{k}\boldsymbol{k}'} \delta_{\alpha\beta} c^\dagger_{\boldsymbol{k}'\beta} c_{\boldsymbol{k}\alpha}], \tag{2.3}$$

where $\boldsymbol{S}$ is the impurity spin operator, and

$$J_{\boldsymbol{k}\boldsymbol{k}'} = 2 V_{\boldsymbol{k}} V_{\boldsymbol{k}'} [\frac{1}{\epsilon_{\boldsymbol{k}'} - \epsilon_f} - \frac{1}{\epsilon_{\boldsymbol{k}} - \epsilon_f - U}], \tag{2.4}$$

$$K_{\boldsymbol{k}\boldsymbol{k}'} = \frac{1}{2} V_{\boldsymbol{k}} V_{\boldsymbol{k}'} [\frac{1}{\epsilon_{\boldsymbol{k}'} - \epsilon_f} + \frac{1}{\epsilon_{\boldsymbol{k}} - \epsilon_f - U}]. \tag{2.5}$$

The model H_{eff} can further be simplified by replacing $V_{\boldsymbol{k}}$ by a constant V, and by assuming that $\epsilon_{\boldsymbol{k}}$ and $\epsilon_{\boldsymbol{k}'}$ are negligible as compared with ϵ_f or $\epsilon_f + U$. In the particular case of $\epsilon_f + U = |\epsilon_f|$, which is called the symmetric case, the potential scattering given by $K_{\boldsymbol{k}\boldsymbol{k}'}$ vanishes, and $J_{\boldsymbol{k}\boldsymbol{k}'}$ becomes $J = 2V^2/|\epsilon_f|$. Then we obtain the so-called the Kondo model (or the s-d model):

$$H_K = H_c + J\boldsymbol{S} \cdot \boldsymbol{s}_c = H_c + H_{ex}, \tag{2.6}$$

where $\boldsymbol{s}_c$ is the spin operator of conduction electrons at the impurity site, and is given by

$$\boldsymbol{s}_c = \frac{1}{2N} \sum_{\boldsymbol{k}\boldsymbol{k}'} \sum_{\mu\nu} c^\dagger_{\boldsymbol{k}\mu} \boldsymbol{\sigma}_{\mu\nu} c_{\boldsymbol{k}'\nu}. \tag{2.7}$$

The Kondo model, which may look even simpler than the Anderson model, generates in fact unmanageable singularities in the perturbation theory in J. It is now understood that the singularities mean that the starting point of the perturbation theory is inappropriate at zero temperature, however small J is. The ground state is more easily understood if one uses the Anderson model for all values of the parameters. On the other hand, at finite temperature the perturbation theory becomes more and more accurate as one goes higher order in J. The best theoretical machinery to understand these contrasting properties of the Kondo model is called the renormalization group, which will be discussed shortly. Before going to the analysis of the Kondo model we introduce another related model. Namely the Coqblin-Schrieffer model H_{CS} [7] is defined by

$$H_{CS} = H_c + \frac{J}{2} \mathcal{P}_{spin}. \tag{2.8}$$

where $\mathcal{P}_{spin}$ is the spin permutation operator which is explicitly written as

$$\mathcal{P}_{spin} = \frac{1}{N} \sum_{\boldsymbol{k}\boldsymbol{k}'} \sum_{\nu\mu} f^\dagger_\nu f_\mu c^\dagger_{\boldsymbol{k}\mu} c_{\boldsymbol{k}'\nu} = 2\boldsymbol{S} \cdot \boldsymbol{s}_c + \frac{1}{2} \hat{n}_f \hat{n}_c. \tag{2.9}$$

where $\hat{n}_f$ $(= 1)$ is the number operator of f electrons, and $\hat{n}_c$ is that of conduction electrons at the impurity site. The Coqblin-Schrieffer model is frequently used in the case of an orbitally degenerate magnetic impurity because of its simplicity to generalize to arbitrary degeneracy.

Let us now turn to the renormalization treatment of the Kondo model. We use the effective Hamiltonian method explained in Chapter I as a variant of the perturbation theory. Suppose that the conduction band extends from $-D$ to D, and the Fermi level is at the center of the band $\mu = 0$. Then we choose the model space as the one which does not involve conduction states near the band edges. With this restriction the exchange interaction should be modified into the effective one. This change of interaction, which occurs in the process of reducing the model space, is called the renormalization. A very powerful way to accomplish the renormalization is to eliminate the high energy states by an infinitesimal amount in each step, and continue the process successively [8]. Let us illustrate the process in the following. In the lowest order of the Brillouin-Wigner perturbation theory, we obtain the effective Hamiltonian as

$$H_{eff} = P(H_c + H_{ex})P + PH_{ex}(E_i - H_c)^{-1} Q H_{ex} P \tag{2.10}$$

where E_i is the energy of the state to be derived. We are interested in low energy states where $|E_i|$ is close to the ground state energy E_g of H_c. Choosing Q to project onto a space with conduction states $[D + \delta D, D]$ and $[-D, -D - \delta D]$ with $\delta D < 0$ infinitesimal, we can safely replace E_i by E_g in the denominator. Figure 2.1 shows the perturbation process.

Let us assign the spins σ, ξ and σ' for the incoming conduction electron, the intermediate state with high energy, and the outgoing electron, respectively. Then we look at scattering with a spin component $JS^\alpha s_c^\alpha$ for the right part, and $JS^\beta s_c^\beta$ for the left part. In Fig.2.1 (a) the matrix elements of $\boldsymbol{s}_c$ are given by

$$\langle \sigma' | s_c^\beta | \xi \rangle \langle \xi | s_c^\alpha | \sigma \rangle, \tag{2.11}$$

which is called the direct scattering. For the scattering shown in Fig.2.1 (b) we similarly obtain

$$\langle \sigma' | s_c^\alpha | \xi \rangle \langle \xi | s_c^\beta | \sigma \rangle. \tag{2.12}$$

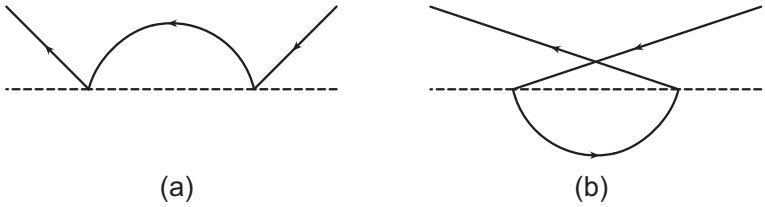

Figure 2.1: Exchange scattering processes in second order. The solid line shows a conduction-electron state, while the dashed line the impurity spin. The projection operator Q requires the intermediate conduction-electron states to have energies near the band edges, which are opposite to each other in the cases (a) and (b).

Since the energy of the intermediate state does not depend on ξ, summation over ξ can be carried out independent of the energy denominator. Note that the process (b) acquires an extra minus sign because an interchange of fermion operators is involved in evaluating the product of operators. Then we obtain as the sum of (a) and (b)

$$\frac{J^2}{-D}\sum_{\alpha\beta} S^\beta S^\alpha [s_c^\beta, s_c^\alpha]|\delta D|\rho_c, \tag{2.13}$$

as the second-order effective Hamiltonian. Here $\rho_c = (2D)^{-1}$ is the density of conduction states per spin per site assumed uniform. By using the commutation rule

$$[s_c^\beta, s_c^\alpha] = -i\epsilon_{\alpha\beta\gamma} s_c^\gamma, \tag{2.14}$$

where $\epsilon_{\alpha\beta\gamma}$ is the completely antisymmetric unit tensor, we find that the effective interaction takes the same form as the original H_{ex}, except that the strength is modified. Thus we obtain the change δJ of the exchange interaction as

$$\delta J = -\frac{\delta D}{D} J^2 \rho_c. \tag{2.15}$$

This differential relationship is called the scaling equation [8], or the renormalization-group equation. The latter name stems from the fact that a succession of two renormalization processes can be regarded as a different single process, and that each process of renormalization constitutes a kind of group element. In contrast to the usual definition of a group, the renormalization group does not necessarily have the inverse of an element. Precisely speaking, therefore, the renormalization group is a semigroup.

One can continue to eliminate the conduction states near the new band edge as long as the final effective band width $2D_{eff}$ is much larger than the energy scale we are interested in. This condition is also necessary to justify the lowest order perturbation theory in each renormalization step. Under this restriction one can integrate the scaling equation with the result

$$J_{eff} = \frac{J}{1 - J\rho_c \ln(D/D_{eff})}. \tag{2.16}$$

Here the boundary condition is such that $J_{eff} = J$ for $D_{eff} = D$.

The important feature of J_{eff} is that it increases as one decreases D_{eff}, and finally diverges at $D_{eff} = D\exp[-1/(J\rho_c)]$. This characteristic energy $D\exp[-1/(J\rho_c)]$ in temperature units is called the Kondo temperature T_K. Note that T_K is a nonanalytic function of the exchange interaction. Of course there is no guarantee for the renormalization to be valid down to $D_{eff} = T_K$. It simply says that the perturbation theory breaks down as one goes lower and lower in energy scales. As we shall see later, T_K also enters into physical quantities such as the susceptibility and specific heat near zero temperature.

If one is working with a temperature T sufficiently higher than T_K, it is necessary to take explicit account of thermally excited conduction states. Then the renormalization should stop at D_{eff} which is of the order of T. The proportionality constant can be set to unity within the logarithmic accuracy. We define the effective interaction in this case as

$$J_{eff}(T) = \frac{J}{1 - J\rho_c \ln(D/T)}. \tag{2.17}$$

If one replaces J by $J_{eff}(T)$ in the lowest order perturbative calculation of a physical quantity, say, the resistivity or the magnetic susceptibility, the result reproduces infinite summation of leading logarithmic terms [9].

Let us first explain the case of the resistivity ρ. In the simplest theory of electronic conduction in metals the conductivity $\sigma = 1/\rho$ is given by

$$\sigma = \frac{ne^2\tau}{m^*}, \tag{2.18}$$

where n is the density of conduction electrons with effective mass m^*. The lifetime τ of conduction electrons near the Fermi surface is given in the Born approximation by

$$\frac{1}{\tau} = 2\pi c_{imp} J^2 \sum_\alpha S_\alpha^2 \mathrm{Tr}_c s_\alpha^2 = \frac{3\pi}{4} c_{imp} \frac{J^2}{\rho}_c, \tag{2.19}$$

where c_{imp} is the concentration of magnetic impurities. We write the resultant resistivity as ρ_0. In the Born approximation, one does not take account of intermediate states with high excitation energies. However in higher order perturbation in J, these states contribute to the leading logarithmic singularity. If one uses $J_{eff}(T)$ in place of J, the intermediate states with high energies are correctly taken into account. As a result of this replacement we obtain

$$\rho(T) = \frac{\rho_0}{[1 - J\rho_c \ln(D/T)]^2} = \frac{\rho_0}{[J\rho_c \ln(T/T_K)]^2}. \tag{2.20}$$

This result is the same as the one obtained by infinite summation of perturbation terms [9], and reduces to the original result of Kondo in $O(J^3)$. The resistivity thus increase logarithmically as the temperature is decreased. The divergence at $T = T_K$ lies beyond the valid region of the effective Hamiltonian theory and is merely an artifact of the approximation. Determination of the range of validity requires more accurate analysis which will be discussed later.

As the next example we consider the relaxation rate Γ of the local moment. In the Born approximation Γ is given by

$$\Gamma = \frac{3\pi}{4N} \sum_{\boldsymbol{k},\boldsymbol{p}} J^2 f(\epsilon_{\boldsymbol{k}})[1 - f(\epsilon_{\boldsymbol{p}})]\delta(\epsilon_{\boldsymbol{k}} - \epsilon_{\boldsymbol{p}}) = \frac{3}{4}\pi(J\rho_c)^2 T, \tag{2.21}$$

which is usually referred to as the Korringa relaxation. Replacing J here by J_{eff} leads to

$$\Gamma(T) = \pi \left(\frac{J\rho_c}{1 - J\rho_c \ln(D/T)} \right)^2 T. \tag{2.22}$$

Thus the relaxation rate is enhanced by the Kondo effect. In contrast to the resistivity to which ordinary scattering also contributes, magnetic relaxation is dominantly given by the exchange interaction. Hence the enhancement by the Kondo effect is conspicuous and the temperature dependence deviates drastically from T-linear behavior. Again the divergence at $T = T_K$ should not be trusted.

2.1.2 Numerical renormalization group method

As the temperature approaches T_K from above, the dimensionless coupling $J_{eff}\rho_c$ becomes of the order of unity. Then the simplest renormalization described above breaks down. In order to proceed further, Wilson developed a numerical renormalization group approach [10]. In this approach one can deal with newly generated terms in the effective Hamiltonian very easily. We first pick out the s-wave part of the whole conduction states since other parts do not couple to the magnetic impurity in the Kondo model. Then we approximate the spectrum ϵ_k by the following form:

$$\epsilon_k = v_F k, \tag{2.23}$$

where k is measured relative to k_F. The range of momentum k is set to be $k \in [-k_F, k_F]$, which means the band width of $2D = 2k_F v_F$. In the following we take choose units so that the Fermi momentum is unity: $k_F = 1$. We introduce a set of discretized spherical orbitals ϕ_n around the impurity by averaging the s-wave states over the k-space interval $[\Lambda^{-n+1}, \Lambda^{-n}]$, where the parameter Λ (> 1) controls the

discretization. For negative momentum we form corresponding states by averaging over $[-\Lambda^{-n+1}, -\Lambda^{-n}]$. Then we make a unitary transformation from ϕ_n to a new Wannier-type basis in terms of which the Hamiltonian matrix for the conduction band is given in the tridiagonal form. We refer to the original paper [10] for the fairly complicated procedure to construct the basis set explicitly. The final form of the Hamiltonian in the new basis is given by

$$H_\Lambda = D\sum_{n=0}^{\infty}\Lambda^{-n/2}\sum_{\sigma}(c^\dagger_{n\sigma}c_{n+1\sigma}+c^\dagger_{n+1\sigma}c_{n\sigma})+\frac{1}{2}\tilde{J}\sum_{\alpha\beta}c^\dagger_{0\alpha}\boldsymbol{\sigma}_{\alpha\beta}c_{0\beta}\cdot\boldsymbol{S}, \tag{2.24}$$

where $\tilde{J}$ is the exchange interaction in the new basis set. It is evident that the new Hamiltonian has the tight-binding form where the transfer $\Lambda^{-n/2}$ decreases exponentially as the orbital number n increases. Only the innermost orbital 0 is coupled to the impurity spin $\boldsymbol{S}$. We note that eq.(2.24) with $\tilde{J}=0$ describes the free electron band by definition.

In order to construct the effective Hamiltonian, which is nothing but the renormalization of the model, we perform the projection Q successively. Namely, we first take certain manageable number ν of Wannier-type orbitals near the origin and diagonalize the Hamiltonian matrix with this truncated subspace. By explicit diagonalization we can arrange the resultant many-body states involving the impurity spin according to their energies in the subspace. Then we shall keep only the lowest N_P states and neglect the others. This neglect amounts to the first step of projection Q in constructing the model space. We newly add the orbital next to the ν-th one and construct many-body states by the direct product with the N_P states obtained by the first step of the renormalization. Then we diagonalize the Hamiltonian within the newly constructed many-body subspace, and keep only the lowest N_P states again. By repeating the same procedure we can include states more and more remote from the origin in the effective Hamiltonian. In this way we can see how the effective Hamiltonian converges in the limit of $n\to\infty$.

The convergent form of the effective Hamiltonian, or the ground and low-lying states it describes, is called a fixed point of the renormalization group. In the special case of $J=0$ the fixed point must be that of free electrons. The energy scale $\Lambda^{-n/2}$ introduced in the n-th iteration corresponds to the separation $2\pi v_F/L_n$ of the free electron spectrum with L_n the size of the system corresponding to the renormalization step. In other words, the minimum momentum in the logarithmic discretization is proportional to the inverse of the system size. The spectrum of a free Fermi gas is given by

$$E=\frac{2\pi v_F}{L_n}\left[\frac{Q^2}{8}+\frac{S(S+1)}{4}+n_Q+n_S\right], \tag{2.25}$$

where $Q=\delta n_\uparrow+\delta n_\downarrow$ describes the number of electrons relative to the pure Fermi sea, and $n_Q(n_S)$ are the number of spin conserving (spin flipping) particle-hole excitations. These numbers are analogous to the number of phonon excitations. Equation (2.25) is just another way of writing the energy of conduction bands. For an even number of free conduction electrons the ground state is non-degenerate and the first excited level is separated by $2\pi v_F/L_n$ which has excess charge $Q=\pm1$ and spin 1/2. For an odd number of free conduction electrons the ground state is doubly degenerate with spin 1/2 since the one-electron level nearest to the Fermi level is singly occupied.

In the case of the Kondo model, the fixed point Hamiltonian turns out to have the same spectrum as the free conduction band. However, the spectrum with an even number of conduction electrons corresponds to that of odd number of free conduction electrons. This represents the fact that the magnetic impurity couples tightly with one conduction electron spin. The resultant spectrum with an even number of conduction electrons has spin 1/2 and that with odd number has spin 0. We discuss this aspect of the spectrum in more detail later in 2.3.1.

One can do the same thing for the Anderson model by just replacing the exchange interaction term in eq.(2.24) by the hybridization term. It was demonstrated by Krishnamurthy et al [11] that as the iteration proceeds the spectrum shows two alternating sequences as in the case of the Kondo model.

The most important conclusion of the numerical renormalization group is to elucidate the way the ground state is approached as temperature is decreased. In the numerical renormalization group method one can calculate the susceptibility for all temperatures [4, 10, 11, 12]. Below T_K, the increase of the impurity susceptibility becomes slow and saturates to a value of the order of C/T_K with C the Curie constant.

2.1.3 Local Fermi-liquid theory

The fixed point of the Kondo model is described by a local Fermi-liquid theory of Nozieres, who revealed that the phase shift of conduction electrons incorporates the many-body effect [13]. The term "local Fermi-liquid" means that low-lying eigenstates of the system are one-to-one correspondence with those of the Anderson model with $U = 0$. Hence the Fermi-liquid fixed point is accessible by perturbation theory with respect to U if one works in the Anderson model. By analysis of the perturbation series up to infinite order, Yamada derived a nontrivial relationship between the susceptibility and the specific heat [14].

Here we present an alternative phenomenological approach which is in parallel to the original Fermi-liquid theory of Landau. We first diagonalize the Anderson model without the Coulomb repulsion. If one assumes spherical symmetry for hybridization, for simplicity, only the s-wave part of conduction states is mixed. We therefore neglect in the following other conduction states with finite angular momentum, since these states are not affected by the magnetic impurity. Each eigenstate is characterized by the radial momentum p of the scattered s-wave and the spin. The Coulomb interaction among f electrons appears now as an interaction among hybridized electrons. The quasi-particles in this case are characterized by p and σ. Then the Landau interaction function is given by $f(p\sigma, k\sigma')$. The quasi-particle distribution function is identical to the noninteracting one in the ground state. Namely it is unity if the energy of the state is below the Fermi level, and zero otherwise. The deviation $\delta n_{p\sigma}$ from the ground state determines the energy of the excited state. The latter is expanded as

$$E = E_g + \sum_{p\sigma} \epsilon_{p\sigma} \delta n_{p\sigma} + \frac{1}{2} \sum_{p\sigma} \sum_{k\sigma'} f(p\sigma, k\sigma') \delta n_{p\sigma} \delta n_{k\sigma'} + O(\delta n_{p\sigma}^3). \tag{2.26}$$

As in the translationally invariant case, the expansion up to second order terms is sufficient to describe the low-energy excitations. This includes the magnetic susceptibility and the low temperature limit of the specific heat. The validity of this assumption can be confirmed by analysis of infinite-order perturbation series [14, 15].

The low-energy excitations have $\delta n_{p\sigma}$ which is strongly peaked around the Fermi level. Provided the interaction $f(p\sigma, k\sigma')$ is a smooth function of the momentum, one may replace p and k here by the Fermi momentum p_F. By rotational invariance we are then left with only two dimensionless parameters F and Z given by

$$F = \frac{1}{2}[f(p_F\sigma, p_F\sigma) + f(p_F\sigma, p_F\bar{\sigma})]\rho^*, \quad Z = \frac{1}{2}[f(p_F\sigma, p_F\sigma) - f(p_F\sigma, p_F\bar{\sigma})]\rho^*, \tag{2.27}$$

where $\bar{\sigma} = -\sigma$ and ρ^* is the density of states of quasi-particles (for both spins) at the Fermi level. Since we are dealing with a single impurity in a macroscopic number N of s-wave states, the parameters F and Z are of order $1/N$.

In terms of the effective Hamiltonian picture, $f(p\sigma, k\sigma')$ is regarded as the effective interaction for zero momentum transfer in a fictitious one-dimensional system. The momentum in this system must be positive since it is originally the radial part. To obtain the scattering amplitude between the quasi-particles with small momentum transfer q and small energy transfer ω, we have to consider the repeated scattering as shown in Fig.2.2. Each bubble in Fig.2.2 corresponds to the zeroth-order susceptibility and is given by

$$\chi_0(q, \omega) = \frac{2}{N} \sum_k \frac{kq/m^*}{\omega - kq/m^* + i\delta} \left(-\frac{\partial f(\epsilon_k)}{\partial \epsilon_k} \right), \tag{2.28}$$

where m^* is the effective mass of quasi-particles. The susceptibility is a function of the ratio $v_F q/\omega$ with v_F being the Fermi velocity. In the case of $v_F q \gg \omega$, which is called the q-limit, $\chi_0(q, \omega)$ tends to ρ^*. In the opposite case of $v_F q \ll \omega$, which is called the ω-limit, it tends to zero. Note that eq.2.28) is the small-momentum limit of the form given by eq.1.46.

The Fermi-liquid parameters F and Z correspond to the forward scattering amplitude of quasi-particles in the ω-limit. On the other hand the forward scattering amplitude $a(p\sigma, k\sigma')$ in the q-limit is given by

$$a(p\sigma, k\sigma') = f(p\sigma, k\sigma') - \rho^* \sum_\tau f(p\sigma, p\tau) a(p\tau, k\sigma'), \tag{2.29}$$

which is obtained by repetition of the correction shown in Fig.2.2. From combinations of $a(p\sigma, k\sigma')$ as in eq.2.27 we introduce the parameters A (spin-symmetric part) and B (spin antisymmetric part) which

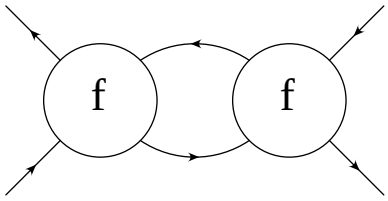

Figure 2.2: Quasi-particle scattering in the second order in the effective interaction $f(p\sigma, k\sigma')$. The bubble in the center corresponds to $\chi_0(q, \omega)$.

are related to F and Z by

$$A = F/(1+F), \quad B = Z/(1+Z). \tag{2.30}$$

In the most general case of the scattering amplitude $\langle p_1\sigma_1, p_2\sigma_2|a|p_3\sigma_3, p_4\sigma_4\rangle$ with incoming quasi-particles with $p_3\sigma_3, p_4\sigma_4$ and outgoing ones $p_1\sigma_1, p_2\sigma_2$, the antisymmetry of the fermionic wave function imposes a constraint:

$$\langle p_1\sigma_1, p_2\sigma_2|a|p_3\sigma_3, p_4\sigma_4\rangle = -\langle p_1\sigma_1, p_2\sigma_2|a|p_4\sigma_4, p_3\sigma_3\rangle. \tag{2.31}$$

In the particular case of the forward scattering we obtain $a(p\sigma, p\sigma) = 0$, which is equivalent to

$$A + B = 0. \tag{2.32}$$

This relation is an example of the so-called forward scattering sum rule [16]. Therefore we are left with a single independent parameter to characterize the quasi-particle interaction in the Anderson model.

Since the low-lying excitations of the system are quasi-particles, they should determine the specific heat and the susceptibility. In the thermally excited case δn_p is an odd function of $p - p_F$. Therefore the increase of energy is dominated by the term linear in δn_p in eq.(2.26), as in the translationally invariant system. This gives $O(T^2)$ correction, while the quasi-particle interaction gives $O(T^4)$ correction. We can extract the impurity contribution to the specific heat from the change in the density of states. Namely we introduce $\alpha = O(1/N)$ by

$$\rho^* = \rho_c(1+\alpha) \tag{2.33}$$

Then we obtain the impurity specific heat C as

$$C = \frac{1}{3}\pi^2\rho_c\alpha T \equiv \gamma T, \tag{2.34}$$

which is of $O(1)$ since ρ_c is of $O(N)$. On the other hand, the spin susceptibility χ_s^{total} of the whole system is calculated as

$$\chi_s^{total} = \frac{\rho^*}{4(1+Z)} = \frac{1}{4}\rho_c(1+\alpha-Z) + O(\frac{1}{N}). \tag{2.35}$$

Thus the impurity contribution χ_s of $O(1)$ is given by

$$\chi_s = \frac{1}{4}\rho_c(\alpha - Z). \tag{2.36}$$

Similarly the impurity contribution to the charge susceptibility χ_c is calculated as

$$\chi_c = \rho_c(\alpha - F). \tag{2.37}$$

We can now deduce an important relation between the specific heat and susceptibilities. Because of the constraint $A + B = F + Z + O(1/N^2) = 0$, we obtain

$$4\chi_s + \chi_c = 6\gamma/\pi^2, \tag{2.38}$$

or in units of noninteracting counterparts with suffix 0:

$$\chi_s/\chi_{s0} + \chi_c/\chi_{c0} = 2\gamma/\gamma_0. \tag{2.39}$$

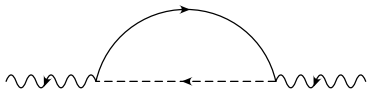

Figure 2.3: Lowest order effective potential in the $1/n$ expansion. For the f states, the wavy line shows the vacant state, while the dashed line shows single occupied states.

In the case where the f level is singly occupied and U is large, the charge susceptibility is almost zero. In this limit the ratio R of χ_s/χ_{s0} to γ/γ_0 goes to 2. Otherwise R takes a value between 1 and 2. The quantity R measures the strength of the electron correlation at the impurity, and is often referred to as the Wilson ratio .

There is also a remarkable dynamical relation as a consequence of the Fermi liquid ground state. Namely the impurity contribution to the dynamical susceptibility is proportional to the square of the static susceptibility. This relation is called the Korringa-Shiba relation. The rigorous proof of the relation requires a detailed diagrammatic analysis for which we refer to the original papers [15, 17, 18]. In this book, we give a less rigorous but more intuitive proof in 2.2.2 leading to eq.(2.71).

2.1.4 The $1/n$ expansion

The fixed point of the Anderson model is a spin singlet, and is connected continuously to the trivial case of the vacant f state. It is found that in the limit of large degeneracy n of the f electron level, the singlet state has an energy lower than the singly occupied state with a local moment. Therefore perturbation theory in terms of $1/n$ should converge. Actually the small parameter $1/n$ appears as scaling of hybridization. There is thus a chance of having a perturbation theory valid for all temperatures T, since at high T the expansion with respect to hybridization guarantees that the atomic limit is recovered.

Let us assume that the spin index σ in the Anderson model H_A takes n different values and that U is infinite. The resultant model, which is called the SU(n) Anderson model, is written as

$$H_{SU(n)} = H_c + H_f + H_{hyb}. \tag{2.40}$$

We introduce the hybridization intensity $W_0(\epsilon)$ by

$$W_0(\epsilon) = \frac{1}{N}\sum_{\boldsymbol{k}} |V_{\boldsymbol{k}}|^2 \delta(\epsilon - \epsilon_{\boldsymbol{k}}), \tag{2.41}$$

which is taken to be a constant W_0 in the range $-D < \epsilon < D$, and zero otherwise. We take nW_0 as the unit of energy, and use the Brillouin-Wigner perturbation theory to calculate the ground-state energy [19]. In the case of the singlet state, the effective interaction (or rather potential in this case) is of $O(1)$ because of summation over all channels. This is shown in Fig.2.3. Taking the direct product of the vacant f state and the Fermi sea as the model space $|0\rangle$, the ground-state energy E_0 relative to the Fermi sea is then given by

$$E_0 = \langle 0|H_{hyb}(E_0 - H_c - H_f)^{-1}H_{hyb}|0\rangle = nW_0\int_{-D}^{0}\frac{d\epsilon}{E_0 + \epsilon - \epsilon_f}. \tag{2.42}$$

In the extreme case of $nW_0 \ll |\epsilon_f| \ll D$, one can solve this equation analytically. Namely one obtains

$$E_0 - \epsilon_f \equiv -T_0 = -D\exp\left(\frac{\epsilon_f}{nW_0}\right). \tag{2.43}$$

On the other hand, the lowest energy of the multiplet state has at most $O(1/n)$ corrections because summation over n channels is absent for the intermediate states. Thus it remains ϵ_f to the leading order and is higher than E_0 by T_0.

It is remarkable that such a simple calculation can identify the characteristic energy scale T_0 in the singlet ground state. The scale T_0 corresponds to the Kondo temperature T_K in the case where the average occupation n_f of the f state is almost 1. In the more general case n_f is calculated as

$$n_f = \frac{\partial E_0}{\partial \epsilon_f} = nW_0\int_{-D}^{0} d\epsilon \frac{1 - n_f}{(E_0 + \epsilon - \epsilon_f)^2} \sim \frac{nW_0}{T_0}(1 - n_f). \tag{2.44}$$

Namely we obtain

$$n_f = \left(1 + \frac{T_0}{nW_0}\right)^{-1}. \tag{2.45}$$

We can also obtain the magnetic susceptibility by the second derivative of $E_0(H)$ with respect to the magnetic field H. The ground-state energy E_0 in the presence of H is given by

$$E_0 = W_0 \sum_{Jz} \int_{-D}^{0} \frac{d\epsilon}{E_0 + \epsilon - \epsilon_f - g_J \mu_B J_z H}. \tag{2.46}$$

Straightforward calculation gives

$$\chi = C_J n_f / T_0, \tag{2.47}$$

where $C_J = (g_J \mu_B)^2 J(J+1)/3$ is the Curie constant with $J = (n-1)/2$ the angular momentum of the f state. Thus the susceptibility is also determined by T_0.

One should recognize here that the excitation gap T_0 between the singlet and the multiplet is an artifact of the leading-order theory. In reality, there is no gap since the multiplet wave function can extend to a macroscopic distance. As a result the lowest multiplet wave function has no difference from the local singlet one near the origin. The presence of the gap is not a problem if one is interested only in static properties, as we have seen above. However, it becomes serious if one discusses the dynamical properties.

2.1.5 Effects of spin-orbit and CEF splittings

In order to understand experimental results, it is very important to take into account spin-orbit and CEF splittings of the f shell. According to the energy scale of excitations or temperature, the apparent Kondo temperature changes. Thus the Kondo temperature derived from the specific heat or the susceptibility at low temperatures is generally smaller than the apparent Kondo temperature derived, for example, by photoemission spectroscopy. Such changes of the Kondo scale explain the temperature dependence of the magnetic relaxation rate measured by neutron scattering. In this section we explain how the real and apparent Kondo temperatures are influenced by the presence of splittings.

Let us assume that each split level E_α in the f^1 state has a degeneracy n_α and hybridization intensity W_α between the band edges $[-D, D]$. In the Brillouin-Wigner perturbation theory, the singlet ground-state energy $E_s \equiv E_0 - T_K$ is given by

$$E_s = \sum_\alpha W_\alpha \int_{-D}^{0} \frac{d\epsilon}{E_s - E_\alpha + \epsilon} \tag{2.48}$$

In the case of D much larger as compared with other energies such as the level splittings and T_K, we may replace E_s in the left-hand side by E_0 to obtain

$$E_0 \sim n_0 W_0 \ln \frac{T_K}{D} + \sum_{\alpha \neq 0} n_\alpha W_\alpha \ln \frac{\Delta_\alpha}{D}, \tag{2.49}$$

where $\Delta_\alpha = E_\alpha - E_0$. From eq.(2.49), we can solve for T_K as

$$T_K = D \exp\left(\frac{E_0}{n_0 W_0}\right) \prod_{\alpha \neq 0} \left(\frac{D}{\Delta_\alpha}\right)^{n_\alpha W_\alpha / (n_0 W_0)}, \tag{2.50}$$

This result was first obtained by ref.[20] by a different method.

It is clear that T_K in eq.(2.50) is enhanced by the presence of higher multiplet. However, if one compares with the hypothetical Kondo temperature without any splitting, the actual T_K is much reduced. This observation becomes important when one consistently interprets experimental data taken with different resolutions and temperature.

2.2 Dynamics of the Kondo Impurity

2.2.1 Mean-field theory

As an approach from the ground state, the simplest is a mean-field theory which starts from the Fermi-liquid ground state. We introduce boson operators b and $b^\dagger$ to represent the vacant f state in the n-fold degenerate Anderson model. The X-operators introduced in 1.3.2 are then represented by

$$X_{00} = b^\dagger b, \quad X_{\sigma\sigma} = f_\sigma^\dagger f_\sigma, \quad X_{\sigma 0} = f_\sigma^\dagger b, \tag{2.51}$$

with the constraint $\sum_\sigma f_\sigma^\dagger f_\sigma + b^\dagger b = 1$. Namely, $b^\dagger$ creates the physical vacant state by operating on the fictitious vacuum of f states. If the constraint is regarded as an operator relation, f_σ and $f_\sigma^\dagger$ do not obey the commutation rule for fermions. The same applies to b and $b^\dagger$. Another viewpoint is that one uses the standard commutation rules for fermions and bosons and imposes the constraint as the relevant subspace to be picked out from the full Fock space. The auxiliary particle representing the vacant state is often called the slave boson . This kind of artifice was in fact used already for the Kondo model [9] to represent the spin operators. The constraint was handled by a fictitious chemical potential which goes to infinity at the end of the calculation. The use of the boson in the case of the Anderson model was proposed later [21, 22] again with use of the Abrikosov technique. Because of the limiting procedure, however, one cannot use the standard linked cluster theorem which leads to the Feynman diagram expansion [23]. If one carefully selects a part of the Feynman diagrams, the result becomes identical to the perturbation theory with use of resolvents as will be discussed later in this section.

In dealing with the Fermi-liquid ground state and low-energy excitations, a mean field theory was introduced [24] in which the constraint is satisfied only as an average. Namely

$$\sum_\sigma \langle f_\sigma^\dagger f_\sigma \rangle + \langle b^\dagger b \rangle = 1. \tag{2.52}$$

The average $\langle b \rangle = r$ should vanish in the exact theory because of the fluctuation of the phase of b. If one neglects this aspect and determines r variationally, the model maps to another Anderson model without the Coulomb repulsion. Namely we try to simulate the low-energy physics by the mean-field Hamiltonian:

$$H_{MF} = \sum_{\boldsymbol{k}\sigma} [\epsilon_{\boldsymbol{k}} c_{\boldsymbol{k}\sigma}^\dagger c_{\boldsymbol{k}\sigma} + \frac{1}{\sqrt{N}} V_{\boldsymbol{k}} r (c_{\boldsymbol{k}\sigma}^\dagger f_\sigma + f_\sigma^\dagger c_{\boldsymbol{k}\sigma})] + \epsilon_f \sum_\sigma f_\sigma^\dagger f_\sigma + \lambda (n_f + r^2 - 1), \tag{2.53}$$

where λ is the Lagrange multiplier to satisfy the constraint on the average, and $V_{\boldsymbol{k}}$ and r are taken to be real. If the right-hand side of eq.(2.52) were n instead of 1, number fluctuations of $O(1)$ are negligible as compared with the average of $O(n)$. Then the mean-field theory would become exact in the limit of large n. Because of the actual constraint of $O(1)$, the mean-field theory is different from the $1/n$ expansion [25]. However the static property agrees with that derived by the lowest-order $1/n$ expansion as will be explained below.

The mean-field parameters λ and r are determined by a variational principle. We write the statistical average of an operator O in terms of the density operator $\exp(-\beta H_{MF})$ as $\langle O \rangle$. Then the exact thermodynamic potential Ω of the SU(n) Anderson model $H_{SU(n)}$ is bounded by the Feynman inequality [26]:

$$\Omega \leq \Omega_{MF} + \langle H_{SU(n)} - H_{MF} \rangle. \tag{2.54}$$

Thus we can optimize the parameters by minimizing the right-hand side. The second term is simply given by $-\lambda(n_f + r^2 - 1)$. The variation with respect to λ gives the constraint $n_f + r^2 = 1$. The optimization of r yields

$$\lambda r = \sum_{\boldsymbol{k}\sigma} V_{\boldsymbol{k}} \langle f_\sigma^\dagger c_{\boldsymbol{k}\sigma} \rangle. \tag{2.55}$$

The stationary condition gives only a trivial solution $r = 0$ above a critical temperature T_B ($\sim T_K$). Below T_B the nontrivial solution $r \neq 0$ is lower in free energy. The phase transition at $T = T_B$ is a fictitious one which shows the inadequacy of the mean-field theory. However, at zero temperature the mean-field theory gives the correct fixed point of the Anderson model. Therefore we restrict in the following to the case of $T = 0$.

It is convenient to use the Green function to calculate the average. The f electron Green function $G_f^*(z)$ is easily derived for H_{MF} as follows:

$$G_f^*(z) = [z - \tilde{\epsilon}_f + i\tilde{\Delta}\mathrm{sgn}(\mathrm{Im}z)]^{-1}, \tag{2.56}$$

with $\tilde{\epsilon}_f = \epsilon_f + \lambda$ and $\tilde{\Delta} = \pi r^2 W_0$. For the mixed type Green function $G_{cf}(k,z) = \langle\{c^\dagger_{\boldsymbol{k}\sigma}, f_\sigma\}\rangle(z)$ we obtain

$$G_{cf}(k,z) = G_{fc}(k,z) = V_{\boldsymbol{k}} r (z - \epsilon_{\boldsymbol{k}})^{-1} G_f^*(z). \tag{2.57}$$

The resultant spectrum is interpreted as that of quasi-particles; hence the star (*) is attached to relevant quantities. For example, the density of f electron states $\rho_f^*(\epsilon)$ for each spin is given by

$$\rho_f^*(\epsilon) = \frac{\tilde{\Delta}}{\pi} \frac{1}{(\epsilon - \tilde{\epsilon}_f)^2 + \tilde{\Delta}^2}. \tag{2.58}$$

The occupation number n_f is given by integration of $\rho_f^*(\epsilon)$ up to the Fermi level. The result is

$$n_f = \frac{n}{\pi} \arctan\left(\frac{\tilde{\Delta}}{\tilde{\epsilon}_f}\right). \tag{2.59}$$

On the other hand, a little algebra with use of G_{cf} gives

$$\sum_{\boldsymbol{k}\sigma} V_{\boldsymbol{k}} \langle f_\sigma^\dagger c_{\boldsymbol{k}\sigma}\rangle = nW_0 r \ln\left(\frac{\sqrt{\tilde{\epsilon}_f^2 + \tilde{\Delta}^2}}{D}\right), \tag{2.60}$$

where we have assumed that ρ_c and $V_{\boldsymbol{k}}$ are constant for $D > \epsilon > -D$ and 0 otherwise. Thus eq.(2.55) is equivalent to

$$\sqrt{\tilde{\epsilon}_f^2 + \tilde{\Delta}^2} = D \exp\left(\frac{\lambda}{nW_0}\right), \tag{2.61}$$

where λ in the exponent can be approximated by $-\epsilon_f$ in view of the relation $|\tilde{\epsilon}_f| \ll |\epsilon_f|$. The left-hand side sets the energy scale of the system. In fact the energy is the same as T_0 obtained in §2.1.4

One can derive the static properties approximately with use of the mean-field theory. For example the density of states $\rho_f^*(0)$ for quasi-particles at the Fermi level determines the specific heat at low temperature. We obtain

$$\rho_f^*(0) = \frac{n\tilde{\Delta}}{\pi(\tilde{\epsilon}_f^2 + \tilde{\Delta}^2)} = \frac{n}{\pi\tilde{\Delta}} \sin^2(\frac{\pi n_f}{n}), \tag{2.62}$$

The specific heat coefficient γ due to the impurity is given by

$$\gamma = \frac{1}{3}\pi^2 \rho_f^*(0), \tag{2.63}$$

while the magnetic susceptibility is computed as

$$\chi = C_J \rho_f^*(0) \to C_J n_f / T_0 \quad (n \to \infty), \tag{2.64}$$

where C_J is the Curie constant. Therefore in the large n limit, the mean-field theory gives the correct result. For finite n, however, the mean-field theory cannot derive the correct Wilson ratio. This is simply because all the Landau parameters vanish by construction in the mean-field theory.

Let us give the relationship between the Green function $G_f^*(z)$derived by the mean-field theory and the formally exact one $G_f(z)$. In terms of the self-energy $\Sigma_f(z)$, the latter is written as

$$G_f(z) = [z - \epsilon_f + i\Delta\mathrm{sgn}(\mathrm{Im}z) - \Sigma_f(z)]^{-1}, \tag{2.65}$$

where $\Delta = \pi W_0$. To extract the quasi-particle dynamics one expands $\Sigma_f(z)$ near the Fermi level $z = 0$ as

$$\Sigma_f(z) = \Sigma_f(0) + \frac{\partial \Sigma_f(z)}{\partial z}\Big|_{z=0} z + O(z^2). \tag{2.66}$$

where the derivative is real in the Fermi-liquid state. Then we obtain near the Fermi level

$$G_f(z) = a_f G_f^*(z), \tag{2.67}$$

where $a_f = [1 - \Sigma_f'(0)]^{-1}$ is called the renormalization factor. The quasi-particle Green function $G_f^*(z)$ corresponds to the one obtained in the mean-field theory provided one makes identification

$$\Sigma_f(0) = \lambda, \qquad a_f = r^2. \tag{2.68}$$

Thus the mean-field theory can be regarded as the simplest approximation to perform the renormalization explicitly.

2.2.2 Dynamical susceptibility in the local Fermi liquid

As the degeneracy n of the f orbital decreases, the interaction among quasi-particles becomes stronger. Then one can improve the mean-field theory to incorporate the Fermi-liquid effects. We apply the quasi-particle RPA explained in Chapter I to the present system. This is in fact exact in the low-energy limit, and constitutes a convenient approximation in the spherically symmetric case because there is only a single parameter to describe the interaction effect. The dynamical susceptibility of f electrons is written as

$$nC_J\chi(\omega)^{-1} = nC_J\chi_1(\omega)^{-1} - U_{eff}, \tag{2.69}$$

where $-U_{eff}$ is the effective interaction corresponding to $Z_0/\rho^*(\mu)$ in eq.(1.78), and $\chi_1(\omega)$ is the polarization function of quasi-particles with the f component given by

$$\chi_1(\omega) = nC_J \int d\epsilon_1 \int d\epsilon_2 \rho_f^*(\epsilon_1)\rho_f^*(\epsilon_2)\frac{f(\epsilon_1) - f(\epsilon_2)}{\omega - \epsilon_1 + \epsilon_2 + i\delta}, \tag{2.70}$$

with $\rho_f^*(\epsilon_1)$ being the density of states of f quasi-particles. The important point here is that the effective interaction is real in the limit of small ω. Taking the imaginary parts of both sides of eq.(2.69) we obtain

$$\lim_{\omega\to 0} \mathrm{Im}\frac{\chi(\omega)}{\omega\chi^2} = \frac{\pi}{nC_J}, \tag{2.71}$$

where the right-hand side is obtained by noting $\chi_1(0) = nC_J\rho_f^*(0)$.

The relation eq.(2.71) is called the Korringa-Shiba relation. The remarkable feature is that the right-hand side is independent of the interaction. The original proof was provided by diagrammatic analysis for the spin 1/2 Anderson model [15].

2.2.3 Self-consistent theory at finite temperatures

We now turn to a microscopic approach to dynamics at finite temperature. As we have seen in the previous section, the $1/n$ expansion is a powerful scheme which can describe correctly the singlet ground state. Once we obtain the approximate wave function of the ground state by the $1/n$ expansion, we can obtain a restricted class of excited states by applying the hybridization operator successively. Within this manifold of states, matrix elements of physical operators are easily obtained, and then the excitation spectrum such as the density of states can be derived at zero temperature. This direct $1/n$ expansion approach to the dynamics has been made extensively to derive the photoemission spectrum [27]. However, the direct expansion cannot eliminate the spurious energy gap of the order of T_K from the singlet ground state. We refer to a review article for further details of the direct expansion method [28].

In a self-consistent perturbation theory it is practical to perform partial summation of relevant perturbation terms to infinite order. Since the spin operators (or more generally the X-operators) do not obey the commutation rules of fermions or bosons, use of the standard many-body technique with Feynman diagrams and the linked cluster expansion cannot be applied. As an alternative, we shall present a resolvent method which permits time-ordered diagrams to represent perturbation terms [29]. The resolvent method leads to an effective atom picture which eliminates the degrees of freedom of the conduction electrons. At zero temperature the effective atom acquires the same effective Hamiltonian as given by the Brillouin-Wigner perturbation theory.

In order to pursue the effective atom picture we try to factorize the partition function Z of the SU(n) Anderson model into the conduction electron part Z_c and the local part Z_f which includes the effect

of interaction with conduction electrons [30]. We divide the Hamiltonian H into the unperturbed part $H_0 = H_c + H_f$ and the perturbation $H_1 = H_{hyb}$. In terms of the integration along a contour C encircling the real axis in the counter-clockwise direction, Z is given by

$$Z = \int_C \frac{dz}{2\pi i} \exp(-\beta z) \mathrm{Tr} \frac{1}{z - H}. \tag{2.72}$$

The trace is over the direct product state $|\gamma, c\rangle$ from an f state $|\gamma\rangle$ and a conduction electron state $|c\rangle$. We introduce a creation operator $a_\gamma^\dagger$ of the f state and represent the direct product state as $a_\gamma^\dagger|c\rangle$. To make a compact description we introduce the Liouville operator L by the relation $LA \equiv [H, A]$ for any operator A. Then we obtain

$$Ha_\gamma^\dagger|c\rangle = ([H, a_\gamma^\dagger] + a_\gamma^\dagger H)|c\rangle = (L + E_c)a_\gamma^\dagger|c\rangle, \tag{2.73}$$

where E_c is the energy of $|c\rangle$. Repeated application H^n leads to $(L + E_c)^n$ operating on $a_\gamma^\dagger|c\rangle$. Thus we rewrite eq.(2.72) as

$$Z = \int_C \frac{dz}{2\pi i} \exp(-\beta z) \sum_{c\gamma} \exp(-\beta E_c) \langle c|a_\gamma \frac{1}{z - L} a_\gamma^\dagger|c\rangle \equiv Z_c Z_f, \tag{2.74}$$

where for each $|c\rangle$ a shift of the integration variable by E_c has been made. Factoring out $Z_c = \sum_c \exp(-\beta E_c)$ for the conduction electron part, the effective partition function Z_f of f states is given by [18]

$$Z_f = \int_C \frac{dz}{2\pi i} \exp(-\beta z) \sum_{\gamma} \langle a_\gamma \frac{1}{z - L} a_\gamma^\dagger \rangle_c, \tag{2.75}$$

with $\langle \cdots \rangle_c$ being the thermal average over conduction states. The average defines the resolvent $R_\gamma(z) = \langle a_\gamma (z - L)^{-1} a_\gamma^\dagger \rangle_c$.

The density of states of the effective atom is given by the spectral intensity

$$\eta_\gamma(\epsilon) = -\frac{1}{\pi} \mathrm{Im} R_\gamma(\epsilon + i\delta) = -\frac{1}{2\pi i}[R_\gamma(\epsilon + i\delta) - R_\gamma(\epsilon - i\delta)] = \langle a_\gamma \delta(\epsilon - L) a_\gamma^\dagger \rangle_c. \tag{2.76}$$

Then Z_f is also written as

$$Z_f = \sum_\gamma \int_{-\infty}^{\infty} d\epsilon \exp(-\beta\epsilon) \eta_\gamma(\epsilon), \tag{2.77}$$

which fits naturally with the effective atom picture. In terms of exact eigenstates $|t\rangle$ of H, R_γ can be represented as

$$R_\gamma(z) = \frac{1}{Z_c} \sum_{c\gamma} \exp(-\beta E_c) \frac{|\langle t|\gamma, c\rangle|^2}{z - E_t + E_c}. \tag{2.78}$$

Perturbation theory with respect to hybridization H_1 can be performed by the expansion

$$\frac{1}{z - L} = \frac{1}{z - L_0} + \frac{1}{z - L_0} L_1 \frac{1}{z - L_0} + \dots, \tag{2.79}$$

where $L = L_0 + L_1$ in accordance with $H = H_0 + H_1$. Since $H_1|c\rangle = 0$, it can be easily shown that

$$L_0 L_1 a_\gamma^\dagger|c\rangle = L_0[H_1, a_\gamma^\dagger]|c\rangle = L_0 H_1 a_\gamma^\dagger|c\rangle = [H_0, H_1 a_\gamma^\dagger]|c\rangle = (H_0 - E_c) H_1 a_\gamma^\dagger|c\rangle. \tag{2.80}$$

Thus when acting on $a_\gamma^\dagger|c\rangle$, L_1 can be replaced by H_1 and L_0 by $H_0 - E_c$. Hence the denominator $z - L_0$ depends only on excitation energies from a state with E_c. This feature is very convenient in taking the average over conduction states. The perturbation series generates a product of creation and annihilation operators of conduction electrons. The average over conduction states can be performed by the use of the factorization property

$$\langle c_\alpha^\dagger c_\beta c_\gamma^\dagger c_\delta \rangle_c = \langle c_\alpha^\dagger c_\beta \rangle_c \langle c_\gamma^\dagger c_\delta \rangle_c + \langle c_\alpha^\dagger c_\delta \rangle_c \langle c_\beta c_\gamma^\dagger \rangle_c, \tag{2.81}$$

which is an example of Wick-Bloch-de Dominicis theorem. A similar factorization property holds for cases with more operators.

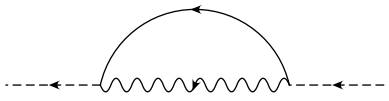

Figure 2.4: The simplest self-energy for $R_1(z)$.

The simplest of perturbation processes for $R_0(z)$ is shown by the same diagram as Fig.2.3. This is the only elementary process which survives in the limit of large n. The repetition of the process is accounted for by the self-energy $\Sigma_0(z)$ defined by

$$R_0(z) = [z - \Sigma_0(z)]^{-1}, \tag{2.82}$$

$$\Sigma_0(z) = nW_0 \int_{-D}^{D} \frac{f(\epsilon)d\epsilon}{z + \epsilon - \epsilon_f}. \tag{2.83}$$

Note that the ground-state energy E_0 relative to the Fermi sea in eq.(2.83) is given by $E_0 = \Sigma_0(E_0)$ at $T = 0$. This leads to a threshold singularity in $R_0(z)$. At finite T or in higher order perturbation, the resolvent has a cut singularity along the real axis of z and is analytic otherwise. In the exact theory at $T = 0$, the cut extends from the ground state energy to infinity, as is clear from eq.(2.78).

The resolvent $R_1(z)$ is common to any of the degenerate f^1 states. In the next leading order, $R_1(z)$ also acquires the self-energy $\Sigma_1(z)$ as shown in Fig.2.4. The resolvent $R_0(z-\epsilon)$ to be used in the intermediate state should not be a bare one, but should be a renormalized one in order to be consistent with the $1/n$ arrangement of perturbation terms. The use of renormalized resolvents in the intermediate states leads to the following integral equations [29, 30, 31]:

$$\Sigma_0(z) = nW_0 \int_{-D}^{D} d\epsilon f(\epsilon) R_1(z + \epsilon), \tag{2.84}$$

$$\Sigma_1(z) = W_0 \int_{-D}^{D} d\epsilon [1 - f(\epsilon)] R_0(z - \epsilon), \tag{2.85}$$

The solution of this set of equations corresponds to summation of all perturbation diagrams without crossing of conduction-electron lines, and is called the non-crossing approximation (NCA) [32].

The NCA can derive not only the thermodynamics through the partition function, but dynamical quantities such as the dynamical magnetic susceptibility $\chi(\omega)$ due to the impurity [30], and the density of f states $\rho_f(\omega)$ for single-particle excitations [30, 33, 34]. It can be shown that the NCA satisfies conservation laws and sum rules required for response functions [30]. Let us first consider the dynamical magnetic susceptibility $\chi(\omega)$. It is given in the imaginary frequency domain by

$$\chi(i\nu_m) = \frac{nC_J}{Z_f} \int_C \frac{dz}{2\pi i} \exp(-\beta z) R_1(z + i\nu_m) R_1(z), \tag{2.86}$$

where the contour C encircles counter-clockwise all singularities of the integrand. After analytically continuing the Matsubara frequency to the real axis, we are left with integration along the real axis with the Boltzmann factor $e^{-\beta\epsilon}$ which becomes singular at $T = 0$. Then the following spectral intensity is conveniently introduced as a quantity supplementary to resolvent:

$$\xi_\gamma(\epsilon) = Z_f^{-1} e^{-\beta\epsilon} \eta_\gamma(\epsilon) = \frac{1}{Z} \sum_{c,t} \exp(-\beta E_t) |\langle t|\gamma, c\rangle|^2 \delta(\epsilon - E_t + E_c) = \langle a_\gamma^\dagger \delta(\epsilon + L) a_\gamma \rangle. \tag{2.87}$$

From the last expression, we understand that $\xi_\gamma(\epsilon)$ corresponds to the spectral intensity after annihilation of the impurity state by a_γ [18]. The spectral function $-\mathrm{Im}\chi(\omega)/\pi$ (see eq.(B.15) in Appendix B) is given by

$$\mathrm{Im}\chi(\omega) = (1 - e^{-\beta\omega}) \frac{nC_J}{Z_f} \int_{-\infty}^{\infty} d\epsilon e^{-\beta\epsilon} \eta_1(\epsilon) \eta_1(\epsilon + \omega) \tag{2.88}$$

$$= nC_J \int_{-\infty}^{\infty} d\epsilon [\xi_1(\epsilon)\eta_1(\epsilon + \omega) - \eta_1(\epsilon)\xi_1(\epsilon + \omega)]. \tag{2.89}$$

This expression naturally follows the effective atom picture, and it is easy to see that the line-width of $\mathrm{Im}\chi(\omega)$ is given in terms of $\eta_1(\epsilon)$ and $\xi_1(\epsilon)$. Thus in the absence of hybridization the width vanishes since we have $\eta_1(\epsilon) = \delta(\epsilon - \epsilon_f)$ and $\xi_1(\epsilon) = (n_f/n)\delta(\epsilon - \epsilon_f)$. The actual width is controlled by the Kondo temperature, as will be discussed later. It is clear that use of $\xi_\gamma(\epsilon)$ permits us to take the zero temperature limit without the singular Boltzmann factor.

The static susceptibility χ on the other hand is given by

$$\chi = \frac{nC_J}{\pi Z_f}\int_{-\infty}^{\infty} d\epsilon e^{-\beta\epsilon}\mathrm{Im}[R_1(\epsilon - i\delta)^2] \tag{2.90}$$

$$= 2nC_J\int_{-\infty}^{\infty} d\epsilon\xi_1(\epsilon)\mathrm{Re}R_1(\epsilon). \tag{2.91}$$

Of course the results given by eqs.(2.89) and (2.91) are consistent with the Kramers-Kronig relation.

The single-particle Green function $G_f(z)$ is given by

$$G_f(z) = -i\int_0^{\infty} dt e^{izt}\langle\{f_\sigma(t), f_\sigma^\dagger\}\rangle = \int_{-\infty}^{\infty} d\epsilon\frac{\rho_f(\epsilon)}{z-\epsilon}, \tag{2.92}$$

where the density of states $\rho_f(\omega)$ has been used. In the NCA, $G_f(i\epsilon_n)$ in the Matsubara frequency domain is given in terms of the resolvents by

$$G_f(i\epsilon_n) = \frac{1}{Z_f}\int_C \frac{dz}{2\pi i}\exp(-\beta z)R_1(z + i\epsilon_n)R_0(z). \tag{2.93}$$

After analytic continuation we obtain the spectral intensity as

$$\rho_f(\omega) = n(1 + e^{-\beta\omega})Z_f^{-1}\int_{-\infty}^{\infty} d\epsilon e^{-\beta\epsilon}\eta_0(\epsilon)\eta_1(\epsilon + \omega) \tag{2.94}$$

$$= n\int_{-\infty}^{\infty} d\epsilon[\xi_0(\epsilon)\eta_1(\epsilon + \omega) + \eta_0(\epsilon)\xi_1(\epsilon + \omega)]. \tag{2.95}$$

The second equation indicates explicitly the excitation from the vacant f state to the filled one (electron addition) and vice versa (electron removal).

At high temperature, the dynamical susceptibility can be calculated analytically since perturbation theory with respect to hybridization is applicable. We introduce the magnetic relaxation rate Γ measured by NMR as follows:

$$\mathrm{Im}\chi(\omega)/\omega = \chi(0)/\Gamma. \tag{2.96}$$

If the dynamical susceptibility can be approximated by a Lorentzian, i.e.

$$\chi(\omega) = \frac{\chi(0)\Gamma}{-i\omega + \Gamma}, \tag{2.97}$$

the rate Γ appears also as the half width in the neutron scattering spectrum.

To calculate Γ we note the identity

$$R_1(z)R_1(z') = \frac{R_1(z) - R_1(z')}{z' - z - \Sigma_1(z') + \Sigma_1(z)}. \tag{2.98}$$

Then we use eq.(2.76) in making eq.(2.89) suitable for perturbation theory for finite but small ω. We obtain

$$\lim_{\omega\to 0}\mathrm{Im}\frac{\chi(\omega)}{\omega} = nC_J\beta\int_{-\infty}^{\infty} d\epsilon\frac{\xi_1(\epsilon)}{\mathrm{Im}\Sigma(\epsilon)}. \tag{2.99}$$

At high temperatures where the Curie law $\chi(0) \sim C_J n_f/T$ holds, we can make an approximation to set $\xi_1(\epsilon) \sim (n_f/n)\delta(\epsilon - \epsilon_f)$. Then we obtain a simple result

$$\Gamma = -2\mathrm{Im}\Sigma_1(\epsilon_f). \tag{2.100}$$

We can evaluate eq.(2.100) by perturbation theory. In the lowest order with respect to hybridization we obtain

$$\Gamma = 2\pi W_0[1 - f(\epsilon_f)] = 2n\pi W_0(n_f^{-1} - 1). \tag{2.101}$$

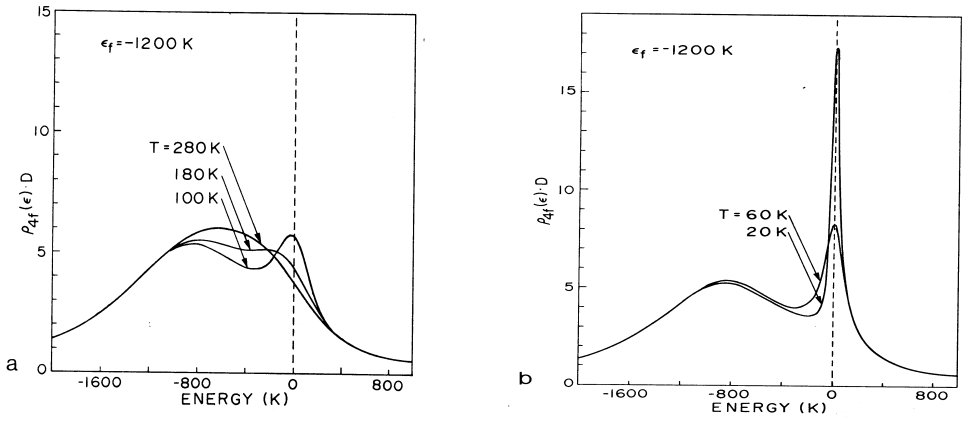

Figure 2.5: The f electron density of states at various temperatures.

This quantity is independent of temperature T provided that the average occupation n_f does not change with T. In the valence fluctuation regime this is the relevant case. The result was first obtained with use of the memory function method [35] which is explained in Appendix D. In the Kondo regime $n_f \sim 1$, on the other hand, the lowest order result is exponentially small. One should therefore go to the fourth order in hybridization. As we have discussed in §1, the evaluation amounts to second order in J. Then the result reproduces eq.(2.21) obtained by the Born approximation. For general T, we can perform numerical calculations to evaluate the integrals for response functions. Many results have been reported [25] which compare favorably with experimental observation by neutron scattering or by photoemission spectroscopy.

Figure 2.5 shows an example of the density of states $\rho_f(\epsilon)$computed in the NCA [36]. A sharp peak develops near the Fermi level at low temperatures, and is called the Kondo resonance. Note that the density of states $\rho_f^*(\epsilon) = \rho_f(\epsilon)/a_f$ for quasi-particles should be even larger because the renormalization factor a_f is much smaller than unity. The NCA can derive the density of states in the presence of spin-orbit and/or the CEF splittings. Figure 2.6 shows an example of numerical results [37]. We note that the overall intensity of the density of states is much larger than that expected from the Kondo temperature. In the energy scale larger than the spin-orbit splitting, the effective degeneracy of the $4f^1$ configuration amounts to 14. Thus according to eq.(2.50) there is a large difference between the actual T_K determined by low-temperature properties and the apparent Kondo temperature determined by the spectral shape. This observation is important to avoid confusion about the correct model to account for spectroscopic results.

At $T = 0$ and in the limit of large n, one can derive nontrivial results analytically [38]. The lowest order in $1/n$ expansion coincides with the mean-field theory with use of the slave boson, which was explained in 2.2.1.

2.3 Deviation from the Canonical Behavior

2.3.1 Non-Fermi liquid ground state

The ground state of the Kondo model is not always the Kondo singlet. In order to explore a possible non-singlet state, we consider H_K given by eq.(2.6), but with the number of orbital channels $n > 1$. Namely we consider the case

$$\boldsymbol{s}_c = \frac{1}{2N} \sum_{\boldsymbol{k}\boldsymbol{k}'} \sum_{m=1}^{n} \sum_{\alpha\beta} c^\dagger_{\boldsymbol{k}m\alpha} \boldsymbol{\sigma}_{\alpha\beta} c_{\boldsymbol{k}'m\beta}, \tag{2.102}$$

where m denotes each channel. The magnitude S of the localized spin $\boldsymbol{S}$ is now not restricted to 1/2.

There are three cases which give different ground states: (i) $n = 2S$; (ii) $n < 2S$; (iii) $n > 2S$. In the case (i) as in $n = 2S = 1$, the ground state is the Kondo singlet. Each channel screens spin 1/2 so that

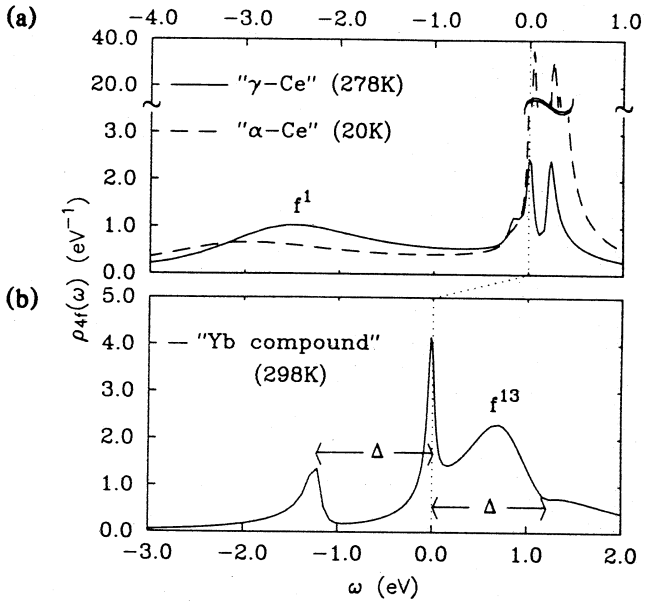

Figure 2.6: The f electron density of states in the presence of spin-orbit interaction

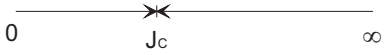

Figure 2.7: Scaling of the exchange interaction in the overscreened case.

the entire local spin S is completely screened by n channels. The fixed point corresponds to $J = \infty$. In the case (ii), even though each conduction channel couples strongly to the impurity spin, the screening is still incomplete because of the large spin S. As a result there remains a localized spin of $S - n/2$ in the ground state. Although this fixed point corresponds to $J = 0$, the ground state cannot be reached by perturbation theory since the localized spin has the magnitude $S - n/2$.

A new situation arises in the case of (iii). The fixed point corresponds to $J = J_c$ which is neither 0 nor infinite [39]. To understand why this is so, let us consider a hypothetical case of $J = \infty$. Then the conduction electrons overscreen the impurity spin by the amount $n/2 - S$. This extra amount now acts as a new impurity spin which couples with the rest of conduction electrons. The resultant coupling is antiferromagnetic since the Pauli principle allows only conduction electrons with spin antiparallel to the new spin $n/2 - S$ to hop into the impurity site and to gain the perturbation energy. Hence $J = \infty$ cannot be a fixed point. It is obvious that $J = 0$ cannot be a fixed point either. Hence the fixed point is forced to have nonzero J_c. The scaling is schematically shown in Fig.2.7.

One can confirm this qualitative reasoning by renormalization to third order. Following the argument of Appendix C, one obtains the scaling equation for the model given by eq.(2.102) as follows:

$$\frac{dg}{d\ln D} = -g^2 + \frac{n}{2}g^3, \tag{2.103}$$

where $g = J\rho_c$ is the effective exchange interaction. The right-hand side becomes zero when $g = g_c = 2/n$, which corresponds to the fixed point of renormalization. The large n means small g_c. Then one can rely on the perturbative renormalization to this order, since higher-order contributions can be shown to be smaller by $1/n$. The linearized scaling equation for $\delta g \equiv g - g_c$ is given by

$$\frac{d\delta g}{d\ln D} = \frac{2}{n}\delta g. \tag{2.104}$$

The plus sign in the right-hand side means that the fixed point is stable.

2.3.2 Mapping to one-dimensional models

From the Wilson form eq.(2.24) of the Hamiltonian, it is obvious that the system of a magnetic impurity in a metal can be mapped to a one-dimensional model where the radial distance from the impurity plays the role of the one-dimensional coordinate. Thus the impurity is on the left end of the system, and the right end grows as the renormalization step proceeds. The s-wave part of conduction band states with momentum k has the incoming and outgoing wave functions, which are interpreted as left-going and right-going waves, respectively. Alternatively, a left-going wave $\exp(-ikx)$ with k and x positive is reinterpreted as a right-going wave with momentum k and coordinate $-x$. In the latter picture the conduction electrons are all right-going with verlocity v_F. Their Hamiltonian is written as

$$H_c = v_F \sum_{k\sigma} k c^\dagger_{k\sigma} c_{k\sigma}, \tag{2.105}$$

where $k \in [-k_F, k_F]$ is measured relative to the Fermi momentum. In order to understand the nature of the spectrum with an impurity, it is necessary to analyze the spectrum of H_c with various kinds of internal degrees of freedom.

The spectrum of H_c depends on the boundary condition. For the system size L, the periodic boundary condition (PBC) and the anti-periodic boundary condition (A-PBC) requires, respectively,

$$k = \frac{2\pi}{L} \times \begin{cases} n & \text{(PBC)} \\ (n + \frac{1}{2}) & \text{(A-PBC)} \end{cases} \tag{2.106}$$

with n integers. We introduce a quantum number Q which measures the change of electron number from a reference state. In the case of spinless fermions, the change ΔE of the ground-state energy is given for the PBC by

$$\Delta E = \frac{2\pi v_F}{L} \sum_{n=0}^{Q-1} n = \frac{\pi v_F}{L} Q(Q-1), \tag{2.107}$$

where we take the vacant zero-energy state as the reference state. If one takes the A-PBC, one should replace $Q(Q-1)$ by Q^2. Actual electrons have spin degrees of freedom. In the absence of orbital degeneracy we put $Q = Q_\uparrow + Q_\downarrow$ and use the identity

$$Q_\uparrow^2 + Q_\downarrow^2 = \frac{1}{2} Q^2 + 2S_z^2, \tag{2.108}$$

where $2S_z = Q_\uparrow - Q_\downarrow$. Then we obtain the energy for the A-PBC by

$$\Delta E = \frac{2\pi v_F}{L} \left[\frac{1}{4} Q^2 + \frac{1}{3} \boldsymbol{S}^2 \right]. \tag{2.109}$$

Here the particle-hole excitations that appeared in eq.(2.25) have been omitted for simplicity. For the PBC one has

$$\Delta E = \frac{2\pi v_F}{L} \sum_\sigma \sum_{n=0}^{Q_\sigma - 1} n = \frac{2\pi v_F}{L} \left[\frac{1}{4} Q^2 - \frac{1}{2} Q + \frac{1}{3} \boldsymbol{S}^2 \right]. \tag{2.110}$$

With the shift $Q \to (Q-1)$ in the above expression, one has the correspondence to the A-PBC result apart from a constant term. The shift corresponds to take the new reference state as having one electron in the zero-energy level. With the PBC we always take this new reference state in the following discussion. Thus the boundary conditions for electrons require particular combination of quantum numbers as

$$(Q, S) = (\text{even, integer}) \oplus (\text{odd, half-integer}), \quad \text{(A-PBC)} \tag{2.111}$$

$$(Q, S) = (\text{even, half-integer}) \oplus (\text{odd, integer}), \quad \text{(PBC)} \tag{2.112}$$

The NRG calculation in the Kondo model shows that the spectrum of the model turns out to be the same as that of free conduction electrons either with the PBC or the A-PBC depending on the odd or even number of the NRG steps. The reason for this simple behavior is that the fixed point corresponds to infinitely strong exchange interaction [40]. Namely the right-going electrons acquire the phase shift $\delta = \pm\pi/2$ after passing through the impurity because of the exchange interaction. This phase shift is equivalent to multiplying the factor $\exp(2i\delta) = -1$ to the wave function. Then the change from the

(a) A-PBC

Q	S	l	$\Delta E/(2\pi v_F/L)$	degeneracy
0	0	0	0	1
0	1	1	1	9
± 1	1/2	1/2	1/2	4
2	0	1	1	3
2	1	0	1	3

(b) PBC

Q	S	l	$\Delta E/(2\pi v_F/L)$	degeneracy
0	1	0	0	3
0	0	1	0	3
± 1	1/2	1/2	0	8
± 2	0	0	0	2
2	1	1	1	9

(c) two-channel Kondo model

Q	S	l	$\Delta E/(2\pi v_F/L)$	degeneracy
0	1/2	0	0	2
0	1/2	1	1/2	6
± 1	0	1/2	1/8	2
± 1	1	1/2	5/8	6
2	1/2	0	1/2	2
2	1	1	1	6

Table 2.1: Spectra of free right-going electrons with the anti-periodic boundary condition (a), and with the periodic one (b). In (b), the origin $Q = 0$ is so chosen that the zero-energy level is filled by two electrons. Also shown is the spectra for the two-channel Kondo model (c).

PBC to the A-PBC, or vice versa, is equivalent to having this phase shift. In other words, the amount 1/2 of conduction-electron spin is swallowed by the impurity by the Kondo screening without changing the total number of conduction electrons. This results in the shift $S \to S \pm 1/2$ in the combination of (Q, S).

Now we turn to the spectrum of the free conduction band with orbital degeneracy. The Hamiltonian is given by

$$H_c = v_F \sum_{k\sigma} \sum_{m=1}^{n} k c^\dagger_{km\sigma} c_{km\sigma}, \tag{2.113}$$

where m denotes the same orbital channel as appears in eq.(2.102). After some algebra the spectrum is now derived as

$$\Delta E = \frac{2\pi v_F}{L} \left[\frac{1}{4n} Q^2 + \frac{1}{2+n} C_l + \frac{1}{2+n} \boldsymbol{S}^2 + n_Q + n_l + n_S \right]. \tag{2.114}$$

where C_l denotes the eigenvalue of the second-order Casimir operator $\sum_\alpha (l^\alpha)^2$ where l^α's are $n^2 - 1$ generators of the SU(n) group. The latter describes symmetry of the orbital channel. In the case of doubly degenerate orbitals with $n = 2$, each generator l^α is reduced to the Pauli spin matrix with $\alpha = x, y, z$, and the squared sum of them gives $l(l+1)$ with l a non-negative integer or a positive half-integer. The quantum numbers n_Q, n_l, n_S, which are non-negative integers, represent particle-hole excitations from the ground state. In the terminology of the conformal field theory, the spectra associated with various values of n_Q, n_l, n_S are called descendants or conformal towers. The ground state of the free electrons has a set $(Q, l, S) = (0, 0, 0)$ with the A-PBC. With the PBC, on the other hand, the ground state is 16-fold degenerate: the degeneracy 2^4 corresponds to filling or not filling the zero-energy level for each species of fermions. One of the ground states has a set $(Q, l, S) = (0, 1, 0)$ for example. Table 2.1 (a), (b) shows the spectrum of two-channel free fermions either with PBC or A-PBC.

We have seen in 2.3.1 that the multi-channel Kondo model has a fixed point which has a finite value of the exchange interaction. As a result one cannot expect that the spectrum of the model is described by a simple change of the boundary condition. The NRG calculation indeed reveals more complex structure

of the spectrum. However description in terms of the spectrum given by eq.(2.114) is still valid provided one attaches particular combinations of quantum numbers. For example the NRG calculation shows that the ground state has a set of quantum numbers $(Q, l, S) = (0, 0, 1/2)$. Obviously this combination of quantum numbers is impossible in the free-electron case whatever the boundary condition chosen. Physically, the quantum number $S = 1/2$ corresponds to overscreening of the impurity spin. Table 2.1 (c) shows the resultant spectrum given by eq.(2.114) with $S = 1/2$ and $n = 2$. It has been confirmed that the low-energy spectrum derived by the NRG can be nicely reproduced by this analytical formula. We refer to review papers [40, 41] for more detailed discussions.

According to the conformal field theory, only a part of the degeneracy in the ground state is associated with the impurity states. This is related to the order of taking the thermodynamic limit and the zero-temperature limit. For example the ground-state degeneracy of the two-channel impurity is derived to be $2^{-1} \ln 2$ instead of $\ln 2$. This feature is consistent with the exact solution by the Bethe ansatz theory [42, 43].

2.3.3 Dynamics of the non-Fermi liquid state

The ground state in the overscreened impurity has many anomalous properties. It is, however, difficult to derive these properties by elementary theoretical methods. Therefore we state only final results referring to the literature [40, 41, 42, 43] for details of derivation. For example, it has been shown that the specific heat is given by the power law:

$$C = C_0 \left(\frac{T}{T_K} \right)^{\alpha} \tag{2.115}$$

where $\alpha = 4/(n+2)$. In the case of $n = 2$, the specific heat acquires the logarithmic term $T \ln T$. The temperature dependence of the susceptibility is also given by the power law with exponent $\alpha - 1$ or by a term $\ln T$ with $n = 2$. The impurity magnetization at $T = 0$ is given for small fields by

$$M \sim (H/T_K)^{2/n}, \tag{2.116}$$

for $n > 2$ and

$$M \sim (H/T_K) \ln(H/T_K), \tag{2.117}$$

for $n = 2$. The resistivity behaves as $\rho(T)/\rho_0 \sim 1 - cT^{\alpha/2}$. The zero-temperature limit ρ_0 is given by

$$\rho_0/\rho_{max} = \frac{1}{2} \left(1 - \frac{\cos[2\pi/(2+n)]}{\cos[\pi/(2+n)]} \right), \tag{2.118}$$

where ρ_{max} is the maximum value realized with $n = 1$, and is called the unitarity limit. The temperature coefficient c is positive if the bare exchange interaction is smaller than the fixed point value J_c, and is negative otherwise. In the latter case the resistivity should decrease with decreasing temperature in the low-temperature limit, which contrasts with the Kondo effect.

There are efforts to investigate the non-Fermi liquid state in real systems. A candidate is a crystal field ground state which is a non-Kramers doublet [44]. An example of this is Γ_3 of $U^{4+}(5f^2)$ ion with in the cubic symmetry. If one introduces a quasi-spin to represent a pair of wave functions constituting the non-Kramers doublet, the conduction electrons get two screening channels since they also have real spins. The quasi-spin actually represents the dynamics of the quadrupole moment. Hence this kind of overscreening is called the quadrupolar Kondo effect [44]. It has been shown that the non-Fermi liquid ground state can be realized even for the Anderson model with a dominant f^2 configuration and with proper crystal field [45]. We discuss the experimental situation in 2.4.3

2.3.4 Pair of local moments with hybridization

Heavy electrons emerge as a result of interaction between many Kondo centers. As a necessary step toward investigation of how the heavy electrons are formed, we consider the two impurity Anderson model where the local moments can form a singlet either by mutual coupling or by the Kondo effect. Suppose that two Anderson impurities are separated from each other by a distance R in a metallic matrix. We assume that the occupation of each impurity is almost unity because of large U and $|\epsilon_f|$. In the limit of large R, the ground state is regarded as two Kondo singlets which are almost independent of each other. The characteristic energy is given by the Kondo temperature T_K.

The Kondo exchange interaction H_{ex} induces a new interaction between the local moments. The new interaction is mediated by propagation of conduction electrons, and is called the RKKY interaction [46]. The effective Hamiltonian up to second order in H_{ex} is given by

$$H_{RKKY} = PH_{ex}(E_0 - H_c)^{-1}H_{ex}P, \tag{2.119}$$

$$H_{ex} = J[\boldsymbol{S}_1 \cdot \boldsymbol{s}_c(\boldsymbol{R}/2) + \boldsymbol{S}_2 \cdot \boldsymbol{s}_c(-\boldsymbol{R}/2)], \tag{2.120}$$

$$\boldsymbol{s}_c(\pm\boldsymbol{R}/2) = \frac{1}{2N}\sum_{\boldsymbol{k}\boldsymbol{k}'}\sum_{\alpha\beta} c^\dagger_{\boldsymbol{k}\alpha}\boldsymbol{\sigma}_{\alpha\beta}c_{\boldsymbol{k}'\beta}\exp[\pm i(\boldsymbol{k}-\boldsymbol{k}')\cdot\boldsymbol{R}/2], \tag{2.121}$$

where $\boldsymbol{S}_i$ with $i = 1, 2$ represents the local spin at site i, and each wave number is a vector instead of the radial component. The projection operator P is onto the ground state of H_c plus all states of local spins, and E_0 is its ground state energy.

Calculation shows that H_{RKKY} is written in the form:

$$H_{RKKY} = J_{RKKY}(\boldsymbol{R})\boldsymbol{S}_1 \cdot \boldsymbol{S}_2, \tag{2.122}$$

$$J_{RKKY}(\boldsymbol{R}) = -\frac{J^2V}{8N^2}\sum_{\boldsymbol{q}}\chi_0(\boldsymbol{q}, 0)\exp(i\boldsymbol{q}\cdot\boldsymbol{R}), \tag{2.123}$$

where $\chi_0(\boldsymbol{q}, 0)$ is the static susceptibility defined by eq.(1.46). It can be shown that $J_{RKKY}(\boldsymbol{R})$ decays as $\cos(2k_FR+\theta)/R^3$ in the free-electron-like conduction band. Thus at large R, $|J_{RKKY}(\boldsymbol{R})|$ becomes much smaller than the Kondo temperature. The ground state in this case is that of two almost independent Kondo impurities, and the wave function is written as ψ_{2K}.

In the opposite limit of small R, intersite interaction becomes significant. If the intersite interaction J_{RKKY} is ferromagnetic, the pair forms the triplet. Then the problem is reduced to the spin 1 Kondo problem. If the interaction is antiferromagnetic, on the contrary, the two impurities form a pair singlet by J_{RKKY}. Then the Kondo effect does not occur. The wave function of the ground state is written as ψ_{PS}. We now ask whether the two kinds of singlet states, ψ_{PS} and ψ_{2K}, can be connected continuously as the distance R changes.

The pair singlet is analogous to the Heitler-London picture for the ground state of the hydrogen molecule. The zero-th order wave function for ψ_{PS} is given by

$$\psi_{PS} = (f^\dagger_{1\uparrow}f^\dagger_{2\downarrow} - f^\dagger_{1\downarrow}f^\dagger_{2\uparrow})\phi_F. \tag{2.124}$$

where ϕ_F represents the ground state of conduction electrons. In the presence of hybridization, ψ_{PS} mixes with various states as shown in Fig.2.8. In particular the effective transfer from site 1 to site 2 becomes possible at the cost of U. In analogy to the hydrogen molecule, one can think of a molecular orbital by linear combination of the two f-orbitals at different sites. The effective transfer causes splitting of levels for bonding and anti-bonding molecular orbitals. In the limit of large transfer as compared with U, the picture for the ground state is such that two electrons with opposite spins are accommodated in the bonding orbital. With $U = 0$ the two-impurity Anderson model can be diagonalized easily. The analogy to the molecular orbital for f electrons applies in this case. Actually the electron correlation mixes the anti-bonding orbital in the ground state to some extent. As U increases, the ground state has more component of the anti-bonding orbital, and changes continuously to the one described by the Heitler-London picture, namely by ψ_{PS}.

On the other hand, the Kondo state is connected continuously to the $U = 0$ limit. Therefore ψ_{PS} and ψ_{2K} can be connected by continuous deformation through the $U = 0$ limit, namely the molecular orbital picture. If one starts from the $U = 0$ limit and increases U, keeping the the total f electron number 2 by appropriate shift of ϵ_f, the charge fluctuation is gradually suppressed. The resultant state is close to ψ_{2K} if J is small, while it tends to ψ_{PS} if J is large enough. This smooth change between ψ_{PS} and ψ_{2K} rests heavily on the presence of charge degrees of freedom. Namely it is important that the splitting between bonding and anti-bonding orbitals does not completely vanish even with large U. On the other hand if one uses the s-d (Kondo) model, the bonding-antibonding splitting does not have a meaning since there is no charge fluctuation. Then in ψ_{2K} the occupation of each orbital is strictly unity. According to the local Fermi liquid theory, the density of states at the Fermi level is equal to $(\pi\Delta)^{-1}$ for each orbital. However ψ_{PS} can have a much smaller density of states at the Fermi level. Therefore the two kinds of states cannot connect continuously. In other words, if one neglects the bonding-antibonding splitting

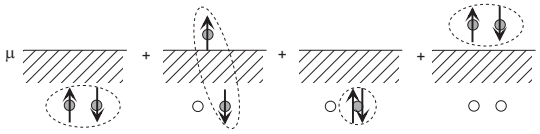

Figure 2.8: Perturbation processes for ψ_{PS}. The two spins inside the dotted oval represents a singlet pair. Circles show localized $f$sites which can have double occupation with finite U.

and increases J/T_K, a discontinuous change should occur. This is an example of the quantum phase transition at zero temperature.

Explicit calculations have been done with use of the numerical renormalization group [47, 48], and the quantum Monte Carlo [49]. In the calculation by Jones et al [47] the s-d model was used and the discontinuity is observed in going from ψ_{2K} to ψ_{PS}. On the contrary Fye and Hirsch[49] used the Anderson model and no discontinuity was found. Sakai and Shimizu [12, 48] clarified how these contrasting behaviors are reconciled by changing the strength of the bonding-antibonding splitting, which is also referred to as parity splitting. Figure 2.9 shows the f-electron density of states in the two-impurity symmetric Anderson model [48]. In the absence of the parity splitting, the density of states at the Fermi level should be the same as the one without the two-body interactions. This is a consequence of the Friedel sum rule in the Fermi liquid side. As the intersite exchange increases, the density of states near the Fermi level becomes narrow, and vanishes at the quantum phase transition to the pair singlet state. The width becomes infinitely narrow just before the transition.

If the f-f hopping t is introduced in the two-impurity symmetric Anderson model, the density of states can be non-symmetric around the Fermi level. Furthermore there is no constraint like the Friedel sum rule at the Fermi level. Figure 2.10 shows the result of the NRG calculation [48] The result in Fig.2.10 shows that a smooth crossover from the local-moment limit and the itinerant Fermi-liquid limit occurs with the f-f transfer. If this kind of smooth change occurs also in heavy-electron systems, the Fermi surface should also change without discontinuity. This subject will be treated in more detail in the next Chapter on heavy electrons.

2.4 Experimental Signatures of Local Spin Dynamics in f-Electron Systems

At temperatures much higher than the characteristic energy of hybridization or intersite exchange interaction, many of lanthanide (Ce, Yb, etc) and actinide (U, Pu, etc) compounds behave as if they consist of an assembly of local moments. This quasi-independent behavior continues sometimes down to low temperatures as shown in Figs.1.1 and 1.2. In this chapter we deal with this regime of heavy electron systems and valence fluctuation systems. In the case where the hybridization energy is larger than the CEF level splittings, the splittings are smeared out. Then the large degeneracy n associated with the J multiplet plays an important role in determining the characteristic energy scale which is typically 100 K. For example we have $n = 6$ for Ce^{3+} and $n = 8$ for Yb^{3+}. In many lanthanide compounds, the valence fluctuating state has been probed by means of X-ray photoemission spectroscopy, measurement of lattice constant and Mössbauer isomer shift. In the valence fluctuation regime, the strong hybridization effect leads to both charge and spin fluctuations. As a consequence the number n_f of f electrons is less than one.

On the contrary, if the hybridization between the f- and conduction electrons is relatively weak, the charge fluctuation is suppressed since the Coulomb repulsion between f electrons is strong. In the latter case the hybridization generates the exchange interaction J_{cf} between f- and conduction electron spins. This case is referred to as the Kondo regime. The characteristic energy scale, T_K, in the Kondo regime is typically 10 K. In most cases, the CEF splitting becomes larger than T_K.s

At high temperatures, an assembly of local moments behaves as independent Kondo scattering centers. For example the Curie-Weiss behavior of the susceptibility appears and the $\log T$-anomalies of the resis-

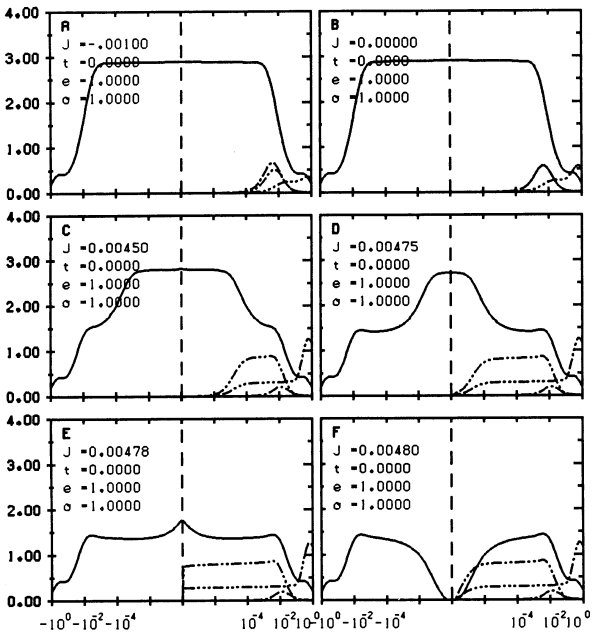

Figure 2.9: Density of states of $f$electrons (solid line) for the model without the parity-splitting terms [48]. The parameter J denotes the intersite exchange in units of the half-width of the conduction band. The other parameters are $\epsilon_f = -0.4$ (f-electron level), $W_i = 0.03$ (hybridization intensity for channels i =even, odd), and $U = 0.8$. The direct f-f transfer energy t is set to zero here, and the even parity occupation number e, and the odd parity occupation number o are the same without the parity splitting. The dot-dashed line represents the imaginary part of the uniform magnetic susceptibility, the two-dot-dashed line the staggered susceptibility (both scaled to 1/4), the three-dot-dashed line the superconducting response function (scaled to 2).

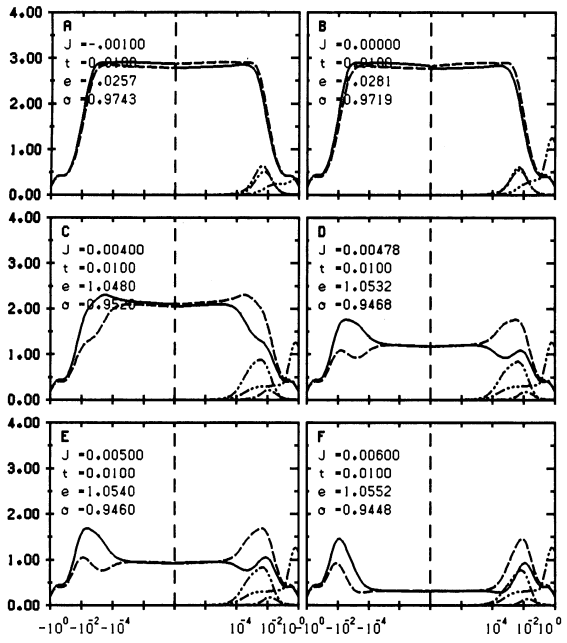

Figure 2.10: Spectral intensities (solid line) of the model with the parity-splitting terms [48]. The solid line (dashed line) denotes the even (odd) component of the f-electron density of states. The other notations are the same as those used in Fig.2.9. The transfer is taken to be $t = 0.01$ in all cases.

tivity takes places. Therefore, various aspects of the Kondo effect including the dynamical characteristics can be investigated by means of NMR and neutron scattering experiments of sufficient accuracy. This situation contrasts with the case of the $3d$-transition-metal alloys, in which the single-ion Kondo effect is easily suppressed by the indirect RKKY interaction and the spin glass transition takes place even with low concentrations of magnetic ions. Furthermore, small numbers of dilute impurities prevent us from extracting reliable data with respect to the spin dynamics of magnetic impurities. In contrast to the transition metal, both the Kondo and the CEF effects should be taken into account self-consistently in rare earths since the splitting of CEF levels becomes comparable to T_K. As a result, the Kondo effect is accompanied by transitions between the levels and causes damping of the levels.

At low temperatures in the Kondo regime, the CEF level scheme can be analyzed in terms of a single ion picture. The crystal field effect arises from the electrostatic potential of surrounding ions acting on f electrons. The CEF Hamiltonian is given by

$$H_{CEF} = e\sum_i V(\boldsymbol{r}_i). \tag{2.125}$$

Since $V(\boldsymbol{r}_i)$ is expanded by the spherical harmonics $Y_l^m(\theta,\phi)$ where l=3 for f electrons, H_{CEF} is expressed by a polynomial of total angular momentum J_z, J_+, J_- and J^2. By introducing the equivalent operators such as $O_2^0 = 3J_z^2 - J(J+1)$, $O_2^2 = J_+^2 + J_-^2$, H_{CEF} is calculated [50, 51] as

$$H_{CEF} = \sum_{n,m} B_n^m O_n^m, \tag{2.126}$$

where B_n^m is the crystal field parameters to be determined from experiments such as inelastic neutron scattering. The CEF Hamiltonian H_{CEF} for a rare-earth ion has the maximum number $n = 6$ which is twice the orbital angular momentum $l = 3$ of the f orbital. For $Ce^{3+}(J = 5/2)$, the maximum is $n = 4$ because $2J < 6$. By diagonalizing eq.(2.126), one can obtain the CEF energies E_n as functions of the CEF parameter B_2^0, B_4^0 and B_4^4. It is also possible to derive the matrix elements. For neutron scattering, relevant matrix elements are $|\langle n|\boldsymbol{J}_\perp|m\rangle|^2$ where $\boldsymbol{J}$ is the projection of the total angular momentum onto the plane perpendicular to the scattering vector $\boldsymbol{Q}$.

The difference in the characteristic energy scales between the valence fluctuation and the Kondo regimes manifests itself in the T dependence of the magnetic relaxation rate. If the dynamical susceptibility is isotropic and can be approximated by a Lorentzian with the relaxation rate Γ, $1/T_1$ is expressed as

$$\frac{1}{T_1} = 2\gamma_n^2 T |A_{hf}|^2 \frac{\chi(T)}{\Gamma}, \tag{2.127}$$

where A_{hf} is the average hyperfine field discussed in Chapter 1. For quasielastic neutron scattering, the magnetic cross section is derived from the combination of eqs.(1.155), (1.156) and (1.85) as

$$\frac{d^2\sigma}{d\Omega d\omega} = A^2 \frac{k_1}{k_0} |F(\boldsymbol{q})|^2 \chi(T) \frac{\omega}{1-\exp(-\omega/T)} \frac{\Gamma}{\Gamma^2+\omega^2}. \tag{2.128}$$

Thus Γ appears as the half width in the quasielastic neutron scattering spectrum.

In the limit of small ω, the imaginary part of $\chi(\omega)$ obeys the Korringa-Shiba relation given by eq.(2.71). Accordingly, with the T_1T=constant law at low temperatures we can estimate Γ by the relation

$$\Gamma = 2\gamma_n^2 T_1 T \chi(0) |A_{hf}|^2 \tag{2.129}$$

The NMR relaxation rate and the half-width of the quasielastic magnetic neutron scattering spectrum to be presented below can be understood in a consistent way.

2.4.1 Valence fluctuating regime

NMR

In most cases, NMR experiments on the valence fluctuating materials are thus far restricted to the non-lanthanide nuclei. The first NMR experiment using ^{139}Yb was reported by Shimizu[52]. The valencies in $YbAl_2$ and $YbAl_3$ are determined from the experiments as 2.4 and $2.7 \sim 3.0$, respectively. The magnetic susceptibility of $YbAl_2$ is T independent below about 200K and exhibits a broad maximum near 850K, which is assigned as T_0. The susceptibility of $YbAl_3$ also exhibits a maximum at T_0=125K above which Curie-Weiss behavior is observed with the effective moment nearly equal to that of a free Yb^{3+} ion.

From the observed spin-echo spectra of ^{139}Yb, the Knight shifts (K) are obtained as $K = 7.7\%$ for $YbAl_2$ and 100% for $YbAl_3$. Both are T independent in the measured temperature range of 4.2−80 K and 1.4−4.2 K, respectively. The Knight shift as well as the susceptibility consists of both contributions from the $4f$ electrons (K_{4f} and χ_{4f}) and the conduction electrons (K_{ce} and χ_{ce}). Since both K_{ce} and χ_{ce} are negligible compared with K_{4f} and χ_{4f}, the hyperfine field $H_{hf} = K_{4f}\mu_B/\chi_{4f}$ due to $4f$ electrons is dominant. Then the hyperfine interaction is obtained as A_s=1.1 and 1.2 MOe/μ_B for $YbAl_2$ and $YbAl_3$, respectively. On the other hand, $A_s(Yb^{3+})$ of a free Yb^{3+} ion is the sum of the orbital and dipole fields. With use of the Hartree-Fock value of $\langle 1/r^3\rangle_{4f}$, they can be calculated as A_s=1.15 and 2.07 MOe/μ_B for J=7/2 and 5/2, respectively. It is notable that the experimentally deduced A_s for both compounds are consistent with the calculated value for the $J = 7/2$ ground state of a free Yb^{3+} ion. Furthermore an experimental value obtained from the hyperfine splitting of Yb^{3+} ESR in CaF_2 is also consistent with these results (A_s(ESR)=1.04 MOe/μ_B). It should be noted that the Yb^{2+} state has no contribution to K_{4f} and χ_{4f}. Accordingly, it is deduced that the character of the $4f$ ground state wave function specified by the total angular momentum $\boldsymbol{J}$ is still conserved in these valence fluctuation compounds in spite of the strong hybridization effect.

Adequate knowledge of the hyperfine interaction allows us to extract the magnetic relaxation rate Γ for $4f$ spins in valence fluctuation compounds from the measurement of $1/T_1$. The T dependence of $1/T_1$ in $YbAl_2$ and $YbAl_3$ is shown in Fig.2.11. For both compounds, $1/T_1$ is proportional to the temperature, having $T_1T = (3.5 \pm 0.1) \times 10^{-2} s$K for $YbAl_2$ and $(1.6 \pm 0.1) \times 10^{-4} s$K for $YbAl_3$. From eq.(2.129), Γ's are evaluated as 1.5×10^4 K for $YbAl_2$ and 9.7×10^2 K for $YbAl_3$, respectively, both being temperature independent. By combining eq.(2.71) and the Knight shift, the Korringa relaxation for nuclei at impurity or f ion sites is obtained at $T \ll T_K$ as

$$T_1 T K^2 = \frac{C_J(2J+1)}{2\pi\gamma_n^2}. \tag{2.130}$$

The Korringa constant in the right hand side in the eq.(2.130) is calculated to be $2.29 \times 10^{-4} s$K for the $J = 7/2$ ground state of Yb^{3+} ions. Experimentally, the Korringa constant on the left hand side

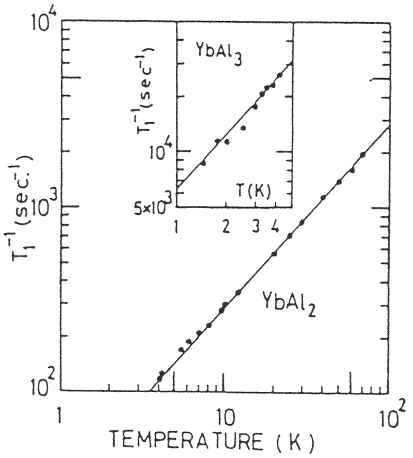

Figure 2.11: Temperature dependences of $^{139}(1/T_1)$ in $YbAl_2$ and $YbAl_3$ (inset) [52].

in eq.(2.130) is obtained as $T_1TK^2 = 2.0 \times 10^{-4} s$K for $YbAl_2$, and $1.6 \times 10^{-4} s$K for $YbAl_3$. The good agreement between the theory and the experiment for $YbAl_2$ implies that the spin fluctuations possess a local character and are well described in the framework of a single impurity model, even though the Yb ions form a periodic lattice. For $YbAl_3$, however, the theoretical value is somewhat larger than the experimental value. This may be because the dynamical response function is different between dilute and periodic $4f$ ion systems and/or the degeneracy of $J = 7/2$ ground states is lifted partially, so that the application of eq.(2.130) becomes unjustified.

neutron scattering

Ce-based compounds in the valence fluctuation regime were extensively studied by magnetic neutron scattering experiments. The quasielastic relaxation rate Γ is very large, reaching to several tens of meV. In the valence fluctuation regime, the intersite magnetic correlation driven by the RKKY interaction is masked by the local hybridization with conduction electrons. No CEF transitions are resolved in these compounds. By integrating the magnetic scattering cross section given by eq.(2.128) over ω for fixed $\boldsymbol{Q}$, one can obtain $g_J^2 J(J+1)F(\boldsymbol{Q})^2$.

Equation (2.128) holds well for all rare earth (RE) metals with a stable valence at high temperatures. However, the energy spectrum becomes more complex upon cooling, as $\Gamma(T)$ is decreased to the order of the CEF splittings or magnetic ordering energies. On the other hand, the scattering profiles in the Ce-based compounds are quite different. As an example, we take $CePd_3$, which is compared with the isostructural reference compounds diamagnetic YPd_3 which has no $4f$ electrons, and $TbPd_3$ with a stable $4f^8$ configuration [53]. Figure 2.12 indicates the energy dependence of the inelastic scattering cross section for those compounds. All three compounds exhibit incoherent elastic scattering at $\omega = 0$ due to nuclear isotopic and/or nuclear spin disorder. This contribution is shown by the shaded part in Fig.2.12. For YPd_3, there is a phonon peak between $\hbar\omega = -20$ meV and -10 meV, while $CePd_3$ has a considerable intensity in this energy window in addition to phonon scattering. In contrast to the coherent phonon scattering, the integrated intensity in this energy window decreases with increasing scattering angle and has the angular dependence expected from the magnetic $4f$ form factor.

The magnetic scattering profile in $CePd_3$ is actually fitted by the solid lines according to eq.(2.128) employing the experimental values of the susceptibility. From this fitting, $\Gamma(T)$ is deduced as shown in Fig.2.13. For $TbPd_3$, the quasi-elastic spectrum becomes sharper upon cooling as seen in Fig.2.13. Its linewidth decreases linearly with temperature, if extrapolated from the resolution limit of the spectrometer. We also note that $TbPd_3$ shows a distinct CEF transition. Thus, difference of the magnetic scattering is clear between $CePd_3$ and $TbPd_3$. For $CePd_3$, a quasi-elastic linewidth amounts to about 20 meV, which is nearly three orders of magnitude larger than that in $TbPd_3$. It is remarkable that this width is nearly T-independent in a range of 200−300K. This is again in contrast to the normal Korringa

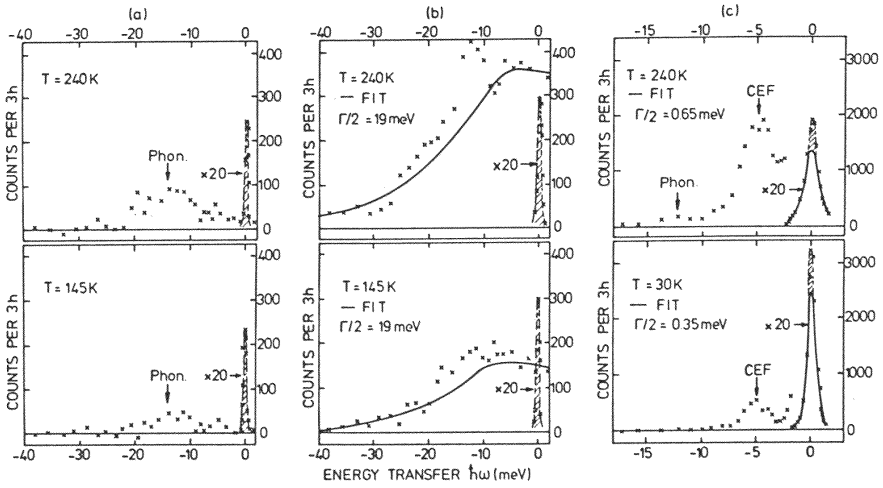

Figure 2.12: Scattered neutron intensity as function of energy for the isostructural compounds, (a) YPd_3, (b) $CePd_3$ and (c) $TbPd_3$[53].

behavior observed for $TbPd_3$. Note that below 200 K, the linewidth actually exceeds k_BT. Therefore, the decay of local $4f$ moments is not driven thermally but quantum mechanically. The hybridization effect between f- and conduction electrons is responsible for the magnetic ordering or the development of CEF spectra on a energy scale smaller than Γ. All these features are a general property in valence fluctuation compounds with nonmagnetic ground states. Apparently the behavior of $\Gamma(T)$ in the valence fluctuation regime is well described by eq.(2.101) [54].

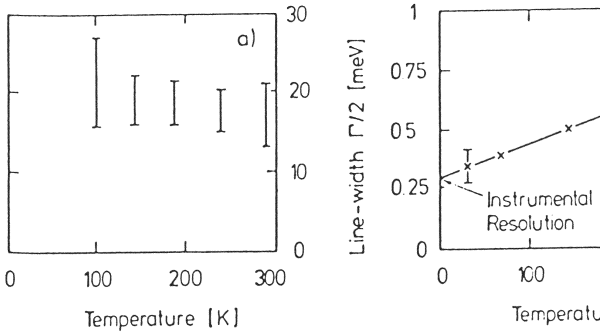

Figure 2.13: Temperature dependences of the quasi-elastic magnetic half-width $\Gamma/2$ for (a) the valence fluctuation system $CePd_3$ and (b) the local moment system $TbPd_3$[53].

2.4.2 Kondo regime

NMR

The Knight shift for non-transition elements such as Al, Si, Sn, As, etc in heavy-electron compounds is dominated by an isotropic hyperfine interaction, even when the magnetic properties are highly anisotropic. This empirical result enables us to estimate the low energy scale in the Kondo regime by comparing NMR of non-Lanthanides elements with the quasi-elastic neutron scattering intensity. In the low energy region, the ground state doublet in the CEF levels plays a primary role. In this case, from the measurement of T_1, the magnetic relaxation rate Γ of the f electron can be extracted by eq.(2.127). In order to compare the results of the NMR and neutron scattering experiments, we present the ^{29}Si NMR investigation in

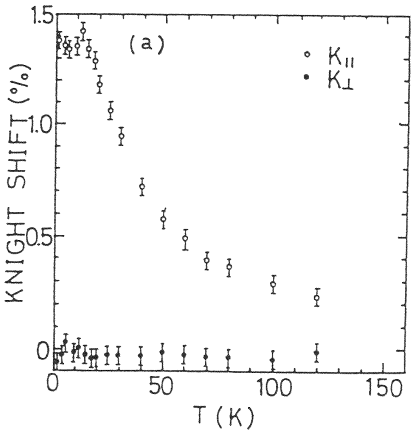

Figure 2.14: Temperature dependence of the Knight shift $K_{\parallel}(T)$ parallel to the tetragonal c-axis, and $K_{\perp}(T)$ perpendicular to the c-axis in $CeRu_2Si_2$ [55].

$CeRu_2Si_2$ [55].

From a characteristic powder pattern of the NMR spectrum, the T dependence of the Knight shift, parallel ($K_{\parallel}$) and perpendicular ($K_{\perp}$) to the tetragonal c-axis in $CeRu_2Si_2$ is obtained as displayed in Fig.2.14. There appears a huge uniaxial anisotropy in the Knight shift. In fact, the anisotropy of susceptibility measured for the single crystal is as large as $\chi_{\parallel}/\chi_{\perp} \simeq 15$. From plotting an isotropic Knight shift defined by $K_{iso} = (K_{\parallel} + 2K_{\perp})/3$ against the susceptibility measured for the powder, we estimate a parallel component of the hyperfine field $A_{\parallel}$ and the anisotropy of the susceptibility at 4.2 K as $A_{\parallel} = 0.91 \pm 0.06$ kOe/μ_B and $\chi_{\parallel}/\chi_{\perp} \simeq 18$, respectively. Thus we conclude that the anisotropy of the Knight shift does not originate from the hyperfine interaction, but from the susceptibility.

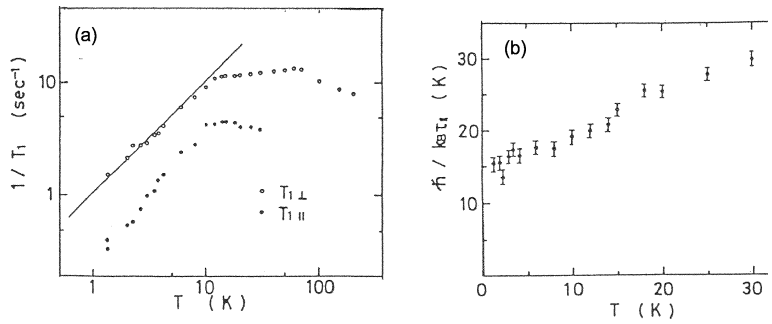

Figure 2.15: (a) Temperature dependences of $(1/T_1)_{\perp}$ and $(1/T_1)_{\parallel}$. (b) Temperature dependence of Ce spin fluctuation rate, $\hbar/(\tau_{\parallel}k_B) = \Gamma_{\parallel}(T)$ parallel to the c-axis [55].

We now have an adequate knowledge of the transferred hyperfine interaction of ^{29}Si, which is isotropic and dominated by the hybridization effect with five nearest neighbor Ce-4f electrons. Next, we inspect the relaxation result shown in Fig.2.15. Part (a) of the figure indicates the $T-$dependences of $(1/T_1)_{\parallel}$ and $(1/T_1)_{\perp}$. Both $(1/T_1)_{\parallel}$ and $(1/T_1)_{\perp}$ exhibit a weak T dependence above the temperature at which both the susceptibility and the Knight shift have a peak. However, below 8 K they follow commonly the relation T_1T=constant. We emphasize that the value of $(T_{1\perp}T)^{-1} = 1.0 \pm 0.05(sK)^{-1}$ is two orders of magnitude larger than $(T_1T)^{-1} = 0.014 \pm 0.005(sK)^{-1}$ for $LaRu_2Si_2$. This verifies that the relaxation process in the former is governed by spin fluctuations of f electrons. If we take into account the anisotropic magnetic property in eq.(2.127), $(1/T_1)_{\parallel}$ and $(1/T_1)_{\perp}$ are related to the dynamical

susceptibility components $\chi_{\parallel}(\omega)$ and $\chi_{\perp}(\omega)$ of $4f$ electrons as

$$\frac{1}{T_{1\parallel}} = 2\gamma_n^2 T \sum_i [A_{\perp,i}]^2 \frac{\mathrm{Im}\chi_{\perp}(\omega_n)}{\omega_n}, \tag{2.131}$$

and

$$\frac{1}{T_{1\perp}} = 2\gamma_n^2 T \sum_i \left([A_{\parallel,i}]^2 \frac{\mathrm{Im}\chi_{\parallel}(\omega_n)}{\omega_n} + [A_{\perp,i}]^2 (1/2) \frac{\mathrm{Im}\chi_{\perp}(\omega_n)}{\omega_n} \right) \tag{2.132}$$

respectively. By combining the above two formulae, we have the relation

$$\frac{1}{T_{1\perp}} - \frac{1}{2T_{1\parallel}} = 2\gamma_n^2 T \sum_i [A_{\parallel,i}]^2 \frac{\mathrm{Im}\chi_{\parallel}(\omega_n)}{\omega_n} \tag{2.133}$$

where $A_{\parallel,i}$ is the transferred hyperfine field parallel to the c-axis due to five nearest neighbor $4f$ spins. In the present case, one can safely approximate $\sum_i [A_{\parallel,i}(R_i)]^2$ by $z(A_{\parallel}/z_n)^2 = A^2/z_n$ where $A_{\parallel} = 0.91 \pm 0.06$ kOe/μ_B is determined from the plot of K_{iso} vs χ_{iso} with z_n the number of nearest neighbor $4f$ ions ($z_n = 5$ for ^{29}Si of $CeRu_2Si_2$).

By combining eqs.(2.127) and (2.133), $(1/T_1)_{\parallel}$ and $(1/T_1)_{\perp}$ are related to the magnetic relaxation rate $\Gamma_{\parallel}$ by the formula:

$$\Gamma(T)_{\parallel} = 2\gamma_n^2 T [\frac{1}{T_{1\perp}} - \frac{1}{2T_{1\parallel}}]^{-1} \frac{K_{\parallel} A_{\parallel}}{\mu_B z_n} \tag{2.134}$$

where the experimental relation $K_{\parallel}(T) = A_{\parallel}\chi_{\parallel}(T)/N\mu_B$ is utilized with $A_{\parallel} = 0.91 \pm 0.06$ kOe/μ_B. Part (b) of Fig.2.15 shows the T dependence of $\Gamma_{\parallel}$ thus estimated. $\Gamma_{\perp}$ is difficult to evaluate since $K_{\perp}$ is almost zero. As seen in the figure, $\Gamma_{\parallel}$ is nearly T independent with $\Gamma_{\parallel} = (16.0 \pm 1.0)$K up to 8K and increases gradually to 30 K.

This value of $\Gamma_{\parallel}$ extracted from NMR is very close to that from neutron scattering: $\Gamma_{\parallel}^{neutron} = (20 \pm 3)K$ as deduced from the quasielastic spectrum at 1.4 K [56]. This may suggest that the spin relaxation is governed by fluctuations of f electrons which are almost independent of wave vector. However, as described in more detail in Chapter 3, intersite magnetic correlations become significant in $CeRu_2Si_2$ at low temperatures. Thus it is likely that the T_1T=constant law below 8 K does not originate from the single-site Kondo effect but from heavy itinerant electrons.

neutron scattering

Experimentally, the magnetic neutron scattering spectra at low T consist of the quasi-elastic and several inelastic spectra. From the former the magnetic relaxation rate Γ is extracted. On the other hand, the inelastic part originates from transitions between the ground state multiplet and several excited CEF multiplets of $4f$ shells. Thus one can extract the CEF level scheme by analyzing the spectra.

As a typical example, we present a systematic study of CeM_2X_2(M=Cu, Ag, Au, Ru, Ni; X=Si, Ge) by means of magnetic neutron scattering experiments [56, 57, 58, 59]. These Ce-based ternary compounds with $ThCr_2Si_2$ type structure involve systems with different ground states: $CeNi_2Ge_2$ is paramagnetic, $CeCu_2Si_2$ is the first heavy-electron superconductor and $CeCu_2Ge_2$ is a heavy-electron antiferromagnetic compound which, interestingly, undergoes a superconducting transition under an application of high pressure. $CeRu_2Si_2$ and $CeNi_2Ge_2$ are characterized by heavy-electron effective masses, which reveal neither a magnetic nor a superconducting phase transition. In $CeRu_2Si_2$, there occurs at low temperatures a pseudo-metamagnetic transition at a critical magnetic field $H_c = 80$ kOe.

We first show the result in $CeCu_2Si_2$ [58]. The neutron scattering experiment has revealed that the inelastic magnetic part of the spectrum consists of a well pronounced peak at $\hbar\omega = 31.5$ meV and, in addition, a less pronounced peak at $\hbar\omega = 12$ meV. Both peaks are reasonably fitted by two Lorentzians centered at $E_1 = \hbar\omega = k_B(135 \pm 15)$K and $E_2 = \hbar\omega = k_B(360 \pm 20)$K, respectively. These two transitions are assigned to two CEF transitions from the ground state doublet, $|0\rangle$, to the excited doublets, $|1\rangle$ and $|2\rangle$, expected for Ce^{3+} ions occupying the tetragonal sites. Thus the CEF parameters such as B_2^0, B_4^0 and B_4^4 are obtained by simultaneously fitting the splittings E_1 and E_2 and the ratio of the intensities. As shown in Fig.2.16, we can find the CEF level scheme.

On the other hand, the width of the quasi-elastic spectrum Γ is a measure of the strength of the hybridization or the exchange interaction between the f- and the conduction electrons. In rare earth

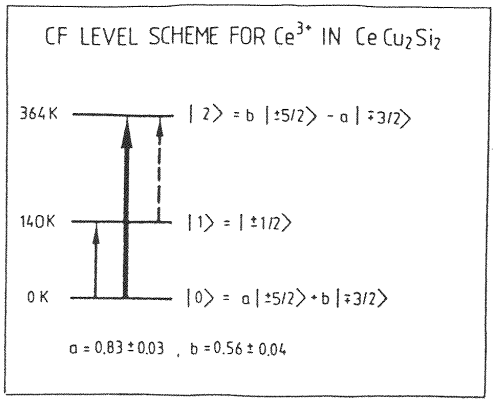

Figure 2.16: Crystal electric field (CEF) level scheme of Ce^{3+} in tetragonal $CeCu_2Si_2$ determined by the neutron scattering experiment [59].

compounds with a magnetically stable $4f$ configuration, one expects a Korringa behavior for the quasi-elastic linewidth as demonstrated for $TbPd_3$ (see Fig.2.13), namely $\Gamma = \alpha T$ where α is typically 10^{-3}, while the valence fluctuation compounds such as $CePd_3$ and $CeSn_3$ show an almost T independent Γ, reaching typically to $20 \sim 30$ meV as represented by $CePd_3$ in Fig.2.13.

In contrast to these, the relaxation rate in the Kondo regime exhibits a characteristic T-dependence and probes the presence of a very low energy scale of $10 \sim 30$ K. Figure 2.17 shows the summary of the magnetic relaxation rate $\Gamma(T)$ versus temperature for $T \geq T_M$, where T_M is the magnetic ordering temperature for a series of CeM_2X_2 compounds with the tetragonal structure. The upper part of Fig.2.17 shows $\Gamma(T)$ of the nonmagnetic $CeRu_2Si_2$ and $CeNi_2Ge_2$, and superconducting $CeCu_2Si_2$. Then the presence of such a low energy scale is related to the huge linear term of the specific heat which amounts to about 1 J/moleK^2. Namely the system can be described by renormalized heavy quasi-particles at low temperatures.

The lower part of Fig.2.17 indicates the results for magnetically ordered compounds with significantly lower values of Γ. Most remarkably, except for $CeRu_2Ge_2$ and $CeAu_2Ge_2$ in which $\Gamma(T)$ follows the Korringa behavior as observed for $TbPd_3$, all other systems show a distinct deviation from a T linear dependence. Instead $\Gamma(T)$ seems to follow roughly a square-root dependence of $\Gamma = A\sqrt{T}$ as drawn by the solid lines in Fig.2.17. These systems are regarded as heavy-electron antiferromagnets with heavy quasi-particles where quasi-elastic Lorentzian intensities still survive even below T_M.

In a cubic crystal such as $Ce_{1-x}La_xAl_2$ and CeB_6, the CEF levels are split into a doublet and a quartet. The ground state is the doublet Γ_7 in $Ce_{1-x}La_xAl_2$ and the quartet Γ_8 in CeB_6. On the other hand, in the tetragonal crystal $CeCu_2Si_2$, the CEF levels consist of three doublets as presented above. Hence, these three crystals have CEF states different from one another. By approximating the inelastic neutron scattering spectra to be of the Lorentzian form, the linewidths of quasi-elastic spectra in $CeCu_2Si_2$, $Ce_{1-x}La_xAl_2$ and CeB_6 are displayed in Fig.2.18. As seen in Fig.2.18, an NCA-type calculation with use of the Coqblin-Schrieffer model reproduces the experiment fairly well, the results of which are indicated by the solid lines[60]. In CeB_6 with the larger CEF splitting, on the other hand, the relaxation rate is closer to the linear behavior.

The $T^{1/2}$ like behavior of Γ seen in $CeCu_2Si_2$ and $Ce_{0.7}La_{0.3}Al_2$ is due to combination of the CEF and the Kondo effects. As we have shown in §2.1.5, the Kondo temperature is influenced by the presence of CEF splittings. If the temperature T is higher than the overall splitting, the effective Kondo temperature is increased to the value without the splitting. Thus the relaxation rate depends on T as if T_K varies when T is comparable to the CEF splittings. In the case of CeB_6, the large CEF splitting (~ 500 K) does not produce this behavior.

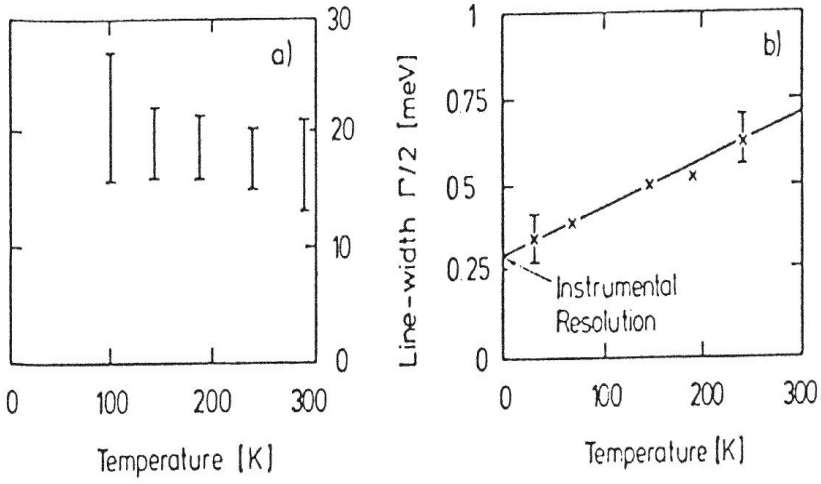

Figure 2.17: Temperature dependences of the quasi-elastic Lorentzian linewidth, $\Gamma/2$ in isostructural compounds CeM_2X_2: (a) nonmagnetic $CeNi_2Ge_2$, $CeRu_2Si_2$, and superconducting $CeCu_2Si_2$; (b) antiferromagnetic $CeCu_2Ge_2$, $CeAg_2Si_2$, $CeAg_2Ge_2$, $CeAu_2Ge_2$ and ferromagnetic $CeRu_2Ge_2$. Solid lines represents fits using a square root dependence of $\Gamma(T)$[58].

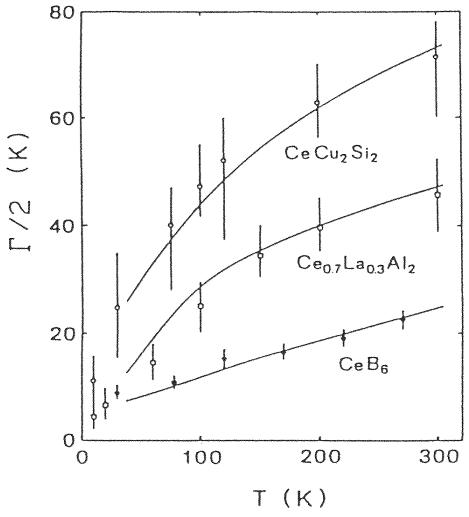

Figure 2.18: Comparison between theoretical calculation (solid lines) and experimental data of $\Gamma(T)/2$ in tetragonal $CeCu_2Si_2$, cubic $Ce_{0.7}La_{0.3}Al_2$ and CeB_6 [60].

2.4.3 Non-Fermi liquid behavior

In contrast to the $4f$ electron systems, the spatial extent of the $5f$ electron states in the uranium based compounds is larger than that of the $4f$ electrons and the hybridization with the valence conduction electrons is stronger. Then the valency of a U ion in a crystal can take either $U^{3+}(5f^3)$, $U^{4+}(5f^2)$ or $U^{5+}(5f^1)$. It was predicted that the interaction between the non-Kramers U^{4+} ion and the conduction electrons leads to non-Fermi liquid behavior which is characterized by logarithmic or power-law divergence of the physical quantities at low temperatures. The two channel Kondo effect ($n = 2$, $S = 1/2$) discussed in 2.3 is invoked with screening channels induced by virtual transitions between the lowest CEF doublet of the $5f^2$ configuration and an excited CEF doublet of the $5f^1$ configuration[41, 44]. A possible experimental signature for the non-Fermi liquid behavior was observed in dilute U system $U_xTh_{1-x}Ru_2Si_2$[61] and $U_{1-x}Y_xPd_3$ [62]. As shown in Fig.2.19, the magnetic susceptibility $\chi_{imp}(T)$ due to U impurity follows the $\ln T$ dependence over two decades of temperature below 10 K. The reason for this behavior is not yet understood. We describe some models proposed so far, although none of them are completely successful.

In the two-channel screening model, the T^{-1} divergence of the paramagnetic susceptibility for the non-Kramers doublet is marginally suppressed. The numerical solution predicted a simple logarithmic function of the susceptibility with $\chi(T) = a/T_K \ln(T/bT_K)$ for $T \ll T_K$ where constant a and b are given as ~ 0.05 and 2.2[63], respectively. The best fit to the experiment was obtained with T_K=11.1 K. This impurity model is convenient to explain the fact that $\chi(T)$ is almost proportional to the U concentration. However, the residual entropy, which should be released by application of magnetic field, has not been observed.

Alternative explanations for the non-Fermi liquid behavior are provided based on distribution of Kondo temperatures [64], and a spin-glass transition very near zero temperature [65].

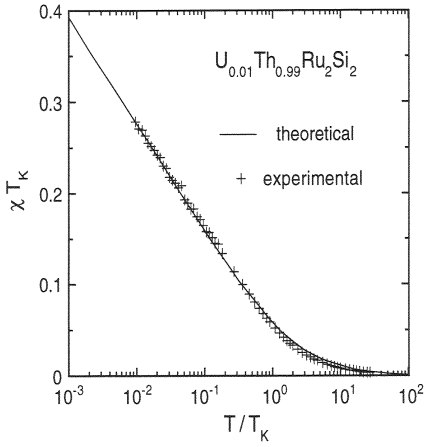

Figure 2.19: Comparison between the U contribution χ_{imp} in $U_{0.01}Th_{0.99}Ru_2Si_2$ and numerical calculation based on the S=1/2 two-channel Kondo model (solid line). Parameters used for fitting are $\mu = 1.7\mu_B$ and T_K=11.1 K [61, 63].

To conclude Chapter 2, we would say that the spin dynamics probed by NMR and neutron scattering techniques can be semiquantitatively interpreted within such impurity models as the degenerate Anderson and the Coqblin-Schrieffer models as long as high temperature behaviors are concerned. In the following chapters, we shall see how the strong interaction effects among electrons lead to richer and more fascinating behaviors at low temperatures.

Bibliography

[1] P.W. Anderson, Phys. Rev. **124**, 41 (1961).

[2] J. Kondo, in *Solid State Physics* Vol.23 (Academic Press, New York, 1969), p.183.

[3] P. Fulde, J. Keller and G. Zwicknagl, in *Solid State Physics* Vol.41 (Academic Press, New York, 1988), p.2.

[4] A.C. Hewson, *The Kondo Problem to Heavy Fermions*, (Cambridge University Press, Cambridge, 1993).

[5] N. Andrei, K. Furuya and J.H. Lowenstein, Rev. Mod. Phys. **55**, 331 (1983).

[6] A.M. Tsvelick and P.B. Wiegmann, Adv. Phys. **32**, 453 (1983).

[7] B. Coqblin and J.R. Schrieffer, Phys. Rev. **185**, 847 (1969).

[8] P.W. Anderson, J. Phys. C**3**, 2439 (1970).

[9] A.A. Abrikosov, Physics **2**, 5 (1965).

[10] K.G. Wilson, Rev. Mod. Phys. **47**, 773 (1975).

[11] H.R. Krishnamurthy, J.W. Wilkins and K.G. Wilson, Phys. Rev. B**21**, 1003 (1980)

[12] O. Sakai, Y. Shimizu and T. Kasuya, Solid State Commun. **75**, 81 (1990)

[13] P. Nozieres, J. Low Temp. Phys. **17**, 31 (1975).

[14] K. Yamada, Prog. Theor. Phys. **53**, 970 (1975).

[15] H. Shiba, Prog. Theor. Phys. **54**, 967 (1975).

[16] D. Pines and P. Nozieres, *The Theory of Fermi Liquids: Volume I*, (W.A. Benjamin, New York, 1966).

[17] A. Yoshimori and A. Zawadowski, J. Phys. C**15**, 5241 (1975).

[18] Y. Kuramoto and H. Kojima, Z. Phys. B**57**, 95 (1984).

[19] J.W. Rasul and A.C. Hewson, J. Phys. C**17**, 2555 & 3332 (1984).

[20] K. Hanzawa, K.Yamada and K. Yoshida, J. Magn. & Magn. Mater. **47**, 357 (1985).

[21] S.E. Barnes, J. Phys. **F6**, 1375 (1976).

[22] P. Coleman, Phys. Rev. B**29**, 3035 (1984).

[23] H. Keiter, Z. Phys. B**214**, 466 (1968).

[24] N. Read and D.M. Newns, J. Phys. C**16**, 3273 (1983).

[25] N.E. Bickers, Rev. Mod. Phys. **59**, 845 (1987).

[26] Feynman, Statistical Mechanics (W.A. Benjamin, Reading, U.S.A., 1972) p.67.

[27] O. Gunnarsson and K. Schönhammer, Phys. Rev. B**28**, 4315 (1983).

[28] O. Gunnarsson and K. Schönhammer, in *Handbook on the physics and Chemistry of Rare Earths,* (K.A. Gschneider et al ed., North-Holland, Amsterdam, 1987) vol.10, p.103.

[29] H. Keiter and J.C. Kimball, Int. J. Magn. **1**, 233 (1971).

[30] Y. Kuramoto, Z. Phys. B**53**, 37 (1983).

[31] S. Inagaki, Prog. Theor. Phys. **62**, 1441 (1979).

[32] Y. Kuramoto, J. Magn. & Magn. Mater. **31-34**, 463 (1983).

[33] F.C. Zhang and T.K. Lee, Phys. Rev. B**30**, 1556 (1983).

[34] N. Grewe Z. Phys. B**53**, 271 (1983).

[35] Y. Kuramoto, Z. Phys. B**37**, 299 (1980).

[36] H. Kojima, Y. Kuramoto and H. Tachiki, Z. Phys. B**54**, 293 (1984).

[37] N.E. Bickers, D.L. Cox and J.W. Wilkins, Phys. Rev. Lett. **54**, 230 (1987).

[38] Y. Kuramoto and E. Müller-Hartmann, J. Magn. & Magn. Mater. **52**, 122 (1985).

[39] P. Nozieres and A. Blandin, J. Physique **41**, 193 (1980).

[40] I. Affleck, Acta Physica Polonica, **26**, 1826 (1995).

[41] D.L. Cox and A. Zawadowski, Adv. Phys. **47**, 599 (1998).

[42] A.M. Tsvelick and P.B. Wiegmann, Z. Phys. B**54**, 201 (1984); J. Stat. Phys. **38**, 125 (1985).

[43] N. Andrei and C. Destri, Phys. Rev. Lett. **52**, 364 (1984).

[44] D.L. Cox, Phys. Rev. Lett. **59**, 1240 (1987).

[45] O. Sakai, S. Suzuki and Y. Shimizu, Solid State Commun. **101**, 791 (1997).

[46] T. Kasuya, in *Magnetism Vol.IIB* (Eds., G.T. Rado and H. Suhl, Academic Press, New York, 1965)

[47] B.A. Jones, C.M. Varma and J.W. Wilkins, Phys. Rev. B**61**, 125 (1988)

[48] O. Sakai, Y. Shimizu J. Phys. Soc. Jpn. **61**, 2333,2348 (1992)

[49] R.M. Fye and J.E. Hirsch, Phys. Rev. B**40**, 4780 (1989).

[50] K.W.H Stevens, Proc. Phys. Soc. **A65**, 209 (1952).

[51] N.T.Hutchings, Solid State Phys. **16**, 227 (1964).

[52] T.Shimizu, M.Takigawa, H.Yasuoka and J.H. Wernick, J. Magn. Magn. Mat. **52**, 187 (1985).

[53] E.Holland-Moritz, M.Loewenhaupt and W. Schmatz, Phys. Rev. Lett. **38**, 983 (1977).

[54] E. Holland-Moritz and G.H. Lander, in *Handbook on the Physics and Chemistry of Rare Earths, Vol.19* (Eds., K.A. Gschneider, L. Eyring, G.H. Lander, and G.R. Choppin, North-Holland, Amsterdam, 1993), ch.130.

[55] Y.Kitaoka, H.Arimoto, Y.Kohori and K.Asayama, J. Phys. Soc. Jpn. **54**, 3236 (1985).

[56] J.Rossat-Mignod, L.P.Regnault, J.L.Jacoud, C.Vettier, P.Lejay, J.Flouquet, E.Walker, D.Jaccard and A.Amato, J. Magn. Magn. Mat. **76 & 77**, 376 (1988).

[57] J.L.Jacoud, L.P.Regnault, J.Rossat-Mignod, C.Vettier, P.Lejay and J.Flouquet, Physica **B156 & 157**, 818 (1989).

[58] A.Loidl, G.Knopp, H.Spille, F.Steglich and A.P.Murani, Physica **B156 & 157**, 794 (1989).

[59] S.Horn, E.Holland-Moritz, M.Loewenhaupt, F.Steglich, H.Scheuer, A.Benoit and J.Flouquet, Phys. Rev. **B23**, 3171 (1981).

[60] S.Maekawa, S.Kashiba, S.Takahashi and M.Tachiki, J. Magn. Magn. Mat. **52**,149 (1985) .

[61] H. Amitsuka and T. Sakakibara, J. Phys. Soc. Jpn. **63**, 736 (1994).

[62] M.B. Maple et al, J. Phys. Condens. Matter **8**, 9773 (1996).

[63] P.D. Sacramento and P. Schlottmann, Phys. Rev. B**43**, 13294 (1991).

[64] E. Miranda, V. Dobrosavljevic, G. Kotliar, J. Phys.: Condens. Matter **8**, 9871 (1996); Phys. Rev. Lett. **78**, 290 (1997).

[65] A. M. Sengupta, A. Georges, Phys. Rev. **B52**, 10295 (1995).

Chapter 3

Metallic and Insulating Phases of Heavy Electrons

In the previous chapters, we have seen that magnetic and thermal properties of heavy electrons are basically determined by strong local correlation. A signature of the local nature is that the susceptibility and specific heat are roughly proportional to concentration of Ce in systems such as $Ce_xLa_{1-x}Cu_6$ or $Ce_xLa_{1-x}B_6$. The RKKY interaction is operative in bringing about magnetic ordering. The energy scale of it is given by $J_{RKKY} \sim J^2\rho_c$ where J is the exchange interaction between f and conduction electrons and ρ_c is the density of conduction band states per site. The RKKY interaction competes with the Kondo effect which points to the non-magnetic singlet ground state. There exists a rather detailed balance between these two tendencies. It is expected that the magnetic transition temperature T_M, if it exists, is lowered due to the Kondo effect. In the opposite case of $T_K \gg J^2\rho_c$, no magnetic order should occur.

Even in the singlet ground state, intersite interaction should influence residual interactions among renormalized heavy quasi-particles. It is this residual interaction that leads to a rich variety in the ground states such as heavy-electron superconductivity, heavy-electron band magnetism, etc. Short-range magnetic correlation might survive even if the dominating Kondo effect prevents development of long-range order. We have already seen in Fig.1.3 that electrical resistivity reveals growing importance of coherence upon increasing concentration of rare-earth ions at low temperatures.

Direct evidence for heavy quasi-particles comes from the de Haas-van Alphen (dHvA) effect which is the oscillation of the magnetic susceptibility coming from Landau quantization of the electron orbits [36]. Geometry of the Fermi surface can be obtained from the period of oscillation in the differential magnetic susceptibility as a function of $1/H$ with H the magnetic field. The effective mass can be deduced from temperature dependence of the oscillation amplitude. To observe these oscillations, the mean free path l of a heavy quasi-particle must be larger than the cyclotron radius: $l \gg v_F/\omega_H$ where v_F is the Fermi velocity, and $\omega_H = eH/m^*c$ is the effective cyclotron frequency of a heavy quasi-particle with effective mass m^*. Furthermore thermal smearing at the Fermi surface must be sufficiently small: $T \ll \omega_H$. With large effective masses and short mean free paths, these conditions require that experiment should be performed at low temperature and in high field. Measurements of dHvA oscillations have been made on UPt_3 [1, 3], $CeRu_2Si_2$ [2, 3] and $CeCu_6$[4]. In all these cases, heavy effective masses have been observed.

For UPt_3, the Fermi surface obtained by the dHvA effect is in good agreement with that obtained from energy-band theory [5]. The effective mass on some sheets of the Fermi surface, however, is about 10 to 30 times larger than that deduced from band-structure calculations. This fact shows that there are significant many body effects which are not described by the standard band theory.

In the present chapter, we shall review paramagnetic heavy-electron states which have both metallic and insulating phases. The ordered states such as magnetic and superconducting phases will be discussed in Chapters 4 and 5, respectively. In the following we focus on the growth of intersite coherence, or the itinerant character of f electrons, mainly in dynamic magnetic properties. As specific examples to see the subtle role of the intersite correlation in the heavy-electron state, we take typical systems $CeCu_6$ and $CeRu_2Si_2$ where the Fermi-liquid remains stable at low temperatures even with significant magnetic correlations. We then discuss UBe_{13} and UPt_3 mainly in their paramagnetic phase to contrast with the

Ce systems.

3.1 Formation of Heavy-Electron Metals with Magnetic Correlation

3.1.1 Metamagnetic behavior

$CeRu_2Si_2$ has electronic specific heat coefficient $\gamma = 0.35$ J/(mole K^2), which is much smaller than 1.6 J/(mole K^2) of $CeCu_6$, and a little smaller than 0.4 J/(mole K^2) of UPt_3. A remarkable feature of this compound is the pseudo-metamagnetic transition. This transition has been observed for a magnetic field H_c=8 T applied along the tetragonal c-axis in $CeRu_2Si_2$, as shown in Fig.3.1 [8]. Similar pseudo-metamagnetic transition has also been reported for UPt_3 at much higher fields of 20 T [18] A metamagnetic behavior has also been observed in $CeCu_6$ at 2 T. In this case the metamagnetism is faint and is seen as a peak only in $\partial^2 M/\partial H^2$.

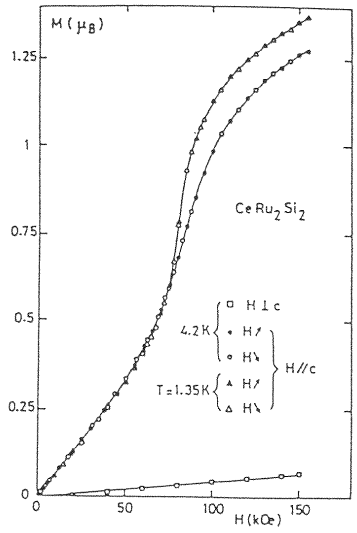

Figure 3.1: Magnetization curves for $CeRu_2Si_2$ up to 150 kOe at 4.2 and 1.35 K [8].

Decline of the heavy-electron state through H_c was found by the dHvA effect [10]. Effective masses up to $120m_0$, which are observed below H_c, decrease significantly around H_c and continue to decrease with increasing field. Then, it has been proposed that the system above H_c may be described in terms of the localized f electron model [10]. A basis of the proposal is that the Fermi surfaces measured above H_c is similar to those with localized f electrons calculated by the band theory [11]. On the other hand, in dHvA experiment for UPt_3 the behavior above the pseudo-metamagnetic transition does not suggest localization of f electrons [3]. We note that if two $5f$ electrons per U^{4+} ion are localized, the size of the Fermi surface can remain the same as that of itinerant $5f$ electrons. This aspect will be discussed in 3.3.

We mention that the metamagnetic behavior accompanies large elastic anomaly. The elastic constants show pronounced softening near the critical magnetic field H_c [12] and the magnetostriction is also anomalous [13]

3.1.2 NMR on $CeCu_6$ and $CeRu_2Si_2$

Figure 3.2 shows the temperature dependence of the nuclear-spin-lattice-relaxation rate $1/T_1$ for $CeCu_6$ and $CeRu_2Si_2$ [6]. In the latter case $1/T_{1\perp}$ of ^{29}Si is measured under the condition that the c-axis is aligned along the magnetic field. For $CeCu_6$, $1/T_1$ of ^{63}Cu was measured in zero field by Cu NQR. As seen in the figure, $1/T_1$ is almost independent of temperature above 6 K for $CeCu_6$ and 12 K for $CeRu_2Si_2$. Then $1/T_1$ begins to decrease gradually above 50 K for $CeRu_2Si_2$. This relaxation behavior

shares a common feature with other heavy-electron systems at high temperatures. As discussed in the previous Chapter, spin correlation between different sites can be ignored at high temperatures, and $1/T_1$ is described by the local spin susceptibility $\chi(T)$ and the magnetic relaxation rate Γ.

The temperature below which $1/T_1$ begins to depend on T is close to the Kondo temperature T_K which is extracted from analysis of the resistivity and the magnetic specific heat. With further decrease of temperature, $1/T_1$ follows a behavior T_1T=constant, which is called the Korringa law. To see this clearly, Fig.3.3 shows $(T_1T)^{-1}$ vs T. It turns out that the Korringa law is valid below 0.2 K for $CeCu_6$ and 8 K for $CeRu_2Si_2$. The characteristic temperature in each case is sometimes called the coherence temperature T^*. As discussed in Chapter 1, the Fermi liquid ground state leads to the Korringa law at low T. This is independent of whether the system is homogeneous or a local Fermi liquid. In the temperature range where the local Fermi liquid description is valid, the Korringa relation given by eq.(1.140) should hold.

In contrast to the expectation based on the single-ion model of spin fluctuations, the ratio of T^*/T_K is quite different in $CeCu_6$ from that in $CeRu_2Si_2$; T^*/T_K=0.2/6 =0.03 for $CeCu_6$ and 8/12=0.67 for $CeRu_2Si_2$. Furthermore T^* decreases to 0.08 K in $Ce_{0.75}La_{0.25}Cu_6$ [1]. These results show that the energy scale T_K is not sufficient to describe the heavy-electron systems. It should also be specified by the coherence temperature, or the effective Fermi temperature, T^* below which heavy-electron bands are formed. In contrast to the universal behavior of the Kondo impurity, the dispersion relations of heavy quasi-particles depend on materials.

Decline of the heavy electron state with the increasing field was also probed by the T_1 measurement of Ru in the field range 0−15.5 T [14]. As shown in Fig.3.4(a), the behavior T_1T=const is not observed down to 1.6 K around H_c. This means that the effective Fermi temperature, T^* around H_c is much lower than that at $H < H_c$; $T^* \sim 8$ K. By contrast, as the field increases more than H_c, $(T_1T)^{-1}$ begins to decrease as indicated in Fig.3.4(b). Then, the T_1T=const behavior is observed only below ∼4 K at 15.5 T.

3.1.3 Neutron scattering on $CeCu_6$ and $CeRu_2Si_2$

Neutron scattering can extract information on the single-site fluctuations and intersite magnetic correlations separately by scanning the wave-number and energy. Inelastic neutron scattering experiments have been performed on single crystals of $CeRu_2Si_2$ and $CeCu_6$. At high temperatures, magnetic scattering can be described by a single quasi-elastic Lorentzian peak corresponding to eq.(2.128). With decreasing temperatures, antiferro and incommensurate magnetic correlations develop below 70 K in $CeRu_2Si_2$ and 10 K in $CeCu_6$.

An inelastic scattering study with applied magnetic field has shown that the pseudo-metamagnetic transition corresponds to the collapse of the incommensurate magnetic correlation. As shown in Fig.3.5 [7], magnetic scattering at incommensurate wave vector $\boldsymbol{Q}$=(0.7, 0.7, 0) and energy transfer $\hbar\omega = 1.6$ meV decreases slightly for field up to H=70 kOe, but more rapidly at higher field. The inflection point for a decrease of the neutron intensity corresponds to the threshold field H_c=83 kOe at 1.4 K in good agreement with magnetization experiment (see Fig.3.1). At H=98 kOe, it is found that the magnetic scattering does not exhibit any $\boldsymbol{q}$-dependence, and the spectrum is quite similar to that observed at $\boldsymbol{Q}$=(0.9, 0.9, 0) which is in between the intensity maximum. The latter spectrum represents the single-site contribution in zero field (see Fig.3.7). Namely, the single-site contribution of quasi-elastic type is not affected by a magnetic field of 98 kOe which exceeds H_c of the pseudo-metamagnetic transition. On the other hand the intersite contribution of inelastic-type is completely suppressed as seen clearly in the energy scans in Fig.3.6.

A similar feature was also observed in $CeCu_6$ at H_c=25 kOe, although only a small anomaly appears in dM/dH [9]. This is probably because the weight of the intersite contribution relative to the single-site contribution is much smaller in $CeCu_6$ than in $CeRu_2Si_2$. In both cases the Zeeman energy $\mu_B H_c$ corresponding to the critical field H_c is of the order of $\hbar\omega_0$ which is the peak energy of the inelastic neutron scattering spectrum. The finite energy $\hbar\omega_0$ suggests the presence of a pseudo gap in the magnetic excitation spectrum. In this case the correlation length naturally saturates when the temperature or the Zeeman energy becomes of the order of the pseudo gap.

Figure 3.7 shows typical $\boldsymbol{q}$-scan spectra for $CeRu_2Si_2$ obtained at 4.2 K with an energy transfer $\hbar\omega$=1.6 meV [7]. In this subsection we take the unit of the wave number as π/ℓ with ℓ the lattice constant along each principal direction. The peak of intensity at incommensurate wave vectors $\boldsymbol{k}_1 = (0.3, 0, 0)$ and $\boldsymbol{k}_2 = (0.3, 0.3, 0)$ indicates the presence of competing in-plane couplings between first and second nearest

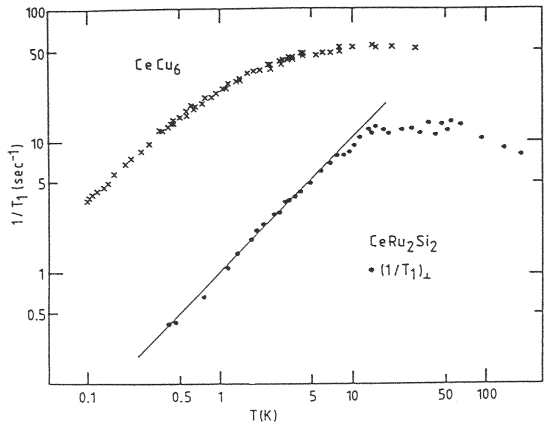

Figure 3.2: Temperature dependence of $(1/T_1)$ of ^{63}Cu in $CeCu_6(\times)$ and ^{29}Si in $CeRu_2Si_2(\bullet)$ [6].

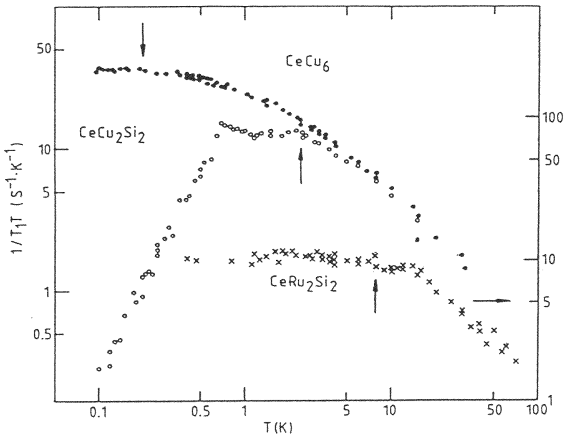

Figure 3.3: Temperature dependence of $1/(T_1T)$ of ^{63}Cu in $CeCu_6(\bullet)$ and $CeCu_2Si_2(\bigcirc)$ and ^{29}Si in $CeRu_2Si_2(\times)$ [6].

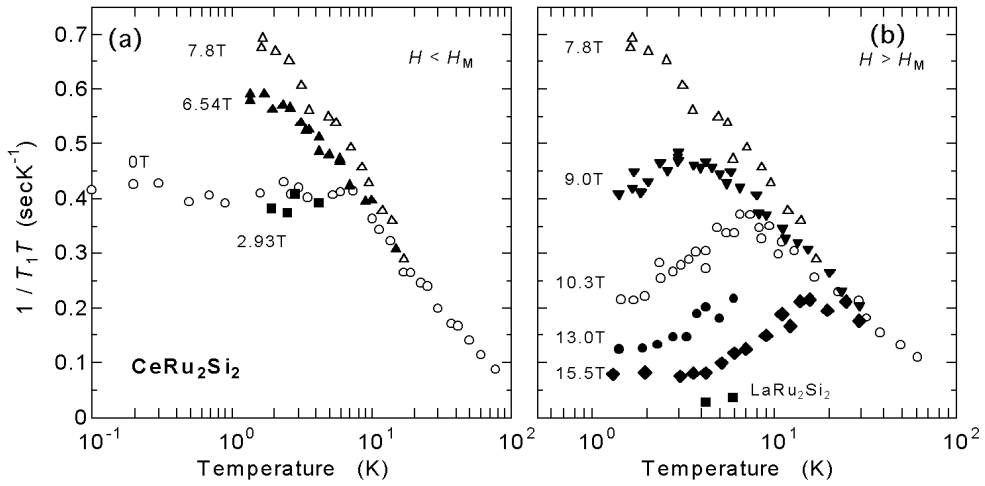

Figure 3.4: Temperature dependence of $(T_1T)^{-1}$ of Ru in $CeRu_2Si_2$ at various fields H: (a) $H \leq H_M =$ 7.8 T; (b) $H \geq H_M$ [14].

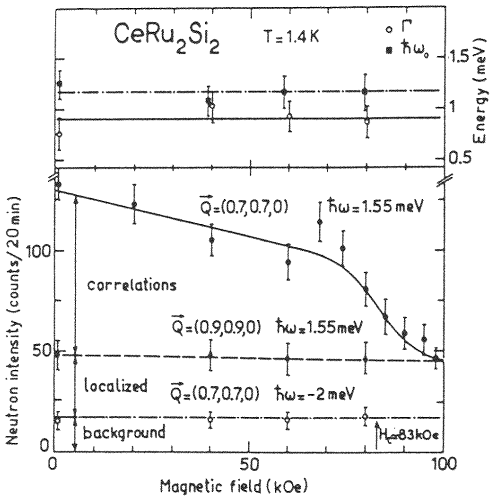

Figure 3.5: Scattered neutron intensities at 1.4 K as a function of magnetic field applied along [001] direction for $CeRu_2Si_2$; they correspond to the peak maximum at $\boldsymbol{Q} = (0.7, 0.7, 0)$ with $\hbar\omega$=1.6 meV, intensity in between the peaks at $\boldsymbol{Q}$=(0.9, 0.9, 0) with $\hbar\omega$=1.6 meV, and the background intensity at $\boldsymbol{Q}$=(0.7, 0.7, 0) with $\hbar\omega = -$ 2 meV [7].

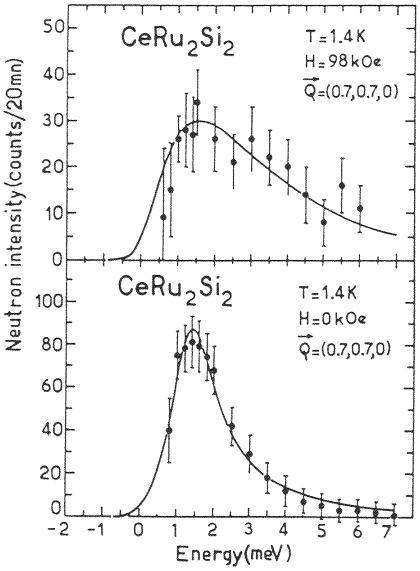

Figure 3.6: Typical fits of energy scans at $\boldsymbol{Q}$=(0.7, 0.7, 0) and T=1.4 K showing the quasi-elastic contribution (H= 98 kOe) and the intersite inelastic contribution (H=0) for $CeRu_2Si_2$ [7].

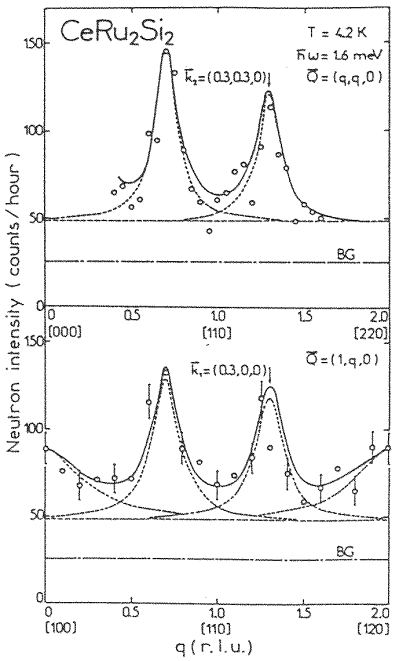

Figure 3.7: $\boldsymbol{q}$ scans at a finite energy transfer $\hbar\omega$ = 1.6 meV along the directions [110] and [010] at T=4.2 K for $CeRu_2Si_2$, showing the two incommensurate wave vectors $\boldsymbol{k}_1$=(0.3,0,0) and $\boldsymbol{k}_2$=(0.3,0.3,0) [7].

neighbors. In addition, there is a significant q independent contribution. In these two compounds, both the single-site and the intersite magnetic correlations seem to coexist at low temperatures. The former contribution represents about 60 % for $CeRu_2Si_2$ and 90 % for $CeCu_6$ of the weight of the signal integrated over the whole q-space. As shown in Fig.3.8 for $CeCu_6$, the magnetic scattering becomes independent of T below T^*. This indicates saturation of the in-plane correlation length. From the energy

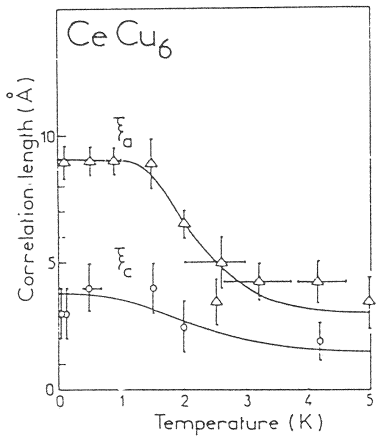

Figure 3.8: Magnetic correlation lengths along the a- and c-directions as a function of temperature for $CeCu_6$ [7].

scans performed for various scattering vectors $\boldsymbol{Q}$, the single- and inter-site contributions are analyzed separately. The single-site contribution can be described by a quasi-elastic Lorentzian, the width Γ_{s-s} of which is 2.0 meV for $CeRu_2Si_2$ and 0.42 meV for $CeCu_6$. These values lead to the Kondo temperature T_K=23 K for $CeRu_2Si_2$ and 5 K for $CeCu_6$. The magnitudes of T_K so determined are compatible with those determined by the coefficient γ of the linear specific heat. For γT_K both compounds possess comparable values $\gamma T_K \sim$ 8000mJ/(mole K). This fact suggests that single-site fluctuations give the main contribution to γ. On the other hand, intersite magnetic fluctuations give rise to a broad inelastic spectrum centered at $\hbar\omega_0 = 1.2$ meV with width $\Gamma_{i-s} = 0.9$ meV for $CeRu_2Si_2$, and at 0.2 meV with width 0.21 meV for $CeCu_6$. Apparently, there exist two energy scales Γ_{s-s} and Γ_{i-s} in the non-magnetic heavy-electron state. Of these, Γ_{s-s} is related to single-site fluctuation with the energy scale comparable to T_K, and $\hbar\omega_0 \sim \Gamma_{i-s}$ reflects the intersite interaction. Without the intersite interaction $\hbar\omega_0$ should tend to zero.

Fig.3.9 represents the temperature dependence of the line width Γ_{s-s} and Γ_{i-s} for $CeCu_6$. Together with the result of the correlation length shown in Fig.3.8, three regimes are identified:

1. The low-temperature regime $T < T_l$ where T_l is $1 - 1.5$ K for $CeCu_6$ and $5 - 6$ K for $CeRu_2Si_2$. The correlation length and the line-widths are independent of T, with the former being about the distance of second nearest neighbors. The magnitude of T_l in $CeCu_6$ is much larger than the coherent temperature $T^* \sim 0.2$ K which is deduced from the temperature dependence of $1/T_1$. On the other hand T_l in $CeRu_2Si_2$ is comparable to $T^* \sim 6$ K determined by the NMR.

2. The intermediate regime with $T_l < T < T_m$ where T_m=3 K for $CeCu_6$ and $10 \sim 15$ K for $CeRu_2Si_2$. The correlation lengths decrease with T and the line-width Γ_{i-s} of the intersite contribution increases rapidly with T. As a result we have $\Gamma_{i-s} \simeq \Gamma_{s-s}$ above T_m. The Fermi liquid description breaks down in this temperature range.

3. The high-temperature regime $T > T_m$ where the intersite magnetic correlations collapse and the single-site fluctuations prevail. The system in this range looks very similar to the dilute Kondo system.

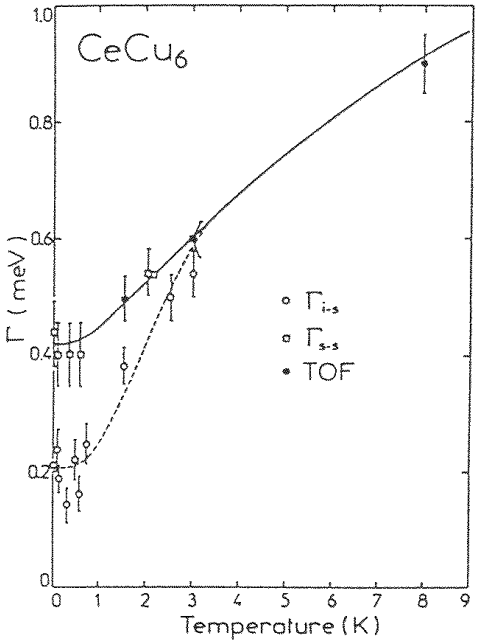

Figure 3.9: Temperature dependence of the line-widths, deduced from energy scans for the single-site (Γ_{s-s}) and the inter-site (Γ_{i-s}) contributions for $CeCu_6$ [7].

3.1.4 UBe_{13} and UPt_3

UBe_{13}, which undergoes superconducting transition at $T_c = 0.9$ K, takes a cubic crystal structure with 8 formula units per unit cell. The U-U distance equals 5.13 Åwhich is much too large for direct overlap of 5f wave functions from adjacent U atoms. Macroscopic physical properties of UBe_{13} are quite unusual. Figure 3.10 shows [15] the electrical resistivity together with that of other systems, scaled to the same value at room temperature, and specific heat. The resistivity increases with decreasing temperature from room temperature down to 2.4 K where a well-defined peak appears. The resistivity just above T_c is larger than $100\mu\Omega$·cm. The magnetic susceptibility χ at high temperature is large and obeys the Curie-Weiss law with μ_{eff}= 3.1 μ_B. With decreasing T, χ tends to a large value. The specific heat coefficient γ increases upon cooling below 10 K, as shown in Fig.3.10(b). It is only below $\sim$ 1. 5 K that T_1T becomes almost constant [17]. The large anomaly of specific heat at T_c indicates that the Cooper pairs consist of heavy electrons. We discuss anomalous superconducting properties of UBe_{13} in Chapter 5.

Properties of UPt_3 are in contrast with those of UBe_{13} in a number of ways. The crystal has the hexagonal structure with the U-U distance 4.1 Å. The electrical resistivity is large ($\sim 100\mu\Omega$) at room temperature, but decreases upon cooling as in ordinary metals. At high temperature, the Curie-Weiss law with $\mu_{eff} = 2.6\mu_B$ is observed with large anisotropy in χ. Namely with H in the basal plane, χ at low temperatures is twice of that with H along the c axis. Although there is a peak in χ at 14 K, no specific heat anomaly is observed.

At temperatures lower than 14 K, neutron scattering probed unusual magnetic correlations. There are three different modes of the magnetic correlations with the propagation vectors $\mathbf{Q}$=(0.5, 0, 1), (0, 0, 0), and (0, 0, 1) in units of the primitive reciprocal lattice vectors. The (0,0,1) mode begins to develop below $\sim$ 14 K [19], and is observed at high-energy transfer more than 5 meV. The mode has an out-of-plane antiferromagnetic polarization. At low energy there is another (0,0,0) mode which is interpreted in terms of paramagnons, or particle-hole excitations of heavy quasi-particles [20]. This "slow" quasi-particle component of the spin relaxation process is similar to what has been identified in other systems such as liquid ^{3}He [21], paramagnetic 3$d$transition metals with strongly enhanced susceptibilities and weak ferromagnetic 3$d$metals with small spin polarizations. These behaviors in the normal state are

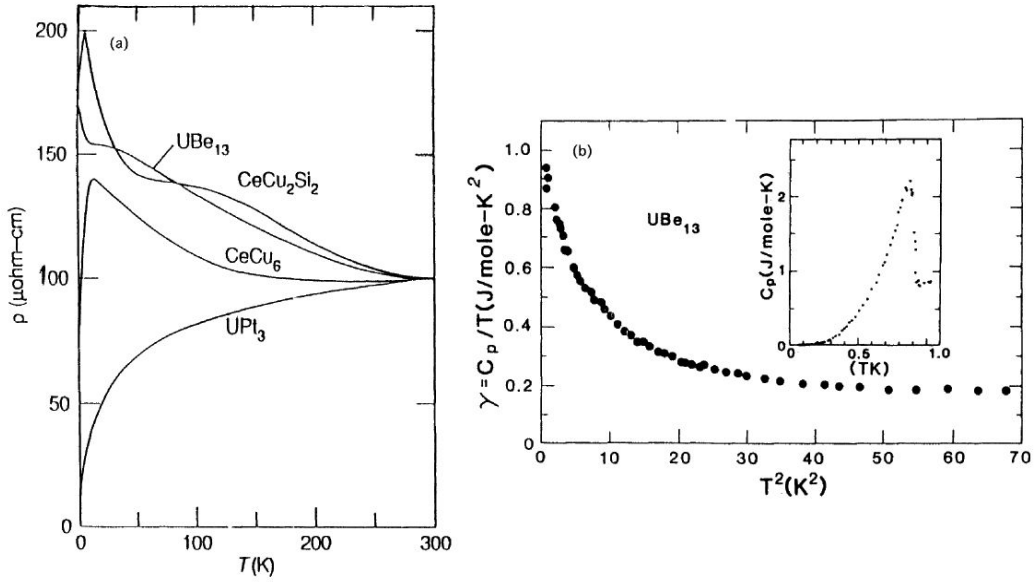

Figure 3.10: (a) The resistivity versus temperature for UBe_{13} together with that of other compounds. Note that resistivities at room temperature have been normalized to the same value as that of UBe_{13} [15]. (b) The specific heat C_p of UBe_{13} divided by temperature in the normal state [16]. The inset shows the specific heat near the transition temperature T_c of superconductivity.

consistent with the itinerant model of f electrons. In UPt_3, however, there is also a "fast" contribution with a weakly q-dependent characteristic frequency. The "slow" component in Im $\chi(q,\omega)$ accounts for about 20% of the total static susceptibility [20] according to the Kramers-Kronig relation. This contrasts with the result in $3d$ transition metals where a well defined quasi-particle contribution to Im $\chi(q,\omega)$ accounts for the total static susceptibility in the limit $q \to 0$. This difference between UPt_3 and $3d$ systems may be ascribed in part to larger strength of the spin-orbit interaction as well as stronger tendency to localization in $5f$ systems. The paramagnon mode may mediate the triplet pairing in UPt_3 as discussed in Chapter 5.

We turn to unusual behavior of antiferromagnetism at $Q = (0.5, 0, 1)$. It was reported by means of neutron scattering [22] that UPt_3 has antiferromagnetic order below 5 K. However the spin correlation length remains finite with $85 \sim 500$ Ådown to 100 mK. No trace of the magnetic transition was reported in the specific heat [23], the static susceptibility [24], and the Knight shift [25] down to 100 mK. With further decreasing temperature, however, neutron scattering [26] and specific heat [27] measurements suggest onset of the long-range order below 20 mK. If this is true, the "quasi-ordering" below 5 K is characterized by a time scale much larger than that of neutrons (typically 10^{-12}s), but much shorter than that detected by NMR (typically $10^{-6} \sim 10^{-8}$s). What is unusual is the spin correlation length of about 300 Åwhich is much longer than that in typical magnetic systems above the magnetic transition. Origin of these unconventional magnetic correlations is not understood yet. Relationship of the quasi-ordering to superconductivity is discussed in Chapter 5.

3.2 Semiconducting and Semimetallic Phases of Heavy Electrons

3.2.1 SmB_6

There is a class of materials called Kondo semiconductors which are characterized by a small energy gap in the electronic excitation spectrum at low temperatures. In SmB_6 and YbB_{12}, the energy gap amounts to 50-100 K as identified by the exponential increase of the resistivity and T_1, or by optical mea-

surements. In contrast with usual semiconductors, the magnetic response of the Kondo semiconductors shows unexpected complexity. A typical example is SmB_6 which is a mixed-valence or valence fluctuating compound with average valency of $Sm^{+2.56}$. In this system, it is established that the two configurations, $|4f^6\rangle$ and $|4f^5 5d\rangle$ of Sm are mixed in the ground state as a result of hybridization. Figure 3.11 shows a set of magnetic neutron scattering spectra obtained at 1.8 K. The $\boldsymbol{Q}$-vectors point to different directions with respect to the crystal axes, but have the same magnitude $|\boldsymbol{Q}| = 1.5\mathring{A}^{-1}$ [28].

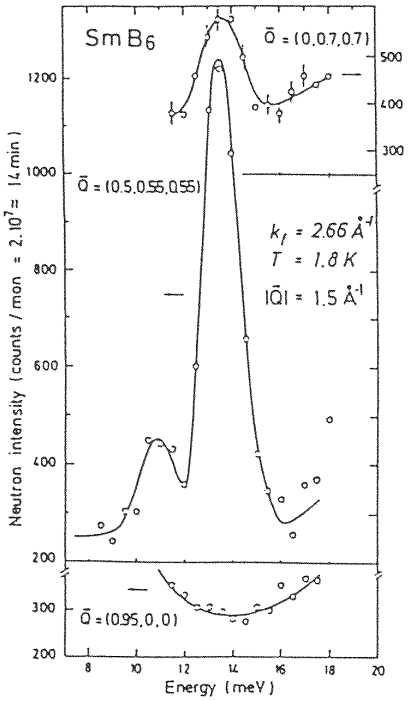

Figure 3.11: Low temperature (T=1.8 K) energy spectra of SmB_6 for three different $\boldsymbol{Q}$ values having identical $|\boldsymbol{Q}|$=1.5 Å^{-1} [28].

A sharp peak appears in the spectrum at $\hbar\omega$=14 meV and $\boldsymbol{Q}$=(0.5, 0.55, 0.5) in units of the primary reciprocal lattice vectors. In the bottom of Fig.3.12, the scattering intensities are plotted for different $\boldsymbol{Q}$ (open circles in the inset). There is a substantial anisotropy that the form factor $F(\boldsymbol{Q})$ is large along the $\boldsymbol{Q}$=(1, 1, 1) direction, whereas it is markedly reduced along $\boldsymbol{Q}$=(0, 1, 1) and vanishes along $\boldsymbol{Q}$=(1, 0, 0). Furthermore, the intensity is unexpectedly reduced with increasing $|\boldsymbol{Q}|$ along the direction $\boldsymbol{Q} = (0.5, q, q)$, which is incompatible with any plausible Sm^{2+} form factor as indicated by dash-dot line in the upper part of Fig.3.12. These features of the magnetic excitation at $\hbar\omega$=14 meV were ascribed to the $4f^5 5d$ component of the mixed-valence state.

An excitonic bound state has been invoked to explain the spectrum [28]. According to this model, electrons in the $4f$ orbital are strongly coupled with holes in the six $5d$ orbitals of the neighboring Sm sites. Then the ground state has bound states analogous to excitons. The inelastic feature observed at low T corresponds to breakup of excitons. As shown in Fig.3.13, the inelastic intensity rapidly falls off in a temperature range of around 20-40 K, which is comparable to the electronic gap Δ. This decrease may indicate that the excitonic bound state becomes unstable by thermal population of itinerant d-band states.

3.2.2 CeNiSn and CeRhSb

CeNiSn and CeRhSb crystallize in the orthorhombic ϵ-TiNiSi type structure, and have a very small pseudo energy gap of a few Kelvin. The magnetic susceptibility, the resistivity and the thermoelectric power have peaks around $T_{coh} \sim$ 12-20 K. These peaks are ascribed to the formation of heavy-electron state and simultaneous development of antiferromagnetic correlations. The transport properties are not

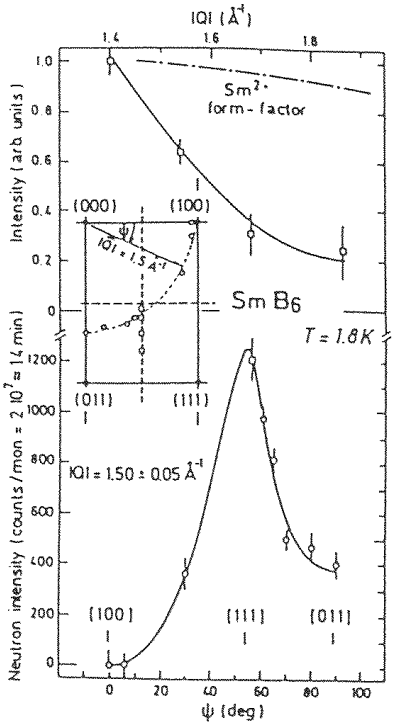

Figure 3.12: Radial (upper part) and angular (lower part) variations of magnetic scattering intensity associated with the peak at $\hbar\omega_2 \simeq 14$ meV in SmB_6; inset shows trajectories within (011) scattering plane corresponding to these plots [28].

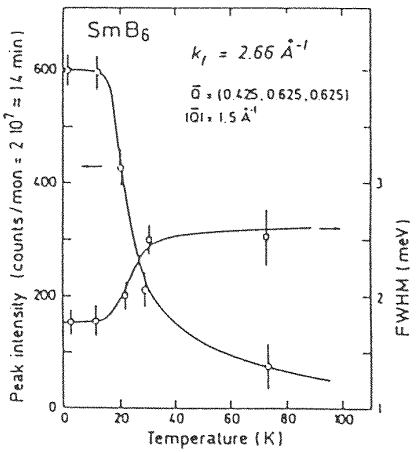

Figure 3.13: Temperature dependence of neutron intensity and line-width of the magnetic peak at $\hbar\omega_2 \simeq 14$ meV in SmB_6 [28].

like a semiconductor, but metallic along all crystal directions [29]. From the temperature dependence of $1/T_1$ of ^{118}Sn and ^{123}Sb in CeNiSn and CeRhSb, the presence of a pseudo energy gap is suggested in the spin excitation spectrum. However the density of states at the Fermi level is finite as shown in Fig.3.14. The T dependence of $1/T_1$ is well reproduced by the effective density of states $N_{eff}(E)$ modeled with a V-shaped structure [30]. for the quasi-particle bands as illustrated in the inset of Fig.3.14. The presence of the tiny density of states at the Fermi level is consistent with a semimetal with very low carrier density. In comparison with the isotropic gap in SmB_6, the pseudo energy gap with a few Kelvin seems to be anisotropic as judged from the temperature dependence of the resistivity. These correlated semimetals exhibit interesting behavior that the pseudo gap of the charge response is larger than that of the spin response.

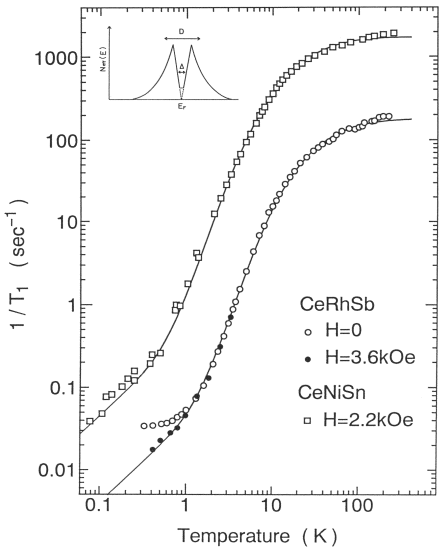

Figure 3.14: Temperature dependence of $1/T_1$ for ^{119}Sn in CeNiSn and ^{123}Sb in CeRhSb. Inset illustrates the effective density of states $N_{eff}(E)$ modeled with a V-shaped structure with a finite value near the Fermi level [30].

From the next section, we turn to theoretical consideration how to understand the metallic and insulating characteristics of heavy electrons.

3.3 Momentum Distribution and the Fermi Surface

However strong the correlation effect, there is a one-to-one correspondence between a quasi-particle state and a noninteracting counterpart provided that the Fermi liquid is realized. If a single-particle state in the free system is occupied, the corresponding quasi-particle state is also occupied. From this it follows that the Fermi surface of quasi-particles encloses the same volume (Fermi volume) in the Brillouin zone as that of free electrons. This property is often referred to as the Luttinger sum rule. We sketch a mathematical proof of the sum rule in Appendix G. In this section we show that the momentum distribution of bare electrons in strongly correlated metals is much different from that of quasi-particles. The global distribution is rather similar to the case of localized electrons. This feature of heavy electrons is important in understanding consistency between various experiments with different energy resolutions.

Let us first consider a trivial case where the system consists of monovalent atoms with a single atom in the unit cell of the lattice. The Fermi volume is half the volume of the Brillouin zone in an ordinary metal. We ask what happens in the case of heavy electrons. If f electrons participate in forming the quasi-particles, the Fermi volume is determined by the total number of electrons including the f electrons. If f electrons are localized, on the contrary, only the conduction electrons contribute to the Fermi volume. Thus information on the size of the Fermi surface gives an important hint on the nature of heavy electrons.

The standard model for investigating heavy electrons is the Anderson lattice. The model is characterized by a periodic arrangement of f electron sites and is given by

$$H_{AL} = \sum_{\boldsymbol{k}\sigma} \left[\epsilon_{\boldsymbol{k}} c^{\dagger}_{\boldsymbol{k}\sigma} c_{\boldsymbol{k}\sigma} + V_{\boldsymbol{k}} (c^{\dagger}_{\boldsymbol{k}\sigma} f_{\boldsymbol{k}\sigma} + f^{\dagger}_{\boldsymbol{k}\sigma} c_{\boldsymbol{k}\sigma}) \right] + \sum_{i} \left[\epsilon_f \sum_{\sigma} f^{\dagger}_{i\sigma} f_{i\sigma} + U f^{\dagger}_{i\uparrow} f^{\dagger}_{i\downarrow} f_{i\downarrow} f_{i\uparrow} \right] \tag{3.1}$$

where $f_{\boldsymbol{k}_\sigma}$ is the annihilation operator of an f electron with momentum $\boldsymbol{k}$ and spin σ, and $f_{i\sigma}$ is the one localized at site i. In the trivial case with $U = 0$, the model can be solved easily and gives two hybridized bands. If the total number N_e of electrons is twice the number N_L of lattice sites, the system becomes an insulator since each $\boldsymbol{k}$ state can accommodate two electrons with up and down spins. Otherwise the Fermi level is somewhere inside the band, and the system becomes metallic. If perturbation theory with respect to U is valid, the area of the Fermi surface must remain the same as U increases. This adiabatic continuity of the states with respect to U is precisely the condition for the validity of the Fermi liquid theory.

In order to clarify the peculiarity of the momentum distribution in heavy-electron systems, we first consider a one-dimensional system and assume the presence of large Coulomb repulsion U. Precisely speaking, the Fermi liquid is unstable in one dimension against formation of the Tomonaga-Luttinger liquid state [31, 32]. We neglect this aspect here because we are interested mainly in the size of the Fermi surface, the location of which is common to that in the Tomonaga-Luttinger liquid. Let us assume for definiteness a particular case where the total number N_e of electrons is $7/4$ times the number N_L of lattice sites. If the f electrons are itinerant, the Fermi momentum is $7\pi/(8a)$, and the lower hybridized band is partially occupied. Here a is the lattice constant. The upper hybridized band is empty. On the other hand, if there is no hybridization nor magnetic ordering in the f electrons, the number of f electrons per site is unity. Then the momentum distributions n^c_k, n^f_k for conduction and f electrons, respectively, become like the ones shown by the dashed line in Fig.3.15. The Fermi surface of conduction electrons is

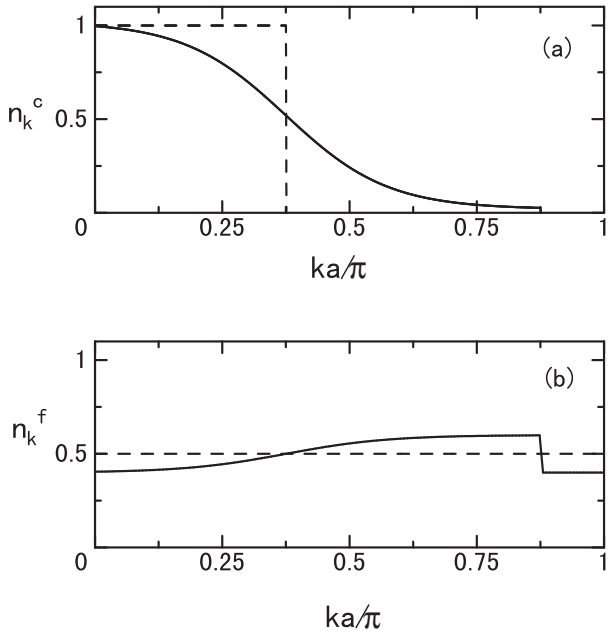

Figure 3.15: Schematic view of the momentum distributions of (a) c electrons, and (b) f electrons.

at $k = 3\pi/(8a)$ without hybridization. The number N_c of conduction electrons is equal to $3N_L/4$. With large U and small hybridization, the momentum distribution becomes like the one schematically shown by the solid line in Fig.3.15. Globally the distribution is not very different from the case of localized f electrons. But the location of the Fermi momentum is the same as the case with $U = 0$. We note that the k-dependence of the f electron distribution means the presence of charge fluctuations. To see this we note that in the case of a pair of Kondo impurities the momentum dependence corresponds to the even-odd splitting of molecular orbitals.

We give a simple example of a variational wave function for the itinerant case. Namely we consider Ψ_B given by [33]

$$\Psi_B = \mathcal{P}\prod_{k\sigma}(1+\alpha_k f^\dagger_{k\sigma}c_{k\sigma})\phi_{N_e} = \mathcal{P}\exp\left(\sum_{k\sigma}\alpha_k f^\dagger_{k\sigma}c_{k\sigma}\right)\phi_{N_e}, \tag{3.2}$$

where ϕ_{N_e} represents the wave function of N_e conduction electrons and vacant f orbitals. The operator $\mathcal{P}$ is a projection operator to exclude double occupation of f electrons at any site, and is often called the Gutzwiller projection. The variational parameter α_k should be optimized so as to minimize the energy. In the case of large U, numerical integration with use of Monte Carlo sampling [34] yields a momentum distribution similar to the solid line in Fig.3.15. If α_k is large compared with unity, each site has almost one f electron. Then the discontinuity in n^f_k at the Fermi surface becomes small, but the location remains the same. In the case of $N_e/N_L = 7/4$, the location of the Fermi surface is at $k = 7\pi/(8a)$ which is called "the large Fermi surface". Here N_e determines the location. We note that a significant but smooth change of n^k_c appears at the position of "the small Fermi surface", which is determined only by N_c, as shown in Fig.3.15(a). The smooth change in n^c_k takes advantage of hybridization. A very simple description of quasi-particles with the large Fermi surface is provided by a mean-field theory. This is sometimes called the renormalized band picture [35] which contains a parameter to describe reduction of hybridization and another to describe the shift in the f electron level. The parameters are optimized by the same procedure as in the case of the impurity Anderson model.

In the particular case where $N_e = 2N_L$, Ψ_B corresponds to a state where the electrons fill completely the lower hybridized band. In this case the Fermi surface is absent and the system becomes an insulator at absolute zero. This state goes continuously to the usual band insulator as U decreases. In the opposite case of large U, however, the magnetic and dielectric properties of the system reflect the effect of strong correlation. This should be evident if one considers the high temperature regime where the localized picture becomes better than the band picture. The system in the large U limit is called the Kondo insulator.

Let us come back to the metallic case with U and $|\epsilon_f|$ large as compared with $V^2\rho_c$. Then the ground state has almost unit occupation of f electrons at each site. The effective model excluding the empty and doubly occupied f sites is given by

$$H_{KL} = \sum_{\boldsymbol{k}\sigma}\epsilon_{\boldsymbol{k}}c^\dagger_{\boldsymbol{k}\sigma}c_{\boldsymbol{k}\sigma} + J\sum_i \boldsymbol{S}_i\cdot\boldsymbol{s}_i, \tag{3.3}$$

where $\boldsymbol{S}_i$ is the spin operator of f electrons, and $\boldsymbol{s}_i$ of conduction electrons at site i. The latter is given by

$$\boldsymbol{s}_i = \frac{1}{2N}\sum_{\boldsymbol{kp}}\sum_{\alpha\beta}c^\dagger_{\boldsymbol{k}\alpha}\boldsymbol{\sigma}_{\alpha\beta}c_{\boldsymbol{p}\beta}\exp[-i(\boldsymbol{k}-\boldsymbol{p})\cdot\boldsymbol{R}_i]. \tag{3.4}$$

The model (3.3) is referred to as the Kondo lattice. Various numerical results show that the location of the Fermi surface in the Kondo lattice is the same as the Anderson lattice with the same number of total electrons [42]. Thus the electronic state is continuously connected even though the charge fluctuations of f electrons become infinitesimal. This situation is analogous to the single-impurity case where the Kondo model without the charge fluctuation has the same fixed point as the Anderson model with $U = 0$ [38].

One might check possibility of the small Fermi surface for the Kondo lattice. With $N_c/N_L = 3/4$, for example, can the discontinuity in n^k_c occur at $k = 3\pi/(8a)$ in a paramagnetic ground state? Such ground state should be realized if the f electrons were completely decoupled from conduction electrons, and would form a spin chain in the presence of additional intersite exchange interaction. Provided that hybridization or the Kondo exchange between f and conduction electrons acts as irrelevant perturbation to this decoupled state, the perturbed ground state would still have the small Fermi surface. Such ground state is often called the doped spin liquid. This name emphasizes the difference from the Fermi liquid with a large Fermi surface. An exact analysis [39] suggests that the doped spin liquid is unlikely to be realized in one dimension; the density fluctuation has zero excitation energy at the wave number $q = 2k_F$, where k_F is the large Fermi surface including localized f electrons. This result is naturally interpreted in terms of the particle-hole excitation across the large Fermi surface, but is hard to be reconciled with the small Fermi surface. Realization of the doped spin liquid in three dimensions is even more unlikely; in higher dimensions with a large number of neighbors the localized f electrons favors a magnetically ordered ground state rather than a singlet liquid.

So far we have assumed that there is at most one f electron per site. In the case of two f electrons per site as in U^{4+}, we encounter different situation concerning the size of the Fermi surface. Namely, the size can be the same independent of whether the f electrons are itinerant or localized since the f electrons in total can fill an energy band completely. This raises an interesting question how one can distinguish between the itinerant and localized states for a system with an f^2 configuration [40]. It cannot be excluded that a band singlet state changes continuously into a localized state with the CEF singlet at each site as parameters of the system are varied [41]. The difference in the dHvA behavior, as discussed in 3.1.1, between UPt_3 and $CeRu_2Si_2$ after the pseudo-metamagnetic transition might be related to different numbers of f electrons per site.

At finite T, the discontinuity in the momentum distribution is absent. Therefore one needs a criterion other than the momentum distribution to distinguish the itinerant and localized states. There are a few experimental methods to measure the Fermi surface. The most popular is the dHvA effect. A characteristic property in some heavy electron systems is that the Fermi surface changes rapidly at a particular value of magnetic field as discussed in 3.1.1. This change, though rapid, seems to be smooth even at the lowest accessible temperature [37]. On the other hand, particular care is required if one tries to measure the Fermi surface with limited resolution, say in photoemission. The large (but smooth) change of n_k^c at $k = 3\pi/(8a)$ in Fig.3.15 might easily be mistaken for the Fermi surface.

In order to treat the correlation effects more quantitatively than presented above, an effective medium theory turns out to be useful, and will be explained below.

3.4 Dynamic Effective Field Theory

As we have seen in Chapter 2, perturbation theory from the limit of infinite degeneracy is very successful in dealing with the Kondo effect. In order to deal with the lattice of Kondo centers, which makes up the heavy-electron state, we also pursue a simplifying limit which makes the problem tractable. The proper limit in this case is the infinite spatial dimension d. The limit makes a kind of effective medium theory exact. This effective medium is not static as in the conventional mean-field theory, but dynamic. The dynamics is to be determined self-consistently [43]. Before considering the dynamic effective field theory for heavy electrons, we take the Ising model to clarify the basic idea of the effective field.

Since the following involve a little advanced mathematics, those who are interested mostly in explicit results for heavy electrons are advised to go straight to 3.6.

3.4.1 Effective field in the Ising model

In the system of Ising spins, it has long been known that one can regard the reciprocal number of neighboring spins as the expansion parameter [46]. In the case of the nearest-neighbor interaction, the number of neighboring spins increases as the dimensions of the system increase. Then the mean-field theory with use of the Weiss molecular field corresponds to the lowest-order theory, which becomes exact in infinite dimensions. In the next order, one partly includes the fluctuation of the mean field. This level of the theory is called the spherical model [46].

The ferromagnetic Ising model under a magnetic field h in the z direction can be written as

$$H = -J\sum_{\langle ij\rangle}\sigma_i\sigma_j - h\sum_i \sigma_i, \tag{3.5}$$

where $\langle ij\rangle$ are the nearest neighbor sites, $J > 0$, and the variable σ_i takes ± 1. The unit of the magnetic field is taken so that h has the dimension of energy. The molecular field h_W at a site i is defined by

$$h_W = J\sum_{j\in n(i)}\langle\sigma_j\rangle = Jz_n m \tag{3.6}$$

where $n(i)$ denote the set of nearest neighbor sites of which number is z_n, and $\langle\sigma_j\rangle = m$ is the average of σ_j to be determined later. In the d-dimensional hypercubic lattice one has $z_n = 2d$. The Hamiltonian is rewritten as

$$H = -(h_W + h)\sum_i \sigma_i - J\sum_{\langle ij\rangle}(\sigma_i - m)(\sigma_j - m) + \frac{N}{2}Jz_n m^2 \equiv H_0 + H_1 + \frac{N}{2}Jz_n m^2, \tag{3.7}$$

where N is the total number of lattice sites. The term H_0 gives the mean-field Hamiltonian, and H_1 accounts for contribution of fluctuations. If we neglect H_1, the spins under the effective field $h_W + h$ become independent of each other. Then we can easily calculate the magnetization as

$$m = \tanh[\beta(h_W + h)], \tag{3.8}$$

with $\beta = 1/T$. Together with eq.(3.6), h_W is determined self-consistently. The susceptibility $\chi = \partial m/\partial h$ in the mean-field approximation (MFA) is calculated as

$$\chi_{MFA} = \frac{\chi_0}{1 - Jz_n\chi_0}, \tag{3.9}$$

in the limit of $h_W + h \to 0$. Here $\chi_0 = \beta$ is the susceptibility of an isolated spin. The χ_{MFA} is divergent at the Curie temperature $T_c = Jz_n$.

Let us now evaluate the importance of H_1 as the perturbation Hamiltonian. The average of H_1 vanishes by the definition of m. Hence the lowest-order contribution to the free energy becomes

$$-\frac{\beta}{2}\langle H_1^2\rangle = -\frac{1}{4z_n}N\beta(Jz_n)^2\langle(\sigma_j - m)^2\rangle^2. \tag{3.10}$$

From eq.(3.8) we obtain

$$\langle(\sigma_j - m)^2\rangle^2 = \cosh^{-4}[\beta(h_W + h)]. \tag{3.11}$$

As z_n gets larger with T_c kept constant, the fluctuation contribution has the extra small factor $1/z_n$. Even in the case of $h = 0$ at $T = T_c$ where the fluctuation reaches a maximum, the contribution is $O(NT_c/z_n)$. This is smaller than the mean-field contribution by $1/z_n$. Higher order contributions have higher powers of $1/z_n$. Hence in the limit of large dimensions one can neglect deviation from the mean-field theory for all temperatures.

In the realistic case of finite d, however, the mean-field theory is only approximate. The most serious drawback is the excess counting of the exchange field. Namely a part of the mean field felt by a spin at certain site originates from this spin itself. A correction of it in dielectric media has led to the Clausius-Mossotti formula for the susceptibility. The correction includes the concept of the reaction field of Onsager[46]. We now derive the $O(1/z_n)$ correction to the susceptibility. For simplicity we consider only the paramagnetic phase with $m = h = 0$. In order to identify the $O(1/z_n)$ correction, it is convenient to introduce spinless fermion operators $f_i^\dagger$ and f_i at site i by

$$\sigma_i = 2f_i^\dagger f_i - 1. \tag{3.12}$$

The spin susceptibility in the mean-field theory corresponds to the RPA for the charge susceptibility of fermions. Some lower order corrections to the elementary bubble are shown in Fig.3.16. The set of diagrams corresponds to the irreducible susceptibility χ_1, which cannot be separated into two pieces by cutting a line representing the exchange interaction. The exact susceptibility is given by the same form

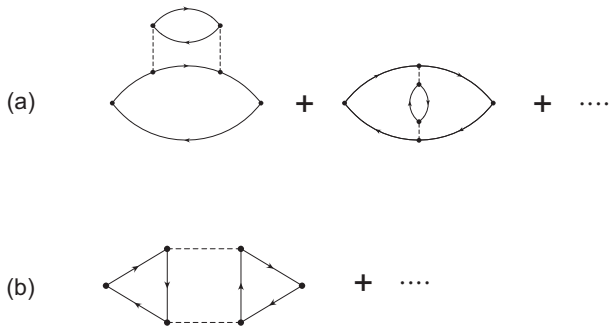

Figure 3.16: Examples of corrections to the bubble: (a) $O(1/z_n)$ corrections, (b) $O(1/z_n^2)$ corrections.

as eq.(3.9) provided the irreducible susceptibility χ_1 is used in place of χ_0. It is important to notice

that the vertex part in the lowest-order is diagonal in site indices. Thus to $O(1/z_n)$ we can regard χ_1 as site-diagonal. The fermion representation is in fact used only to show this property.

We parametrize χ_1 as

$$\chi_1^{-1} = \chi_0^{-1} + \lambda, \tag{3.13}$$

where λ represents the local-field correction. The $\boldsymbol{k}$-dependent susceptibility $\chi(\boldsymbol{k})$ is given by

$$\chi(\boldsymbol{k})^{-1} = \chi_1^{-1} - J(\boldsymbol{k}), \tag{3.14}$$

where $J(\boldsymbol{k}) = J\sum_{\boldsymbol{\delta}} \cos(\boldsymbol{k}\cdot\boldsymbol{\delta})$ is the Fourier transform of the exchange interaction with $\boldsymbol{\delta}$ pointing to each nearest-neighbor. Let us now consider the local susceptibility which is given by the $\boldsymbol{k}$-average of $\chi(\boldsymbol{k})$. The very special feature of the Ising model is that each spin is a conserved quantity independent of the exchange interaction. Then the local susceptibility is simply given by $\beta\langle\sigma_i^2\rangle = \beta$ which is the same as χ_0. Then we obtain

$$1 = \mathrm{Av}_{\boldsymbol{k}} \frac{1}{1-(J_{\boldsymbol{k}}-\lambda)\beta}, \tag{3.15}$$

which determines λ at each temperature. Equation (3.15) is known as the spherical model condition [46]. With this condition the right-hand side of eq.(3.15) without $\mathrm{Av}_{\boldsymbol{k}}$ gives $\chi(\boldsymbol{k})/\beta$. We remark the similarity of the susceptibility given by eq.(3.14) to eq.(1.107) of the mode-coupling theory of itinerant magnetism. However the different definitions of λ in these two cases should be noted. The reaction field included in the $1/z_n$ correction can also be interpreted as a mode-coupling effect.

3.4.2 Dynamic effective field for fermions

One can naturally ask whether it is possible to set up a mean field for itinerant electrons so that the theory becomes exact at $d=\infty$. Provided such a mean field is found, the problem is reduced to solving an effective single-site problem under the mean field, together with determining the mean field self-consistently. Obviously the mean field introduced in the Hartree-Fock approximation is inappropriate in this case because the number operator for each spin experiences large fluctuations.

As a preliminary to set up the mean field, we derive an important bound for the thermal Green function $g_{\boldsymbol{k}}[\tau] = -\langle \mathrm{T}_\tau c_{\boldsymbol{k}\sigma}(\tau) c^\dagger_{\boldsymbol{k}\sigma}(0)\rangle_0$ for noninteracting electrons. Let the single-particle energy $\epsilon_{\boldsymbol{k}}$ be measured from the Fermi level. By definition we have

$$g_{\boldsymbol{k}}[\tau] = \begin{cases} -[1-f(\epsilon_{\boldsymbol{k}})]\exp(-\epsilon_{\boldsymbol{k}}\tau), & (\tau>0) \\ f(\epsilon_{\boldsymbol{k}})\exp(-\epsilon_{\boldsymbol{k}}\tau), & (\tau<0). \end{cases} \tag{3.16}$$

Combining both signs of τ we obtain the bound [47]

$$|g_{\boldsymbol{k}}[\tau]| \le \frac{1}{2}\exp(\beta|\epsilon_{\boldsymbol{k}}|/2)\cosh^{-1}(\beta|\epsilon_{\boldsymbol{k}}|/2) \le 1. \tag{3.17}$$

Therefore the site representation $g_{ij}[\tau] = -\langle \mathrm{T}_\tau c_{i\sigma}(\tau) c^\dagger_{j\sigma}(0)\rangle_0$ of the Green function satisfies the inequality

$$\sum_j |g_{ij}[\tau]|^2 = \frac{1}{N}\sum_{\boldsymbol{k}} |g_{\boldsymbol{k}}[\tau]|^2 \le 1. \tag{3.18}$$

We note that the number of lattice sites N is equal to the number of wave numbers $\boldsymbol{k}$ inside the Brillouin zone. If the number of equivalent sites from a site i is z_n, the inequality leads to the upper bound for the off-diagonal element as $g_{ij}[\tau] = O(1/\sqrt{z_n})$. On the other hand, the diagonal element $g_{ii}[\tau]$ is of order unity. One can prove the same inequality for the exact Green function $G_{ij}[\tau]$ by using the spectral representation. Hence at $d=\infty$, one can neglect the off-diagonal element $G_{ij}[\tau] = -\langle \mathrm{T}_\tau c_{i\sigma}(\tau) c^\dagger_{j\sigma}(0)\rangle$ in comparison with the diagonal one. One should notice that the inequality is valid for all temperatures, and is independent of the choice of the energy scale.

Arbitrary Feynman diagram for the self-energy $\Sigma[\tau]$ has its skeleton consisting of U and $G_{ij}[\tau']$. We can now see that dominant contribution comes from $G_{ii}[\tau']$ at $d=\infty$. Thus $\Sigma[\tau]$ does not depend on k [48]. This local property of the self-energy is in common with the result of the Coherent Potential Approximation (CPA) for disordered systems without mutual interactions [49, 51]. The CPA becomes indeed exact in infinite dimensions, and the Fourier transform of $\Sigma[\tau]$ to the frequency space is called the coherent potential, which is a kind of mean field. In interacting many-body systems it is convenient to introduce the self-energy, or a related quantity $\lambda(z)$, as the dynamic mean field as we shall now explain.

Falicov-Kimball model

We explain the concept of the dynamic effective field first by taking the Falicov-Kimball model [57]. Because of the simplicity of the model, the self-consistent solution can be derived analytically. The model is given by

$$H_{FK} = -\sum_{ij} t_{ij} c_i^\dagger c_j + \sum_i \epsilon_f f_i^\dagger f_i + U \sum_i f_i^\dagger f_i c_i^\dagger c_i, \tag{3.19}$$

It is equivalent to the special case of the Hubbard model where the down-spin electrons have zero transfer and are regarded as spinless f electrons. We first derive intuitively the equation to determine the effective field. Let us look at a site $i = 0$ and remove for the moment the Coulomb repulsion U only at the site. The on-site Green function in this fictitious system $\tilde{H}$ is written as $\tilde{D}[\tau] = -\langle \mathrm{T}_\tau c_{0\sigma}(\tau) c_{0\sigma}^\dagger(0)\rangle_0$. The Fourier transform $\tilde{D}(z)$ is given by $\tilde{D}(z)^{-1} = z - \lambda(z)$ where $\lambda(z)$ accounts for the hopping motion to and from the other sites. The actual Green function $D(z)$ of H_{FK} should incorporate the effect of U at the site in the form of the self-energy $\Sigma(z)$. Then we obtain the relation

$$D(z)^{-1} = z - \lambda(z) - \Sigma(z). \tag{3.20}$$

On the other hand, $D(z)$ is also regarded as the site-diagonal element of the Green function $G_{ij}(z)$ with full inclusion of U at each site. In other words $D(z)$ is given by the momentum average of the Green function $G(\boldsymbol{k}, z) = [z - \epsilon_{\boldsymbol{k}} - \Sigma(z)]^{-1}$. Namely

$$D(z) = \mathrm{Av}_{\boldsymbol{k}} \frac{1}{z - \epsilon_{\boldsymbol{k}} - \Sigma(z)} = D_0(z - \Sigma(z)), \tag{3.21}$$

where $D_0(z)$ is the Green function with $U = 0$ at all sites. Note that the appearance of $D_0(z)$ is due to the momentum independence of the self-energy. This relation to $D_0(z)$ simplifies the calculation enormously. Figure 3.17 shows schematically the concept of the effective impurity.

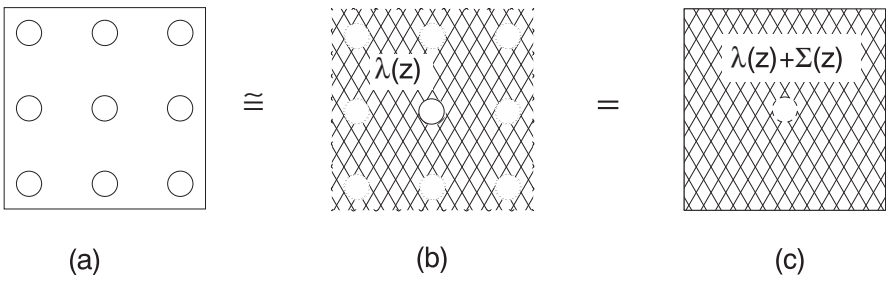

Figure 3.17: Illustration of an effective impurity and the dynamic effective field. In (b) the interaction with other sites is represented by $\lambda(z)$, and in (c) the Coulomb interaction at the impurity site is further represented by $\Sigma(z)$.

In this way we have obtained two independent relations eqs.(3.20) and (3.21) for each z among the unknowns $D(z), \lambda(z), \Sigma(z)$. This relations match the effective field and the intersite interaction. If one can solve the effective single impurity problem and can establish another relation between $D(z), \lambda(z), \Sigma(z)$, then the Green function $G(\boldsymbol{k}, z)$ can be derived explicitly.

The Falicov-Kimball model has the special feature that the f electron occupation number n_f is a constant at each site. Because of this, one can solve the effective impurity problem exactly. Namely $D(z)$ is given by

$$D(z) = \frac{1 - n_f}{z - \lambda(z)} + \frac{n_f}{z - \lambda(z) - U}, \tag{3.22}$$

The Green function for the Falicov-Kimball model is thus derived with use of eqs.(3.20), (3.21) and (3.22).

Examples of density of states often used are the Gaussian $\rho_G(\epsilon)$, the semielliptic $\rho_E(\epsilon)$, and Lorentzian $\rho_L(\epsilon)$ ones. The actual forms are given by

$$\rho_G(\epsilon) = \frac{1}{\sqrt{2\pi}\Delta} \exp[-\frac{\epsilon^2}{2\Delta^2}], \quad \rho_E(\epsilon) = \frac{1}{\pi}\sqrt{\Delta^2 - \epsilon^2}, \quad \rho_L(\epsilon) = \frac{1}{\pi} \cdot \frac{\Delta}{\epsilon^2 + \Delta^2}. \tag{3.23}$$

The Gaussian $\rho_G(\epsilon)$ is obtained by extrapolating the simple cubic lattice to $d = \infty$. The nearest neighbor hopping t is scaled so as to give $\Delta^2 = z_n t^2$ [60]. On the other hand $\rho_E(\epsilon)$ corresponds to the Bethe lattice of the Cayley tree with infinite number of nearest neighbors [61]. It is known that one can construct the single particle spectrum from arbitrary density of states [62].

As the simplest case to derive the analytic solution, we take the Lorentzian density of states $\rho_L(\epsilon)$ for the conduction band. We have $D_0(z) = (z + i\Delta)^{-1}$ with Im $z > 0$, and from comparison of eqs. (3.21) and (3.22) we obtain $\lambda(z) = -i\Delta$. Here Δ has the meaning of the half-width of the band. The Green function is given by

$$D(z) = \frac{1 - n_f}{z + i\Delta} + \frac{n_f}{z + i\Delta - U}, \tag{3.24}$$

and the self-energy by

$$\Sigma(z) = Un_f + \frac{U^2 n_f(1 - n_f)}{z + i\Delta - U(1 - n_f)}. \tag{3.25}$$

In eq(3.25) we see how the higher-order correlation modifies the MFA result given by the term Un_f.

It turns out that the self-consistency equations for $D(z)$ are the same as the one in the CPA [49, 51]. To see the origin of equivalence we may regard ϵ_f as a random variable so that the probability of having potential U for conduction electrons is given by n_f. For the Hubbard model, the CPA corresponds to an approximation called the alloy analogy [15]. Of course the alloy analogy is not exact in the Hubbard model in contrast to the Falicov-Kimball model. This is simply because the occupation number of either spin is not a constant of motion in the Hubbard model.

We comment on the stability of the solution for the Falicov-Kimball model. If the average occupation n_f is between 0 and 1, the homogeneous state corresponding to the above Green function becomes unstable at low temperatures. This instability shows up as divergence of the charge susceptibility with a certain wave number, which corresponds to a charge density wave pattern [57]. The instability inevitably arises because the entropy associated with the charge disorder is not removed in the homogeneous state even at $T = 0$.

dynamic variational principle

In the intuitive derivation above, one may wonder whether the self-energy $\Sigma(z)$ of the effective impurity is indeed the same as that of the whole system. In order to inspect the problem on a more solid basis, it is convenient to use the variational principle combined with path integral representation of the partition function Z. Instead of the Falicov-Kimball model we now take the Hubbard model as the next simplest model. In a symbolic notation, the partition function Z is represented by

$$\begin{aligned} Z &= \mathrm{Tr}\exp(-\beta H) = \int \mathcal{D}c^\dagger \mathcal{D}c \exp(-\beta \mathcal{L}), \\ \mathcal{L} &= -\mathrm{tr}(c^\dagger g^{-1} c) + H_U, \end{aligned}$$

where g^{-1} is the inverse matrix of the Green function without the interaction part H_U, and the two-component Grassmann numbers c (spin index omitted) correspond to annihilation operators of up- and down-spin electrons. The symbol tr represents the trace over sites, spins and Matsubara frequencies. The path integral representation is explained in detail in Appendices F and G. With use of the site-diagonal self-energy matrix Σ, we define the renormalized Green function matrix G by $G^{-1} = g^{-1} - \Sigma$. The unknowns Σ and G are to be optimized variationally.

According to the many-body perturbation theory [52, 53] as explained in Appendix G, the thermodynamic potential Ω of the system is given by

$$\beta\Omega = \Phi\{G\} - \mathrm{tr}(\Sigma G) - \mathrm{tr}\ln(\beta G^{-1}), \tag{3.26}$$

where $\Phi\{G\}$ satisfies the relation $\delta\Phi/\delta G = \Sigma$. Since Σ is diagonal in site indices, Φ depends actually only on D which is the site-diagonal element of G. Hence the second term in the right hand side also depends only on D. In order to exploit the situation we decompose the Lagrangian $\mathcal{L}$ as $\mathcal{L} = \mathcal{L}_G + \mathcal{L}_{\mathrm{int}}$ [54]. Here

$$\mathcal{L}_G = -\mathrm{tr}(c^\dagger G^{-1} c), \quad \mathcal{L}_{\mathrm{int}} = H_U - \mathrm{tr}(c^\dagger \Sigma c). \tag{3.27}$$

We regard $\mathcal{L}_G$ as the unperturbed Lagrangian. If one keeps this part only, the path integral leads to the third term of eq.(3.26). The sum of the first and the second terms represents the correction due to

$\mathcal{L}_{\rm int}$, which depends only on D at $d=\infty$. Hence in evaluating the interaction parts with the statistical distribution specified by $\mathcal{L}_G$, one may replace every Green function G by D. Namely we can approximate the partition function as $Z = Z_G(Z_1/Z_D)^N$ where

$$Z_G = \det(\beta G^{-1}),\ Z_D = \det(\beta D^{-1}), \tag{3.28}$$

$$Z_1 = \int \mathcal{D}c_0^\dagger \mathcal{D}c_0 \exp[\beta \sum_{n\sigma} c_{0\sigma}^\dagger (D^{-1}+\Sigma)c_{0\sigma} - \beta H_{U1}]. \tag{3.29}$$

Here Z_1 and H_{U1} stand for the single-site contribution, and the summation in eq.(3.29) is over spin states and the Matsubara frequency $i\epsilon_n$.

Evaluation of Z_1 is tantamount to solving the effective single-site problem in the presence of a dynamic external field. If one can solve the problem for arbitrary Σ, one can optimize Σ such that the thermodynamic potential $\Omega = -T\ln Z$ is minimized. Then one can get the exact solution at $d=\infty$. In reality the stationary condition instead of the minimum condition is used to obtain the self-consistency equation for the Green function. By differentiating each term constituting $-\beta\Omega = \ln Z$, we get the equation

$$\frac{1}{N}\frac{\delta \ln Z}{\delta \Sigma(i\epsilon_n)} = -D(i\epsilon_n) - D(i\epsilon_n)\frac{\delta D(i\epsilon_n)^{-1}}{\delta\Sigma(i\epsilon_n)} + G_l(i\epsilon_n)[1+\frac{\delta D(i\epsilon_n)^{-1}}{\delta\Sigma(i\epsilon_n)}], \tag{3.30}$$

where the third term in the right hand side comes from Z_1, and $G_l(i\epsilon_n)$ represents the Green function of the effective single impurity. We notice that the Green function without H_{U1} is given by $[D(i\epsilon_n)^{-1} + \Sigma(i\epsilon_n)]^{-1}$. Introducing the self-energy correction due to H_{U1} as $\Sigma_l(i\epsilon_n)$, we obtain

$$G_l(i\epsilon_n)^{-1} = D(i\epsilon_n)^{-1} + \Sigma(i\epsilon_n) - \Sigma_l(i\epsilon_n). \tag{3.31}$$

Then the stationary condition $\delta\Omega/\delta\Sigma = 0$ leads to $G_l(i\epsilon_n) = D(i\epsilon_n)$, namely $\Sigma(i\epsilon_n) = \Sigma_l(i\epsilon_n)$. Thus the relationship between $D(z)$ and $\Sigma(z)$ reproduces eq.(3.21). Note that the stationary condition is independent of the way we solve the effective single-site problem. Equation (3.21), which has been derived for the Falicov-Kimball model on intuitive grounds, is in fact valid also for the Hubbard model [58, 59]. It is also valid for the f electron Green function in the Anderson lattice model [54, 55, 56] which we now discuss.

The partition function for the Anderson lattice is given by

$$\begin{aligned} Z &= \mathrm{Tr}\exp(-\beta H_{AL}) = \int \mathcal{D}f^\dagger \mathcal{D}f \mathcal{D}c^\dagger \mathcal{D}c \exp\left(-\int_0^\beta d\tau \mathcal{L}(\tau)\right), \\ \mathcal{L} &= \sum_{k\sigma}(c_{k\sigma}^\dagger \frac{\partial}{\partial\tau} c_{k\sigma} + f_{k\sigma}^\dagger \frac{\partial}{\partial\tau} f_{k\sigma}) + H_{AL}. \end{aligned}$$

Since the Lagrangian is bilinear in $c^\dagger$ and c, the integration over them can be done explicitly. The result is

$$\begin{aligned} Z &= Z_c \int \mathcal{D}f^\dagger \mathcal{D}f \exp\left(-\int_0^\beta d\tau(\mathcal{L}_f + \mathcal{L}_{hyb})\right), \\ \mathcal{L}_f &= \sum_{i\sigma} f_{i\sigma}^\dagger \frac{\partial}{\partial\tau} f_{i\sigma} + H_f, \\ \mathcal{L}_{hyb}(\tau) &= V^2 \sum_{ij\sigma} \int_0^\beta d\tau' f_{i\sigma}^\dagger(\tau) g_{ij}(\tau-\tau') f_{j\sigma}(\tau'). \end{aligned}$$

where Z_c is the partition function of the conduction electrons without hybridization, and the hybridization is assumed to be local for simplicity.

The f electron Lagrangian obtained above is reduced to that in the Hubbard model if $\mathcal{L}_{hyb}$ is replaced by the transfer term without retardation. The presence of retardation in $\mathcal{L}_{hyb}$ makes no difference, however, in deriving the self-consistent medium. Writing the on-site Green function of f electrons as $D_f(z)$ we again introduce $\lambda(z)$ and $\Sigma_f(z)$ the former of which represents effective hopping through

hybridization, and the latter accounts for the Coulomb interaction at the site. The variational procedure gives the self consistency equation

$$D_f(z) = [z - \epsilon_f - \lambda(z) - \Sigma_f(z)]^{-1} = \frac{1}{N}\sum_{\boldsymbol{k}} \left(z - \epsilon_f - \frac{V^2}{z - \epsilon_{\boldsymbol{k}}} - \Sigma_f(z) \right)^{-1}. \tag{3.32}$$

One has to solve the effective single-impurity problem to derive $\Sigma_f(z)$ under given values of $\lambda(z)$ and U.

reduction to the Anderson impurity model

In order to solve the effective single-impurity problem in the Anderson lattice or in the Hubbard model, it is convenient to map to the single-impurity Anderson model [58]. Namely we use the spectral representation of the effective field $\lambda(z)$ as

$$\lambda(z) = \Delta\epsilon_f + \frac{1}{N}\sum_k \frac{|V_k|^2}{z - \epsilon_c(k)}, \tag{3.33}$$

where the constant part $\Delta\epsilon_f$ represents a shift in the local electron level, V_k is the effective hybridization, and $\epsilon_c(k)$ represents the spectrum of fictitious conduction electrons in the Anderson model. For a given $\lambda(z)$, V_k and $\epsilon_c(k)$ are not uniquely determined. Thus one has a freedom to choose a combination that is most convenient for the calculation.

In the case of the paramagnetic ground state, the mapping to the Anderson lattice leads to two remarkable identities related to local response functions. The first is that the Wilson ratio tends to 2 according to eq.(2.39) as the charge fluctuation is suppressed. The second is the Korringa-Shiba relation given by eq.(2.71) is valid. Note, however, that the local static susceptibility can be much different from the homogeneous susceptibility in the presence of intersite interactions. The local dynamic susceptibility, on the other hand, is directly probed by the NMR.

As the special case where the self-consistency equation is solved analytically, we take the Hubbard model at $d = \infty$ with the Lorentzian density of states for the conduction band. The center of the band is taken to be ϵ_f, namely

$$\rho_L(\epsilon) = (\Delta/\pi)[(\epsilon - \epsilon_f)^2 + \Delta^2]^{-1}.$$

To see why the analytic solution is possible in this case, we observe that eq.(3.21) leads for $\mathrm{Im}z > 0$ to

$$D(z) = [z - \epsilon_f - \Sigma(z) + i\Delta]^{-1}, \tag{3.34}$$

which takes the same form as the f electron Green function in the single-impurity Anderson model with the constant density of states ρ_c for the conduction band and hybridization V. Namely the correspondence is $\Delta = \pi V^2 \rho_c$. The resultant Anderson model in this case can be solved exactly by the Bethe Ansatz method [54]. Then one can derive thermodynamic quantities such as the susceptibility and the specific heat of the Hubbard model. Since the ground state of the Anderson model is always the Fermi liquid, the Hubbard model with the Lorentzian density of states also has a paramagnetic Fermi-liquid ground state. As U is increased the effective band-width of the Hubbard model decreases just like the Kondo temperature T_K of the Anderson model. From this solvable case one can imagine that the Hubbard model in general can have a minute structure of the density of states near the Fermi level as in the Anderson model. This structure represents formation of a narrow band with a large effective mass.

Except for this particular density of states, one must solve the effective single-impurity problem either approximately, or by numerical methods. One has to determine the effective medium self-consistently, which is usually done by iteration. Thus the numerical calculation is much more laborious than the single-impurity case. We should notice that the self-consistent solution does not necessarily correspond to the local minimum of energy, but to a stationary solution. One has to examine fluctuations around the stationary state in order to study the stability of the solution.

special situation in the half-filled case

Although the effective impurity model to be solved is the same for both Hubbard and Anderson lattice models, the most significant difference between the two models appears if the ground state is insulating. Namely the Hubbard model with one electron per site, which is conventionally referred to as the half-filled case, has the Mott insulating state explained in Chapter 1. Namely as the Coulomb interaction U

increases, the ground state of the model can change from a paramagnetic metal to an antiferromagnetic insulator with doubling of the unit cell. We note that the Mott insulating state does not always have a magnetic order. The clearest counter-example is the one-dimensional Hubbard model where the ground state in the half-filled case is a paramagnetic insulator. In the infinite-dimensional theory, however, the insulating paramagnetic state has a residual entropy since the effective impurity spin has no relaxation in the presence of an excitation gap. To improve the situation one has to include spin-fluctuation effects which enters only in finite dimensions.

In the exactly soluble case of the infinite-dimensional Hubbard model with $\rho_L(\epsilon)$, there is no metal-insulator transition even in the half-filled case with large U. The absence of the transition is connected to the divergent energy of the Lorentzian density of states:

$$\int_{-\infty}^{0} \epsilon \rho_L(\epsilon) d\epsilon = -\infty. \tag{3.35}$$

In this case the localization of electrons is energetically unfavorable. The metallic ground state corresponds to the fact that the Anderson model, which is mapped from the Hubbard model, remains a Fermi liquid even in the limit of large U.

On the other hand the insulating ground state in the Anderson lattice model connects continuously to the band insulator which does not have a residual entropy even without magnetic order. We note that the Kondo lattice model with half-filled conduction band is also connected continuously to the band insulator.

3.5 Methods for Solving the Effective Impurity Model

In this section we turn to practical ways to solve the model and corresponding results of the dynamical effective field theory. A large number of investigations have been performed particularly for the Hubbard model with use of the dynamic effective field theory. Many of them are motivated by the presence of the metal-insulator transition and deal with the half-filled case. For general filling, one has to adjust the chemical potential so as to reproduce the desired number of electrons, and the calculation becomes much more laborious. The same remark applies to the Anderson lattice model. We shall explain below various methods to solve the effective impurity model.

3.5.1 Perturbation theory with respect to the Coulomb interaction

Let us consider the half-filled case in the Hubbard model. The Hartree term shown in Fig.3.18(a) pushes up the localized level from ϵ_f to 0. A particular feature in the half-filled case is that the second-order

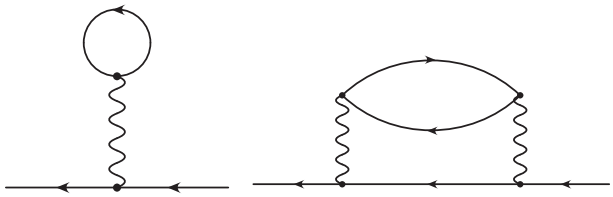

Figure 3.18: The Feynman diagrams for the self-energy: (a) the first order approximation, (b) the second-order one.

theory for the Green function fortuitously reproduces the atomic limit $\Delta/U \to 0$. In order to see this we use the Hartree result as the Green function in Fig.3.18(b): $G^{(1)}(i\epsilon_n) = (i\epsilon_n)^{-1}$. In the imaginary time domain this becomes $G^{(1)}[\tau] = -\mathrm{sign}(\tau)/2$. Hence we obtain the self-energy $\Sigma^{(2)}[\tau] = -U^2\mathrm{sign}(\tau)/8$ whose Fourier transform is $\Sigma(i\epsilon_n) = U^2/(4i\epsilon_n)$. Thus the Green function $G^{(2)}(i\epsilon_n)$ in the second approximation is given by

$$G^{(2)}(i\epsilon_n) = \frac{1}{i\epsilon_n - U^2/(4i\epsilon_n)} = \frac{1}{2}\left(\frac{1}{i\epsilon_n + U/2} + \frac{1}{i\epsilon_n - U/2}\right), \tag{3.36}$$

which actually gives the correct atomic limit [58]. If U is small, the low-order perturbation should obviously be reasonable. Thus if one uses the renormalized Green function which includes both the Hartree field and the dynamic effective field in determining the self-energy, one obtains an interpolation which reproduces both the atomic limit and the band limit. It is also known in the Anderson model [63] that the second-order self-energy constitutes a good approximation in the case of $\epsilon_f + U/2 = 0$.

We emphasize that this fortuitous situation is strictly limited to the half-filled case. In the non-half-filled case the second-order theory becomes insufficient for large U. Moreover, in order to satisfy conservation laws in response functions, it is necessary to use the Green function which includes the Coulomb interaction self-consistently[64, 65]. Unfortunately the atomic limit is then no longer reproduced even in the half-filled case.

3.5.2 Perturbation theory from the atomic limit

As we have seen in Chapter 2, the NCA gives reasonable dynamical and thermodynamical results in the case of large degeneracy for the local electron level. Thus it is also applicable to solving the effective impurity problem. The effective hybridization is determined by eq.(3.21). This scheme has first been proposed as the extended NCA (XNCA) for the Anderson lattice [67, 54, 68]. The same theory is applicable to the Hubbard model with the generalization of the NCA to the case of finite U [69, 70]. As will be shown in the next section, the numerical result for the density of states is in very good agreement with the quantum Monte Carlo simulation. Since the NCA cannot describe the Fermi liquid ground state [45], however, minute-energy excitations from the metallic ground state of the Hubbard and Anderson models cannot be discussed by the XNCA.

3.5.3 Quantum Monte Carlo method

The quantum Monte Carlo (QMC) method has been applied to the single-impurity Anderson model with an infinite number of conduction electrons, and is explained in detail in ref.[71]. The basic idea of the method is very briefly explained in Appendix G. Dynamical results such as the density of states have also been derived by combination with the maximum entropy method which effectively maps a quantity in the imaginary-time domain to real frequencies [77]. Application of the QMC to solving the effective impurity model has been made [59, 72, 73, 74, 75, 76]. The method is powerful in giving overall features at finite temperatures. There is, however, a serious technical difficulty in approaching the low energy range at low temperatures.

3.5.4 Numerical renormalization group

A powerful method complementary to the QMC is the numerical renormalization group (NRG) explained in 2.1.2. Extension of the approach to dynamical quantities has been also made [78, 79]. We refer to original articles [79, 80] on how to implement calculations for dynamics. Since the NRG is most powerful in the low-energy excitations at zero temperature, its application to the infinite dimensional model shares the same advantage. In the case of the Hubbard model at half-filling, for example, a minute energy scale analogous to the Kondo temperature has been identified near the metal-insulator transition [82].

3.6 Explicit Results by Dynamic Effective Field Theory

We show in this section some explicit numerical results for the Hubbard model and the Anderson lattice in infinite dimensions.

3.6.1 Hubbard model

The Hubbard model can teach us how the heavy energy band is formed within the single band which has both itinerant and localized characters. Figure 3.19 shows the density of states for single-particle excitations [66]. The half-filled case is shown in (I) and a doped case in (II). The Gaussian density of states is used as the noninteracting one to start with. It is remarkable that the agreement of the Monte Carlo result with the XNCA one is excellent. This is because the numerical results are for temperatures well above the critical one where the inadequacy of the NCA appears.

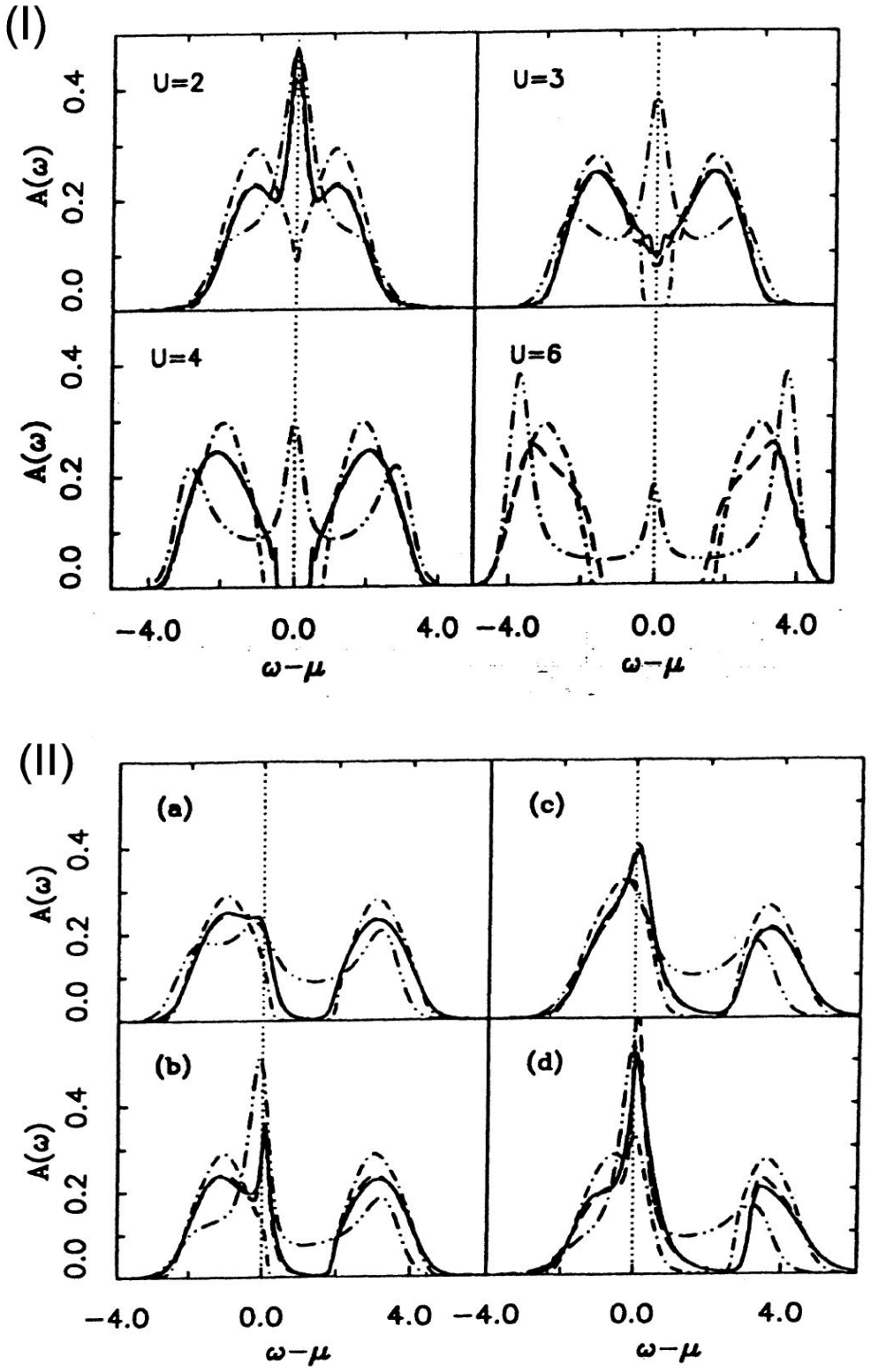

Figure 3.19: Numerical results for the density of states written as $A(\omega)$ here. The half-width Δ is taken as the unit of energy. The temperature in (I) corresponds to $\beta = 7.2$. Each line represents the following: solid line — QMC; dashed line almost overlapping with the solid line — XNCA; double-dot-dashed line — second order perturbation in U; dot-dashed line — an approximation called LNCA [81]. The temperatures in (II) are $\beta = 3.6$ in (a) and (c), while $\beta = 14.4$ in (b) and (d). The electron number per site is $n_e \sim 0.94$ in (a) and (b), while $n_e \sim 0.8$ in (c) and (d).

Figure 3.20 shows the result of the numerical renormalization group [82]. The most significant feature is the very sharp density of states. This means that the energy scale near the metal-insulator transition becomes extremely small. Such a small energy scale is hardly accessible by other methods including the quantum Monte Carlo method.

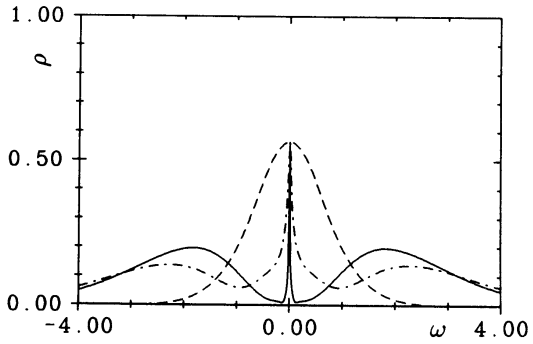

Figure 3.20: The density of states $\rho(\omega)$ calculated by the numerical renormalization group method. The half-width Δ is taken as the unit of energy. The solid line shows the result for the Hubbard model with $U = 4$, while the dashed line shows the noninteracting one ρ_0. The dot-dashed line shows the Anderson impurity with hybridization intensity corresponding to ρ_0 with $U = 4$.

Figure 3.21 shows the excitation spectra of spin and charge calculated by the numerical renormalization group [82]. These spectra correspond to the momentum average of the imaginary part of response functions. The local spin excitation spectrum is relevant to the NMR. It is evident that the characteristic energy of charge excitation is much larger than that of spin.

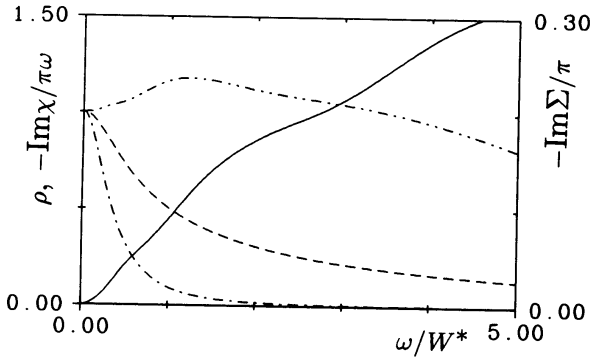

Figure 3.21: Excitation spectra computed by the numerical renormalization method. The dashed line shows ρ with the half width $W^* = 8.3 \times 10^{-3}$. The dot-dashed line shows $\mathrm{Im}\chi_s(\omega)/\omega$ representing the local spin spectrum and double-dot-dashed line does the charge one. They are normalized to unity at $\omega = 0$, and the absolute magnitude of $\mathrm{Im}\chi_s(\omega)/\omega$ is larger than $\mathrm{Im}\chi_c(\omega)/\omega$ by 10^4. The solid line shows $\mathrm{Im}\Sigma(\epsilon)$ with the scale on the right.

3.6.2 Anderson lattice

The f-electron density of states in the Anderson lattice with infinite U was computed by the use of the XNCA [68]. Figure 3.22 shows some examples of results where the f-electron level is sixfold degenerate. The parameters in the model are chosen so that the bare f-electron level is $\epsilon_f = -1500$ K, the

hybridization intensity $W_0(\epsilon)$ defined in eq.(2.41) is 135 K for $|\epsilon| < 10^4$ K and is zero otherwise. With these parameters we obtain the Kondo temperature $T_K \sim 16$ K. Here T_K is calculated from the formula

$$T_K = D\left(\frac{nW_0}{D}\right)^{1/n} \exp\left(\frac{\epsilon_f}{nW_0}\right), \tag{3.37}$$

which corresponds to the next-leading order theory in the $1/n$ expansion discussed in Chapter 2. The f-electron occupation number n_f is computed as $n_f \sim 0.91$ for $T \sim T_K$. The actual calculation was performed for the grand canonical ensemble. It is seen in Fig.3.22 that a double-peaked structure develops

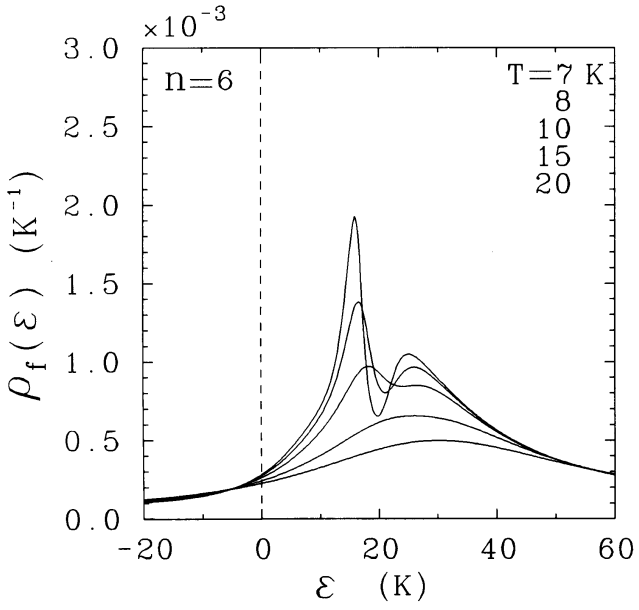

Figure 3.22: The f-electron density of states in the Anderson lattice at finite temperatures [68]. The Kondo temperature T_K is 16 K according to eq.(3.37).

in the density of states as temperature decreases below about T_K. This dip is interpreted as a remnant of the hybridization gap which would result in the case of electrons without Coulomb interaction. In this interpretation the effective f-electron level $\tilde{\epsilon}_f$ lies about 17 K above the Fermi level although the bare level ϵ_f lies deep below the Fermi level. Because of the finite life time of correlated electrons away from the Fermi level, the hybridization gap may not open completely even at $T = 0$. It should be remarked that the characteristic energy in the Anderson lattice is slightly enhanced over that of the impurity Anderson model with the same $W_0(\epsilon)$ and ϵ_f. This is judged [68] from single-particle properties such as $\tilde{\epsilon}_f$ and the renormalization factor a_f defined by eq.(2.67).

Suppose now that the Anderson lattice with a single conduction band and without orbital degeneracy of f electrons has two electrons per unit cell. According to the energy-band theory, the ground state is insulating since the lower hybridized band is completely filled and the upper one is completely empty. One can ask if the situation remains the same under a large value of U. It may happen that the system orders magnetically. In such a case the f electrons get localized and do not contribute to the band filling. For the simplest case of ferromagnetic order, the conduction band is half-filled and the system becomes metallic. In the case of antiferromagnetism with doubling of the unit cell, the ground state can be insulating. Another interesting case is when the system remains paramagnetic and can be adiabatically continued from the noninteracting limit. Then the band picture holds and the hybridization gap separates the filled and empty Bloch states.

This hybridization-gap picture is quantitatively tested by the quantum Monte Carlo simulation [83]. The result shows that although the Coulomb interaction reduces the energy gap, the hybridization gap picture is supported by the result that the spin excitation gap is twice the gap in the density of states.

With increasing temperature, however, the gap disappears in strong contrast with the noninteracting system. Thus the density of states is strongly dependent on temperature for large U.

Such an insulating ground state has also been studied by means of the numerical renormalization group [84]. The results for the density of states and dynamical susceptibilities of spin and charge are shown in Fig.3.23. We remark that the thresholds for the spin and charge excitations are the same in agreement with the band picture. However, the dominant spectral weight of the charge excitation lies in a much higher energy range than that of the spin excitation.

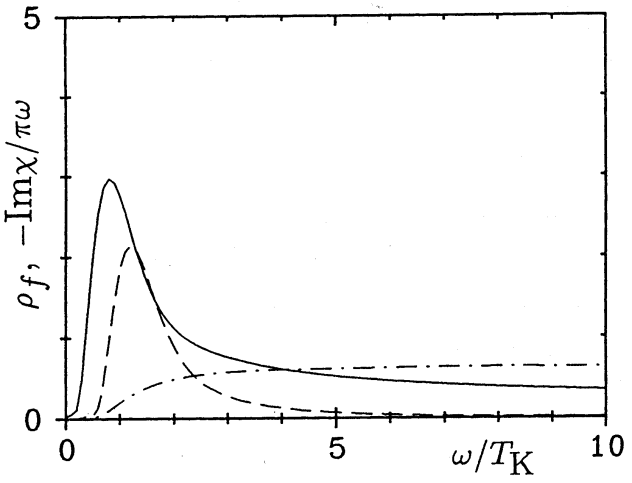

Figure 3.23: Local excitation spectra of f electrons in the Anderson lattice. The unit of energy is T_K defined from the Anderson impurity model with the same parameters. The solid line shows $\rho_f(\epsilon)$, while the dashed line does $\mathrm{Im}\chi_s(\omega)/\omega$. The dot-dashed line shows $\mathrm{Im}\chi_c(\omega)/\omega$ multiplied by $(D/T_K)^2 \sim 10^3$.

The Anderson lattice neglects the Coulomb interaction between f and conduction electrons. In the insulating state, this interaction gives rise to exciton-like correlation which is commonly observed in the optical property of semiconductors and insulators. In order to understand the experimental result on SmB_6 [28], it seems necessary to include this Coulomb interaction.

3.6.3 Limitation of the infinite dimensional model

The infinite dimensional model, which is powerful in deriving dynamical properties of heavy electrons, is by no means a complete theory. Since the intersite correlation is treated only in the mean-field level, it cannot deal with phenomena which depend on more details of correlation. For example the spin-pair singlet correlation is specific to finite dimensionality and can only be dealt with in higher order in the $1/d$ expansion. The pseudo-metamagnetic behavior in some heavy electrons, as discussed in this Chapter, also seems to require more detailed account of electron correlations than is possible in the infinite dimensional model. We shall come back to this problem in Chapter 4.

Going beyond the large d limit, however, encounters violation of the analyticity in the Green functions [50]. The same difficulty was found in the effort to improve over the CPA [51]. On the other hand, the thermodynamic quantities such as static susceptibilities do not have such problems and should be easier for the $1/d$ expansion beyond the lowest order. We note that the susceptibility of the Ising model as explained in section 3.4.1 actually includes the $1/d$ correction.

In dealing with the insulating ground state in the Hubbard model, one must be careful about the residual entropy problem. The finite entropy problem does not arise in the metallic state because the itinerant electron motion of the effective impurity removes the spin entropy as temperature decreases. On the other hand, a localized spin has a finite entropy unless it is completely polarized or fluctuates quantum mechanically. In the infinite-dimensional theory, however, the quantum fluctuation of spins is not taken into account although it does account for the quantum charge fluctuation. In other words, in the half-filled Hubbard model with charge fluctuations suppressed by large U, the entropy can vanish only

with complete polarization at each site. Thus it is not compatible with quantum magnetism where zero-point motion reduces more or less the magnitude of ordered moments, or prevents magnetic order as in one dimension. To deal with the quantum magnetism, an extension of the spherical model approximation has recently been proposed [85].

Bibliography

[1] L. Taillefer, R. Newbury, G. G. Lonzarich, Z. Fisk, J. L. Smith, J. Magn. Magn. Mater. **63& 64**, 372 (1987).

[2] G.G.Lonzarich, J. Magn. Magn. Mater. **76-77**, 1 (1988). H.Aoki, S.Uji, A.K.Albessard and Y.Onuki, J. Phys. Soc. Jpn. **62**, 3157 (1993);

[3] S.R.Julian, F.S.Tautz, G.J.McMillan and G.G.Lonzarich, Physica B **199 - 200**, 63 (1994).

[4] P.H. P. Reinders, M. Springford, P. T. Coleridge, R. Boulet, D. Ravot, Phys. Rev. Lett. bf 57, 1631 (1986).

[5] T. Oguchi and A.J. Freeman, J. Magn. Magn. Mater. **61**, 233 (1986); M.R. Norman, R.C. Albers, A.M. Boring and N.E. Christensen, Solid State Commun. **68**, 245 (1989).

[6] Nuclear Magnetic Resonance in Heavy Fermion systems: Theoretical and Experimental Aspects of Valence Fluctuations and Heavy Fermions, eds. L.C. Gupta and S.K. Malik (Plenum,1987) 297, Y. Kitaoka, K. Ueda, T. Kohara, Y. Kohori and K. Asayama.

[7] J.Rossat-Mignod, L.P.Regnault, J.L.Jacoud, C.Vettier, P.Lejay, J.Flouquet, E.Walker, D.Jaccard and A.Amato, J. Magn. Magn. Mat. **76-77**, 376 (1988).

[8] P.Haen, J.Flouquet, F.Lapierre, P.Lejay and G.Remenyi, J. Low. Tem. Phys. **67**, 391 (1987).

[9] A de Visser, J.J.M. Franse and J. Flouquet, Physic **B161**, 324 (1989) .

[10] H. Aoki, S. Uji, A.K. Albessard, and Y. Ōnuki, Phys. Rev. Lett. **71**, 2110 (1993) .

[11] H. Yamagami and A. Hasegawa, J. Phys. Soc. Jpn. **61**, 3457 (1992),625921993.

[12] I. Kouroudis et al, Phys. Rev. Lett. **58**, 820 (1987).

[13] A. Lacerda et al, Phys. Rev. B**40**, 11429 (1990).

[14] K. Ishida, Y. Kawasaki, Y. Kitaoka, K. Asayama, N. Nakamura and J. Flouquet, Phys. Rev. B **57**. R11050 (1998).

[15] Z. Fisk et al., Science **239**, 33 (1988).

[16] H. R. Ott, H. Rudigier, Z. Fisk, J. L. Smith, Phys. Rev. Lett. **50**, 1595 (1983); H. R. Ott, J. Magn. Magn. Mater. **108**, 1 (1992).

[17] D.E. MacLaughlin, J. Magn. Magn. Mater. **47&48**, 121 (1985).

[18] J.J.M. Franse, P.M. Fring, A de Visser, A. Menovsky, T.T.M. Palstra, P.H. Kess, J.A. Mydosh, Physica B**126**, 116 (1984).

[19] A.I. Goldman, G. Shirane, G. Aeppli, E. Bucher, and J. Hufnagil, Phys. Rev. B **36**, 8523 (1987).

[20] N.R. Bernhoeft and G. G. Lonzarich, J. Phys. Condens. Matter **7**, 7325 (1995).

[21] R. Scherm, K. Guckelsberger, B. Fak, K. Skold, A.J. Dianoux, H. Godfrin and W.G. Stirling, Phys. Rev. Lett. **59**, 217 (1987).

[22] G. Aeppli, E. Bocher, C. Broholm, J.K. Kjems, J. Baumann and J. Hufnagl, Phys. Rev. Lett. **60**, 615 (1988).

[23] A. de Visser, A. Menovsky and J.J.M. Franse, Physica B **147**, 81 (1987).

[24] P.H. Frings, J.J.M. Franse, F.R. de Boer and A. Menovsky, J. Magn. Magn. Mater. **31-34**, 240 (1983).

[25] H. Tou, Y. Kitaoka, K. Asayama, N. Kimura, Y. Onuki, E. Yamamoto and K. Maezawa, Phys. Rev. Lett. **77**, 1374 (1996).

[26] Y. Koike, N. Metoki, N. Kimura, E. Yamamoto, Y. Haga, Y. Onuki and K. Maezawa, J. Phys. Soc. Jpn. **67**, 1142 (1998).

[27] E. A. Schuberth, B. Strickler and K. Andres, Phys. Rev. Lett. **68**, 117 (1992).

[28] P.A. Alekseev, J.-M. Mignot, J. Rossat-Mignod, V.N. Lazukov and I.P. Sadikov, Physica **B186-188**, 384 (1993); J. Phys. Condens. Matter **7**, 289 (1995).

[29] T. Takabatake et al, Physica **B 206-207**, 804 (1995).

[30] K. Nakamura, Y. Kitaoka, K. Asayama, T. Takabatake, H. Tanaka and H. Fujii, J. Phys. Soc. Jpn. 63 (1994) 433; ibid, Phys. Rev. B **53**, 6385 (1996).

[31] S. Tomonaga, Prog. Theor. Phys. **5**, 349 (1950).

[32] F.D.M. Haldane, J. Phys. C**14**, 2585 (1981)

[33] B.H. Brandow, Phys. Rev. B**33**, 215 (1986).

[34] H. Shiba, J. Phys. Soc. Jpn. **55**, 2765 (1986).

[35] G. Zwicknagl, Adv. Phys. **41**, 203 (1992).

[36] D. Shoenberg, *Magnetic Oscillation in Metals*, (Cambridge University Press, Cambridge, 1984).

[37] T. Sakakibara, T. Tayama, K. Matsuhira, H. Mitamura, H. Amitsuka, K. Maezawa, and Y. Onuki, Phys. Rev. B**51**, 12303 (1995).

[38] P. Nozieres, J. Low Temp. Phys. **17**, 31 (1975).

[39] M. Yamanaka, M. Oshikawa and Affleck Phys. Rev. Lett. **79**, 1110 (1997).

[40] S. Watanabe and Y. Kuramoto, Z. Phys B**104**, 535-540 (1997).

[41] S. Watanabe, Y. Kuramoto, T. Nishino and N. Shibata, J. Phys. Soc. Jpn. **68**, 159-165 (1999).

[42] H. Tsunetsugu, M. Sigrist and K. Ueda, Rev. Mod. Phys. **69**, 3042 (1997).

[43] A. Georges, G. Kotliar, W. Krauth, M.J. Rozenberg, Rev. Mod. Phys. **68**, 13 (1996).

[44] K.G. Wilson, Rev. Mod. Phys. **47**, 773 (1975).

[45] N.E. Bickers, Rev. Mod. Phys. **54**, 845 (1987).

[46] R. Brout, Phys. Rev. **122**, 469 (1961).

[47] K. Miyake, private communication (1990).

[48] E. Müller-Hartmann, Z. Phys. B**74**, 507 (1989).

[49] F. Yonezawa and K. Morigaki, Suppl. Prog. Theor. Phys. **76**, 621 (1973).

[50] A. Schiller and K. Ingersent, Phys. Rev. Lett. **75**, 113 (1995).

[51] R.J. Elliott, J.A. Krumhansl and P.A. Leath, Rev. Mod. Phys. **46**, 465 (1974).

[52] J. Luttinger and J. Ward, Phys. Rev. **118**, 1417 (1960)

[53] G. Baym, Phys.Rev. **127**, 835 (1962).

[54] Y. Kuramoto and T. Watanabe, Physica **148B**, 80 (1987).

[55] V. Janis and D. Vollhardt, Int.J.Mod.Phys. **B6**, 283 (1992).

[56] F.J. Ohkawa, Phys. Rev. B**46**, 9016 (1992).

[57] U. Brandt and C. Mielsch, Z. Phys. B**75**, 365 (1989);*ibid.* **79**, 295 (1990); *ibid.* **B82**,37 (1991).

[58] A. Georges and G. Kotliar, Phys. Rev. B**45**, 6479 (1992).

[59] M. Jarrell, Phys. Rev. Lett. **69**, 168 (1992).

[60] W. Metzner and D. Vollhardt, Phys. Rev. Lett. **62**, 324 (1989).

[61] W.F. Brinkman and T.M. Rice, Phys. Rev. B**2**, 1324 (1970).

[62] B. Velicky, S. Kirkpatrick and H. Ehrenreich, Phys. Rev. **175**, 747 (1968).

[63] K. Yamada, Prog. Theor. Phys. **53**, 970 (1975).

[64] E. Müller-Hartmann, Z. Phys. B**76**, 211 (1989).

[65] D.S. Hirashima, Phys. Rev. B**47**, 15428 (1994).

[66] Th. Pruschke, D.L. Cox and M. Jarrell, Phys. Rev. B**47**, 3553 (1993).

[67] Y. Kuramoto, *Theory of Heavy Fermions and Valence Fluctuations,* edited by T. Kasuya and T. Saso (Springer Verlag, 1985), p.152.

[68] C.-I. Kim, Y. Kuramoto and T. Kasuya, J. Phys. Soc. Jpn. **59**, 2414 (1990).

[69] O. Sakai, M. Motizuki and T. Kasuya, *Core-Level Spectroscopy in Condensed Systems,* edited by J. Kanamori and A. Kotani (Springer Verlag, 1988), p.45.

[70] Th. Pruschke and N. Grewe, Z. Phys. B**74**, 439 (1989).

[71] J. Hirsch and R. Fye, Phys. Rev. Lett. **56**, 2521 (1986).

[72] X.Y. Zhang, M.J. Rozenberg and G. Kotliar, Phys. Rev. Lett. **70**, 1666 (1993).

[73] A. Georges and W. Kraut, Phys. Rev. B**48**, 7167 (1993).

[74] A. Georges, G. Kotliar and Q. Si, Int.J.Mod.Phys. **B6**, 257 (1992).

[75] M.J. Rozenberg, G. Kotliar and X.Y. Zhang, Phys. Rev. B**49**, 10181 (1994).

[76] M. Jarrell, H. Akhlaghpour and Th. Pruschke, *Quantum Monte Carlo Methods in Condensed Matter Physics,* edited by M. Suzuki (World Scientific, 1993), p.221.

[77] J.E. Gubernatis et al., Phys. Rev. B**44**, 6011 (1991).

[78] L.N. Oliveira and J.W. Wilkins, Phys. Rev. B**23**, 1553 (1981).

[79] O. Sakai, Y. Shimizu and T. Kasuya, J. Phys. Soc. Jpn. **58**, 3666 (1989).

[80] T. A. Costi and A.C. Hewson, J. Phys. Condens. Matter **5**, 361 (1993).

[81] N. Grewe, Z. Phys. B**67**, 323 (1987).

[82] O. Sakai and Y. Kuramoto, Solid State Commun. **89**, 307 (1994).

[83] M. Jarrell, H. Akhlaghpour and Th. Pruschke, Phys. Rev. Lett. **70**, 1670 (1993).

[84] Y. Shimizu and O. Sakai, *Computational Physics as an New Frontier in Condensed Matter Research* ed. by H. Takayama et al. (The Physical Society of Japan, 1995), p.42.

[85] Y. Kuramoto and N. Fukushima, J. Phys. Soc. Jpn. **67**, 583 (1998).

Chapter 4

Anomalous Magnetism

4.1 Characteristics of Heavy-Electron Magnetism

In this Chapter, we discuss magnetically ordered or nearly ordered states of heavy electrons. In describing heavy-electron magnetism there are two complementary pictures: one from the high temperature side and the other from the ground state. In the former picture, one regards heavy-electron systems as a lattice of Kondo centers coupled to each other by the RKKY interaction. Of central interest is the competition between the RKKY interaction toward magnetic order and the Kondo screening toward the nonmagnetic singlet state. The RKKY interaction is mediated by conduction band electrons which are only weakly renormalized. The resultant exchange interaction can be represented by $J(\boldsymbol{q})$ with no retardation. Let us assume that the system has strong antiferromagnetic (AF) correlation with the wave number $\boldsymbol{Q}$. From eqs.(1.84) $-$ (1.89), the temperature dependence of $1/T_1$ is given by

$$\frac{1}{T_1} = 2\gamma_n^2 T |A_{hf}|^2 \left(\frac{\chi_L}{\Gamma}\right) \sum_{\boldsymbol{q}} \frac{1}{[1 - J(\boldsymbol{q})\chi_L]^2} \tag{4.1}$$

If magnetic order occurs close to the Kondo temperature T_K characterizing single-site spin fluctuations, both χ_L and Γ are weakly temperature dependent near the transition temperature T_N. Then by expanding around $\boldsymbol{q} = \boldsymbol{Q}$ according to eqs.(1.88) and (1.89), the temperature dependence of $1/T_1$ is roughly expressed by

$$\frac{1}{T_1 T} \propto \frac{\sqrt{\chi_Q(T)}}{|J''(\boldsymbol{Q})|^{\frac{3}{2}} \chi_L \Gamma}, \tag{4.2}$$

where $J''(\boldsymbol{Q})$ is the second derivative of $J(\boldsymbol{q})$ at $\boldsymbol{q} = \boldsymbol{Q}$. Provided that $\chi_Q(T)$ follows the Curie-Weiss law near T_N, $1/(T_1T)$ behaves as $(T - T_N)^{-1/2}$. In some heavy-electron systems such as UNi_2Al_3, the above picture on the dynamical response function seems to hold qualitatively.

In the alternative picture from the ground state, one assumes that the magnetic degrees of freedom are described in terms of itinerant heavy quasi-particles. The dynamical properties reflect strong residual interaction among quasi-particles. The itinerant picture is supported by the fact that even in the magnetically ordered state the density of states near the Fermi level remains finite. Then interesting diversity arises in electronic excitation spectra according to the band structure. For example, there are cases where the critical behavior is not seen even around T_N, and where the Korringa law T_1T=constant is valid even at T far below T_N. On the contrary, if a nesting of the Fermi surface is significant, the excitation gap opens for a large part of the Fermi surface. Then physical quantities have nearly exponential T dependence below T_N, which saturates at lower T because of the residual density of states. In the following we take up representative examples of anomalous magnetism of heavy electrons.

4.2 Weak Antiferromagnetism in URu_2Si_2

We first study spin dynamics in URu_2Si_2. This compound undergoes two phase transitions: First at T_N=17.5 K to an antiferromagnetic (AF) phase with a tiny moment of $\sim 0.04\mu_B$, and second to the superconducting state at T_c=1.2 K. The AF order coexists with the superconducting order. Above 70 K, the resistivity decreases with increasing temperature as is usually observed in the high temperature range

representation	basis functions
Γ^1_{t1}	$\epsilon[\|4\rangle + \|-4\rangle)] + \gamma\|0\rangle$
Γ^2_{t1}	$\gamma[\|4\rangle + \|-4\rangle)] - \epsilon\|0\rangle$
Γ_{t2}	$2^{-1/2}[\|4\rangle - \|-4\rangle]$
Γ_{t3}	$2^{-1/2}[\|2\rangle + \|-2\rangle]$
Γ_{t4}	$2^{-1/2}[\|2\rangle - \|-2\rangle]$
Γ^1_{t5}	$\alpha\|\pm 3\rangle + \beta\|\mp 1\rangle$
Γ^2_{t5}	$\beta\|\pm 3\rangle - \alpha\|\mp 1\rangle$

Table 4.1: CEF states with $J = 4$ for the tetragonal symmetry with $\alpha, \beta, \gamma, \epsilon$ being numerical coefficients.

of heavy-electron systems. The temperature independence of $1/T_1$ is also consistent with the picture that the system is described as an assembly of independently fluctuating local moments. Below 70 K the resistivity drops rapidly upon cooling, and the Korringa law appears as shown in Fig.4.1 [1]. The

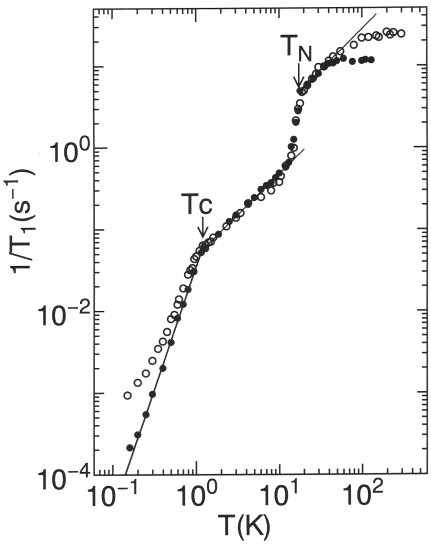

Figure 4.1: Temperature dependence of $(1/T_1)$ of ^{29}Si (open circle) in external field and ^{105}Ru (solid circle) in zero field in URu_2Si_2 [1].

electronic specific heat just above T_N is approximately linear in T with γ=180 mJ/(mole K^2). Below T_N, the heat capacity and T_1 indicate the presence of a gap $E_g \sim 100$ K in the spectrum. Nevertheless a relatively large γ=50 mJ/(mole K^2) still remains around T_c.

The bulk susceptibility of URu_2Si_2 shows a large anisotropy with an easy direction along the c-axis of the tetragonal symmetry. This is interpreted in terms of the CEF splitting of the J multiplet[2]. A few schemes of the CEF levels have been proposed for the $5f^2$ configuration of U^{4+}. In terms of the basis set $|J_z\rangle$ with $|J_z| \leq 4$ for the $^3H_4$ configuration, the CEF eigenstates in tetragonal symmetry are given in Table 4.1. In the model of Niuenhuys [3], the energies of the levels are assumed to be

$$E(\Gamma^1_{t1}) = 0, \quad E(\Gamma_{t2}) = 46\text{K}, \quad E(\Gamma^2_{t1}) = 170\text{K}, \quad E(\Gamma^1_{t5}) = 550\text{K}. \tag{4.3}$$

The model calculation based on this scheme leads to an anisotropic susceptibility because the matrix element $\langle\Gamma^1_{t1}|J_z|\Gamma_{t2}\rangle$ is finite while $\langle\Gamma^1_{t1}|J_\alpha|\Gamma_{t2}\rangle$ with $\alpha = x, y$ is 0. However, the Van Vleck term given by

$$\chi_{vv} = |\langle\Gamma^1_{t1}|J_z|\Gamma^2_{t1}\rangle|^2 \frac{2}{\Delta} \tanh\left(\frac{\Delta}{2T}\right)$$

does not decrease at low temperatures in contrast with experimental results [3]. In an alternative scheme

[4], the CEF levels are assumed to be

$$E(\Gamma_{t3}) = 0, \quad E(\Gamma^1_{t1}) = 44\text{K}, \quad E(\Gamma_{t2}) = 111\text{K}, \quad E(\Gamma^1_{t5}) = 485\text{K}. \tag{4.4}$$

In the latter scheme the ground state does not have a finite off-diagonal matrix element of J_z with nearby levels, but the first and second excited states give rise to finite matrix elements. By this reason the resultant χ_{zz} decreases as the population of Γ^1_{t1} becomes small with decreasing temperature, in consistency with experiments. However, the neutron scattering results to be presented below are hard to explain in the scheme of eq.(4.4). We should mention that in the dilute alloy $U_{0.01}Th_{0.99}Ru_2Si_2$, $\chi_{zz}(T)$ increases as $\ln T$ with decreasing T down to 0.1 K. (see Fig.2.19). This non-Fermi liquid behavior has been interpreted by the assumption that the ground state CEF level consists of the doublet Γ^1_{t5} [5].

The antiferromagnetic order and fluctuations in URu_2Si_2 have been extensively studied by magnetic neutron scattering . The ordering pattern below 17.5 K is that of a type-I antiferromagnet with spins along the c-axis and antiparallel between adjacent planes. The ordered moment has magnitude $(0.04 \pm 0.01)\mu_B$, and is polarized along the c-axis [6]. A striking feature of the magnetic response is that both CEF and itinerant natures appear. Namely, at low energies sharp CEF-like excitations propagate along the tetragonal basal plane, whereas at high energies and for fluctuations propagating along the c-axis the excitations constitute broad magnetic fluctuations as observed in other heavy-electron systems.

Figure 4.2 shows the spectrum of inelastic neutron scattering. Well-defined peaks are observed in energy scans at 1 K for various values of momentum transfer along $\boldsymbol{q_a}=(1,\zeta,0)$ [6]. These dispersive

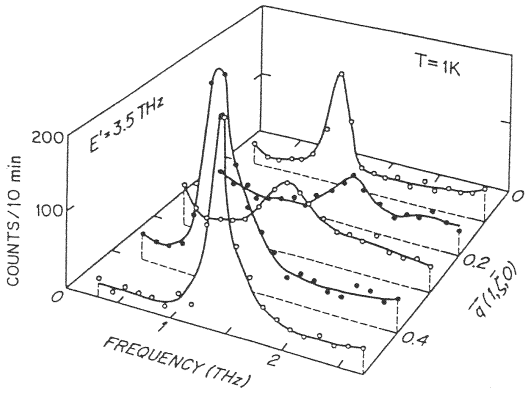

Figure 4.2: Constant-$\boldsymbol{Q}$ scans in URu_2Si_2 along the $(1, -\zeta, 0)$ direction showing sharp magnetic excitations [6]. The energy corresponding to 1THz is 4.1meV.

excitations have a gap of 2 meV at the AF zone center, and are damped out above T_N. We note that the nuclear scattering is forbidden for $\zeta = 0$ because of the body-centered tetragonal structure. From a series of measurements with various energy and momentum transfers, the dispersion relation for the magnetic excitation is extracted as indicated in Fig.4.3.

From the integrated intensity of magnetic excitations for polarization along the c-axis, it is found that the magnetic form factor is typical of $5f$ electrons like that of UO_2. The spin-wave like excitation at $\boldsymbol{Q}$=(1, 0, 0) has a large transition-matrix element of $g\mu_B|\langle i|J^z|f\rangle| = 1.2\mu_B$. Furthermore, this longitudinal inelastic scattering exhibits no broadening beyond the resolution upon application of magnetic field along the c-axis. The last fact is consistent with transitions between the two singlets and confirms that the dispersive state is not a part of continuum excitations.

We now turn to low-temperature magnetic excitations at energies well above the dispersive excitation. Figure 4.4 shows a perspective view of the neutron intensity vs energy and momentum transfer along $\boldsymbol{q}_c = (1, 0, \zeta)$ at 5 K. This makes it possible to compare between the dispersive excitation and the high-energy overdamped response. In the energy region higher than 5 meV, there emerges a continuous spectrum of dominantly AF spin fluctuations. As seen in the constant-energy scan data at 8 meV, the scattered intensity decreases when the momentum transfer varies from $\boldsymbol{Q}$=(1, 0, 0) to $\boldsymbol{q}_F = (1, 0, \pm 1)$. The latter wave number $\boldsymbol{q}_F$ corresponds to the ferromagnetic fluctuation. From the width of the peak

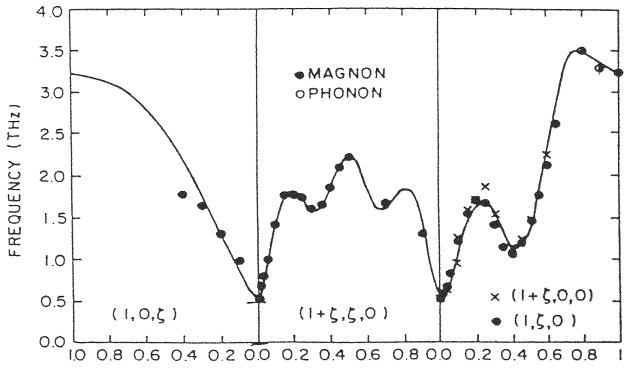

Figure 4.3: Dispersion of excitations in URu_2Si_2 along the (1, 0, ζ), (1+ζ, ζ, 0) and (1, ζ, 0) directions [6].

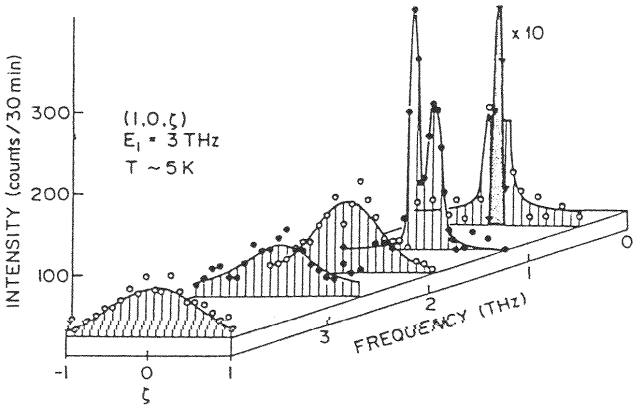

Figure 4.4: Perspective view of scattered neutron intensity vs energy transfer and momentum transfer along (1, 0, ζ). The data are taken in the ordered phase at T=5 K. At ν=0.5 THz (2 meV), the hatched region has been reduced by a factor of 10 [6].

in this scan, it is deduced that the magnetic correlation length along the c-axis is only about one lattice unit.

Figure 4.5 shows the temperature dependence of the scattered intensity with energy transfer 8 meV at $\boldsymbol{Q}$=(1, 0, 0) and $\boldsymbol{q}_F$=(1, 0, 1). The intensity of inelastic scattering above 6 meV remains almost unaffected by the magnetic transition at 17.5 K, and persists up to 40 K. Whereas the inelastic scattering intensity at $\boldsymbol{Q}$=(1, 0,0) decreases slightly with increasing temperature, the intensity at $\boldsymbol{q}_F$=(1, 0, 1) increases so that both intensities become comparable above 100 K. Thus the difference between ferro and AF correlations become significant only below 100 K. It should be noted that the development of AF correlations roughly coincides with the temperature below which the resistivity of URu_2Si_2 begins to decrease.

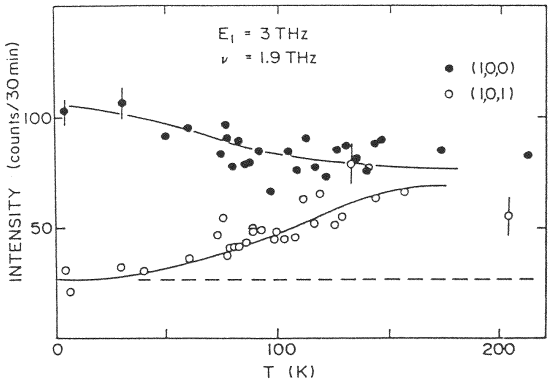

Figure 4.5: Scattered neutron intensity vs temperature at energy transfer of 1.9 THz (8 meV) and scattering vectors (1, 0, 0) and (1, 0, 1). The dashed line is the background [6].

The high-energy response may be regarded as due to itinerant particles which have a large f electron weight. This view is supported by the variable amplitude of the magnetization and by the f electron-like magnetic form factor. Thus the response bears a resemblance to that observed in other heavy-electron systems. The formation of fermionic itinerant particles is also manifested by the onset of metallic T dependence in the resistivity, and the NMR result with the Korringa law. The itinerant particles become antiferromagnetically correlated below 100 K. We note that these itinerant particles may have a character much different from that of Landau quasi-particles since the temperature is high.

The presence of sharp magnetic excitation in URu_2Si_2 is unique among heavy-electron systems. The dispersion relation and intensities of low-energy CEF excitations are well described by the singlet-singlet model. The model was also applied to explaining the T dependence and anisotropy of the magnetic susceptibility. With assumption of a singlet ground state and with a quadrupole ordering [4], the CEF model of eq.(4.4) can roughly describe observed behaviors of linear and non-linear susceptibilities and λ-type anomaly of the specific heat at T_N. However the ordered moment predicted by this simple model is an order of magnitude larger than the experimental value.

The reason for the presence of the tiny ordered moment is an unresolved problem. Actually, no hyperfine broadening of the Si-NMR spectrum is detected at the onset of the long-range order. If the AF sublattice moment of 0.03 μ_B is really static, this amount of moment should have led to observable hyperfine broadening. Thus another possibility is that the magnetic order is not static but is slowly fluctuating. If this is the case, the time scale should be longer than the one for the neutron scattering, but shorter than the one for the NMR. We note that this anomalous magnetic property resembles with the one found in UPt_3.

In concluding this section we mention a related material UPd_3 although it is not classified as a heavy fermion system but as a localized 5f system. This compound crystallizes in a hexagonal structure with U ions occupying either hexagonal sites or quasi-cubic sites. The U ion at the hexagonal site shows a clear crystal field splitting of the order of 10 meV, but the CEF splitting at the quasi-cubic site is much smaller [7]. It has been shown by neutron scattering that the paramagnetic phase enters an ordered phase with no magnetic moment at T_1 =6.5 K, and further to the weak antiferromagnetic phase at T_2 =4.5 K [8]. The intermediate phase has in fact a quadrupole order with triple-$\boldsymbol{Q}$ structure. The relationship to weak

magnetism in URu_2Si_2 should be investigated further. We shall explain in more detail the quadrupole order in 4.6 for the case of CeB_6.

4.3 Antiferromagnetism in UPd_2Al_3 and UNi_2Al_3

UNi_2Al_3 and UPd_2Al_3 form a new series of antiferromagnetic heavy-electron superconductors with large uranium-derived moments 0.24 μ_B and 0.85μ_B, respectively [9]. The transition temperatures are T_N=4.6 K and T_c=1 K for UNi_2Al_3 and T_N=14.5 K and T_c=2K for UPd_2Al_3. Of these, UPd_2Al_3 exhibits the highest T_c and the largest ordered moments as heavy-electrons. The superconducting properties will be discussed in detail in Chapter 5.

The magnetic susceptibility $\chi(T)$ of single crystal UPd_2Al_3 shows easy plane anisotropy in contrast to the case of URu_2Si_2. A Curie-Weiss-type behavior with effective moment 3.6 μ_B/U-atom is observed for both directions at temperatures higher than 150 K. $\chi(T)$ shows a maximum at around 35 K and abruptly decreases below T_N=14.5 K. The magnetic order consists of ferromagnetic sheets in the basal plane which are coupled antiferromagnetically along the c-axis with an ordering vector $\boldsymbol{Q} = (0, 0, 1/2)$. The large λ-type anomaly of the specific heat at T_N for UPd_2Al_3 accompanies a large T-linear term with γ=150 mJ/(molK^2). These features are similar to those in URu_2Si_2, but the size of the ordered moment and the nature of the ordered state are very different.

By contrast, the T-dependence of $1/T_1$ of ^{27}Al in UPd_2Al_3 shows a behavior common to that in URu_2Si_2 [10]. Below T_N, $1/T_1$ drops markedly, and is fitted by the following simple form:

$$\frac{1}{T_1T} = A + B\exp(-\frac{E_g}{T}).$$

The first term originates from the particle-hole excitation in the Fermi liquid state. When the superconductivity is suppressed by the magnetic field, the Korringa law remains valid down to $T < T_N$. This result means that the spin-wave excitation is not responsible for the relaxation process in the low T regime. The second term should be related to the energy gap due to the magnetic ordering. According to a tentative estimate, a half of the density of states is lost below T_N.

The susceptibility $\chi(T)$ in UNi_2Al_3 does not exhibit a Curie-Weiss behavior below 300 K. A small maximum of $\chi(T)$ vs T appears around 100 K, which is followed by a minimum around 30 K and a clear peak at T_N=4.6 K[9]. Elastic neutron scattering measurement on a single crystal has revealed that this compound has an incommensurate SDW-type order. The wave vector is $\boldsymbol{Q}$=$(1/2 \pm \tau, 0, 1/2)$ with $\tau = 0.11$ and the size of the ordered moment is 0.24 μ_B/U. As shown in Fig.4.6, $1/T_1$ of ^{27}Al does not follow the Korringa law in the paramagnetic state. It tends to saturate above room temperature [10]. $1/T_1$ approaches a linear T dependence well below T_N = 4.6 K when the superconducting transition is suppressed by the magnetic field. These features are different from those commonly observed in other heavy-electron systems. Namely $1/T_1$ usually undergoes a smooth crossover from the behavior $1/T_1$=constant at the T region higher than the Kondo temperature to the Korringa law at low T (see Fig.4.1).

The T dependence of the relaxation in UNi_2Al_3 is well described by the following expression:

$$\frac{1}{T_1T} = a + b\frac{1}{\sqrt{(T - T_N)}}. \tag{4.5}$$

Here the first term is due to the Al-3p orbital relaxation, and the second is due to the the transferred hyperfine interactions of ^{27}Al nuclei with uranium 5f electron spins. The characteristic T dependence of the second term coincides with the expression eq.(4.2) of the staggered susceptibility which follows the Curie-Weiss law at the wave vector $\boldsymbol{q} = \boldsymbol{Q}$ above T_N. From the T dependence of $^{27}(1/T_1)$, it is concluded that the spin fluctuation in UNi_2Al_3 possesses a large q dependence in contrast to the standard behavior of heavy-electron compounds. In the latter case the magnetic response is described as coming from an assembly of local moments at high T, whereas the response at low T is that of the Fermi liquid. Even in the latter case the $\boldsymbol{q}$ dependence is weak.

For comparison, we mention that the relaxation of a typical heavy-electron antiferromagnet UCu_5 follows eq.(4.5) only just above T_N [11]. In the case of UNi_2Al_3, on the other hand, the wave-number dependent spin correlations dominate in the wide temperature range from far above T_N. Concerning this difference we remark that the spin fluctuation temperature T^* of UNi_2Al_3 is about 300 K which is much larger than T_N.

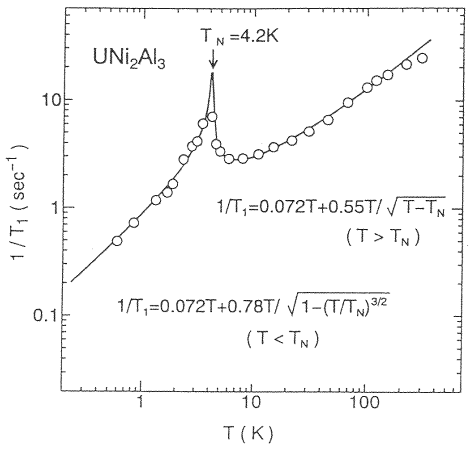

Figure 4.6: Temperature dependence of $(1/T_1)$ of ^{27}Al In UNi_2Al_3 [10].

We have thus seen that the nature of magnetic fluctuation and spin structure of two isostructural U compounds are different from each other. Nevertheless it is remarkable that the Korringa law is commonly valid in the magnetically ordered state well below T_N for both compounds.

4.4 Magnetic Correlation in $CeCu_2Si_2$

According to the inelastic neutron experiment on polycrystalline samples of $CeCu_2Si_2$, the quasi-elastic scattering intensity has a width of $\Gamma \sim 10$ K [12], which suggests $T_K \sim$10 K. This value lies between the case of $CeCu_6$ with T_K=6 K and that of $CeRu_2Si_2$ with T_K=23 K. As expected, the value of the T linear coefficient γ of specific heat is correspondingly large; γ=800 mJ/(mole K^2) and we obtain $\gamma T_K/k_B \sim 6\times10^{23}$ /mole. Note that we have reinstated the Boltzmann constant here. The latter value, close to the Avogadro's number, is comparable to those in $CeCu_6$ and $CeRu_2Si_2$, and is a measure of numbers of heavy electrons.

$CeCu_2Si_2$ shows anomalous magnetism near the superconducting transition at T_c=0.7 K. The NQR intensity observed around 3.435 MHz decreases upon cooling below 1 K without any broadening associated with spontaneous magnetic moments [13, 14]. This anomalous state is called the phase A which does not have a static magnetic order, but has a very slow magnetic fluctuation with frequencies comparable to the NQR frequency ω_N [14]. This dynamical character of the phase A is consistent with recent μSR experiments [15]. Neutron scattering experiments detect neither magnetic Bragg peaks nor any superstructure which indicates an order parameter of spin-density-wave (SDW) or charge-density-wave (CDW) for the phase A. We mention that the phase A was first suggested by magneto-resistance [16], and its magnetic nature was confirmed by NMR [13, 17, 18] and muon spin rotation (μSR) [19].

A series of polycrystalline $Ce_xCu_{2+y}Si_2$ in the vicinity of stoichiometric composition together with a high-quality single crystal have been studied by measurements of elastic constant and thermal expansion [15, 20, 21, 22, 23]. In this process another phase called the phase B was identified above 7 T. Figure 4.7 shows the phase diagram obtained on a high quality single crystal of $CeCu_2Si_2$ [20]. The phase A and the superconducting phase are extremely sensitive to sample preparation, especially to the nominal content x [22] of Ce. The phase A under zero field seems to be expelled below T_c by the onset of superconductivity in both high-quality single crystalline [20] and polycrystalline samples [22]. From these macroscopic measurements it is suggested that $CeCu_2Si_2$ is close to a quantum critical point [23] where different ground states meet each other.

Figure 4.8 shows the temperature dependence of $1/T_1$ of ^{63}Cu under zero field for a series of $Ce_xCu_{2+y}Si_2$ compounds [24]. For x=0.975 below 1 K, there appear long (T_{1L}) and short (T_{1s}) components in the relaxation. In this case both components are estimated as shown in Fig.4.8. In other cases of $Ce_xCu_{2+y}Si_2$, there is only a single component in T_1

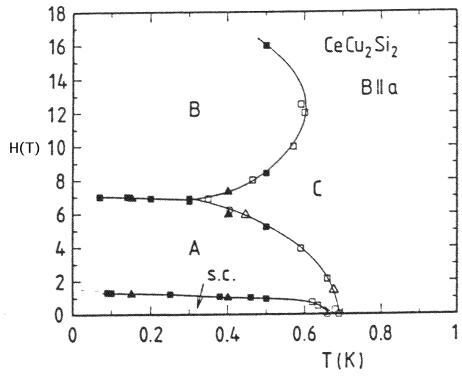

Figure 4.7: Magnetic field H vs temperature phase diagram of $CeCu_2Si_2$ with H in the tetragonal basal plane ($H \perp c-$axis). The phase boundaries are determined from elastic constant, magnetostriction and thermal expansion anomalies [20].

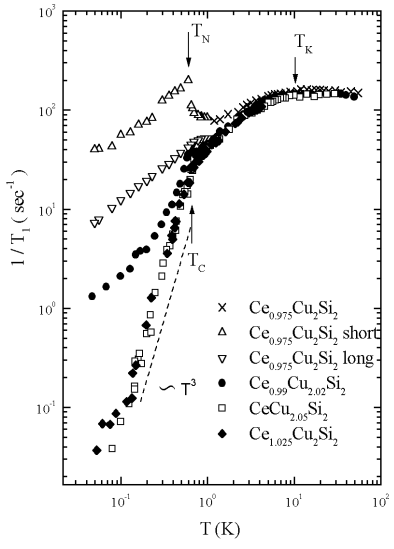

Figure 4.8: T dependence of NQR $1/T_1$ in $Ce_xCu_{2+y}Si_2$. In the particular case of $Ce_{0.975}Cu_2Si_2$ below 1 K, short (T_{1S}) and long (T_{1L}) components of $1/T_1$ appear [24].

Above 3 K, $1/T_1$'s for all the samples fall on the same curve, which shows that $T_K \sim 10K$ is nearly independent of Ce concentration x. Below 2 K, the T dependence of $1/T_1$ reflects the difference in the ground state of each concentration. We note that $1/T_1$ below 1 K has both short (T_{1S}) and long (T_{1L}) components [24]. A cusp in $1/T_{1S}$ for x =0.975 is observed at 0.6 K. This cusp is associated with the onset of a static magnetic order. On the other hand, $1/(TT_1)$ for x =1.025 is nearly constant between 1.2 K and T_c. This behavior reflects formation of a Fermi liquid state before the superconductivity appears. For the state with x =0.99, which seems to have the phase A as the ground state, slow magnetic fluctuations comparable to $\omega_N \sim 3.4$MHz dominate down to 0.012 K. In this sense, the phase A is characterized as a "critically magnetic phase". Note that $1/T_1$'s in the superconducting state for x =1.025 and x =1.00 follow the T^3 dependence in the range T=0.6 K – 0.1 K, and fall on the single line. This result supports the conclusion of elastic measurement on a high-quality single crystal [20] that the phase A is expelled below T_c by the onset of superconducting phase.

Figure 4.9 shows the phase diagram of $Ce_{1-x}Th_xCu_2Si_2$ with Th-content x as the abscissa. Shown together is that of $CeCu_{2.02}Si_2$ with magnetic field taken as the abscissa [14]. The solid line in the

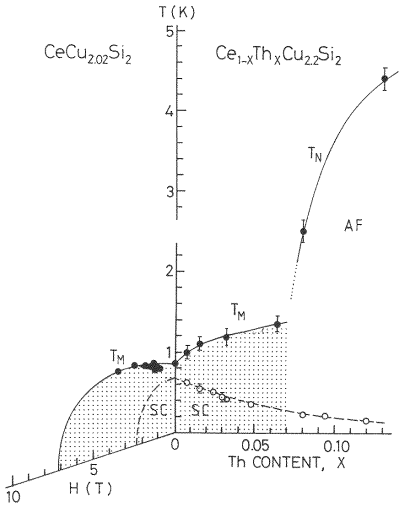

Figure 4.9: Magnetic and superconducting phase diagrams for $CeCu_2Si_2$ as functions of Th content and magnetic field [14].

H-T plane in $CeCu_{2.02}Si_2$ above 4 T corresponds to those temperatures and fields at which anomalies appear in the magnetoresistance and the dHvA signal [25]. For $CeCu_2Si_2$, T_M, which is the transition temperature to the phase A, is determined as the temperature below which the NQR intensity decreases without broadening. On the other hand, the (static) magnetic ordering temperature T_N is determined as the temperature below which the NQR linewidth starts to increase. A lattice anomaly has been found at T_M from measurements of thermal expansion and elastic constant [26]. It is seen that antiferromagnetic order is induced by substitution of Ce for the Th. This seems to be due to the decrease of an effective f electron number.

As shown by the dashed line in Fig.4.9, T_c of $CeCu_2Si_2$ decreases gradually with increasing magnetic field or content of Th. On the contrary, T_c is enhanced by applying pressure from 0.7 K at ambient pressure to 2.2 K at 30 kbar [27]. This is understood if one assumes that $CeCu_2Si_2$ is on the border of antiferromagnetism. Then magnetic fluctuations above T_c should have extremely low frequencies. The application of pressure increases hybridization and hence T_K, which means increase of bandwidth of heavy quasi-particle [18]. The superconducting ground state is favored in such a condition, whereas the magnetically ordered state is favored by the opposite condition; decrease of either T_K or the effective f electron number.

4.5 Non-Fermi Liquid Behavior near the Antiferromagnetic Phase Boundary

When the Kondo exchange interaction J between f and conduction electrons is strong enough, the ground state is the paramagnetic Fermi liquid. Then weakening the exchange interaction, i.e., reducing the $c-f$ hybridization can lead to long-range magnetic order. For example in nonmagnetic $CeCu_6$, Au substitution of Cu expands the lattice parameter, and as result, reduces J_K. Actually AF order is observed in $CeCu_{6-x}Au_x$ above a critical concentration $x_c \sim 0.1$ [28]. Conversely, in a $CeCu_{5.7}Au_{0.3}$ alloy with $T_N = 0.49$ K at zero pressure, the breakdown of the AF order occurs at a critical value $p_c \sim 8$ kbar. In the vicinity of such a magnetic-nonmagnetic transition, strong deviations from Fermi-liquid behavior are seen. Typical anomalies in physical quantities are: $C/T \sim -\ln(T/T_0)$, $\chi \sim (1-\alpha T^{1/2})$ and $\rho \sim \rho_0 + AT$. Figure 4.10 shows the temperature dependence of C/T at various pressure values. Strong deviation from the canonical behavior C/T=const is evident from its logarithmic dependence $C/T \sim -\ln(T/T_0)$ in a wide T range [28]. This non-Fermi liquid behavior has a different microscopic origin from that in the single ion case discussed in Chap. 2. In the present case the anomalies originate from dominant collective magnetic excitations caused by the incipient AF order near the magnetic-nonmagnetic phase boundary.

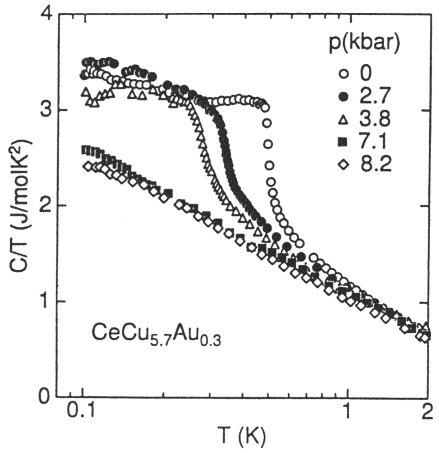

Figure 4.10: Specific heat C of $CeCu_{5.7}Au_{0.3}$ plotted as C/T vs $\ln T$ for various values of pressure p [28].

4.6 Quadrupolar and Magnetic Orderings in CeB_6

CeB_6 crystallizes in a Cubic CsCl-type structure with a B_6 octahedron in the body center of the cube. The cubic crystal field around each Ce ion lifts the degeneracy of the sixfold multiplet with J=5/2 of the trivalent $4f^1$ configuration into two CEF levels: the ground-state quartet Γ_8 and the excited doublet Γ_7 lying above 530 K from Γ_8. The phase diagram of CeB_6 exhibits anomalous features with two kinds of ordered phases as shown in Fig.4.11[29]. In the paramagnetic phase (called phase I) at $T > T_Q = 3.2$ K in zero field, the resistivity shows a Kondo-type behavior with $T_K = 1$ K. In the temperature range of T_N=2.4 K $< T < T_Q$, a new phase called II appears which is characterized by the antiferro quadrupolar (AFQ) ordering with the ordering vector $\boldsymbol{Q} = [1/2, 1/2, 1/2]$ in units of the reciprocal lattice vectors. With the quadrupole order the Γ_8 ground-state should be split into two doublets. Although the AFQ order itself cannot be observed directly by neutron scattering experiments, the external magnetic field induces an AF order with the same wavevector as that of the AFQ ordering. The induction is due to different local susceptibilities associated with two inequivalent Ce ions. In the phase III, which appears in the lowest T range, a magnetic order develops with the ordered moment $0.28\mu_B$ and with a double-$\boldsymbol{k}$ commensurate structure of wave vectors $\boldsymbol{k}_\pm = [1/4, \pm 1/4, 1/2]$.

The anomalous magnetism apparently originates from the interplay of a few relevant effects such as the single-site Kondo-type fluctuation and intersite quadrupolar and RKKY interactions. We note that

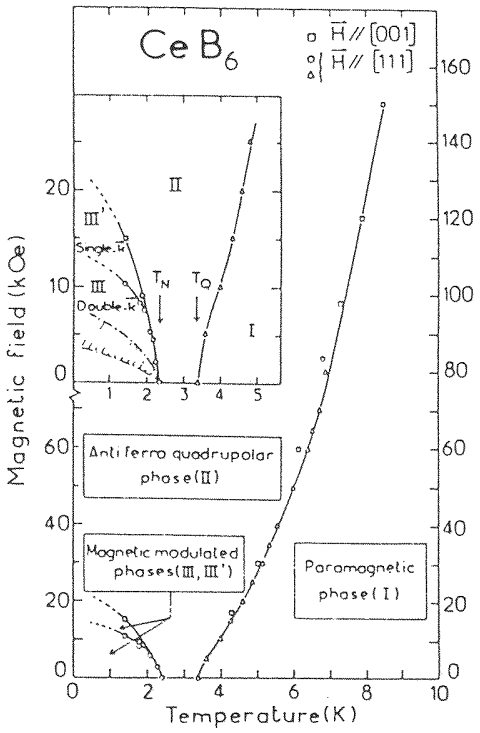

Figure 4.11: Phase diagram of CeB_6 obtained for a magnetic field along [001] and [111] direction of the cubic structure [29].

T_K and T_Q are of the same order of magnitude in CeB_6.

The Kondo effect appears also as the reduced magnetic moment and a large residual value of electronic specific heat with $\gamma = 240$ mJ/mole·K^2 below T_N. Furthermore, applied magnetic field enhances T_Q and the specific heat anomaly markedly. An interpretation for this is that application of magnetic field progressively suppresses the Kondo state; as a result T_Q shifts to higher temperature. It is also suggested [30, 31] that the actual T_Q has been reduced much from the mean-field value by fluctuations of the AFQ order. The number of fluctuating components is an important parameter for the reduction. Since the applied magnetic field suppresses the fluctuation by lowering the number of equivalent components, T_Q is enhanced. By the same reason the specific heat anomaly is also enhanced. There is also an interpretation which assumes the octupolar intersite interaction is enhanced by the spin polarization [32, 33]. The octupole degrees of freedom plays an important role to reconcile the NMR results [34] with the order parameter in phase II [35].

Upon alloying with La, the system $Ce_xLa_{1-x}B_6$ shows a complex phase diagram with intriguing dependence on x. A new phase called IV appears with $x < 0.75$ in the low-field region. On entering this phase from the phase I, the susceptibility shows a cusp as if it entered a Néel state [36]. However, the phase IV has very small magnetic anisotropy and small magnetoresistance [37] in contrast with the phase III. The phase IV also shows a prominent elastic anomaly [38]. It seems that the orbital degrees of freedom play an important role in realizing these unusual properties.

4.7 Systems with Low Density of Carriers

There are classes of Ce and Yb compounds which have a low carrier density of the order of only $10^{-3} - 10^{-2}$ per formula unit, but which exhibit phenomena like those seen in Kondo systems. They also show anomalous magnetic properties. Here we present typical examples such as Ce-monopnictides CeX (X=P, As, Sb, Bi) which show complicated phase diagrams in the plane of magnetic field and temperature, and Yb_4As_3 where spin excitations have the one-dimensional character.

4.7.1 CeP

CeP crystallizes in the NaCl structure. Figure 4.12[39] shows the magnetic phase diagram of CeP. The

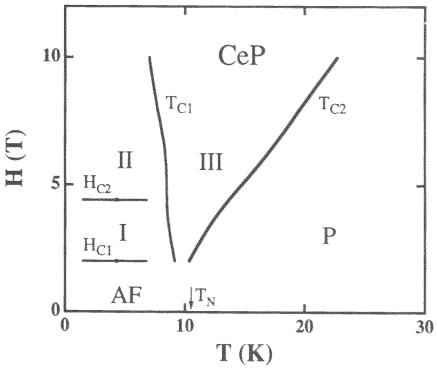

Figure 4.12: Phase diagram of CeP for magnetic field along [001] direction[39].

phase boundaries $H_{c1}(T)$ and $H_{c2}(T)$ are determined from the values of field where a step-wise increase in magnetization appears. Figure 4.13 shows the magnetic structures as determined by elastic neutron scattering [39]. In the phase I, Ce spins in each (001) plane align ferromagnetically perpendicularly to the plane. What is unusual is that the magnetic unit cell is very long along the [001] direction; the ferromagnetic double layers containing Ce moment of $\sim 2\mu_B$ are stacked periodically. The Ce ions in intervening nine layers have moment of 0.7 μ_B. The values 2 μ_B and 0.7 μ_B of ordered moments are close to those of CEF states labeled as Γ_8 and Γ_7 in the cubic symmetry.

In the phase II, the AF ordered moments of the Γ_7 layers change their direction as shown in Fig. 4.13, while there is no change in the ordering of Γ_8 double layers. In the phase III, the period of ordered Γ_8 Ce layers changes into *ten* layers, and the Γ_7 Ce layers sandwiched by the Γ_8 layers become paramagnetic.

These anomalous magnetic structures seem to originate from the low carrier density of this compound [40]. At low temperatures, holes tend to localize so as to obtain the energy gain through the p-f mixing interaction. This results in the polarization of $4f\Gamma_8$ state. It is not fully understood why the Γ_8 double layers have such long periodicity as *eleven* layers.

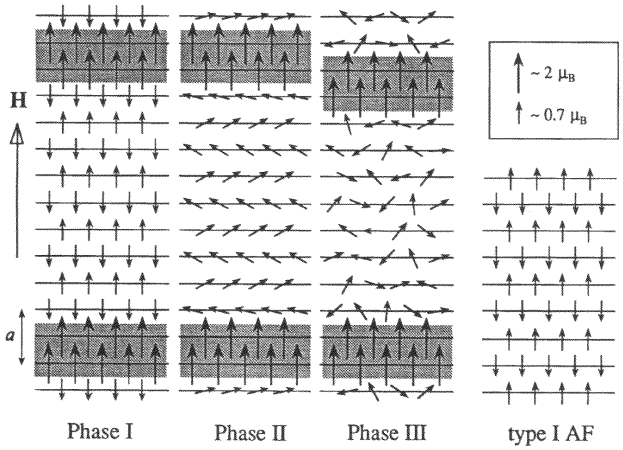

Figure 4.13: Magnetic structure of CeP under magnetic field [39].

4.7.2 Yb_4As_3

Yb_4As_3 exhibits a structural phase transition at 290 K from the mixed valent state in the cubic phase to the charge ordered state in the trigonal phase. In the mixed valent state the proportion of two valences is about Yb^{+3}:$Yb^{+2} \sim 1:3$, and the average $4f$ hole number is $\sim$0.25 per Yb. This leads to metallic character of the system. On the other hand, the carrier density at low temperatures is extremely low (10^{-3} per formula). Nevertheless, the low temperature properties look like those in typical heavy electron materials. It shows a large T-linear term in specific heat with γ=205 mJ/K^{2}mole, and the resistivity has a T-square dependence at low temperature, followed by a $-\log T$ behavior at higher T [41].

In the charge ordered state, the distance between Yb atoms becomes shorter in the chain along one of [111] axes and longer in the other directions. This trigonal distortion makes the linear chains of $Yb^{+3}(4f^{13})$, which are magnetically active. The chains seem to interact only weakly with each other in the nonmagnetic background consisting of divalent Yb^{+2} $(4f^{14})$. As a matter of fact, inelastic neutron scattering experiments revealed that the magnetic excitation shows the characteristics of a one-dimensional (1D) Heisenberg antiferromagnet [42, 43]. The spectrum indicated in Fig.4.14 is close to the des Cloiseaux-Pearson mode with $E_1(q) = \pi J \sin(dq)$ where d is the atomic distance in the Yb^{3+} along the chain. Here q is the projection of the wave vector along the Yb^{3+} chain direction. In the 1D Heisenberg model, the specific heat at low T is linear in T with $\gamma = 190$ mJ/moleK^2 at $\pi J = 3.5$ meV. Then with this value of J, the temperature giving the maximum of the susceptibility is predicted to be 17 K which is close to the experimental observation. Hence the heavy electron behavior in Yb_4As_3 seems to be due to the 1D-like spin excitation caused by the charge ordering, rather than due to the Kondo effect.

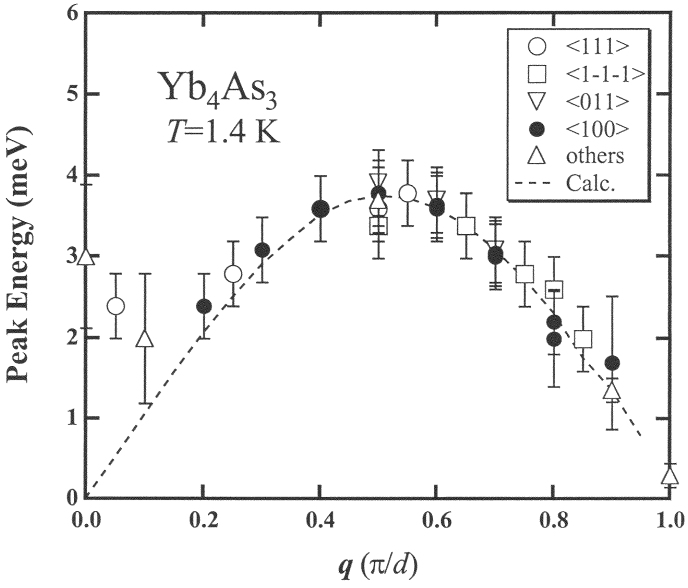

Figure 4.14: Dispersion relation of inelastic peaks of Yb_4As_3 in the 1D representation. The open triangles show the newest results, and other symbols indicate previous results for different directions from the (002) reciprocal lattice point. The broken line represents the peak position calculated in the 1D Heisenberg model [42].

4.8 Quantum Phenomenology for the Dual Character

4.8.1 Coexistence of itinerant and localized characters

At present there is no microscopic theory to explain the small ordered moment and anomalous magnetism in heavy electrons. The origin of the difficulty lies in the fact that these properties depend rather strongly

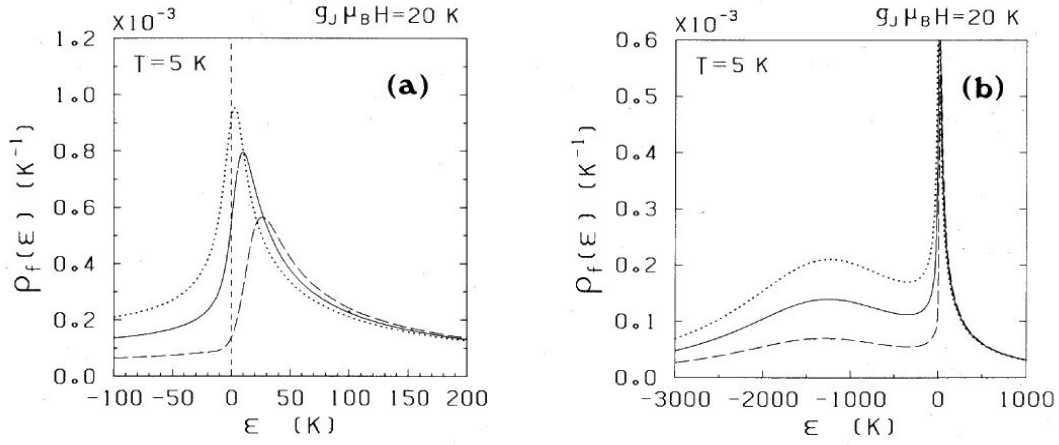

Figure 4.15: The density of states of the Anderson model in a magnetic field calculated in the NCA. The solid lines show the zero-field results, while the dotted lines correspond to majority spins in a magnetic field, and the dashed lines to minority spins.

on the details of the individual system. Some heavy electrons do not show any magnetic order, nor any metamagnetism. While others do show such behavior. Because the magnetic fluctuation depends strongly on momentum in the case of anomalous magnetism, the renormalization theory utilizing $1/n$ or $1/d$ as small parameters is not straightforwardly applied. Hence the description in the present section becomes necessarily qualitative, and contains physical ideas of the authors without confirmation of their relevance.

In considering the anomalous magnetism of heavy electron systems, it is instructive to see the effect of magnetic field on the f-electron density of states. Figure 4.15 shows sample results for the single impurity Anderson model calculated by the NCA [44]. The parameters in the calculation are $\epsilon_f = -1500K, \pi W_0 = 500K$ and the density of states for the conduction band is constant for $|\epsilon| < D = 10^4 K$ and 0 otherwise. Then the Kondo temperature T_K which is given by

$$T_K = D\left(\frac{2W_0}{D}\right)^{1/2} \exp\left(\frac{\epsilon_f}{2W_0}\right),$$

amounts to 16 K. As shown in Fig.4.15(a) the magnetic field splits the Kondo resonance into up- and down-spin resonances, which is analogous but not identical to the Zeeman splitting of a fermion level. The first difference from the simple level splitting is that the up- and down-spin resonances have different weights, and the second one is that the splitting is not symmetric about the zero-field peak. The strong correlation is responsible for the deviation. A dramatic effect of the correlation appears in the energy range deep below the Fermi level. As Fig.4.15(b) shows, the minority spin component loses much of the spectral weight although the magnetic energy is very small as compared with $|\epsilon_f|$. This demonstrates that the magnetic polarization of f electrons has little to do with the scale ϵ_f, but is controlled by the scale T_K.

In the case of the Anderson lattice, as we have seen in Chapter 3, the momentum distribution of f electrons has only a small discontinuity at the Fermi surface, and globally is rather similar to the localized case. This shows that the f electrons possess an itinerant character close to the Fermi level, but show a dominantly localized character for the magnetization. At temperatures above T_K, many features of heavy electron systems are common to dilute Kondo systems. This means that the excitation spectrum except for the low-energy limit is similar in both systems. The essential idea for constructing a quantum phenomenology is that in the intermediate stage of the renormalization toward the Fermi-liquid fixed point, there should be local variables which are common in the single-site Anderson model and the Anderson lattice. It is reasonable to assume that the Kondo spin compensation is already substantial at this stage.

We set up an effective Lagrangian which includes itinerant fermions and local spin fluctuations. These variables represent the dual nature of strongly correlated f electrons. Hence we call the present scheme

the duality model [45]. In this model we make maximum use of known results for the single-site system in order to understand heavy electrons. Fortunately the single-site Kondo system is now well understood both for static and dynamic properties with use of various theoretical methods. A renormalization flow which goes ultimately off the paramagnetic Fermi liquid toward the superconducting phase for example can also be treated by the duality model.

The separation into the fermion degrees of freedom and the spin-fluctuation part in the effective Lagrangian makes it possible to introduce a new approximation scheme. As an example we propose a classical approximation for the most dominant component of spin fluctuations. The approximation is applied to discussion of metamagnetism and weak antiferromagnetism.

4.8.2 Effective action for the Anderson lattice

We use the Anderson lattice as the starting microscopic model with U much larger than the hybridization V_μ between f states and the μ-th conduction band. We take V_μ real and neglect its possible dependence on momentum. As explained in Chapter 3 and Appendix F, the partition function Z at temperature $T = 1/\beta$ is written in the form of a functional integral over Grassmann numbers with imaginary time τ. It is trivial to integrate over the conduction-electron part. For the f electron at site i with spin σ, we use Grassmann numbers $f^{\pm}_{i\sigma}(\tau)$ where $f^{\pm}_{i\sigma}$ denotes either $f^{\dagger}_{i\sigma}$ or $f_{i\sigma}$. The Fourier transforms with odd Matsubara frequency $\epsilon_n = (2n+1)\pi T$ with n integer are given by

$$f^{\pm}_{i\sigma}(\tau) = \sum_n f^{\pm}_{i\sigma}(i\epsilon_n)\exp(-i\epsilon_n\tau). \tag{4.6}$$

For low-energy fermion excitations only those components with $|\epsilon_n|$ of $O(T_K)$ are relevant. However spin excitations with low energy are dominated by $f^{\pm}_{i\sigma}(i\epsilon_n)$ with $|\epsilon_n|$ much larger than T_K. This is because the low-energy spin excitations are represented by a bilinear form of Grassmann numbers each of which can have high frequencies.

In order to realize the idea we introduce the auxiliary field via the Hubbard-Stratonovich identity as explained in Appendix F. The partition function is represented by

$$Z_f \equiv Z/Z_c = \int \mathcal{D}f^{\dagger}\mathcal{D}f\mathcal{D}\boldsymbol{\phi}\exp(-A) \tag{4.7}$$

where Z_c is the conduction electron part, and $\boldsymbol{\phi}$ is an auxiliary variable representing the fluctuating magnetic field. The action $A = A_0 + A_1$ is given by

$$A_0 = -\sum_{ij\sigma n} f^{\dagger}_{i\sigma}(-i\epsilon_n)[g_f(i\epsilon_n)^{-1}]_{ij}f_{j\sigma}(i\epsilon_n) - \frac{1}{2U}\sum_{im}|\boldsymbol{\phi}_i(i\nu_m)|^2, \tag{4.8}$$

$$A_1 = -\sum_{i\alpha\beta}\sum_{mn} f^{\dagger}_{i\alpha}(-i\epsilon_n - i\nu_m)f_{i\beta}(i\epsilon_n)\boldsymbol{\sigma}_{\alpha\beta}\cdot\boldsymbol{\phi}_i(i\nu_m), \tag{4.9}$$

where $g_f(i\epsilon_n)$ is the Green function matrix of f electrons with no Coulomb interaction. We integrate over high frequency variables in the action. The remaining ones are $f^{\pm}_{i\sigma}(i\epsilon_n)$ and $\boldsymbol{\phi}_i(i\nu_m)$ with $|\epsilon_n|$ and $|\nu_m|$ smaller than cutoffs of $O(T_K)$. Furthermore we change variables from $\boldsymbol{\phi}_i(i\nu_m)$ to magnetization $\partial A_1/\partial\boldsymbol{\phi}_i(i\nu_m)$. Then we need to incorporate the Jacobian associated with this change of variables. Since the correlation function of magnetization coincides with that of the f-electron spin at low frequencies, we choose the notation $\boldsymbol{S}(i\nu_m)$ to represent the slow part of magnetization. Note that the quantity $\boldsymbol{S}(i\nu_m)$ is a c-number.

With this formal procedure we are left with an effective Lagrangian or its integral, the action A_{eff}, which has only low-frequency variables. Namely

$$Z_f = \int \mathcal{D}f^{\dagger}\mathcal{D}f\mathcal{D}\boldsymbol{S}\exp(-\beta A_{eff}), \tag{4.10}$$

where all variables have now a cut-off energy of $O(T_K)$. It is not possible to obtain the explicit form of the action A_{eff} by microscopic calculation, since important terms are spread over many orders in perturbation theory. We thus construct the action phenomenologically following the "minimal coupling"

principle. Namely we assume a local and instantaneous interaction between fermions and "spins" represented by $\boldsymbol{S}(i\nu_m)$. The action, with neglect of the shift of the ground-state energy, consists of three parts as [45]

$$\begin{aligned} A_{eff} &= A_f + A_s + A_{int}, && (4.11)\\ A_f &= -\sum_{ij\sigma n} f^\dagger_{i\sigma}(-i\epsilon_n)[G^{(0)}_\sigma(i\epsilon_n)^{-1}]_{ij} f_{j\sigma}(i\epsilon_n), && (4.12)\\ A_s &= \sum_{ijm} \boldsymbol{S}_i(-i\nu_m)\cdot \boldsymbol{S}_j(i\nu_m)[\chi_0(i\nu_m)^{-1}\delta_{ij} - J_{ij}] - \sum_i h_i S_{iz}(0), && (4.13)\\ A_{int} &= -\lambda_0 \sum_{i\alpha\beta}\sum_{mn} f^\dagger_{i\alpha}(-i\epsilon_n - i\nu_m) f_{i\beta}(i\epsilon_n)\boldsymbol{\sigma}_{\alpha\beta}\cdot \boldsymbol{S}_i(i\nu_m). && (4.14) \end{aligned}$$

In the fermion part A_f, $G^{(0)}_\sigma(i\epsilon_n)^{-1}$ is the Green function matrix of f electrons. This involves the site-diagonal self-energy $\Sigma^{(0)}_\sigma(i\epsilon_n)$ caused by many-body interactions other than those by spin fluctuations. The matrix element is given by

$$[G^{(0)}_\sigma(i\epsilon_n)^{-1}]_{ij} = [i\epsilon_n - \epsilon_f - \Sigma^{(0)}_\sigma(i\epsilon_n) - \frac{1}{2}\sigma h_i]\delta_{ij} - \sum_\mu V_\mu^2 g^\mu_{ij}(i\epsilon_n), \tag{4.15}$$

where ϵ_f denotes the f-electron level, $g^\mu_{ij}(i\epsilon_n)$ is the bare propagator of μ-th conduction band and h_i is a magnetic field at site i. The Green function $g_f(i\epsilon_n)$ in eq.(4.8) corresponds to the one without $\Sigma^{(0)}_\sigma(i\epsilon_n)$ in eq.(4.15).

In the spin part A_s, $\chi_0(i\nu_m)$ is a partially renormalized spin susceptibility before inclusion of the RKKY interaction and the coupling with fermions. For the RKKY interaction J_{ij} we neglect dependence on energy since the characteristic energy in J_{ij} is usually much larger than T_K. We deal with an exceptional case where the energy dependence cannot be neglected later. In the lowest order in hybridization J_{ij} is written as

$$J_{ij} = 2\sum_\mu \left(\frac{V_\mu^2}{\epsilon_f}\right)^2 T\sum_n g^\mu_{ij}(i\epsilon_n) g^\mu_{ji}(i\epsilon_n). \tag{4.16}$$

If we integrate over the spin degrees of freedom in eq.(4.10), we are left with the standard Fermi liquid theory. In order to discuss magnetic properties, it is convenient to integrate first over the fermion variables. The result is given by

$$\begin{aligned} Z &= \det G^{(0)} \int \mathcal{D}\boldsymbol{S}\exp(-\beta A_m), && (4.17)\\ A_m &= A_s - T\mathrm{Tr}\,\ln(1+\lambda_0 G^{(0)}\boldsymbol{\sigma}\cdot\boldsymbol{S}) && (4.18) \end{aligned}$$

where the partially renormalized Green function $G^{(0)}$ is a matrix in the space of site, spin and frequency. Let us first derive the dynamical susceptibility. By taking the second derivative of A_m with respect to $\boldsymbol{S_q}(i\nu_m)$, which is the Fourier transform of $\boldsymbol{S}_i(i\nu_m)$, we obtain the Gaussian approximation for the dynamical susceptibility. We improve the result by renormalizing the coupling constant λ_0 and the Green function in the polarization bubble. The RKKY interaction is treated in the mean-field approximation, and intersite effects on the renormalized spin-fermion interaction vertex λ are neglected. Then we obtain

$$\chi(\boldsymbol{q}, i\nu_m)^{-1} = \chi_0(i\nu_m)^{-1} - 2\lambda^2\Pi(\boldsymbol{q}, i\nu_m) - J(\boldsymbol{q}), \tag{4.19}$$

where $J(\boldsymbol{q})$ is the Fourier transform of J_{ij} and

$$\Pi(\boldsymbol{q}, i\nu_m) = -\frac{1}{N}\sum_{\boldsymbol{k}} T\sum_n G_f(\boldsymbol{k}, i\epsilon_n) G_f(\boldsymbol{k}+\boldsymbol{q}, i\epsilon_n + i\nu_m). \tag{4.20}$$

4.8.3 Duality picture applied to the Anderson impurity

We assume that the local susceptibility $\chi_0(i\nu_m)$ and the coupling constant λ are determined mainly by the local correlation. Then these magnitudes can be estimated by applying the duality model to the

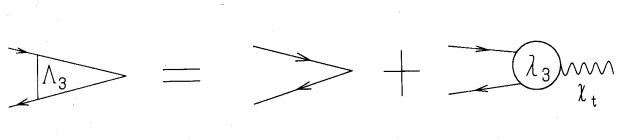

Figure 4.16: Feynman diagrams for eq.(4.23).

single-site Anderson model. For this purpose we first reformulate the local Fermi-liquid theory at zero temperature in terms of spin fluctuations and fermion excitations. For simplicity we assume a single conduction band with constant density of states ρ_c near the Fermi level. The vertex parts Λ_3 and λ_3 are introduced through the relation:

$$\langle T_\tau f_\uparrow^\dagger(\tau_1) f_\downarrow(\tau_2) f_\downarrow(\tau) f_\uparrow^\dagger(\tau)\rangle = -\int_{-\infty}^{\infty}\frac{d\epsilon_1}{2\pi}\int_{-\infty}^{\infty}\frac{d\epsilon_2}{2\pi}\exp[-i\epsilon_1\tau_1 + i\epsilon_2\tau_2 \tag{4.21}$$

$$-i(\epsilon_1-\epsilon_2)\tau]G_\uparrow(i\epsilon_1)G_\downarrow(i\epsilon_2)\Lambda_3(i\epsilon_1, i\epsilon_2; i\epsilon_2 - i\epsilon_1), \tag{4.22}$$

$$\Lambda_3(i\epsilon_1, i\epsilon_2; i\epsilon_2 - i\epsilon_1) = 1 + 2\lambda_3(i\epsilon_1, i\epsilon_2; i\epsilon_2 - i\epsilon_1)\chi(i\epsilon_2 - i\epsilon_1), \tag{4.23}$$

where $G_\sigma(i\epsilon)$ is the renormalized f-electron Green function. Figure 4.16 shows the relation diagramatically. It is obvious that λ_3 has a meaning of coupling strength between fermions and spin fluctuations. In terms of the self-energy $\Sigma_\sigma(i\epsilon)$ the Green function is given by

$$G_\sigma(i\epsilon) = [i\epsilon - \epsilon_f - \frac{1}{2}h\sigma - \Sigma_\sigma(i\epsilon) + i\Delta \mathrm{sgn}\epsilon]^{-1}, \tag{4.24}$$

where $\Delta = \pi V^2\rho_c$ is assumed to be a constant in the relevant energy range.

We invoke an important relation which is an example of the Ward-Takahashi identity [46]:

$$\Sigma_\uparrow(i\epsilon) - \Sigma_\downarrow(i\epsilon) = -2M\lambda_3(i\epsilon, i\epsilon; 0), \tag{4.25}$$

where $M = \langle S_z\rangle$ with $S_z = [f_\uparrow^\dagger f_\uparrow - f_\downarrow^\dagger f_\downarrow]/2$. The identity represents the many-body correction to the Zeeman splitting. It will be shown later that in the Kondo regime where charge fluctuations are suppressed, the many-body correction overwhelms the bare Zeeman energy.

It is possible to derive $\lambda_3(0,0;0) \equiv \lambda$ exactly in the case of $h = 0$. We make use of the Friedel sum rule for the spin polarization as explained in Appendix G. The result is given by

$$M = \frac{1}{2\pi}\sum_\sigma \sigma \mathrm{Im}\ln G_\sigma(0), \tag{4.26}$$

where (and in the following) we omit writing the positive infinitesimal imaginary part in the argument of the Green function. Then the static susceptibility χ is given by

$$\chi = \frac{\partial M}{\partial h} = \frac{1}{2}\rho_f(0)[1 + 2\lambda\chi], \tag{4.27}$$

where $\rho_f(0) = -\mathrm{Im}G_\sigma(0)/\pi$. Thus λ is given in terms of $\rho_f(0)$ and χ. In the Kondo limit where $\chi \gg \rho_f(0)$ we obtain

$$\lambda = \pi\Delta.$$

The full self-energy $\Sigma_\sigma(\epsilon)$ near the Fermi level depends so strongly on ϵ that the wave function renormalization factor is much smaller than unity. Then the fermion degrees of freedom alone do not contribute to charge and spin susceptibilities. However the magnetic response is influenced by fermions through the coupling λ. It follows that for small magnetic field the effective Zeeman splitting of the fermion levels is *twice* of that without hybridization. This is seen if we recognize that the effective Zeeman splitting is given by $a_f[\Sigma_\uparrow(0) - \Sigma_\downarrow(0)]$ and $M = h/(4T_K)$.

In the duality picture, the contribution of the local part of the f electrons to the dynamical susceptibility is written as $\chi_0(\omega)$. This is fixed by the condition that the full susceptibility $\chi(\omega)$ given by the

duality model must be identical to that given by the Fermi-liquid formula eq.(2.69). In the duality model we regard the spin-fermion coupling constant λ as independent of ω. Then we obtain

$$\chi(\omega) = \frac{\chi_0(\omega)}{1 - 2\lambda^2 \Pi(\omega)\chi_0(\omega)} \tag{4.28}$$

where $\Pi(\omega)$ is given by eq.(4.20) with $G_f(\boldsymbol{k}, i\epsilon_n)$ replaced by the impurity counterpart:

$$G_f(i\epsilon_n) = a_f \Big/ \left(i\epsilon_n - \tilde{\epsilon}_f - a_f \sum_k \frac{V^2}{i\epsilon_n - \epsilon_k} \right). \tag{4.29}$$

Equation (4.28) is exact in the static limit since the coupling constant $\lambda = \pi\Delta$ takes precise account of the vertex correction there. By comparing eq.(4.28) with eq.(2.69) we obtain

$$\chi_0(\omega)^{-1} = 2\lambda^2 \Pi(\omega) + \frac{2}{\Lambda_0^2 \Pi(\omega)} - 4T_K, \tag{4.30}$$

There is no ω-linear imaginary part in $\chi_0(\omega)$ because of the cancellation between the first and second terms. This quasi-gap behavior is consistent with our definition of the spin degrees of freedom which do not involve the low-energy fermion excitations as their constituents. Thus the spin fluctuations do not contribute to the T-linear specific heat without coupling to fermion degrees of freedom. The specific heat $C = \gamma T$ of the Anderson model is determined by the renormalized Green function $G_f(\epsilon)$ as

$$\gamma = \frac{4\pi}{3} \mathrm{Im} \frac{\partial}{\partial \epsilon} \ln G_\sigma(\epsilon)\big|_{\epsilon=0},$$

just as in the Fermi-liquid theory.

We can rely on eq.(2.69) up to frequencies of the order of T_K. Then eq.(4.30) fixes $\chi_0(\omega)$ for these frequencies. Figure 4.17 shows the real and imaginary parts of the susceptibilities $\chi(\omega), \chi_0(\omega)$ and $\Lambda_0^2\Pi(\omega)$. As is evident in Fig.4.17(a), $\mathrm{Im}\chi_0(\omega)/\omega$ displays a structure which is interpreted as a pseudo-gap of the order of T_K for spin excitations. There is a corresponding structure in $\mathrm{Re}\chi_0(\omega)$ as shown in Fig.4.17(b). Note that $\chi_0(0) = \chi(0)/3$. We remark that $\Lambda_0^2\Pi(\omega)/2$ corresponds to the dynamical susceptibility of ref.[47] if one regards $2T_K$ as the Kondo temperature. At high frequencies the imaginary parts converge to the same asymptotic behavior proportional to ω^{-3}. The odd power is caused by the logarithmic singularity at $\omega = \infty$ in eq.(4.30). By comparison with a numerical result obtained by the Wilson-type renormalization theory [45, 48], it is seen that the quasi-particle RPA given by eq.(2.69) is an excellent approximation for all frequencies. Hence we expect that eq.(4.30) is also a reasonably accurate representation of $\chi_0(\omega)$ for all ω.

4.8.4 Metamagnetism in the Duality Model

We study the magnetic equation of state on the basis of eqs.(4.17) and (4.18). The basic observation is that the coupling between spins and fermions causes a large nonlinear effect as the spin polarization increases. The experimental results on $CeRu_2Si_2$ have been discussed in 3.1.1. Now we give a theoretical aspect of the metamagnetic behavior of heavy electrons. It should be remarked that there is no established result on the mechanism of the phenomena. Therefore the discussion below is presented just to show a consequence of the duality model.

We assume the presence of a static magnetic field $\boldsymbol{h_q}$ which is modulated with wave number $\boldsymbol{q}$. Then the spin variable $\boldsymbol{S_q} \equiv \boldsymbol{S_q}(i\nu_m = 0)$ becomes macroscopic. We treat this component in the saddle point approximation, and spin fluctuations with other wave numbers and frequencies as Gaussian. The equation of state is given by the zero average of $\partial A_m/\partial \boldsymbol{S}_{-\boldsymbol{q}}$ over the Gaussian variables as follows:

$$[\chi_0(0)^{-1} - J(\boldsymbol{q}) - 2\lambda^2 \Pi(\boldsymbol{q}; \boldsymbol{S_q})]\boldsymbol{S_q} = \boldsymbol{h_q}, \tag{4.31}$$

where $\Pi(\boldsymbol{q}; \boldsymbol{S_q})$ is the polarization function of fermions under finite $\boldsymbol{S_q}$. For general values of $\boldsymbol{q}$, $\Pi(\boldsymbol{q}; \boldsymbol{S_q})$ does not have a simple expression. However for the case of $\boldsymbol{q} = 0$ or $\boldsymbol{q} = \boldsymbol{Q}$ with $\boldsymbol{Q}$ being a reciprocal lattice vector, we obtain the compact formula

$$\Pi(\boldsymbol{q}; \boldsymbol{S_q}) = -\frac{1}{N} \sum_{\boldsymbol{k}} T \sum_n [G_f(\boldsymbol{k}, i\epsilon_n)^{-1} G_f(\boldsymbol{k}+\boldsymbol{q}, i\epsilon_n)^{-1} - |\lambda \boldsymbol{S_q}|^2]^{-1}, \tag{4.32}$$

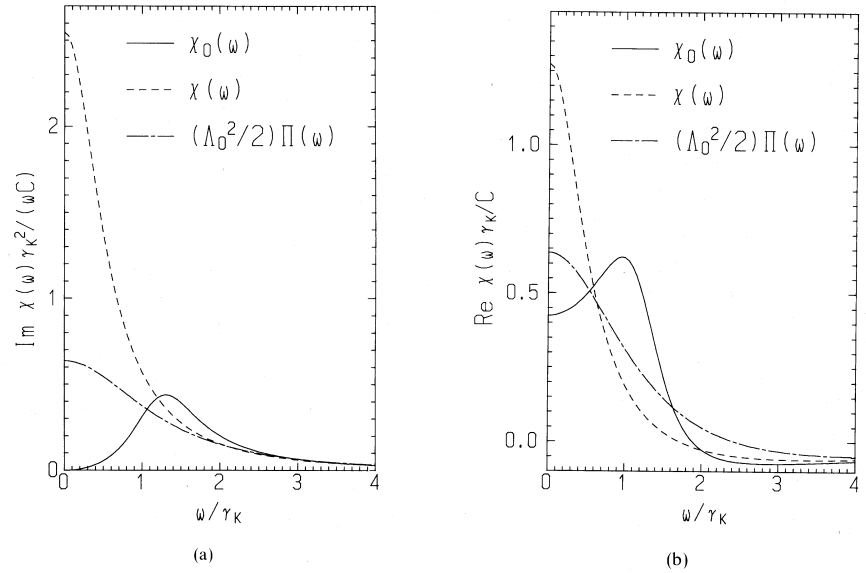

Figure 4.17: Three kinds of susceptibilities: $\chi_0(\omega)$ (solid line), $\chi(\omega)$ (dashed line), and $a_f^{-2}\Pi(\omega)$ (dash-dotted line). Imaginary parts are shown in (a) and real parts in (b).

which of course reduces to Eq.(4.20) in the case of $\boldsymbol{S_q} = 0$. The itinerant fermions feel $\lambda \boldsymbol{S_q}$ as a fictitious magnetic field with wave number $\boldsymbol{q}$.

Figure 4.18 shows an example of numerical calculation [49]. The parameters in the calculation are taken in units of the half-width D of the conduction band as follows:

$$\rho_c = 1/2,\ a_f\lambda = 0.01\pi^2/2,\ a_f V^2\rho_c = 5\times 10^{-3},\ \chi_0(0)^{-1} - J(0) = 2a_f\lambda.$$

The parameter ξ_F is the energy (measured from the Fermi level) of the conduction electron with the Fermi wave number. The magnetization jumps for large enough coupling between fermions and spins. This jump corresponds to the first-order metamagnetic transition. With smaller coupling there appears smooth but nonlinear behavior of the magnetization, which seems to related to the pseudo-metamagnetic transition discussed in 3.1.1. This behavior in the duality model comes from non-monotonic dependence of $\Pi(0;\boldsymbol{S_0})$ on the magnetization $M = |\boldsymbol{S_0}|$. The itinerant band has a peak in density of states near the Fermi level due to hybridization, and the Zeeman splitting pushes the peak of either up or down spins toward the Fermi level. Then $\Pi(0;\boldsymbol{S_0})$ increases up to certain magnitude of M. With further increase of M the Zeeman-split peaks of both spins go off the Fermi level so that $\Pi(0;\boldsymbol{S_0})$ turns to decrease. We note that the mechanism in the present model calculation is not qualitatively different from a rigid band picture of f-electrons. The many-body effect is taken into account only in reducing the energy scale. It is difficult in the duality model to incorporate more details of interaction between quasi-particles and magnetization.

A very interesting feature in heavy electron systems is that the external magnetic field causes a nonlinear effect in the itinerant state of f electrons. Experimentally this appears as a change of the Fermi surface probed by the de Haas-van Alphen effect. In the case of $CeRu_2Si_2$ the Fermi surface below $H = 7.7T = H_M$ is roughly consistent with the one predicted by the energy band theory. As the magnetic field becomes close to H_M, the signal shows a strange temperature dependence, suggesting that the effective mass and/or the Zeeman splitting depend on T. Above H_M the Fermi surface observed has a shape consistent with the localized picture [50]. We note that $CeRu_2Si_2$ has a strong Ising-type anisotropy. Similar magnetization is observed in UPt_3 which has a strong XY-type (easy-plane) anisotropy [51].

There are also many heavy electron systems without the metamagnetic behavior. The characteristics in magnetization thus depend on details of the system. Such details are best dealt with by the energy-band theory. In the purely itinerant picture, the metamagnetic behavior is ascribed to characteristic band structures such as a high peak in the density of states near the Fermi level. Since the Zeeman

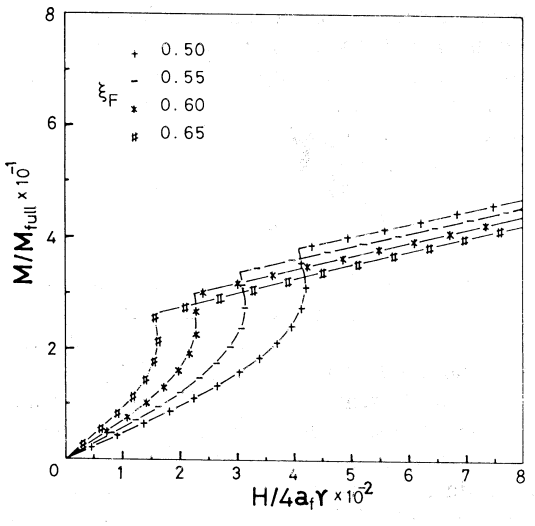

Figure 4.18: Magnetization vs applied magnetic field calculated in the duality model. The parameters in the calculation are explained in the text. The parameter γ in the abscissa should read λ in the text.

splitting of the energy band causes the peak to cross the Fermi level, the differential susceptibility should be enhanced at the crossing. In this picture, however, the structure of the density of states should be extremely sharp, of the order of 0.1 K in $CeRu_2Si_2$. It is impossible to reproduce such a tiny structure by the ordinary band calculation. We remark that the energy scale of 0.1 K is much smaller than the Kondo temperature of $CeRu_2Si_2$ which is of the order of 10 K. In the duality model the tiny structure comes from combination of the Kondo effect and the coherent hybridization in the periodic lattice. It is an open problem whether such tiny structure reflects an intersite spin-spin correlation in addition to the Kondo effect.

4.8.5 Weak antiferromagnetism

On the basis of the magnetic equation of state in the duality model, we proceed to discuss weak antiferromagnetism. In this section we take a one-dimensional model to demonstrate the effect of nesting in the simplest way. In the duality model the weak antiferromagnetism results from strong sensitivity of the itinerant exchange to the magnitude of magnetization. Let us assume that there is only one heavy electron band which crosses the Fermi level. We evaluate $\Pi(Q; \boldsymbol{S_Q})$ with use of the quasi-particle form given by eq.(4.29). We note that the renormalization factor a_f is the order of $T_K/(\pi^2 V^2 \rho_c)$.

The spectrum E_k of the heavy electron is derived very simply provided that $|E_k| \ll |\epsilon_k|$ is satisfied for each k near the Fermi surface. We expand ϵ_k around the Fermi wave number $\pm k_F$ as

$$\epsilon_k = \epsilon_F \pm v_c(k \mp k_F), \tag{4.33}$$

where v_c is the velocity of the conduction band. Then we obtain

$$E_k \cong \pm a_f \sum_{\mu} (V/\epsilon_F)^2 v_c(k \mp k_F) \equiv \pm v_f(k \mp k_F), \tag{4.34}$$

$$G_f(k, i\epsilon_n) \cong a_f/(i\epsilon_n - E_k). \tag{4.35}$$

The interaction strength between quasi-particles and spins is determined by $\lambda_f \equiv a_f \lambda$. We introduce the misfit energy δ_m by $\delta_m \equiv v_f|Q - 2k_F|$ which simulates deviation from complete nesting in higher dimensions. Then with use of Eq.(4.34) up to a cut-off energy $\pm D_f$, which should be of $O(T_K)$, we

evaluate Eq.(4.32) at $T = 0$. Straightforward integration gives

$$\Pi(Q;\boldsymbol{S}_Q) = \begin{cases} \dfrac{1}{2}a_f^2\rho_f \ln \dfrac{D_f}{[(\delta_m)^2 - |\lambda_f \boldsymbol{S}_Q|^2]^{1/2} + \delta_m}, & (\delta_m > |\lambda_f \boldsymbol{S}_Q|) \\ \dfrac{1}{2}a_f^2\rho_f \ln \left|\dfrac{D_f}{\lambda_f \boldsymbol{S}_Q}\right|, & (\delta_m < |\lambda_f \boldsymbol{S}_Q|) \end{cases} \tag{4.36}$$

where we have defined the quasi-particle density of states $\rho_f \equiv (\pi v_f)^{-1}$ with the lattice constant being unity. In the case of complete nesting the spontaneous magnetization at $T = 0$ is given by the solution of

$$\frac{1}{\chi_0(0)} - J(Q) - \lambda_f^2\rho_f \ln \left|\frac{D_f}{\lambda_f \boldsymbol{S}_Q}\right| = 0. \tag{4.37}$$

In eq.(4.37) the smaller magnetization causes larger exchange field from the itinerant part. Since we have $D_f \sim \lambda_f \sim \lambda_f^2\rho_f \sim T_K$ as order of magnitudes, the condition for weak antiferromagnetism under the very good nesting is that $\chi_0(0)^{-1} - J(Q)$ should be much larger than T_K. Namely the relevant exchange interaction responsible for the weak antiferromagnetism is not the usual RKKY interaction. Instead the heavy electrons themselves mediate the coupling of spins. In this respect the weak antiferromagnetism of heavy electrons is very similar to that of band electrons in transition metals [52].

In contrast to transition metals, however, the presence of the RKKY interaction leads to specific dynamical and temperature effects. Suppose that the RKKY interaction does not favor the wave number Q so that $J(Q)$ is negative. Then $\chi_0(0)^{-1} - J(Q)$ can be much larger than T_K, and hence than $\lambda_f^2\rho_f$. In the present model the dominant exchange interaction changes from the RKKY type at high T to the anomalous one mediated by itinerant heavy electrons with decreasing T. In this connection we note that the wave number of most dominant magnetic fluctuations in UPt_3 depend on temperature and excitation energy. The relevant Q for the Néel order can be seen only at low temperature and with low excitation energy [53].

The Néel temperature T_N can be derived by evaluating $\Pi(Q;0)$ at finite temperatures. The result at T larger than δ_m is given by

$$\Pi(Q;\boldsymbol{S_Q}) \cong \frac{1}{2}a_f^2\rho_f \ln\left(\frac{D_f}{T}\right). \tag{4.38}$$

Comparison with Eq.(4.37) gives the relation between T_N and the zero-temperature magnetization $\boldsymbol{S}_Q$ as

$$T_N \cong \lambda_f |\boldsymbol{S}_Q|. \tag{4.39}$$

Thus in the present model the weak antiferromagnetism requires T_N to be much smaller than λ_f and, hence than T_K. The small energy scale T_N is generated by the nesting property of the heavy-electron band. This is again similar to the weak antiferromagnetism in itinerant electrons where the role of T_K is played by the Fermi energy of the conduction band.

Bibliography

[1] T. Kohra, Y. Kohori, K. Asayama, Y. Kitaoka, M.B. Maple and M.S. Torikachvilli, Jpn.J.Appl.Phys. **26**, 1247 (1987) ; Y. Kohori et al, J. Phys. Soc. Jpn. **65**, 679 (1996).

[2] T.T.M. Palstra, A.A. Menovsky, J. van den Berg, A.J. Dirkmaat, P.H. Kes,G.J. Nieuwenhuys and J.A. Mydosh, Phys. Rev. Lett. **55**, 2727 (1985).

[3] G.J. Nieuwenhuys, Phys. Rev. B**35**, 5260 (1987).

[4] P. Santini and G. Amoretti, Phys. Rev. Lett. **73**,1027 (1994).

[5] H. Amitsuka and T. Sakakibara, J. Phys. Soc. Jpn. **63**, 736 (1994).

[6] C. Broholm, H. Lin, P.T. Matthews, T.E. Mason, W.J.L. Buyers, M.F. Collins, A.A. Menovsky, J.A. Mydosh and J.K. Kjems, Phys. Rev. **B43**,12809(1991).

[7] W.J.L. Buyers and T.M. Holden, *Handbook on the Physics and Chemistry of Actinides*, eds. G.H. Lander and A.J. Freeman (North-Holland 1985) vol.2, p.239.

[8] M.B. Walker, C. Kappler, K.A. McEwen, U. Steigenberger, K.N. Clausen, J. Phys. Condens. Matter **6**, 7365 (1994).

[9] C. Geibel, S. Thies, D. Kaczorowski, A. Mehner, A. Grauel, B. Seidel, U. Ahlheim, R. Helfrich, K. Peterson, C.D. Bredl, F. Steglich, Z. Phys. **B 83**, 305 (1991).

[10] M. Kyogaku, Y. Kitaoka, K. Asayama, C. Geibel, C. Schank and F. Steglich, J. Phys. Soc. Jpn. **62**, 4016 (1993).

[11] S.Takagi, T. Homma and T. Kasuya, J. Phys. Soc. Jpn. **58**, 4610 (1989).

[12] S.Horn, E.Holland-Moritz, M.Loewenhaupt, F.Steglich, H.Scheuer, A.Benoit and J.Flouquet, Phys. Rev. **B23**, 3171 (1981).

[13] H.Nakamura, Y.Kitaoka, T.Iwai, H.Yamada and K.Asayama, J. Phys. Condens. Matter. **4**, 473 (1992).

[14] Y. Kitaoka, H. Nakamura, T. Iwai, K. Asayama, U. Ahlheim, C. Geibel, C. Schank and F. Steglich.J. Phys. Soc. Jpn. **60**, 2122 (1992).

[15] R. Feyerherm *et al.*, Physica B **206-207**, 596 (1995) ; Phys. Rev. B **56**, 699 (1997).

[16] U. Rauchschwalbe et al., J. Magn. Magn. Mater. **63-64**, 347 (1987).

[17] H.Nakamura, Y.Kitaoka, H.Yamada and K.Asayama, J. Magn. Magn. Mater. **76-77**, 517 (1988).

[18] Y. Kitaoka, H. Tou, G.-q. Zheng, K. Ishida, K. Asayama, T.C. Kobayashi, A. Kohda, N. Takeshita, K. Amaya, Y. Onuki, G. Geibel, C. Schank and F. Steglich, Physica B **206-207**, 55 (1995).

[19] Y. J. Uemura *et al.*, Phys. Rev. B **39**, 4726 (1989); G.M.Luke *et al.*, Phys. Rev. Lett. **59**, 1853 (1994).

[20] G. Bruls, B. Wolf, D. Finsterbusch, P. Thalmeier, I. Kouroudis, W. Sun, W. Assmus, and B. Luthi, Phys. Rev. Lett. **72**, 1754 (1994).

[21] F. Steglich *et al.*, J. Phys. Cond. Matter. **8**, 9909 (1996).

[22] R. Modler *et al.*, Physica B **206-207**, 586 (1995).

[23] P. Gegenwart *et al.*, Phys. Rev. Lett. **81**, 1501 (1998).

[24] K. Ishida et al, Phys. Rev. Lett. **82**, 5353 (1999).

[25] M.Hunt, P.Messon, P.A.Probst, P.Reinders, M.Springford, W.Assmus and W.Sun, J. Phys. Condens. Matter. **2**, 6859 (1990).

[26] M.Lang, R.Molder, U.Ahlheim, R.Helfrich, P.H.P.Reinders and F.Steglich, Phys. Scripta **T39**, 135 (1991).

[27] F.Thomas, J.Thomasson, C.Ayache, C.Geibel and F.Steglich, Physica **B186-188**, 303 (1993).

[28] B. Bogenberger and H. v. Lohneysen, Phys. Rev. Lett. **74**, 1016 (1995).

[29] J.M. Effantin, J. Rossat-Mignod, P. Burlet, H. Bartholin, S. Kunii and T. Kasuya, J. Magn. Magn. Mater. **47&48**, 145 (1985).

[30] G. Uimin, Y. Kuramoto and N. Fukushima, Solid State Commun. **97**, 595 (1996).

[31] N. Fukushima and Y. Kuramoto, J. Phys. Soc. Jpn. **67**, 2460 (1998).

[32] F. Ohkawa, J. Phys. Soc. Jpn. **52**, 3897 (1983).

[33] R. Shiina, H. Shiba and P. Thalmeier, J. Phys. Soc. Jpn. **67**, 1741 (1997).

[34] M. Takigawa, H. Yasuoka, T. Tanaka and Y. Ishizawa, J. Phys. Soc. Jpn. **52**, 728 (1983).

[35] O. Sakai, R. Shiina, H. Shiba and P. Thalmeier, J. Phys. Soc. Jpn. **66**, 3005 (1997).

[36] T. Tayama, T. Sakakibara, K.Tenya, H. Amitsuka and S. Kunii, J. Phys. Soc. Jpn. **66**, 2268 (1997).

[37] M. Hiroi, M. Sera, N. Kobayashi and S. Kunii, Phys. Rev. B**55**, 8339 (1997).

[38] S. Nakamura, O. Suzuki, T. Goto, S. Sakatsume, T. Matsumura and S. Kunii, J. Phys. Soc. Jpn. **66**, 552 (1997).

[39] M. Kohgi, T. Osakabe, K. Ohyama and T. Suzuki, Physica B **213&214**, 110 (1995).

[40] T. Suzuki, Physica B **186-189**, 347 (1993).

[41] A. Ochiai et al, J. Phys. Soc. Jpn. **59**, 4129 (1990)

[42] M. Kohgi et al., Physica B**259-261** 269 (1999).

[43] P. Fulde, B. Schmidt and P. Thalmeier, Europhys. Lett., **31** 323 (1995).

[44] Y. Kuramoto, Physica **B156&157**, 789 (1989).

[45] Y. Kuramoto and K. Miyake, J. Phys. Soc. Jpn. **59**, 2831 (1990).

[46] T. Koyama and M. Tachiki, Prog. Theor. Phys. **Suppl. 80**, 108 (1984).

[47] Y. Kuramoto and E. Mueller-Hartmann, J. Magn. & Magn. Mater. **52**, 122 (1985).

[48] O. Sakai, Y. Shimizu and T. Kasuya, J. Phys. Soc. Jpn. **58**, 3666 (1989).

[49] K. Miyake and Y. Kuramoto, J. Magn. & Magn. Mater. **90&91**, 438 (1990).

[50] M. Takashima et al., J. Phys. Soc. Jpn. **65**, 515 (1996).

[51] A. de Visser et al., Physica **B171**, 190 (1991).

[52] T. Moriya, *Spin Fluctuations in Itinerant Electron Magnetism*, (Springer, Berlin, 1985).

[53] G. Aeppli et al., Phys. Rev. Lett. **60**, 615 (1988).

Chapter 5

Superconducting States

5.1 Historical Overview

Superconductivity, which was one the best understood many-body problems in physics[1], became again a challenging problem when a new kind of superconductivity was discovered in $CeCu_2Si_2$ by Steglich et al [2]. The system is one of heavy-electron materials close to magnetic instability. In the subsequent decade, intensive investigations of a class of uranium compounds established a new field of heavy-electron superconductivity by successive discoveries of superconductivity in UBe_{13}, UPt_3, URu_2Si_2, UPd_2Al_3 and UNi_2Al_3 [3, 4]. The most important characteristics for a series of uranium heavy-electron superconductors are that superconductivity coexists with the antiferromagnetism except for UBe_{13}, and that the specific heat coefficient γ lies in a broad range from 700 mJ/(mole K^2) (UBe_{13}) to 60 mJ/(mole K^2)(URu_2Si_2). The f-shell electrons, which are strongly correlated by Coulomb repulsive interaction, determine the properties of heavy quasi-particles at the Fermi level. This gives rise to a large γ value as well as an enhanced spin susceptibility. Hence, the Fermi energy is also quite small: $T_F = 10 \sim 100$K and, as a result, the transition temperature is also small, ranging from $T_c = 0.5$K to 2K. The magnetic ordering temperature $T_N = 5 \sim 20$K is by one order of magnitude higher than T_c. A jump $(C_s - C_n)/C_n$ of the specific heat normalized by the value C_n just above T_c is of $O(1)$ in all compounds. This result demonstrates that the superconductivity is produced mainly by the heavy quasi-particles. Due to the strong Coulomb repulsion among f electrons, it seems hard for the heavy quasi-particles to form ordinary s-wave Cooper pairs with large amplitude at zero separation of the pair. In order to avoid Coulomb repulsion, the system would favor an anisotropic pairing channel like spin triplet p-wave or spin singlet d-wave. These types of paired states are actually realized in superfluid ^{3}He where pairings with p-wave spin triplet are formed with a few phases of different symmetries such as A, A_1 and B phases [5].

Ferromagnetic spin fluctuations (paramagnons) play a major part in the effective potential which produces the anisotropic pairing. For example the pairing in the A-phase of ^{3}He was identified as an anisotropic type called the Anderson-Brinkman-Morel (ABM) state with the energy gap vanishing on points at the Fermi surface [6]. In many respects, the analogy with ^{3}He is a good guide for the interpretation of the experimental results in heavy-electron superconductors. The on-site Coulomb repulsive interaction produces AF spin fluctuations as a low-energy excitation, which play a role similar to ferromagnetic spin fluctuations in liquid ^{3}He. There are, on the other hand, important differences between these two systems. The strong correlation effect, the spin-orbit interaction, and the CEF characterize the heavy-electron systems. Thus the problem of the heavy-electron superconductivity turns out to be much more complicated than in ^{3}He.

The heavy-electron superconductivity has also intimate connection to another new kind of superconductivity; the high-temperature superconductivity discovered in a copper-oxide $La_{2-x}Ba_xCuO_4$ by Bednorz and Müller in 1986[7]. Intensive study of the class of copper oxides led to successive discoveries of new superconducting systems, each exceeding the other in T_c value: Y-Ba-Cu-O system with $T_c \sim 90$K, Bi-Sr-Ca-Cu-O system with $T_c \sim 110$K, Tl-Ba-Ca-Cu-O system with $T_c \sim 120$K and Hg-Ba-Cu-O system with $T_c \sim 130$K[8]. These new superconductors exhibit unconventional properties, and there is increasing evidence that order parameter symmetry could be of the anisotropic $d_{x^2-y^2}$ type. In copper oxides AF spin fluctuation is considered to play a vital role in producing the anisotropic pairing [9, 10]. Even if there is a difference of more than two orders of magnitude between the T_c's in heavy-

electron and high-T_c copper oxide superconductors, they share the common feature of strongly correlated electrons in partially filled f- or d-shells. It is a common property of the anisotropic superconductivity that low-lying excitations in the quasi-particle spectrum originate from the presence of zero gap either on points or along a line at the Fermi surface. These zeroes give rise to a power-law temperature dependence of various physical quantities instead of the exponential dependence seen in conventional s-wave superconductors. We resume more detailed comparison in Chapter 6.

5.2 Fundamentals of Anisotropic Pairing

5.2.1 Symmetry of the pairing

spherical symmetry

Let us consider the symmetry property of the pairing. For simplicity we first assume spherical symmetry in the system and neglect the spin-orbit interaction. The situation is approximately realized in superfluid ^{3}He. In the case of heavy electrons, the effects of CEF and spin-orbit interaction are very important and will be discussed later. For description of the symmetry we draw an analogy with the one-body density matrix given by $\rho_{\alpha\beta}(\boldsymbol{k}) = \langle a_\beta(\boldsymbol{k})^\dagger a_\alpha(\boldsymbol{k})\rangle$ in k-space. This can be parametrized as

$$2\rho_{\alpha\beta}(\boldsymbol{k}) = n(\boldsymbol{k})\delta_{\alpha\beta} + \boldsymbol{m}(\boldsymbol{k})\cdot\boldsymbol{\sigma}_{\alpha\beta}(\boldsymbol{k}), \tag{5.1}$$

where $n(\boldsymbol{k})$ is the occupation number and $\boldsymbol{m}(\boldsymbol{k})$ is the spin polarization. Here $\boldsymbol{\sigma}$ is the vector composed of the Pauli matrices. The average magnetization $\langle \boldsymbol{M}(\boldsymbol{k})\rangle$ is given by

$$\langle \boldsymbol{M}(\boldsymbol{k})\rangle = -\frac{1}{4}g\mu_B \mathrm{Tr}[\boldsymbol{\sigma}\rho(\boldsymbol{k})] = -\frac{1}{2}g\mu_B \boldsymbol{m}(\boldsymbol{k}), \tag{5.2}$$

where g is the g-factor.

We now turn to the pairing amplitude $\Psi_{\alpha\beta}(\boldsymbol{k})$ defined by

$$\Psi_{\alpha\beta}(\hat{k}) = \langle a_\alpha(\boldsymbol{k})a_\beta(-\boldsymbol{k})\rangle, \tag{5.3}$$

where we have assumed zero total momentum of the pair. Here $\hat{k}$ denotes a unit vector in the direction of $\boldsymbol{k}$ which is near the Fermi surface. Because of the small energy scale of superconductivity as compared with the Fermi energy, we have neglected in $\Psi_{\alpha\beta}(\hat{k})$ slight dependence on $|\boldsymbol{k}|$. In order to make analogy to the symmetry of the density matrix, we introduce the time reversal operator K acting on the single-particle state ϕ_α with a spin component α as

$$\langle \boldsymbol{r}\beta|K\phi_\alpha\rangle \equiv \phi_\beta(\boldsymbol{r})^*(i\sigma_y)_{\beta\alpha}, \tag{5.4}$$

If $\phi_\alpha(\boldsymbol{r})$ is an eigenstate of the single-particle Hamiltonian with a magnetic field, $K\phi_\alpha$ represents a solution with reversed magnetic field. Equation (5.4) for spin 1/2 is an example of the more general property of K as the product of a unitary operator and taking the complex conjugate of the wave function. The appearance of the real unitary operator $i\sigma_y$ here is connected with the property

$$i\sigma_y\boldsymbol{\sigma}(i\sigma_y)^{-1} = -\boldsymbol{\sigma}^*,$$

which means that the spin operator $\boldsymbol{\sigma}/2$ is odd under time reversal.

The convenience of using $i\sigma_y$ is clear from the identity for the singlet pair creator:

$$a_\uparrow^\dagger(\boldsymbol{k})a_\downarrow^\dagger(-\boldsymbol{k}) - a_\downarrow^\dagger(\boldsymbol{k})a_\uparrow^\dagger(-\boldsymbol{k}) = \sum_{\alpha\beta} a_\alpha^\dagger(\boldsymbol{k})(i\sigma_y)_{\alpha\beta}a_\beta^\dagger(-\boldsymbol{k}),$$

where both sides transform as a scalar. On the other hand, the triplet pair with $S_z = 1$ is given by

$$a_\uparrow^\dagger(\boldsymbol{k})a_\uparrow^\dagger(-\boldsymbol{k}) = \frac{1}{2}\sum_{\alpha\beta} a_\alpha^\dagger(\boldsymbol{k})[(\sigma_x + i\sigma_y)i\sigma_y]_{\alpha\beta}a_\beta^\dagger(-\boldsymbol{k}).$$

It can easily be checked that the triplet pair with $S_z = -1$ obtains $(\sigma_x - i\sigma_y)$ instead of $(\sigma_x + i\sigma_y)$ in the above, and the pair with $S_z = 0$ obtains $2\sigma_z$ instead. Thus we parametrize the pairing amplitude as

$$\Psi_{\alpha\beta}(\hat{k}) = \{[\Psi_s(\hat{k}) + \boldsymbol{\Psi}_t(\hat{k})\cdot\boldsymbol{\sigma}]i\sigma_y\}_{\alpha\beta}, \tag{5.5}$$

where $\Psi_s(\hat{k})$ describes the singlet part and the vector $\boldsymbol{\Psi}_t(\hat{k})$ describes the triplet one. In the case of s-wave pairing, $\Psi_s(\hat{k})$ is just a constant. With finite angular momentum l, it is expanded in terms of spherical harmonics as

$$\Psi_s(\hat{k}) = \sum_m c_m Y_{lm}(\hat{k}).$$

On the other hand, for the triplet pair with $S_z = 0$, for example, we obtain

$$\boldsymbol{\Psi}_t(\hat{k}) = \hat{z} f(\hat{k}), \tag{5.6}$$

where $\hat{z}$ is the unit vector along the z axis and $f(\hat{k})$ specifies the orbital degrees of freedom. The latter is expanded in terms of spherical harmonics as the singlet pairing. In the case of $S_z = \pm 1$, $\hat{z}$ is replaced by $\hat{x} \pm i\hat{y}$. Fermi statistics require that $\Psi_s(\hat{k})$ is an even function of $\hat{k}$ and $\boldsymbol{\Psi}_t(\hat{k})$ is odd. These types of pairing do not occur at the same time.

Let us introduce the gap function $\Delta_{\alpha\beta}(\hat{k})$ which is related to the pairing amplitude by

$$\Delta_{\alpha\beta}(\hat{k}) = \sum_{\mu\nu} \sum_p \langle \alpha\beta | V(\boldsymbol{k}, \boldsymbol{p}) | \nu\mu \rangle \Psi_{\mu\nu}(\hat{p}).$$

Here $\langle \alpha\beta | V(\boldsymbol{k}, \boldsymbol{p}) | \nu\mu \rangle$ is the matrix element of the pairing interaction. As before the convention $|\alpha\beta\rangle^\dagger = \langle \beta\alpha |$ is taken in ordering the one-particle states. Then we parametrize

$$\Delta_{\alpha\beta}(\hat{k}) = \{ [D(\hat{k}) + \boldsymbol{d}(\hat{k}) \cdot \boldsymbol{\sigma}] i\sigma_y \}_{\alpha\beta} \tag{5.7}$$

The quantity $D(\hat{k})$ and $\boldsymbol{d}(\hat{k})$ have the same transformation properties as $\Psi_s(\hat{k})$ and $\boldsymbol{\Psi}_t(\hat{k})$, respectively. In contrast to $n(\hat{k})$ and $\boldsymbol{m}(\hat{k})$ in the density matrix, the gap function need not be real. This is associated with the gauge symmetry spontaneously broken in the superconducting phase.

In addition to gauge symmetry, other symmetries like spherical symmetry and time reversal can be broken. In order to deal with a general case we introduce [11] the four component field $\psi_i(\boldsymbol{k})$ $(i = 1, 2, 3, 4)$ by the vector

$$\boldsymbol{\psi}(\boldsymbol{k}) = (a_\uparrow(\boldsymbol{k}), a_\downarrow(\boldsymbol{k}), a_\uparrow^\dagger(-\boldsymbol{k}), a_\downarrow^\dagger(-\boldsymbol{k}))^t. \tag{5.8}$$

We call the first and second components conjugate to each other. The third and the fourth components are also conjugate partners, while the first and the fourth, as well as the second and the third, are time-reversal partners. The mean-field Hamiltonian is written as

$$H = \sum_k \sum_{ij} h_{ij}(\boldsymbol{k}) \psi_i^\dagger(\boldsymbol{k}) \psi_j(\boldsymbol{k}) = \sum_k \boldsymbol{\psi}^\dagger(\boldsymbol{k}) \hat{h}(\boldsymbol{k}) \boldsymbol{\psi}(\boldsymbol{k}),$$

where the 4×4 matrix $\hat{h} = \{h_{ij}\}$ is given by

$$\hat{h}(\boldsymbol{k}) = \begin{pmatrix} \epsilon_{\boldsymbol{k}} & \Delta(\hat{k}) \\ \Delta(\hat{k})^\dagger & -\epsilon_{-\boldsymbol{k}} \end{pmatrix}. \tag{5.9}$$

Here the entries in the right hand side are 2×2 matrices.

The eigenvalues of $\hat{h}(\boldsymbol{k})$ are most easily obtained by taking the square of it. Then we get

$$\hat{h}(\boldsymbol{k})^2 = \begin{pmatrix} \epsilon_{\boldsymbol{k}}^2 + \Delta\Delta^\dagger & 0 \\ 0 & \epsilon_{\boldsymbol{k}}^2 + \Delta^\dagger\Delta, \end{pmatrix}. \tag{5.10}$$

where

$$\Delta\Delta^\dagger = |D|^2 + |\boldsymbol{d}|^2 + \boldsymbol{w} \cdot \boldsymbol{\sigma}, \quad \Delta^\dagger\Delta = |D|^2 + |\boldsymbol{d}|^2 - \boldsymbol{w} \cdot \boldsymbol{\sigma},$$

with $\boldsymbol{w} = i\boldsymbol{d} \times \boldsymbol{d}^* = \boldsymbol{w}^*$. One calls the pairing with $\boldsymbol{w} = 0$ unitary and the other case non-unitary.

We diagonalize the 2×2 submatrices in eq.(5.10) and obtain the quasi-particle spectrum as

$$E_{\tau\sigma}(\boldsymbol{k}) = \tau \sqrt{\epsilon(\boldsymbol{k})^2 + |D(\hat{k})|^2 + |\boldsymbol{d}(\hat{k})|^2 + \sigma |\boldsymbol{w}(\hat{k})|},$$

where $\tau = \pm 1$ specifies the orbital (or the particle-hole) branch and $\sigma = \pm 1$ the spin branch. In the non-unitary case the spin degeneracy is removed, which means that time-reversal symmetry is spontaneously

broken. The superconducting gap vanishes at $\boldsymbol{k}$ such that $|\boldsymbol{d}(\hat{k})|^2 - |\boldsymbol{w}(\hat{k})| = 0$ in the triplet case, and $|D(\hat{k})|^2 = 0$ in the singlet case. In the non-unitary case the gap may open only in one spin branch.

In the case of superfluid ^{3}He, the following types of p-wave pairing have been considered:

$$\boldsymbol{d}(\hat{k}) \propto \begin{cases} \hat{x}k_x + \hat{y}k_y + \hat{z}k_z, & \text{[BW]} \\ \hat{z}(k_x + ik_y), & \text{[ABM]} \\ \hat{z}k_z, & \text{[polar].} \end{cases} \tag{5.11}$$

Here and in the following we write $\hat{k}_\alpha$ ($\alpha = x, y, z$) simply as k_α for notational simplicity. The first pairing type corresponds to vanishing total angular momentum, namely $\boldsymbol{J} = \boldsymbol{L} + \boldsymbol{S} = 0$, and is called the Balian-Werthamer (BW) state [11]. The BW state has no node. The second one, with $S_z = 0$ and $L_z = 1$, is realized in a narrow range of the phase diagram and is called the Anderson-Brinkman-Morel (ABM) state [12]. The ABM state has a point node at $k_x = k_y = 0$. The third one with $S_z = L_z = 0$ is called the polar state which has a line node at $k_z = 0$. It is noted that spherical symmetry is spontaneously broken in the ABM and polar states.

singlet pairing under tetragonal symmetry

In the presence of a periodic potential, the degeneracy associated with a finite angular momentum of the pair is lifted. The pair should instead be labeled by an irreducible representation of the point group [13, 14, 15]. As long as the deviation from spherical symmetry is small, one can still use terminology such as the s-wave or p-wave pairing. Under strong crystal potential, however, wave functions with different angular momenta are mixed. Then labeling by the angular momentum loses its significance. Let us take as an example tetragonal symmetry. The simplest pairing has Γ_1^+ (A_{1g}) symmetry represented by

$$D_0(\hat{k}) = a + b(k_x^2 + k_y^2) + ck_z^2 + \ldots, \tag{5.12}$$

where $a, b, c, \ldots$ are parameters to be determined on energetic grounds. Here a originates from the s-wave, b and c from the d-wave and so on. One has $|a| \gg |b|, |c|$ if the pairing is predominantly of s-wave character. The function $D_0(\hat{k})$ transforms as a scalar under the point-group operation, and obviously there are no nodes.

Another type of the singlet pairing has the Γ_3^+ (B_{1g}) symmetry and is represented by

$$D_1(\hat{k}) = (k_x^2 - k_y^2) f_0(\hat{k}) = \mathrm{Re} k_+^2 f_0(\hat{k}),$$

where $k_+ = k_x + ik_y$ and $f_0(\hat{k})$ is a scalar function which is in general different from $D_0(\hat{k})$ in eq.(5.12). The function $D_1(\hat{k})$ vanishes on the planes $k_x = \pm k_y$. Therefore along the intersection of the plane with the Fermi surface, which makes a line, the gap vanishes.

The pairing symmetry Γ_5^+ (E_g) belongs to a two-dimensional representation where the Cooper pair has an internal degree of freedom like finite angular momentum. The gap function is given by

$$D_2(\hat{k}) = (\eta_1 k_x + \eta_2 k_y) k_z [f_0(\hat{k}) + k_z^2 f_1(\hat{k})],$$

The coefficients η_1, η_2 are arbitrary in contrast to the case of eq.(5.12). On the other hand the scalar functions $f_0(\hat{k})$ and $f_1(\hat{k})$ are completely determined by minimizing the energy. Again the gap vanishes on the line $k_z = 0$.

The list including other representations is given in Table 5.1(a). We notice that all the basis functions in these tables should be multiplied by a scalar function which depends on each irreducible representation.

triplet pairing under tetragonal symmetry

We now turn to triplet pairing. The simplest pairing has Γ_1^- (A_{1u}) symmetry represented by

$$\begin{aligned} \boldsymbol{d}(\hat{k}) &= \hat{z}k_z f_0(\hat{k}) + (\hat{x}k_x + \hat{y}k_y) f_1(\hat{k}) + (\hat{x}k_x - \hat{y}k_y)(k_x^2 - k_y^2) f_2(\hat{k}) \\ &= \hat{z}k_z f_0(\hat{k}) + (\mathrm{Re} k_+ \hat{r}_-) f_1(\hat{k}) + (\mathrm{Re} k_+^3 \hat{r}_+) f_2(\hat{k}), \end{aligned} \tag{5.13}$$

where $\hat{x}$ denotes the unit vector along the x-axis and $\hat{r}_\pm = \hat{x} \pm i\hat{y}$. The scalar functions $f_i(\hat{k})$ ($i = 0, 1, 2$) are to be determined to minimize the energy. There is no node because $f_0 f_1 f_2 \neq 0$ in general. If, however,

(a) singlet pairing

representation	basis functions
Γ_1^+ (A_{1g})	1
Γ_2^+ (A_{2g})	$\mathrm{Im}k_+^4$
Γ_3^+ (B_{1g})	$\mathrm{Re}k_+^2$
Γ_4^+ (B_{2g})	$\mathrm{Im}k_+^2$
Γ_5^+ (E_g)	$k_zk_\pm; k_zk_\pm^3$

(b) triplet pairing

representation	basis functions
Γ_1^- (A_{1u})	$\hat{z}k_z; \mathrm{Re}k_+\hat{r}_-; \mathrm{Re}k_+^3\hat{r}_+$
Γ_2^- (A_{2u})	$\mathrm{Im}k_+\hat{r}_-; \mathrm{Im}k_+^3\hat{r}_+; k_z\mathrm{Im}k_+^4\hat{z}$
Γ_3^- (B_{1u})	$\mathrm{Re}k_+\hat{r}_+; k_z\mathrm{Re}k_+^2\hat{z}; \mathrm{Re}k_+^3\hat{r}_-$
Γ_4^- (B_{2u})	$\mathrm{Im}k_+\hat{r}_+; k_z\mathrm{Im}k_+^2\hat{z}; \mathrm{Im}k_+^3\hat{r}_-$
Γ_5^- (E_u)	$k_\pm^{n+1}\hat{z}; k_zk_\pm^n\hat{r}_\pm; k_zk_\pm^{n+2}\hat{r}_\mp$ $(n=0;2)$

Table 5.1: Pairing basis functions in tetragonal symmetry D_{4h}. The functions separated by a semicolon are to be taken as linear combinations to minimize the energy. The functions with the suffix $\pm$ or $\mp$ denote degenerate partners.

there is a spontaneous breakdown of symmetry to realize $S_z = 0$, for example, we have $f_1 = f_2 = 0$ and a line node appears at $k_z = 0$.

The other simple symmetry is Γ_3^- (B_{1u}) with

$$\boldsymbol{d}(\boldsymbol{k}) = (\hat{x}k_x - \hat{y}k_y)f_0(\hat{k}) = (\mathrm{Re}k_+\hat{r}_+)f_0(\hat{k}),$$

which has zeroes at $k_x = k_y = 0$. The list including other representations is given in Table 5.1 (b). We quote also all basis functions for hexagonal and cubic symmetries [15] in Tables 5.2 to 5.3.

5.2.2 Effect of spin-orbit interaction

In the presence of the spin-orbit interaction, the Bloch function is specified by a pair of indices: the crystal momentum $\boldsymbol{k}$ and the quasi-spin index σ, which reduces to the pure spin as the spin-orbit interaction decreases. The energy level for each $\boldsymbol{k}$ is doubly degenerate as long as the time reversal symmetry is not broken. We call the degenerate states a conjugate pair. Since the choice of the quasi-spin is not unique, it is convenient to formulate the theory so that the symmetry appears independently of the representation [16]. We shall illustrate this for the case with the Zeeman splitting. We introduce the g-tensor $\hat{g}(\boldsymbol{k}) = \{g_{ij}(\boldsymbol{k})\}$ and a vector $\boldsymbol{\gamma}(\boldsymbol{k})$, which describes the magnetic moment, by the relation

$$\gamma_i(\boldsymbol{k}) = \frac{1}{2}\sum_j g_{ij}(\boldsymbol{k})\sigma_j, \tag{5.14}$$

where each component $\gamma_i(\boldsymbol{k})$ is a matrix. Then the magnetic moment operator $\boldsymbol{M}(\boldsymbol{k})$ is given by

$$\boldsymbol{M}(\boldsymbol{k}) = -\mu_B \sum_{\alpha\beta} a_\alpha(\boldsymbol{k})^\dagger \boldsymbol{\gamma}_{\alpha\beta}(\boldsymbol{k}) a_\beta(\boldsymbol{k}). \tag{5.15}$$

Under the crystal symmetry operation, $\boldsymbol{M}(\boldsymbol{k})$ transforms like a vector and is independent of the choice of basis. With the one-body density matrix parametrized by eq.(5.1) we obtain the magnetization

$$\langle \boldsymbol{M}(\boldsymbol{k})\rangle = -\mu_B \mathrm{Tr}[\boldsymbol{\gamma}(\boldsymbol{k})\rho(\boldsymbol{k})] = -\frac{1}{2}\mu_B \hat{g}(\boldsymbol{k})\boldsymbol{m}(\boldsymbol{k}).$$

The Zeeman splitting $2E_Z(\boldsymbol{k})$ is given by the eigenvalues $\pm E_Z(\boldsymbol{k})$ of the Hermitian matrix

$$-\boldsymbol{M}(\boldsymbol{k})\cdot\boldsymbol{H}.$$

We obtain from eqs.(5.14) and (5.15)

$$E_Z(\boldsymbol{k})^2 = \frac{1}{4}\mu_B^2 \boldsymbol{H}\cdot\hat{G}(\boldsymbol{k})\boldsymbol{H},$$

(a) singlet pairing

representation	basis functions
Γ_1^+ (A_{1g})	1
Γ_2^+ (A_{2g})	$\mathrm{Im}k_+^6$
Γ_3^+ (B_{1g})	$k_z\mathrm{Im}k_+d^3$
Γ_4^+ (B_{2g})	$k_z\mathrm{Re}k_+^3$
Γ_5^+ (E_{1g})	$k_zk_\pm; k_zk_\mp^5$
Γ_6^+ (E_{2g})	$k_\pm^2; k_\mp^4$

(b) triplet pairing

representation	basis functions
Γ_1^- (A_{1u})	$\hat{z}k_z; \mathrm{Re}k_+\hat{r}_-; \mathrm{Re}k_+^5\hat{r}_-$
Γ_2^- (A_{2u})	$\mathrm{Im}k_+\hat{r}_-; \mathrm{Im}k_+^5\hat{r}_-; k_z\mathrm{Im}k_+^6\hat{z}$
Γ_3^- (B_{1u})	$\mathrm{Im}k_+^3\hat{r}_-; k_z\mathrm{Im}k_+^2\hat{r}_+; k_z\mathrm{Im}k_+^4\hat{z}$
Γ_4^- (B_{2u})	$\mathrm{Re}k_+^3\hat{r}_-; k_z\mathrm{Re}k_+^2\hat{r}_+; k_z\mathrm{Re}k_+^4\hat{z}$
Γ_5^- (E_{1u})	$k_\pm\hat{z}; k_z\hat{r}_\pm; k_zk_\pm^2\hat{r}_\mp; k_\mp^5\hat{z}; k_zk_\pm^4\hat{r}_\mp; k_zk_\mp^6\hat{r}_\pm$
Γ_6^- (E_{2u})	$k_\pm\hat{r}_\pm; k_zk_\pm^2\hat{z}; k_\pm^3\hat{r}_\mp; k_\mp^3\hat{r}_\mp; k_\mp^5\hat{r}_\pm; k_zk_\mp^4\hat{z}$

Table 5.2: Basis functions for the pair in the hexagonal symmetry D_{6h}.

(a) singlet pairing

representation	basis functions
Γ_1^+ (A_{1g})	1
Γ_2^+ (A_{2g})	$(k_x^2-k_y^2)(k_y^2-k_z^2)(k_z^2-k_x^2)$
Γ_3^+ (E_g)	$2k_z^n-k_x^n-k_y^n, k_x^n-k_y^n$ $(n=2;4)$
Γ_4^+ (T_{1g})	$k_yk_z(k_y^n-k_z^n), k_zk_x(k_z^n-k_x^n), k_xk_y(k_x^n-k_y^n)$ $(n=2;4;6)$
Γ_5^+ (T_{2g})	$k_yk_zk_x^n, k_zk_xk_y^n, k_xk_yk_z^n$ $(n=0;2;4)$

(b) triplet pairing

representation	basis functions
Γ_1^- (A_{1u})	$\hat{x}k_x^n+\hat{y}k_y^n+\hat{z}k_z^n$ $(n=1;3;5)$
Γ_2^- (A_{2u})	$\hat{x}k_x^n(k_y^2-k_z^2)+\hat{y}k_y^n(k_z^2-k_x^2)+\hat{z}k_z^n(k_x^2-k_y^2)$ $(n=1;3;5)$
Γ_3^- (E_u)	$\hat{x}k_x^n+\hat{y}k_y^n-2\hat{z}k_z^n, \hat{x}k_x^n-\hat{y}k_y^n$ $(n=1;3;5)$
	$(k_x^n-k_y^n)\hat{d}_{BW}, (2k_z^n-k_x^n-k_y^n)\hat{d}_{BW}$ $(n=1;3;5)$
	$(k_x^5k_z^2\hat{x}+k_x^2k_z^5\hat{z})+(x\leftrightarrow y), [k_x^5(k_z^2-2k_y^2)\hat{x}+k_x^2k_z^5\hat{z}]+(x\leftrightarrow y)$
Γ_4^- (T_{1u})	$k_x^m(\hat{y}k_z^n-\hat{z}k_y^n), k_y^m(\hat{z}k_x^n-\hat{x}k_z^n), k_z^m(\hat{x}k_y^n-\hat{y}k_x^n)$ $(m=0;2, n=1;3;5)$
	$k_xk_y(k_x^2-k_y^2)k_z^n\hat{z}, k_yk_z(k_y^2-k_z^2)k_x^n\hat{x}, k_zk_x(k_z^2-k_x^2)k_y^n\hat{y}$ $(n=1;3;5)$

Table 5.3: Basis functions for the pair in the cubic symmetry O_h. Functions separated by a comma represent degenerate partners, and $\hat{d}_{BW}=k_x\hat{x}+k_y\hat{y}+k_z\hat{z}$. The semicolons mean that linear combinations are to be taken of terms with different n's indicated in each parenthesis.

where $\hat{G}(\boldsymbol{k}) = \hat{g}(\boldsymbol{k})\hat{g}(\boldsymbol{k})^t$ with ^{t} denoting the transpose. Note that this result is independent of the choice of basis. The gap function is now parametrized by

$$\Delta_{\alpha\beta}(\hat{k}) = \{[D(\hat{k}) + \boldsymbol{d}(\hat{k}) \cdot \boldsymbol{\gamma}(\hat{k})]i\sigma_y\}_{\alpha\beta}. \tag{5.16}$$

Then we get

$$\Delta\Delta^\dagger = |D(\hat{k})|^2 + (\boldsymbol{d} \cdot \boldsymbol{\gamma})(\boldsymbol{\gamma} \cdot \boldsymbol{d^*}) = |D(\hat{k})|^2 + |\boldsymbol{d}_g|^2 + \boldsymbol{w} \cdot \boldsymbol{\sigma},$$

where $\boldsymbol{d}_g = \hat{g}^t\boldsymbol{d}$ and $\boldsymbol{w} = i\boldsymbol{d}_g \times \boldsymbol{d}_g^* = \boldsymbol{w}^*$. The symmetry property of $\boldsymbol{d}_g(\hat{k})$ is the same as that of $\boldsymbol{d}(\hat{k})$. Thus the energy spectrum in the presence of the spin-orbit interaction is obtained just by using $\boldsymbol{d}_g(\hat{k})$ in place of $\boldsymbol{d}(\hat{k})$ in the previous section.

It has been argued that the triplet in general cannot have line nodes [16]. The main line of argument for this is the following: The gap vanishes if an eigenvalue of the matrix $\{h_{ij}(\boldsymbol{k})\}$ is given by $\pm\epsilon(\boldsymbol{k})$. Namely we require

$$\det\{\Delta_{\alpha\beta}(\hat{k})\} = D(\hat{k})^2 - \boldsymbol{d}_g(\hat{k}) \cdot \boldsymbol{d}_g(\hat{k}) = 0. \tag{5.17}$$

In the singlet case, $D(\hat{k})$ can be made real. Then the zero condition specifies a plane in the $\boldsymbol{k}$-space, and the intersection with the Fermi surface constitutes the line node. For the unitary triplet case, $\boldsymbol{d}_g(\hat{k})$ can also be made real. Then the left-hand side of eq.(5.17) is the sum of three non-negative quantities. If these quantities are independent, there is no solution on the Fermi surface. If the number of independent equations is reduced to two by symmetry, then a point zero is realized. In order to have a line node, there must be only one independent equation. This however cannot be expected from the symmetry alone. In the non-unitary case $\boldsymbol{d}_g(\hat{k})$ is a complex vector, and eq.(5.17) leads to two real equations. Therefore some special situation is also necessary in order to have line nodes in the non-unitary triplet pairing.

A candidate realizing such situation is the pair with a definite direction of $\boldsymbol{d}_g(\hat{k})$ as in the case of the polar state of eq.(5.11). Under hexagonal symmetry, for example, the E_{1u} pair with $S_z = \pm 1$ of the quasi-spin always contains a factor k_z as seen from Table 5.2. The same remark applies also to the E_{2u} pair with $S_z = 0$. These pairs with line nodes are suggested for pairing in UPt_3 as will be explained later.

5.2.3 Density of states of quasi-particles

In the superconducting state, the energy of quasi-particles is given as the eigenvalues of $\hat{h} = \{h_{ij}\}$ given by eq.(5.9). The density of states $N(E)$ of quasi-particles is then

$$N(E) = \frac{1}{2}\sum_{\boldsymbol{k}\tau\sigma} \delta(E - E_{\tau\sigma}(\boldsymbol{k})) = |E| \sum_{\boldsymbol{k}\sigma} \delta(E^2 - E^2_{\boldsymbol{k}\sigma}), \tag{5.18}$$

where $E_{\boldsymbol{k}\sigma} = |E_{\tau\sigma}(\boldsymbol{k})|$. By putting the eigenvalues of $\hat{h}(\boldsymbol{k})^2$ we can derive the density of states. For simplicity we first treat cases with spherical symmetry.

s-wave pairing

In BCS superconductivity mediated by the electron-phonon interaction [1] the energy gap opens over the entire Fermi surface. With the notation $D(\hat{k}) = \Delta$, the density of states $N_{BCS}(E)$ in the superconducting state is given by

$$N_{BCS}(E) = N_0 \frac{|E|}{\sqrt{E^2 - \Delta^2}}, \ (|E| > \Delta) \tag{5.19}$$

and $N_{BCS}(E) = 0$ for $|E| < \Delta$. Here $N_0 = 2\sum_{\boldsymbol{k}} \delta(\epsilon_{\boldsymbol{k}})$ is the density of states at the Fermi level in the normal state. Therefore, various physical quantities obey an exponential-law well below T_c.

p-wave pairing

In the case of a p-wave triplet pairing we obtain

$$N(E) = N_0 \int \frac{d\Omega}{8\pi} \sum_{\sigma=\pm 1} \mathrm{Re}\frac{|E|}{\sqrt{E^2 - |\boldsymbol{d}(\hat{k})|^2 - \sigma|\boldsymbol{w}(\hat{k})|}}, \tag{5.20}$$

where the integral is over the solid angle of $\hat{k}$. In the ABM state in the superfluid ^{3}He-A, the Cooper pair consists of parallel spin pairing as given by eq.(5.11). Then we have $|\boldsymbol{d}(\hat{k})|^2 = \Delta^2 \sin^2\theta$ and $\boldsymbol{w}(\hat{k}) = 0$. Correspondingly, the quasi-particle density of states in the ABM state is given by

$$N_{ABM}(E) = \frac{N_0|E|}{4\pi}\int_0^{2\pi} d\phi \int_0^{\pi} d\theta \ \mathrm{Re}\frac{\sin\theta}{\sqrt{E^2 - \Delta^2\sin^2\theta}} = \frac{N_0 E}{2\Delta}\ln|\ \frac{E+\Delta}{E-\Delta}\ |. \tag{5.21}$$

This result is obtained by choosing $x = \Delta\cos\theta/\sqrt{E^2-\Delta^2}$ as the integration variable for the case of $|E| > \Delta$. The result in the case of $|E| < \Delta$ is obtained by analytic continuation of E. Hence eq.(5.21) is valid for both cases. We note that $N_{ABM}(E)$ exhibits a divergence at the gap edge, which is weaker than the BCS case, and is proportional to E^2 at low energy as shown in Fig.5.1.

In the case of the p-wave polar type with $\boldsymbol{d}(\hat{k}) = \Delta\hat{z}k_z$, the gap vanishes along a line at the Fermi surface. Accordingly we have

$$N_{polar}(E) = \frac{1}{2}N_0|E|\int_0^{\pi} d\theta \ \mathrm{Re}\frac{\sin\theta}{\sqrt{E^2-\Delta^2\cos^2\theta}} = \begin{cases} \pi N_0|E|/(2\Delta), & (|E|<\Delta) \\ N_0(E/\Delta)\arcsin(\Delta/E). & (|E|>\Delta) \end{cases} \tag{5.22}$$

This result is obtained with $x = \Delta\cos\theta/|E|$ taken as the integration variable. In this case, $N_{polar}(E)$ is finite at the gap edge and is proportional to $|E|$ at low energy. In the triplet BW [11] state realized in the superfluid ^{3}He-B phase, the density of states is the same as the BCS state since the energy gap is isotropic. These results are summarized in Figure 5.1.

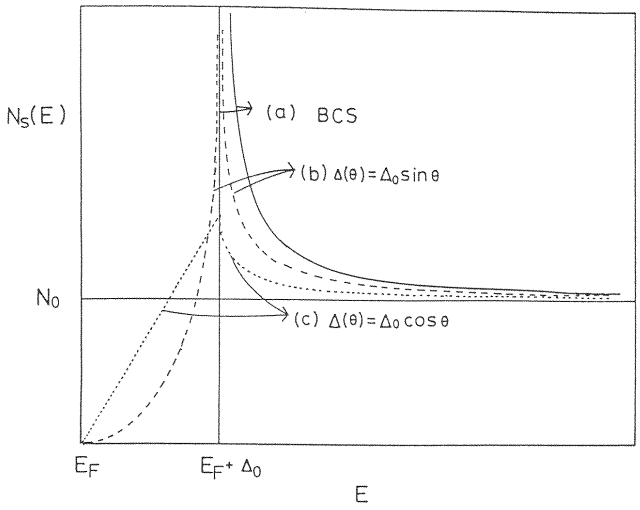

Figure 5.1: Quasi-particle density of states in the superconducting phase, (a) s-wave, (b) axial (ABM) p-wave with vanishing gap at points and (c) polar p-wave with vanishing gap along a line.

5.3 NMR as a Probe of Superconducting States

5.3.1 Knight shift

The Knight shift is the only convenient measure of the local spin susceptibility reflecting the symmetry of the order parameter, since the diamagnetic shielding by supercurrents overwhelms all other contributions to the bulk susceptibility. In the presence of a weak magnetic field H along the z axis, the itinerant part of the magnetization M_z is given by

$$M_z = -\frac{1}{2}g\mu_B\sum_{\boldsymbol{k}}[f(E_{\boldsymbol{k}\uparrow}) - f(E_{\boldsymbol{k}\downarrow})] \tag{5.23}$$

where $f(E_{\boldsymbol{k}\sigma})$ is the Fermi distribution function for a quasi-particle with a spin-dependent energy $E_{\boldsymbol{k}\sigma}$. We derive the spin susceptibility χ_s for various cases.

s-wave pairing

In the case of s-wave singlet pairing we obtain $E_{\boldsymbol{k}\sigma} = E_{\boldsymbol{k}} + \sigma h$ with $h = g\mu_B H/2$. Then χ_s for the s-wave is derived [17] with use of $N_{BCS}(E)$ in eq.(5.19),as

$$\chi_s = \frac{1}{4}(g\mu_B)^2 \int_{-\infty}^{\infty} N_{BCS}(E) \left(-\frac{df}{dE}\right) dE \tag{5.24}$$

This result is plotted in Fig.5.2. At low-T, χ_s decreases exponentially as $\exp(-\Delta/T)$. In the d-wave, since $N_d(E)$ is proportional to the energy E, or its square ($\propto E^2$), χ_s becomes zero in proportion to T or T^2 respectively, at low T.

The argument above is valid only in the clean limit where the transport mean free path, l_{tr} is larger than the superconducting coherence length ξ, i.e. $\Delta > 1/\tau$. Here the scattering time τ is defined by $l_{tr} = v_F\tau$. In the case where a strong spin-orbit scattering ($\lambda \boldsymbol{L}\cdot\boldsymbol{S}$) with $\lambda \gg \Delta$ occurs by the presence

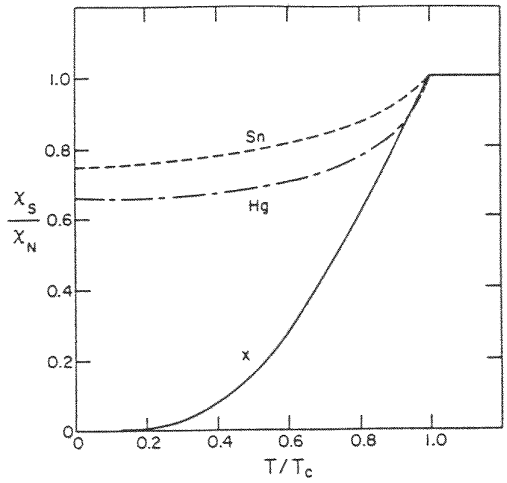

Figure 5.2: Temperature dependence of Knight shift in s-wave superconductors as given by eq.(5.24). In actual materials there remains residual shift due to the spin-orbit interaction.

of imperfections and the boundary in small particles, those states which would be different eigenstates in the absence of the spin-orbit interaction can be admixed. This is time-reversal invariant so that the new eigenstates can retain the same pairing in the superconducting state as in the absence of spin-orbit scattering. However, these eigenstates contain admixtures of both up and down spin directions. As a result, a conventional picture of spin-singlet pairing no longer holds. In the limit of large spin-orbit interaction, the opening of a finite energy gap below T_c does not produce large perturbation on the spin susceptibility. For the two limits of strong and weak spin-orbit scattering, Anderson derived the fraction of the residual spin susceptibility at T=0 as [18]

$$\begin{aligned} \chi_s/\chi_n &\simeq 1 - 2\Delta\tau_{so} && \xi \gg l_{so} \\ \chi_s/\chi_n &\simeq (6\Delta\tau_{so})^{-1} && \xi \ll l_{so} \end{aligned}$$

where τ_{so} is the mean time between spin-reversing scattering events and the spin-orbit mean free path is defined by $l_{so} = v_F\tau_{so}$.

p-wave pairing

In the p-wave case, the susceptibility depends on the direction of $\boldsymbol{d}$. Let us first consider the case where $\boldsymbol{d} \parallel \hat{z}$. Then in the matrix $\hat{h}(\boldsymbol{k})$ we have no coupling between the conjugate partners. The non-zero off-diagonal elements couple the time-reversal partners. Then the Zeeman splitting of quasi-particle states becomes the same as the s-wave case, i.e., $E_{\boldsymbol{k}\sigma} = E_{\boldsymbol{k}} + \sigma h$. Thus χ_s is given by eq.(5.24) provided that $N_{BCS}(E)$ is replaced by the triplet one.

If $\boldsymbol{d} \perp \hat{z}$, on the other hand, the spin is parallel to the magnetic field. We assume the case of equal-spin pairing with $\boldsymbol{d}(\hat{k}) = \Delta \hat{x} k_+$. Then in the matrix $\hat{h}(\boldsymbol{k})$ we again have no coupling between the conjugates. This time the non-zero off-diagonal elements couple components with equal spin. We obtain

$$E^2_{\boldsymbol{k}\sigma} = (\epsilon_{\boldsymbol{k}} + \sigma h)^2 - \Delta^2 \sin^2\theta,$$

which leads to

$$\frac{\partial E_{\boldsymbol{k}\sigma}}{\partial H} = \frac{1}{2}\mu_B \sigma \frac{\partial E_{\boldsymbol{k}\sigma}}{\partial \epsilon_{\boldsymbol{k}}}.$$

Then χ_s is given by

$$\chi_s = \sum_{\boldsymbol{k}\sigma} \frac{\partial}{\partial H}[f(E_{\boldsymbol{k}\sigma})\frac{\partial E_{\boldsymbol{k}\sigma}}{\partial H}] = -\frac{1}{4}(g\mu_B)^2 N_0 \int_{-\infty}^{\infty} d\epsilon \frac{\partial}{\partial \epsilon}[f(E_\epsilon)\frac{\partial E_\epsilon}{\partial \epsilon}] = \frac{1}{4}(g\mu_B)^2 N_0. \tag{5.25}$$

Namely the spin susceptibility remains the same as that in the normal state.

If one can neglect the anisotropy in the system as in liquid ^{3}He, $\boldsymbol{d}$ can rotate so that $\boldsymbol{d} \perp \hat{z}$ is satisfied. Then χ_s stays constant in any direction in the parallel spin pairing (ABM) state. On the contrary provided that the spin is pinned along an easy axis or an easy plane due to the anisotropy below T_c, χ_s with H perpendicular to such axis or plane is reduced. In the isotropic triplet state (BW state), χ_s is decreased down to 2/3 of the value in the normal state. This is interpreted as coming from the average $|d_z|^2$ of the component parallel to H is 1/3 of $|\boldsymbol{d}|^2$ in the BW state. Thus the Knight shift measurement provides an important clue for the determination of the symmetry of the order parameter.

5.3.2 Nuclear-spin-lattice relaxation rate

A modification of the excited state spectrum by the onset of superconductivity has a substantial effect on the temperature dependence of the NMR relaxation rate $1/T_1$. The dynamical response of the excited states is also affected by the presence of the mixed state, or magnetic and non-magnetic impurities. All these effects can be probed by the nuclear relaxation study.

At finite temperature some pairs are broken up into single-particle excitations, while the presence of the coherent condensed state modifies the matrix element of external perturbations. This latter effect is called a coherence effect. Since the nuclear relaxation in the superconducting state is significantly affected by the coherence effect, NMR serves as a good probe of coherence. We consider a case where the magnetic field is along the z axis and we have axial symmetry in the x-y plane. Then by eqs.(1.129) and (1.130) we have

$$\frac{1}{T_1 T} = A_\perp^2 (g_J \mu_B)^2 \sum_{\boldsymbol{q}} \frac{1}{\omega_n} \mathrm{Im}\chi_\perp(\boldsymbol{q}, \omega_n). \tag{5.26}$$

where $A_\perp$ is the momentum average of the hyperfine interaction. The transverse dynamical susceptibility is derived in the mean-field approximation in the superconducting state. As $\chi_\perp$ we consider the y-component. We note

$$\sum_{\boldsymbol{k},\boldsymbol{p}} \sum_{\alpha\beta} a^\dagger_{\boldsymbol{k}\alpha} (\sigma_y)_{\alpha\beta} a_{\boldsymbol{p}\beta} = \frac{1}{2} \sum_{\boldsymbol{k},\boldsymbol{p}} \boldsymbol{\psi}(\boldsymbol{k})^\dagger \begin{pmatrix} \sigma_y & 0 \\ 0 & \sigma_y \end{pmatrix} \boldsymbol{\psi}(\boldsymbol{p}), \tag{5.27}$$

where $\boldsymbol{\psi}(\boldsymbol{p})$ is the four-component field given by eq.(5.8). The 4×4 matrix in eq.(5.27) is written as $\hat{\sigma}_y = \sigma_y \otimes \tau_0$ where τ_0 is the 2×2 unit matrix. By evaluating the zero-th order polarization part in the Green function formalism we obtain

$$\mathrm{Im}\chi_{yy}(\boldsymbol{q}, \omega) = \sum_{\boldsymbol{k},\boldsymbol{p}} \int_{-\infty}^{\infty} d\epsilon [f(\epsilon) - f(\epsilon + \omega)] \mathrm{Tr}[\hat{\sigma}_y \delta(\epsilon - \hat{h}(\boldsymbol{k})) \hat{\sigma}_y \delta(\epsilon + \omega - \hat{h}(\boldsymbol{p}))], \tag{5.28}$$

where the delta function corresponds to the imaginary part of the retarded Green function of the 4-component field. In the unitary case to which we restrict ourselves from now on, the latter is given by

$$-\frac{1}{\pi}\mathrm{Im}[\epsilon - \hat{h}(\boldsymbol{k}) + i\delta]^{-1} = \frac{1}{2}\left(1 + \frac{\hat{h}(\boldsymbol{k})}{E_{\boldsymbol{k}}}\right)\delta(\epsilon - E_{\boldsymbol{k}}) + \frac{1}{2}\left(1 - \frac{\hat{h}(\boldsymbol{k})}{E_{\boldsymbol{k}}}\right)\delta(\epsilon + E_{\boldsymbol{k}}), \tag{5.29}$$

where we have used the fact that $\hat{h}(\boldsymbol{k})^2$ is proportional to a unit matrix given by $E_{\boldsymbol{k}}^2\sigma_0\otimes\tau_0$.

We divide $\hat{h}(\boldsymbol{k})$ into the diagonal part $\hat{h}_0(\boldsymbol{k})=\epsilon_{\boldsymbol{k}}\sigma_0\otimes\tau_z$ and the rest $\hat{h}_1(\boldsymbol{k})$ which depends on the pairing type. Each case is discussed in the following.

s-wave pairing

In this case we have $\hat{\sigma}_y\hat{h}(\boldsymbol{k})=\hat{h}(\boldsymbol{k})\hat{\sigma}_y$. Then the trace in eq.(5.28) is calculated as

$$\left(1+\frac{\epsilon_{\boldsymbol{k}}\epsilon_{\boldsymbol{p}}+D(\hat{k})D(\hat{p})}{E_{\boldsymbol{k}}E_{\boldsymbol{p}}}\right)\left[\delta(\epsilon-E_{\boldsymbol{k}})\delta(\epsilon+\omega-E_{\boldsymbol{p}})+\delta(\epsilon+E_{\boldsymbol{k}})\delta(\epsilon+\omega+E_{\boldsymbol{p}})\right], \tag{5.30}$$

where the factor in front of the delta functions is an example of the coherence factor. We note that summation over $\boldsymbol{k}$ makes the term with $\epsilon_{\boldsymbol{k}}$ vanish because it is an odd function of $\epsilon_{\boldsymbol{k}}$. Then for the s-wave pairing we obtain

$$\frac{1}{T_1T}=\pi A^2\int_0^\infty dE\left(1+\frac{\Delta^2}{E^2}\right)N_{BCS}(E)^2\left(-\frac{\partial f}{\partial E}\right), \tag{5.31}$$

where $\omega\ll T$ is assumed. The density of states, $N_{BCS}(E)$ diverges at $E=\Delta$ as shown in Fig.5.1. Near T_c, where $|f'(\Delta)|$ is still large, the divergence of $N_{BCS}(E)$ gives rise to a divergence of $1/T_1$. However, the life-time effect of quasi-particles by the electron-phonon and/or the electron-electron interactions, and the anisotropy of the energy gap due to the crystal structure broadens the quasi-particle density of states. This results in the suppression of the divergence of $1/T_1$. Instead, a peak of $1/T_1$ is seen just below T_c. This peak, which is characteristic of singlet pairing, was observed first by Hebel and Slichter [19] in the nuclear relaxation rate of Al, and is called the coherence peak. At low temperatures, $1/T_1$ decreases exponentially due to the uniform gap.

The coherence peak is not always seen in the case of strong-coupling superconductors. As an example of the relaxation behavior for weak and strong coupling s-wave superconductors, Fig.5.3 shows $1/T_1$ of ^{119}Sn and ^{205}Tl in the Chevrel phase superconductors, $Sn_{1.1}Mo_6Se_{7.5}$ and $TlMo_6Se_{7.5}$with T_c=4.2 K and T_c=12.2 K, respectively [20]. In the normal state, the T_1T=constant law holds for both compounds. In the superconducting state, $1/T_1$ of ^{119}Sn in $Sn_{1.1}Mo_6Se_{7.5}$ has a coherence peak just below T_c and decreases exponentially with $2\Delta=3.6k_BT_c$, while $1/T_1$ of ^{205}Tl in the strong coupling superconductor $TlMo_6Se_{7.5}$ has no coherence peak just below T_c and decreases exponentially over five orders of magnitude below $0.8T_c$ (10 K) with $2\Delta=4.5k_BT_c$. Even though the coherence peak is depressed, the s-wave picture is evidenced by the exponential decrease of $1/T_1$ below T_c. Figure 5.3 also shows another important example, the high-T_c cuprates, which are discussed in the next Chapter.

p-wave pairing

In the p-wave case the coherence factor for $\mathrm{Im}\chi_{yy}$ is calculated from eq.(5.30) as [11]

$$1+\frac{1}{E_{\boldsymbol{k}}E_{\boldsymbol{p}}}\mathrm{Re}\left(\epsilon_{\boldsymbol{k}}\epsilon_{\boldsymbol{p}}+\boldsymbol{d}(\hat{k})\cdot\boldsymbol{d}(\hat{p})^*-2d_y(\hat{k})d_y(\hat{p})^*\right). \tag{5.32}$$

Because $\epsilon_{\boldsymbol{k}}$ and $\boldsymbol{d}(\hat{k})$ are odd functions of $\hat{k}$, the bilinear terms in them vanish by summation over $\boldsymbol{k}$. Then the coherence factor is reduced to unity. The same situation occurs in the case of $\mathrm{Im}\chi_{xx}$. Therefore, the relaxation rate is obtained by replacing the quasi-particle density of states in eq.(5.31) by $N_{ABM}(E)$ as follows:

$$\frac{1}{T_1T}=\frac{\pi A^2N_0^2}{4\Delta^2}\int_0^\infty E^2\left(\ln|\frac{E+\Delta}{E-\Delta}|\right)^2(-\frac{\partial f}{\partial E})dE \tag{5.33}$$

Since the divergence of $N_{ABM}(E)$ at $E=\Delta$ is weak, the peak of $1/T_1$ just below T_c is much smaller than the BCS case. The larger Δ_0/T_c is, where Δ_0 is the gap at zero temperature, the more suppressed is the peak of $1/T_1$. At low temperatures $T\ll T_c$, we obtain

$$\frac{1}{T_1}\propto\int_0^\infty E^4\exp(-\frac{E}{T})dE=T^5\Gamma(5) \tag{5.34}$$

which gives the T^5 dependence at low T.

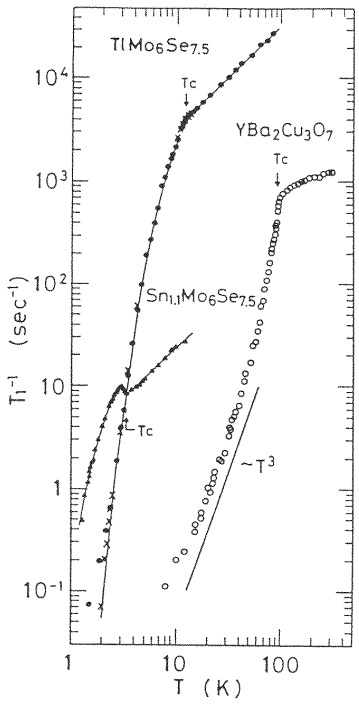

Figure 5.3: Temperature dependence of $1/T_1$ of ^{205}Tl and ^{119}Sn in strong coupling ($TlMo_6Se_{7.5}$) and weak coupling ($Sn_{1.1}Mo_6Se_{7.5}$) s-wave superconductors, and of ^{63}Cu in $YBa_2Cu_3O_7$ at zero field. Solid lines above T_c represent the T_1T=constant law, and below T_c the exponential law with $1/T_1 = A\exp(-\Delta/k_BT)$. For $TlMo_6Se_8$, the ratio $2\Delta/k_BT_c$=4.5 is obtained and for $SnMo_6Se_8$ the ratio is 3.6 [20].

In the polar-type pairing where the gap vanishes along a line on the Fermi surface, $1/T_1$ is calculated as

$$\frac{1}{T_1T} = \frac{\pi A^2 N_0^2}{\Delta^2}\left[\frac{\pi^2}{4}\int_0^\Delta E^2(-\frac{\partial f}{\partial E})dE + \int_\Delta^\infty E^2\{\arcsin(\frac{\Delta}{E})\}^2(-\frac{\partial f}{\partial E})dE\right], \tag{5.35}$$

where we use eq.(5.22) for $N_{polar}(E)$. Since $N_{polar}(E)$ remains finite at $E=\Delta$, the peak of $1/T_1$ is significantly suppressed. When Δ_0/T_c is large, $1/T_1$ decreases rapidly just below T_c. At $T \ll T_c$ with $N_{polar}(E) \propto E$, $1/T_1$ is given by

$$\frac{1}{T_1} \propto \int_0^\infty E^2 f(E)(1-f(E))dE \propto T^3. \tag{5.36}$$

quadrupolar relaxation

We now consider the nuclear relaxation brought about by the interaction between the nuclear quadrupole moment and the electric field gradient due to the non-spherical part of the conduction electron wave function. The interaction is expressed by

$$H_Q = \sum_{\boldsymbol{k}\boldsymbol{p}\sigma} B_{\boldsymbol{k}\boldsymbol{p}} a^\dagger_{\boldsymbol{k}\sigma} a_{\boldsymbol{p}\sigma}, \tag{5.37}$$

which does not break time-reversal symmetry. If one replaces $B_{\boldsymbol{k}\boldsymbol{p}}$ by an average, the relevant coupling is written as

$$\sum_{\boldsymbol{k},\boldsymbol{p}}\sum_\alpha a^\dagger_{\boldsymbol{k}\alpha} a_{\boldsymbol{p}\alpha} = \frac{1}{2}\sum_{\boldsymbol{k},\boldsymbol{p}} \boldsymbol{\psi}(\boldsymbol{k})^\dagger \begin{pmatrix} \sigma_0 & 0 \\ 0 & -\sigma_0 \end{pmatrix} \boldsymbol{\psi}(\boldsymbol{p}), \tag{5.38}$$

where we have neglected a contribution coming from anticommutation of fermion operators with $\boldsymbol{k}=\boldsymbol{p}$ because it is smaller by $O(1/N)$. Then we obtain

$$\frac{1}{T_1T} = B^2 \sum_{\boldsymbol{q}} \frac{1}{\omega}\mathrm{Im}\chi_c(\boldsymbol{q},\omega), \tag{5.39}$$

where the charge susceptibility is given by

$$\mathrm{Im}\chi_c(\boldsymbol{q},\omega) = \sum_{\boldsymbol{k},\boldsymbol{p}} \int_{-\infty}^\infty d\epsilon [f(\epsilon)-f(\epsilon+\omega)]\mathrm{Tr}[\hat\tau_z \delta(\epsilon-\hat h(\boldsymbol{k}))\hat\tau_z \delta(\epsilon+\omega-\hat h(\boldsymbol{p}))], \tag{5.40}$$

with $\hat\tau_z = \sigma_0 \otimes \tau_z$. The coherence factor for singlet pairing is now given by

$$1 + \frac{\epsilon_{\boldsymbol{k}}\epsilon_{\boldsymbol{p}} - \Delta(\hat k)\Delta(\hat p)}{E_{\boldsymbol{k}}E_{\boldsymbol{p}}}, \tag{5.41}$$

where the minus sign originates from $\hat\tau_z \hat h_1(\boldsymbol{k}) = -\hat h_1(\boldsymbol{k})\hat\tau_z$. We note that the coherence factor $(1-\Delta^2/E^2)$ cancels the divergence of $N_{BCS}(E)$. Explicitly we have

$$\frac{1}{T_1T} = \pi B^2 \int_{-\infty}^\infty dE \left(1-\frac{\Delta^2}{E^2}\right) N_{BCS}(E)^2 \left(-\frac{\partial f}{\partial E}\right) = \frac{\pi B^2 N_0}{1+\exp(\beta\Delta)}. \tag{5.42}$$

In this case the coherence peak just below T_c disappears. We note that the temperature dependence of $1/(T_1T)$ is the same as that of ultrasonic attenuation. These contrasting relaxation behaviors between the magnetic and quadrupole processes were reported in the ^{119}Sn and ^{181}Ta relaxation in $TaSn_3$[21].

As for the impurity effect on the relaxation behavior in conventional s-wave superconductors, we note that non-magnetic impurities smear the anisotropy due to the crystal structure. Since the anisotropy has an effect of suppressing the coherence peak just below T_c, such impurities *enhance* the peak. On the other hand, magnetic impurities broaden the density of states by the pair-breaking effect, and substantially suppress the peak of $1/T_1$. With increasing number of impurities, the superconductivity becomes gapless, leading to the T_1T=constant behavior below T_c. The magnetic field, which lowers T_c, also depresses the peak.

5.4 Characteristic Features of Heavy-Electron Superconductivity

The heavy-electron superconductors discovered to date may be classified into two groups depending on their different magnetic behaviors and extent of quasi-particle renormalization. The first group comprises $CeCu_2Si_2$, UBe_{13}, and UPt_3, which exhibit weak or no magnetic order. The quasi-particle masses as derived from the specific-heat coefficient $\gamma = C(T)/T$ are as large as $\gamma \geq 0.4$ J/mole K^2.

The second group includes URu_2Si_2, UNi_2Al_3 and UPd_2Al_3, which show antiferromagnetic order. The effective masses are not so large with $\gamma \sim 0.1$ J/mole K^2, but T_c of 1-2 K are higher than that in the first group. The highest T_c is 2 K in UPd_2Al_3. Most remarkably, UNi_2Al_3 and UPd_2Al_3 possess sizable magnetic moments of 0.24 and 0.85 μ_B/(U atom), respectively. In both groups, heavy quasi-particles are responsible for the superconductivity. This follows from the large jump of the specific heat ΔC at T_c with $\Delta C/\gamma T_c \sim 1$, which is close to the value 1.43 for conventional superconductors, and from the large slope of the upper critical field $(dH_{c2}/dT)_{T=T_c}$. The multiplicity of the superconducting phases in UPt_3 is analogous to the complex phase diagram of superfluid ^{3}He. This suggests the unconventional nature of the superconductivity. We focus on selected properties studied by the NMR and the neutron scattering experiments. We should mention that enormous amount of work has also been done on thermodynamic and transport properties, which cannot be covered in the following.

5.4.1 $CeCu_2Si_2$

phase diagram under pressure

As discussed in Chapter 4, superconductivity in $CeCu_2Si_2$ occurs close to a mysterious magnetic phase called the phase A. In order to gain further insight into the relationship between the magnetism and superconductivity, we show the pressure and temperature $(P-T)$ phase diagram in Fig.5.4 for $CeCu_2Si_2$ and $CeCu_2Ge_2$ [22, 23, 24]. The heavy-electron antiferromagnet $CeCu_2Ge_2$ exhibits a pressure-induced superconducting transition around P=7 GPa [22]. The phase diagrams show nearly identical pressure dependence if they are transposed so that P=0 for $CeCu_2Si_2$ coincides with P=7.6 GPa for $CeCu_2Ge_2$[24]. The electronic state of $CeCu_2Ge_2$ at P=7.6 GPa seems nearly identical to that of $CeCu_2Si_2$ at P=0. The enhancement of T_c observed for $CeCu_2Si_2$ in Fig.5.4 in a P-range of 2-3 GPa [23] is observed for $CeCu_2Ge_2$ as well. Since application of pressure increases the hybridization between $4f$- and conduction electrons, there exists an optimum strength of hybridization for the superconductivity. Namely, as the hybridization increases, the heavy-electron superconductivity emerges immediately after disappearance of antiferromagnetic order.

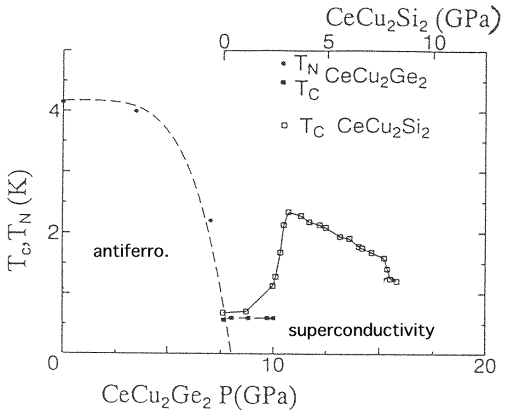

Figure 5.4: Combined phase diagram for superconductivity and antiferromagnetism in $CeCu_2Si_2$ and $CeCu_2Ge_2$ as a function of pressure. Normal and superconducting states for $CeCu_2Ge_2$ at 7 GPa bear resemblance to those in $CeCu_2Si_2$ at ambient pressure [22, 23, 24].

Pressure-induced superconductivity is often seen in heavy electron systems when the AF order is

suppressed under pressure. For example, close to the border of AF order, an unconventional normal-state property is observed in the heavy-electron antiferromagnet $CePd_2Si_2$ (T_N=10 K) which crystallizes in the same tetragonal structure as $CeCu_2Si_2$. Near the critical pressure $p_c \sim 30$ kbar, at which the AF ordering temperature is extrapolated to zero, the electrical resistivity, $\rho(T)$ exhibits a quasi-linear variation over two orders of magnitude. This non-Fermi liquid form of $\rho(T)$ extends down to the onset of the superconducting transition below 0.43 K [25].

Besides the series of CeM_2X_2 tetragonal compounds, the cubic stoichiometric AF compound $CeIn_3$ displays an unusual normal-state resistivity followed by superconductivity around 0.2 K near $p_c \sim 25$ kbar [26]. For the onset of superconductivity near the border of AF order, a possible scenario is that critical low-lying magnetic excitations caused by the incipient AF order contribute to formation of anisotropic even-parity Cooper pairs.

symmetry of the order parameter

The temperature dependence of the Knight shift provides a clue to the parity of the order parameter. From the Knight shift measurements of ^{29}Si and ^{63}Cu, the spin susceptibilities parallel and perpendicular to the tetragonal c-axis have been extracted with the use of oriented powder. From the T dependence of the Knight shift, appreciable reduction of the spin susceptibility is found. This suggests strongly the singlet nature of the order parameter, hence the even-parity superconductivity. The normalized T dependence of the spin susceptibility in the superconducting state is plotted in Fig.5.5 against (T/T_c) [27]. The residual shift at T=0 is attributed to the spin-orbit scattering and/or the T-independent Van Vleck shift. Because of the residual shift, detailed structure of the gap function is hard to deduce from the T dependence of the spin susceptibility.

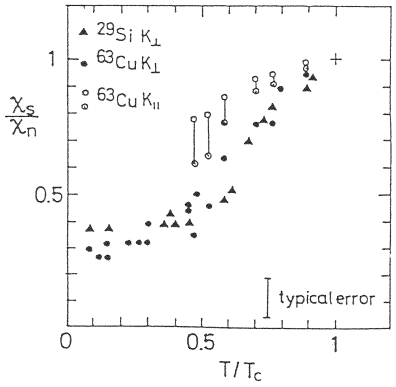

Figure 5.5: Temperature dependence of spin susceptibility $\chi_s(T)$ below T_c. This is deduced from the Knight shift of ^{63}Cu and ^{29}Si in $CeCu_2Si_2$, and is normalized by the value at T_c [27].

As shown in Figure 4.8 [28], the T^3 law for $x = 1.00$ and 1.025 reveals that the gap function of the order parameter vanishes along lines on the Fermi surface. Application of a simple model with $\Delta(\theta) = \Delta_0 \cos(\theta)$ yields the best fit to the experiment with $2\Delta_0 = 5T_c$. Both Knight and T_1 results of $CeCu_2Si_2$ are consistent with a d-wave superconductor with vanishing gap along lines on the Fermi surface. The specific heat $C(T)$, however, does not confirm the line node: Although $C(T)$ follows a T^2 dependence near T_c which is consistent with a line node, $C(T)$ goes like $\sim T^3$ at low temperatures [29].

5.4.2 UPd_2Al_3

coexistence of AF order and superconductivity

The Néel temperature T_N of UPd_2Al_3 is 14.5 K and the superconducting transition temperature T_c is 1.98 K [30, 31, 32]. Various measurements such as Al-NQR [33], Pd-NQR [34], specific heat [35] and neutron diffraction [31] have established the coexistence of the AF magnetic order with the superconductivity and no modification of the magnetic structure at the superconducting transition. Observation of the T_1T=constant law far below T_N confirmed the quasi-particle excitations in the Fermi-liquid state, but

spin waves were not found. Neutron scattering measurements, on the other hand, have probed spin-wave excitations, which are reduced below T_c [31, 32]. Magnetic excitations develop a gap feature which seems to be related to the anisotropic superconductivity [36]. These observation should constrain the theory of superconductivity in the presence of well-developed antiferromagnetism, which has not been worked out.

symmetry of order parameter

Figure 5.6 shows the T dependence of the Knight shift below T_c for polycrystalline and single crystalline samples of UPd_2Al_3 [37]. In the μSR experiment similar results are also reported [38]. Reduction of

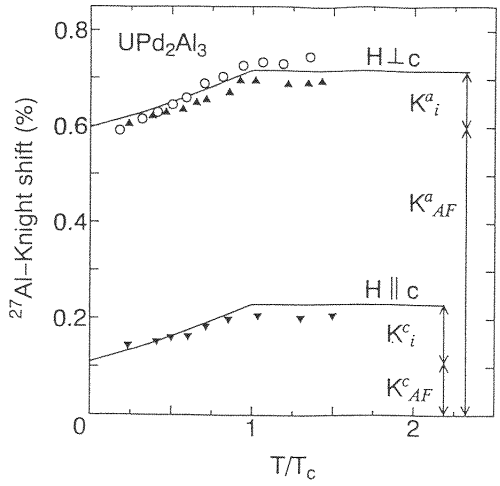

Figure 5.6: Temperature dependence of Knight shifts. Open circles show Knight shift perpendicular to the field in oriented powder of UPd_2Al_3. Solid up-triangles denote the shifts with c-axis perpendicular to the magnetic field, and down-triangles those parallel to the field. Solid lines represent the calculation based on the d-wave model [37]. See text for the meaning of K_i and K_{AF}.

the Knight shift is only about 0.08% $\sim$ 0.11% at 0.4 K for all directions. Since the sample is in the clean limit, impurity scattering should not be the origin of the anisotropy in the residual Knight shift. Therefore, the anisotropy in the residual Knight shift should be ascribed to that of the AF susceptibility which does not change below T_c. This contribution is shown as K_{AF} in Fig.5.6. If one subtracts K_{AF} from the total, the rest decreases nearly isotropically. The latter part is written as K_i and is ascribed to the itinerant part forming Cooper pairs. The division of f-electron degrees of freedom into itinerant and localized parts has been discussed in detail in 4.8

According to the Fermi liquid picture, a simple estimate of the itinerant part χ_i of the susceptibility yields $\chi_i \sim 1.6 \times 10^{-3}$ emu/mole with γ=150 mJ/(mole$\cdot K^2$) in the normal state. On the other hand, a polarized neutron experiment extracted a value $\chi_i \sim 1.8 \times 10^{-3}$ (emu/mole) as the itinerant part [31] which is nearly the same as the above value. By using these values of χ_i, and the ^{27}Al hyperfine coupling constant H_{hf}=3.5 kOe/μ_B, the itinerant part K_i of the Knight shift is estimated from the formula:

$$K_i = \frac{H_{hf}}{(N_A \mu_B)} \chi_i,$$

to be $\sim$ 0.1%. Since the observed reduction 0.08$\sim$ 0.11% is comparable to K_i, the Knight shift due to quasi-particles becomes almost zero well below T_c for all directions. This result provides strong evidence that the superconductivity is due to singlet Cooper pairs in a clean limit.

gap anisotropy

In the superconducting state, $1/T_1$ in zero field obeys the T^3 law very well down to 0.15 K as seen in Fig.5.7 [33]. This is the first case where the T^3 dependence of $1/T_1$ is observed down to such a low

temperature as $0.08T_c$. Since the order parameter stays constant below $0.5T_c$, the T^3 law of $1/T_1$ in the low T range of $0.5T_c$(1 K)-$0.08T_c$(0.15 K) is evidence of anisotropic superconductivity with vanishing gap along lines on the Fermi surface. It is noteworthy that at Al sites the T dependence of $^{27}(1/T_1)$ below T_c is determined only by quasi-particle excitations in the superconducting state. This might be partly because the magnetic form factor at the Al-site filters away the fluctuating hyperfine field from two adjacent uranium planes. However, the T^3 law of $1/T_1$ was also confirmed for the Pd sites where the fluctuating hyperfine fields in the basal uranium plane are not filtered away [34].

By contrast, the specific heat $C(T)$ probes not only quasi-particle excitations but also magnetic excitations in the AF ordered state which coexists with the superconductivity. In fact $C(T)$ is not consistent with the line-node [39]; it takes the form $\gamma_r T + \beta T^3$. It seems that the T linear term with γ_r=24 mJ/(mole$\cdot K^2$) well below T_c originates from gapless magnetic excitations localized at U sites.

In anisotropic superconductors, the impurity effect gives an important clue to identify the symmetry of the order parameter. This is because even potential scattering causes the reduction of T_c in contrast to the s-wave pairing. A slight inhomogeneity at the Al-site, which shows up in a larger FWHM, causes a decrease of T_c from 2 K to 1.75 K and yields a residual density of states. Actually a T_1T=constant behavior was reported on a sample of UPd_2Al_3 which has lower T_c (=1.75 K) and larger FWHM=20 kHz than the standard sample with T_c=1.98 K and FWHM=12 kHz. Apparently, the T dependence of $^{27}(1/T_1)$ can sensitively probe an intrinsic quasi-particle excitation near the Fermi level. The rate R of T_c reduction was found to be $R = T_c(1.75K)/T_{co}(1.98K) = 0.88$ when the fraction of residual to normal density of states, $N_{res}/N_0 = [(T_1T)^{-1}_{res}/(T_1T)^{-1}_n]^{1/2} = 0.23$. This is consistent with a predicted value $N_{res}/N_0 = 0.36$ with $T_c/T_{co} = 0.88$ in the *unitarity limit* for anisotropic superconductivity with vanishing gap along a line [40, 41].

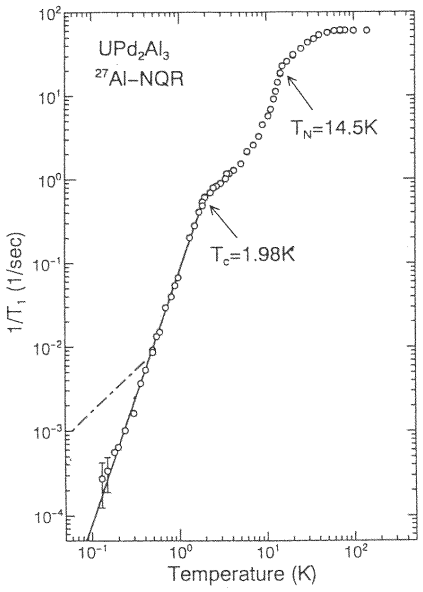

Figure 5.7: Temperature dependence of $^{27}(1/T_1)$ in zero field Al-NQR for UPd_2Al_3. The solid line shows T^3 dependence deduced from the d-wave model by using $\Delta(\theta) = \Delta\cos\theta$, with $2\Delta/T_c$=5.5. Dash-dotted line shows the T_1T=constant law which would be expected from residual density of states by impurities [33].

The same d-wave model as the one used for $CeCu_2Si_2$ in the clean limit successfully interprets both the T dependence of $1/T_1$ and Knight shift of ^{27}Al. The solid lines in Figs.5.6 and 5.7 are calculated results with the gap parameter $2\Delta_0 = 5.5T_c$. Here it is assumed that $\Delta(T)$ follows the same T dependence as that in the BCS case. Both experiments are in favor of the d-wave pairing model with a line node.

From the Knight shift result below T_c, it is shown that the large residual shift originates from the antiferromagnetic susceptibility, while the isotropic reduction of the spin shift below T_c is due to the formation of the singlet pairing among quasi-particles near the Fermi level. Combining results of both

the Knight shift and $^{27}(1/T_1)$, which includes the impurity effect, it is concluded that UPd_2Al_3 is a d-wave superconductor characterized by a vanishing energy gap along lines on the Fermi surface.

5.4.3 UPt_3

superconducting phase diagram

UPt_3 exhibits many indications of anisotropic superconductivity [42, 43, 44]. Figure 5.8 shows the phase diagram in the magnetic field (B) vs temperature (T) plane with magnetic field perpendicular (a) and parallel (b) to the hexagonal c-axis. These phases have been mapped out by a number of different

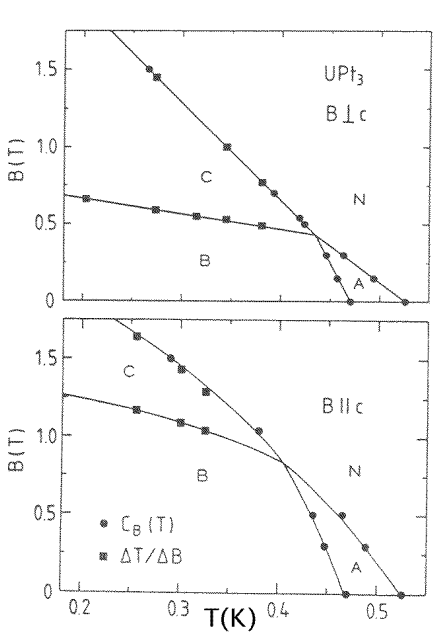

Figure 5.8: The phase diagram of UPt_3 with magnetic field B (a) perpendicular and (b) parallel to the c-axis determined by specific heat, ultrasonic attenuation and magnetocaloric effect [42, 43, 44].

measurements. The multiplicity of superconducting phases in UPt_3 is reminiscent of the complex phase diagram of superfluid ^{3}He. Various scenarios to interpret the complex phases of UPt_3 have been proposed with unconventional order parameters[45, 46]. All the possible order parameter representations allowed for the hexagonal point group of UPt_3 have been enumerated under the assumption of strong spin-orbit coupling (see Table 5.2). In the presence of the inversion symmetry the parity of order parameter is a good quantum number. A possible scenario is that the two phases at zero field belong to different order parameter representations which are nearly degenerate accidentally. The other scenario is that the two transitions arise from splitting of an otherwise degenerate state within a single representation. In the latter case, a symmetry-breaking field is responsible for the splitting, in the same way as the magnetic field lifts the two-fold degeneracy of the A-phase in superfluid ^{3}He. A candidate for the symmetry-breaking field in UPt_3 is the proposed weak AF order below T_N=5 K with moments aligned in the basal plane. In fact, direct coupling of the weak AF to the double superconducting transitions was found by neutron diffraction and specific heat measurements under hydrostatic pressure. As indicated in Fig.5.9, the coalescence of two superconducting transitions correlates well with the disappearance of elastic neutron intensity around a critical pressure of P_c=3.2 kbar [47].

It is unusual that T_N itself does not show any appreciable change with pressure. Moreover the neutron intensity, which grows linearly with temperature, behaves differently from that expected for Bragg scattering. We note that no evidence for the magnetic transition has been obtained by experiments other than neutron scattering. These include thermal and transport measurements. In particular, Pt-NMR on a high-quality single crystal has not detected any signature of hyperfine broadening or a frequency shift which should follow the onset of magnetic ordering [49]. On the other hand, in $U(Pt_{0.95}Pd_{0.05})_3$

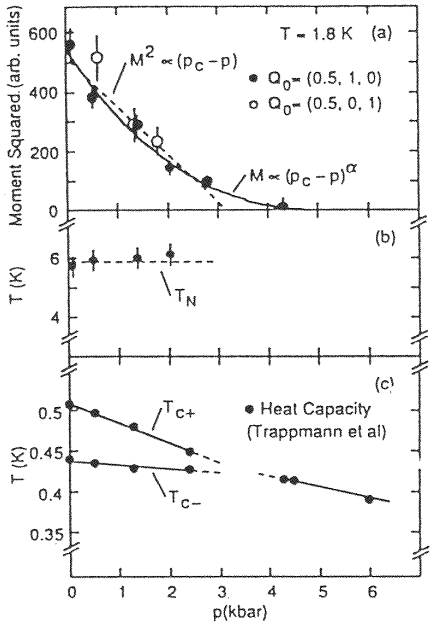

Figure 5.9: (a) Variation of integrated neutron intensity of magnetic peak (1/2, 1, 0) (closed circle) and (1/2, 0, 1) (open circle) with hydrostatic pressure. This is a measure of square of sublattice magnetization, M_Q^2. Solid line is a fit of $M_Q^2 \propto (p_c - p)^\alpha$ with α=2.6 ± 1.9 and p_c = 5.4 ± 2.9. The dashed line shows $M_Q^2 \propto (p_c - p)$ which yields and 3.2 ± 0.2 kbar. (b) Pressure dependence of T_N. (c) Pressure dependence of the temperatures of double transitions [47, 48].

which undergoes the AF transition at T_N=5 K with the same spin structure as UPt_3 but with a larger moment of 0.6 μ_B, Pt-NMR is dominated by the hyperfine field which amounts to 32 kOe [50]. Thus the Pt-NMR results rule out the presence of a static hyperfine field of about 1 kOe, which is expected if the ordered moment of $0.02\mu_B$ is present. A possible way out is that uranium-derived moments fluctuate with a frequency larger than the Pt-NMR frequency. It seems unlikely that such fluctuating moment can be the symmetry-breaking field to lift the two-fold degeneracy of the order parameter. Most phenomenological approaches incorporate this as the symmetry-breaking field to interpret the multiplicity of the superconducting phase [45, 46, 51].

The parity of the order parameter in UPt_3 has been determined by precise Pt Knight shift measurements of a high quality single crystal. As shown in Fig.5.10 [52], the spin part of the Knight shift does not decrease below T_c at all in a field range of 4.4 -15.6 kOe down to 25 mK. This result provides evidence that odd-parity superconductivity with parallel spin pairing is realized. By contrast, the Knight shift decreases below T_c for magnetic field parallel to the b axis with $H < 5$ kOe, and for magnetic field parallel to the c axis with $H_c < 2.3$ kOe. Magnetic field along the a axis does not lead to a change of Knight shift down to 1.7 kOe. This set of Pt Knight shift data seems consistent with odd-parity superconductivity including a non-unitary pairing [52, 53].

5.4.4 UBe_{13}

In the superconducting state of UBe_{13}, specific heat follows approximately the T^3 law below $T_c = 0.9$ K [54]. This power-law behavior is consistent with a gap vanishing at points. On the other hand, the T^3 dependence found in $1/T_1$ suggests a gap with line nodes [55]. Power-law behaviors are also reported in ultrasonic attenuation [56] and the penetration depth [57]. Figure 5.11 [58] shows the upper critical field $H_{c2}(T)$ with the following features:
(1) The slope $|dH_{c2}/dT|$ of the critical field is anomalously large;
(2) $H_{c2}(T)$ is almost linear in T over a large temperature range;
(3) $H_{c2}(0)$ at T=0 is larger than the value calculated within the BCS theory assuming a magnetic

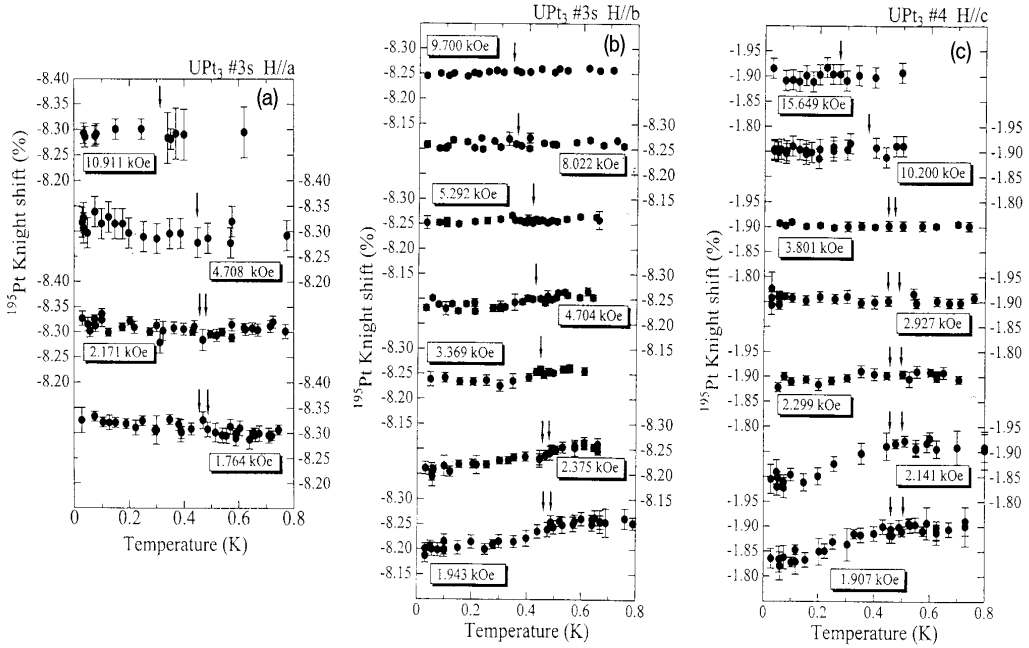

Figure 5.10: T dependence of the ^{195}Pt Knight shift for various magnetic fields: (a) K_a for $H_a \parallel a$, (b) K_b for $H_b \parallel b$, and (c) K_c for $H_c \parallel b$. respectively [52]. Arrows (↓) show superconducting transition temperatures.

moment comparable to μ_B.

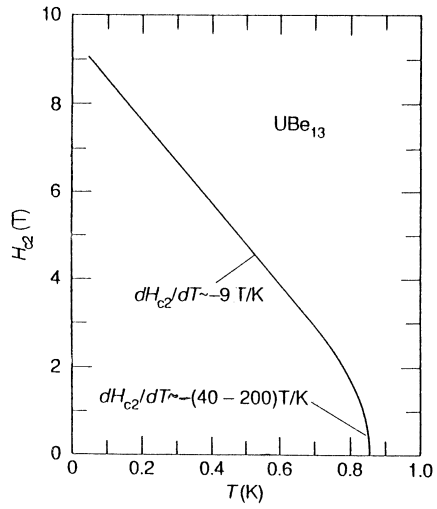

Figure 5.11: Upper critical magnetic field H_{c2} versus temperature T for UBe_{13} [58].

The superconducting states of heavy electrons are very sensitive to impurities and defects. T_c can be strongly depressed in UPt_3 by grinding the sample. The substitution of a small amount of Th for U in UBe_{13} leads to a rapid decrease of T_c. For Th concentrations between x=0.017 and 0.05 in $U_{1-x}Th_xBe_{13}$, two phase transitions were observed in specific-heat measurements [59] with comparable discontinuities at T_c's. The phase diagram is shown in Fig.5.12. It has been proposed [60] that the order parameter belongs to a one-dimensional representation Γ_1 for $x < x_c \sim 0.018$, and a three-dimensional one Γ_5 for $x > x_c$ and $T > T_{c2}$ (see Fig.5.12). It is possible that Γ_1 and Γ_5 are interchanged. For $T < T_{c2}$ the time-reversal symmetry may be broken and a mixture of the two representations may be realized.

5.4.5 Implication for the superconducting mechanism

In the three compounds above, the dynamical magnetic properties are different in each case. Nevertheless in all three the superconducting energy gap vanishes along lines on the Fermi surface. It is almost certain that anisotropic order parameters with spin singlet are realized in $CeCu_2Si_2$ and UPd_2Al_3, and that a different anisotropic order parameter with non-unitary spin-triplet pairing is realized in UPt_3, which is the first example of this pairing symmetry in charged many body systems. These variations of the anisotropic order parameter could be due to the different characters of the magnetic fluctuations which lead to the Cooper pairing. We note that the integrated spectral weight of magnetic fluctuations is smaller for Ce compounds with the $4f^1$ than for U compounds with $5f^2 - 5f^3$. Although it is not certain to what extent of the fluctuation frequency is relevant to the pairing, this difference in the number of f-electrons may be a reason why the magnetism and superconductivity compete in $CeCu_2Si_2$ and can coexist in UPd_2Al_3.

In the phase A of $CeCu_2Si_2$, the AF spin fluctuations which have a large spectral weight at low energy are expelled by the onset of the superconducting transition. Application of pressure makes T_K shift to high temperature and hence transfers the spectral weight of the spin fluctuations to higher energy. As a result T_c rapidly increases from 0.7 K at ambient pressure to around 2 K at 3 GPa. It is noteworthy that the superconductivity is enhanced when the spectral weight is transferred to a relatively higher energy region. This transfer is derived from the T_1T=constant law, which means that the Fermi liquid description is valid for the lowest energy excitations. An important feature is that the ground state adjacent to the AF phase in $CeCu_2Si_2$ and $CeCu_2Ge_2$ is not the normal phase but the superconducting one.

By contrast, UPd_2Al_3 is characterized by AF magnetic order with a large moment of 0.8 μ_B per U atom. At the same time the Fermi liquid description is valid well below T_N with a large density of states γ=150mJ/mole K^2. The record high value T_c=2 K is realized in the presence of static AF order. These

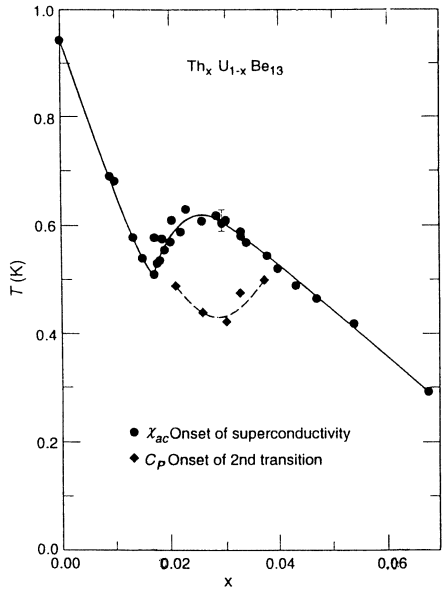

Figure 5.12: The temperature vs Th concentration (x) phase diagram of $U_{1-x}Th_xBe_{13}$. Note the rapid change in $T_c(x)$ (solid line) as x increases up to x_c ∼0.018, and the second phase transition at $T_{c2}(x)$ (dashed line) [54].

features seem to originate from the large degrees of freedom for magnetic fluctuations associated with $5f^2 - 5f^3$-electrons.

UPt_3 has remarkable features of spin fluctuations: First, although any conventional AF order is not present, its spectral weight comes partly from a quasielastic AF contribution with the wave vector $\boldsymbol{Q}_b$ in the hexagonal plane. Secondly, there is also a sizable AF fluctuation with wave vector $\boldsymbol{Q}_c$ along the c-axis and with a rather high excitation energy of 5meV[61]. Thirdly the ferromagnetic fluctuation near $q = 0$ (so-called paramagnon) is also seen in neutron scattering experiments [62]. The Fermi liquid description applies below 1 K with the density of states γ=420 mJ/mole K^2. It seems possible that paramagnons play a role in producing the anisotropic p- or f-wave superconductivity with parallel spin pairing in UPt_3.

5.5 Toward a Microscopic Theory

The fundamental problem in the superconductivity of heavy electrons is why the strongly repulsive f electrons form pairs. There is no definite answer to this question yet. It is instructive to compare with triplet pairing in ^{3}He where there is also a strongly repulsive core in the interaction [63]. At the same time there is an attractive region in the pair potential which comes from the van der Waals force. The triplet pairing has zero amplitude at the origin so that the repulsive core is not critical. We recall that the van der Waals force originates from virtual polarization of valence electrons which has much higher characteristic energy than the Fermi energy of liquid ^{3}He. In the BCS theory, the electrons feel the attractive force mediated by virtual lattice vibrations which have much lower energy than the Fermi energy. In the case of ^{3}He there is no lattice in the background, but the role of phonons is played partly by nuclear spin fluctuations of ^{3}He. It has been shown that ferromagnetic fluctuations favor triplet pairing rather than singlet [63].

In heavy electrons the relative importance of phonons and spin fluctuations is still uncertain. In any case, because of the strongly repulsive core, the s-wave pair seems to be difficult to be realized. The anisotropic pairing force due to the electron-phonon interaction is much weaker than the isotropic one .

We discuss the pairing force qualitatively with use of the Landau quasi-particle picture. In the usual strong coupling theory for superconductors [64], one derives the self-energy and the pairing force simultaneously. Then the solution of the resultant Eliashberg equation gives the transition temperature and

the quasi-particle spectrum microscopically. This is unfortunately not possible for heavy electrons, because the renormalization leading to the Kondo state cannot be represented by any simple perturbation processes. Thus one has to assume the spectrum of the quasi-particles, and then consider the interaction among them. A similar situation occurs in the superfluidity of ^{3}He [65].

We start with the linearized gap equation which is formally exact:

$$\Delta_{\alpha\beta}(\boldsymbol{k}, i\epsilon_n) = -T_c \sum_m \sum_p \sum_{\mu\nu} \langle \alpha\beta|\Gamma(\boldsymbol{k}, \boldsymbol{p}; i\epsilon_n, i\epsilon_m)|\nu\mu\rangle G_\mu(\boldsymbol{p}, i\epsilon_m) G_\nu(-\boldsymbol{p}, i\epsilon_m) \Delta_{\mu\nu}(\boldsymbol{p}, i\epsilon_m)$$

where $\langle \alpha\beta|\Gamma(\boldsymbol{k}, \boldsymbol{p}; i\epsilon_n, i\epsilon_m)|\nu\mu\rangle$ is the irreducible vertex part for the pairing interaction. Being irreducible in this case means that the Feynman diagram cannot be separated into two pieces by cutting the two Green functions going parallel. We assume that T_c is much smaller than T_K, which plays the role of the Fermi energy for heavy electrons. Then we make an approximation, replacing the vertex part by its value at the Fermi surface, and imposing the cut-off energy ω_c in the summation over Matsubara frequencies. The result is

$$\Delta_{\alpha\beta}(\boldsymbol{k}) = -\ln\left(\frac{\omega_c}{T_c}\right) \rho(0) a_f^2 \int \frac{d\Omega_p}{4\pi} \langle \alpha\beta|\Gamma(\boldsymbol{k}, \boldsymbol{p})|\nu\mu\rangle \Delta_{\mu\nu}(\boldsymbol{p}), \tag{5.43}$$

where the integral is over the solid angle of the Fermi surface. This equation takes almost the same form as the mean-field approximation for the pairing. What is different here is that the renormalization factor a_f is present. In other words, it is in the quasi-particle picture that we make the mean-field theory in the spirit of the Landau theory.

In order to see the effect of ferromagnetic and antiferromagnetic spin fluctuations in the simplest way, we assume for the moment spherical symmetry and neglect the spin-orbit interaction. Then the effective interaction is decomposed as

$$\langle \alpha\beta|\Gamma(\boldsymbol{k}, \boldsymbol{p})|\mu\nu\rangle = U(\boldsymbol{k}, \boldsymbol{p}) \delta_{\alpha\nu}\delta_{\beta\mu} + J(\boldsymbol{k}, \boldsymbol{p}) \boldsymbol{\sigma}_{\alpha\nu} \cdot \boldsymbol{\sigma}_{\beta\mu}. \tag{5.44}$$

We note that the right hand side gives $U + J$ for the triplet pair and $U - 3J$ for the singlet pair. Since both $\boldsymbol{k}$ and $\boldsymbol{p}$ are at the Fermi surface, i.e. with length k_F, the vertex part can be expanded in terms of spherical harmonics as

$$\langle \alpha\beta|\Gamma(\boldsymbol{k}, \boldsymbol{p})|\mu\nu\rangle == \sum_{lm} \langle \alpha\beta|\Gamma_l|\mu\nu\rangle Y_{lm}(\hat{k}) Y_{lm}(\hat{p})^*, \tag{5.45}$$

where $\hat{k}$ denotes the solid angle of $\boldsymbol{k}$. This equation together with eq.(5.44) leads to the parameters U_l and J_l which characterize the strength of potential scattering and exchange one, respectively.

The pairing amplitude is also expanded as

$$\Delta_{\alpha\beta}(\hat{k}) = \sum_{lm} \Delta_{\alpha\beta}^{lm} Y_{lm}(\hat{k}).$$

Then the gap equation given by eq.(5.43) turns into

$$1 = -\ln(\omega_c/T_c)\rho(0)a_f^2(U_l + J_l), \quad (\text{triplet},\ l : \text{odd}) \tag{5.46}$$

$$1 = -\ln(\omega_c/T_c)\rho(0)a_f^2(U_l - 3J_l), \quad (\text{singlet},\ l : \text{even}). \tag{5.47}$$

The actual pairing occurs for the type with the highest T_c, i.e, with a negative coupling constant with the largest absolute magnitude.

To clarify the role of spin fluctuations we take the so-called potential scattering model [65] where U and J depend only on the momentum transfer $\boldsymbol{k} - \boldsymbol{p}$. This model enables us to make a connection between $\Gamma(\boldsymbol{k}, \boldsymbol{p})$ and the Landau parameters. The spin-independent scattering $U(\boldsymbol{k} - \boldsymbol{p})$ should be dominated by the strong on-site repulsion. Then its angle dependence should be weaker and U_l is dominated by the component $l = 0$. Because of the large positive value of U_0, s-wave pairing is strongly suppressed. On the other hand, the spin-dependent part $J(\boldsymbol{k} - \boldsymbol{p})$ is related to the magnetic susceptibility $\chi(\boldsymbol{q}, \omega)$. If we assume a constant λ for the spin-fermion coupling constant, the relation reads

$$J(\boldsymbol{k} - \boldsymbol{p}) = \lambda^2 \chi(\boldsymbol{k} - \boldsymbol{p}, 0)/4.$$

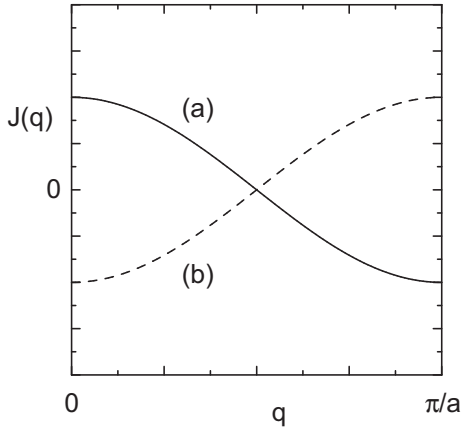

Figure 5.13: Momentum dependence of the exchange interaction shown schematically: (a) antiferromagnetic case, (b) ferromagnetic case.

If the spin fluctuation is dominantly ferromagnetic, $J(\boldsymbol{q})$ becomes negative near the center of the Brillouin zone as shown schematically in Fig.5.13(b). The angular momentum component is given by the transformation which is the inverse of eq.(5.45):

$$J_l = (l + \frac{1}{2}) \int_{-1}^{1} dx P_l(x) J(\boldsymbol{q}),$$

where $x = 1 - q^2/(2k_F^2)$. In this case J_1 tends to be negative because $P_1(x)J(\boldsymbol{q})$ is negative over most of the integration range. Thus triplet pairing is favorable with the ferromagnetic spin fluctuation. On the other hand, if the spin fluctuation is dominantly antiferromagnetic, $J(\boldsymbol{q})$ becomes negative near the boundary of the Brillouin zone. This is illustrated in Fig.5.13(a). In this case J_1 tends to be positive and triplet pairing does not occur. With antiferromagnetic fluctuation, J_2 becomes positive because of dominant contribution from $q \sim 2k_F$. Thus d-wave singlet pairing is favored [66].

The connection to the Landau parameters is given via consideration of the general form of the t-matrix for the quasi-particles. For incoming particles of momenta p_1 and p_2, and outgoing particles with p_3 and p_4, the t-matrix T depends on two parameters $x_3 = \hat{p}_1 \cdot \hat{p}_3$ and $x_4 = \hat{p}_1 \cdot \hat{p}_4$. Then the spin dependence can be parametrized as

$$\langle \alpha\beta | T(x_3, x_4) | \mu\nu \rangle = T^d(x_3, x_4)\delta_{\alpha\nu}\delta_{\beta\mu} + T^x(x_3, x_4)\boldsymbol{\sigma}_{\alpha\nu} \cdot \boldsymbol{\sigma}_{\beta\mu}. \tag{5.48}$$

The t-matrix is in general different from the vertex part in eq.(5.43) since the latter should exclude the pair propagator in the intermediate state. In the potential scattering model this intermediate state is not included even in the t-matrix and we obtain the relation

$$T^d(x_3, x_4) = U(x_3) - U(x_4), \quad T^x(x_3, x_4) = J(x_3) - J(x_4),$$

where the second terms with minus signs take account of exchange of the outgoing momenta.

The forward scattering amplitudes A_l and B_l in the Landau theory (see 1.3.4) are obtained by setting $x_3 = 1$ and expanding in terms of Legendre polynomials. As a result we obtain

$$A_l = U(1)\delta_{l,0} - U_l, \quad B_l = J(1)\delta_{l,0} - J_l.$$

This model automatically satisfies the forward scattering sum rule

$$\langle \alpha\alpha | T(x_3, x_4) | \alpha\alpha \rangle = \sum_l (A_l + B_l) = 0.$$

Thus if some Landau parameters are known from properties of the normal state, the parameters in the potential scattering model are constrained.

We remark again that the analysis above assumes spherical symmetry and neglects the spin-orbit interaction. In actual heavy-electron systems, the quantitative analysis should respect the point group symmetry. One can deal with the symmetry in terms of appropriate basis functions instead of the spherical harmonics used above. Much less is known about the effect of strong anisotropy in the g-factor.

Bibliography

[1] J. Bardeen, J.N. Cooper and J.R. Schrieffer, Phys. Rev. **108**, 1175 (1957).

[2] F. Steglich et al, Phys. Rev. Lett. **43**, 1892 (1979).

[3] For review, see for example, Proc. Int. Conf. Strongly Correlated Electron Systems, Physica **B259-261** (1999).

[4] N. Grewe and F. Steglich, Handbook on the Physics and Chemistry of Rare Earths, edited by K.A. Gschneider and L. Eyring (North-Holland, Amsterdam, 1991), Vol. **14**.

[5] A.J. Leggett, Rev. Mod. Phys. **47**, 331 (1975) .

[6] P.W. Anderson and P. Morel, Phys. Rev. **123**, 1911 (1961) .

[7] J.G. Bednorz and K.A. Müller, Z. Phys. **B64**, 189 (1986).

[8] For review, see for example, Proc. Int. Conf. Material and Mechanism of Superconductivity: High-Temperature Superconductivity V, Physica **C 282-287** (1997).

[9] T. Moriya and K. Ueda, J. Phys. Soc. Jpn. **63**, 1871 (1994).

[10] P. Monthoux and D. Pines, Phys. Rev. **B49**, 4261 (1994).

[11] R. Balian and N.R. Werthamer, Phys. Rev. **131**, 1553 (1963).

[12] P.W. Anderson and W.F. Brinkman, Phys. Rev. Lett. **30**, 1108 (1973).

[13] G.E. Volovik and L.P. Gorkov, Sov. Phys. JETP **61**, 843 (1985).

[14] M. Sigrist and K. Ueda, Rev. Mod. Phys. **63**, 239 (1991).

[15] S. Yip and A. Garg, Phys. Rev. B**48**, 3304 (1993).

[16] E. Blount, Phys. Rev. B**22**, 2935 (1985).

[17] K. Yosida, Phys. Rev. **110**, 769 (1958).

[18] P.W. Anderson, Phys. Rev. Lett. **3** 325 (1959).

[19] L.C. Hebel and C.P. Slichter, Phys Rev. **113**, 1504 (1959).

[20] S. Ohsugi, Y. Kitaoka, M.Kyogaku, K. Ishida, K. Asayama and T. Ohtani, J. Phys. Soc. Jpn. **61** 3054 (1992).

[21] S. Wada and K. Asayama, J. Phys. Soc. Jpn. **34**, 1168 (1973).

[22] D. Jaccard, K. Behnia and J. Sierro, Phys. Lett. A **163**, 475 (1992).

[23] F.Thomas, J.Thomasson, C.Ayache, C.Geibel and F.Steglich,Physica **B186-188**, 303 (1993).

[24] Y. Kitaoka, H. Tou, G.-q. Zheng, K. Ishida, K. Asayama, T.C. Kobayashi, A. Kohda, N. Takeshita. K. Amaya, G. Geibel, C. Schank and F. Steglich, Physica **B206&207**, 55 (1995).

[25] F.M. Grosche, S.R. Julian, N.D. Mathur and G. G. Lonzarich, Physica **B 223-224**, 50 (1996).

[26] I.R. Walker, F.M. Grosche, D.M. Freye and G.G. Lonzarich, Physica **C 282-287**, 303 (1997).

[27] Y. Kitaoka, H. Yamada, K. Ueda, Y. Kohori, T. Kohara, Y. Odd and K. Asayama, Jpn. Apply Phys. Suppl. **26**, 1221 (1987).

[28] K. Ishida et al, Phys. Rev. Lett. **82**, 5353 (1999).

[29] F. Steglich, Springer Series in Solid-State Sciences **62**, 23 (1985).

[30] C. Geibel, C. Shank, S. Thies, H. Kitazawa, C.D. Bredl, A. Bohm, M. Rau, A. Grauel, R. Caspary, R. Hefrich, U. Ahlheim, G. Weber and F. Steglich, Z. Phys. **B84** ,1 (1991).

[31] N. Sato, N. Aso, G.H. Lander, B. Roessli, T. Komatsubara and Y. Endoh, J. Phys. Soc. Jpn. **66**, 2981 (1997).

[32] N. Metoki, Y. Haga, Y. Koike, N. Aso and Y. Onuki, J. Phys. Soc. Jpn. **66**, 2560 (1997).

[33] H. Tou, Y. Kitaoka, K. Asayama, C. Geibel, C. Schank and F. Steglich, J. Phys. Soc. Jpn. **64**, 725 (1995).

[34] K. Matsuda *et al.*, Phys. Rev. B**55**, 15223 (1997).

[35] R. Caspary, P. Hellmann, m. Keller, G. Sparn, C. Wassilew, R. Kohler, C. Geibel,C. Schank, F. Steglich and N.e. Phillips, Phys. Rev. Lett. **71**, 2146 (1993).

[36] N. Metoki *et al.*, Phys. Rev. Lett. **24**, 5417 (1998).

[37] M. Kyogaku, Y. Kitaoka, K. Asayama, N. Sato, T. Sakon, T. Komatsubara, Physica B **186-188**, 285 (1993).

[38] R. Feyerherm et al, Phys. Rev. Lett. **73**, 1849 (1994).

[39] F. Steglich *et al.*, in: Physical Phenomena at High Magnetic Fields-II, Z. Fisk *et al.*, eds., World Scientific, Singapore, 1996, p.185.

[40] S. Shimitt-Rink, K. Miyake and C.M. Varma, Phys. Rev. Lett. **57**, 2575 (1986).

[41] P. Hirschfeld, D. Vollhardt and P. Wölfle, Solid State Commun. **59**, 111 (1986).

[42] L. Taillefer, J. Flouquet and G. G. Lonzarich, Physica **B169**, 257 (1991).

[43] H.v. Lohneysen, Physica **B197**, 551 (1994).

[44] K. Hasselbach, L. Taillefer and J. Flouquet, Phys. Rev. Lett. **63**, 93 (1989).

[45] T.Ohmi and K. Machida, Phys. Rev. Lett. **71**, 625 (1993) ; K. Machida et al, J. Phys. Soc. Jpn. **62**, 3216 (1993).

[46] J.A. Sauls, J. Low Temp. Phys. **95**, 153 (1994).

[47] S.M. Hayden, L. Taillefer, C. Vettier and J. Flouquet, Phys. Rev. **B46**, 8675 (1992).

[48] T. Trappmann, H.v. Lohneysen and L. Taillefer, Phys. Rev. **B43**, 13714 (1991).

[49] H. Tou, Y. Kitaoka, K. Asayama, N. Kimura, Y. Ōnuki, E. Yamamoto, and K. Maezawa, Phys. Rev. Lett. **77**, 1374 (1996).

[50] Y. Kohori, M. Kyogaku, T. Kohara, K. Asayama, H. Amitsuka and Y. Miyako, J. Magn. Magn. Mater. **90-91**, 510 (1990).

[51] D.W. Hess, T.A. Tokuyasu and J.A. Sauls, J. Phys. Condens. Matter. **1**, 8135 (1989).

[52] H. Tou et al, Phys. Rev. Lett. **80**, 3129 (1998).

[53] T. Ohmi and K. Machida, J. Phys. Soc. Jpn. **65**, 4018 (1996).

[54] H. R. Ott, H. Rudigier, P. Delsing, Z. Fisk, Phys. Rev. Lett. **50**, 1595 (1983).

[55] D.E. MacLaughlin, J. Magn. Magn. Mater. **47&48**, 121 (1985).

[56] B. Golding, D. J. Bishop, B. Batlogg, W. H. Haemmerle, Z. Fisk, J. L. Smith, H. R. Ott, Phys, Rev. Lett. **55**, 2479 (1985).

[57] D. Einzel, P. J. Hirschfeld, F. Gross, B. S. Chandrasekhar, K. Andres, H. R. Ott, J. Beuers, Z. Fisk, J. L. Smith, Phys. Rev. Lett. **56**, 2513 (1986).

[58] M. B. Maple, J. W. Chen, E. E. Lambert, Z. Fisk, J. L. Smith, H. R. Ott, J. S. Brooks, M. J. Naughton, Phys. Rev. Lett. **54**, 477 (1985).

[59] H. R. Ott, H. Rudigier, E. Felder, Z. Fisk, J. L. Fisk, Phys. Rev. B **33**, 126 (1986).

[60] M. Sigrist and T. M. Rice, Phys. Rev. B**39**, 2200 (1989).

[61] G.Aeppli et al, Phys. Rev. Lett. **60**, 615 (1988); ibid, **63**, 676 (1989).

[62] N. R. Bernhoeft and G. C. Lonzarich, J. Phys. C **7**, 7325 (1995).

[63] see e.g. D. Vollhardt and P. Wölfle, *The Superfluid Phases of Helium 3*, (Taylor and Francis, London, 1990).

[64] A.A. Abrikosov, L.P. Gorkov, I.E. Dzyaloshinskii, *Methods of Quantum Field Theory in Statistical Physics*, (Dover, New York, 1975).

[65] J.W. Serene and D. Rainer, Phys. Rep. **101**, 221 (1983).

[66] K. Miyake, J. Magn. & Magn. Mater. **63 & 64**, 411 (1987).

Chapter 6

Comparison with High-Temperature Superconductors

6.1 Characteristics of Copper Oxides

The discovery by Bednorz and Müller(1986) of superconductivity at 30 K in the ceramic copper oxides [1] $La_{2-x}Ba_xCuO_4$(abbreviated as 2-1-4) has had great impact on solid-state physics. This breakthrough was followed soon by the discovery of the 90 K-class superconductor $YBa_2Cu_3O_{7-y}$(1-2-3) and recently by that of 130 K-class $HgBa_2Ca_2Cu_3O_{8+y}$ (Hg1223). These cuprates have the following characteristic properties [2]:

1. The CuO_2 planes are commonly present, and are separated by bridging blocks which act as charge reservoirs for the planes. Fig.6.1 illustrates the structure of the (2-1-4) system.

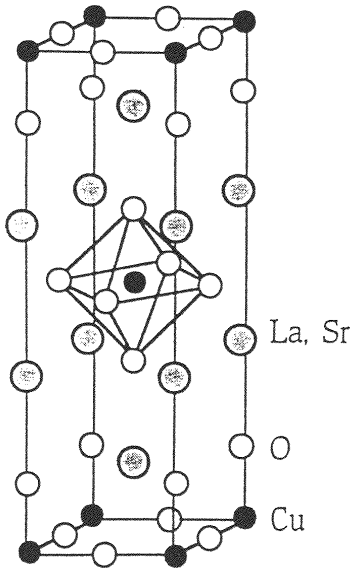

Figure 6.1: Crystal structure of La_2CuO_4.

2. The undoped compounds, La_2CuO_4 and $YBa_2Cu_3O_6$ are antiferromagnetic (AF) insulators (Mott insulators) in which strong Coulomb correlations act to localize the Cu^{2+} electrons with spin-1/2 so that the system behaves like a two dimensional (2D) Heisenberg antiferromagnet. The long-range order is caused by weak interlayer magnetic coupling between the CuO_2 planes. As holes are added into the plane through the substitution of Sr into La sites for the 2-1-4, or through oxygen doping

into the CuO chain sites in the 1-2-3, the Néel temperature is reduced. The Cu^{2+} spins no longer exhibit long range AF order beyond a critical hole content which corresponds to $La_{1.95}Sr_{0.05}CuO_4$ and $YBa_2Cu_3O_{6.4}$. At higher doping level, the system enters an anomalous metallic phase which exhibits the superconducting transition with high-T_c value. Fig.6.2 shows the phase diagram for the 2-1-4 including magnetic and structural phase transitions as a function of the doping level [3].

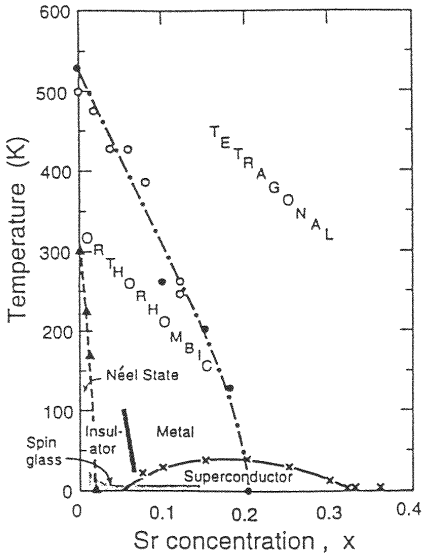

Figure 6.2: Antiferromagnetic, superconducting and structural phase diagram of $La_{2-x}Sr_xCuO_4$ [3].

3. Properties in the normal state deviate from those of the Fermi liquid in contrast to conventional and heavy electron superconductors. For example, the resistivity shows a T-linear behavior over a wide temperature range for most cases. With increasing carrier content, however, it changes from T-linear to T^2 behavior characteristic of the Fermi liquid. Eventually the superconductivity disappears. Figure 6.3 shows the T-dependence of the resistivity for $Tl_2Ba_2CuO_{6+y}$ (Tl2201) compounds with different T_c [4].

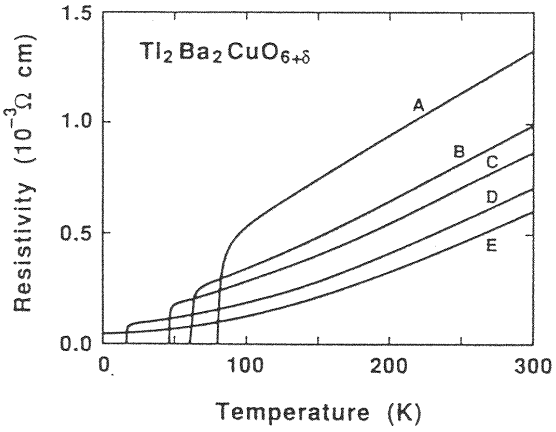

Figure 6.3: Temperature dependence of resistivity in $Tl_2Ba_2CuO_{6+\delta}$ with various T_c. All measurements were made using the same sample whose T_c was controlled [4].

4. None of the superconducting properties resemble those of the singlet s-wave in which the energy gap is finite and isotropic. A growing list of experimental results are consistent with the $d_{x^2-y^2}$ pairing state where the energy gap vanishes along lines. The NMR experiments such as nuclear relaxation[5, 6], Knight shift and impurity effect [7, 8, 9, 10] have provided important clues to identifying the pairing symmetry of the high-T_c superconductivity as the d-wave. The NMR study was the first to find the unconventional impurity effect: T_c is insensitive to the presence of impurities and other imperfections, whereas the low T properties in the superconducting state are extremely sensitive to the presence of a minute concentration of impurities and imperfections. In contrast to the novel properties in the normal state, the superconducting properties share the anisotropic character with that in heavy-electron superconductors. This commonality seems to originate from the strong repulsive interaction in both systems; the node is favorable to reducing the energy cost of forming the pair.

There is no consensus on theoretical models to explain the anomalous normal and superconducting properties over the entire doping level in a unified way. However, a modified form of the BCS theory, which incorporates an unconventional pairing state mediated by magnetic fluctuations, seems a valid phenomenology in describing the anisotropic superconducting state with the d-wave pairing symmetry.

6.2 Spin Dynamics Probed by NMR

6.2.1 Static spin susceptibility

Following Mila and Rice [11], we take the Hamiltonian for the ^{63}Cu nuclear spin as given in terms of the on-site hyperfine coupling A_α ($\alpha = \perp, \parallel$) with d-electrons, and the supertransferred hyperfine coupling B with four nearest-neighbor Cu sites. The latter coupling is through the Cu ($3d$)-O($2p_\sigma$)-Cu($4s$) covalent bond. The Hamiltonian at site i is expressed as

$$^{63}H_i = A_\parallel I_{iz} \cdot S_{iz} + A_\perp (I_{ix} \cdot S_{ix} + I_{iy} \cdot S_{iy}) + B \sum_j \boldsymbol{I}_i \cdot \boldsymbol{S}_j, \tag{6.1}$$

where summation is over the four Cu nearest neighbors. On the other hand, the Hamiltonian with the ^{17}O nuclear spin at site k is given in terms of the transferred hyperfine coupling constant C between the oxygen nuclei and the Cu spins as follows:

$$^{17}H_k = C \sum_l \boldsymbol{I}_k \cdot \boldsymbol{S}_l \tag{6.2}$$

where summation is over the two Cu nearest neighbors. The spin part $^{63}K_s$ of the Knight shift is expressed as

$$^{63}K_s(T) = (A_\alpha + 4B)\chi_s(T) \qquad (\alpha = \parallel, \perp). \tag{6.3}$$

From the relation

$$\chi_s(T) = (K_{\perp obs}(T) - K_{orb}) N\mu_B/(A_\perp + 4B), \tag{6.4}$$

the T dependence of the spin susceptibility $\chi_s(T)$ is deduced as indicated in Fig.6.4[12]. Here we use the results for the T independent orbital shift of $K_{orb} = 0.24\%$ and the on-site anisotropic and the isotropic hyperfine field, $A_\perp$ and B with 35 and 40 kOe/μ_B, respectively. Experimentally the value of K_{orb} is found to be independent of the hole content over a wide doping level, while the value of B increases with increasing hole content beyond the optimum value.

In underdoped high-T_c cuprates where the hole content is smaller than the optimum value, the spin susceptibility $\chi_s(T)$ increases monotonically with increasing T, whereas in overdoped cases, $\chi_s(T)$ stays constant.

6.2.2 Spin dynamics

The nuclear-spin-lattice relaxation rate, $1/T_1$ of ^{63}Cu is dominated by the AF spin fluctuations around the zone boundary $\boldsymbol{Q} = (\pi/a, \pi/a)$ for the square lattice, whereas $1/T_1$ of ^{17}O is not affected by the AF

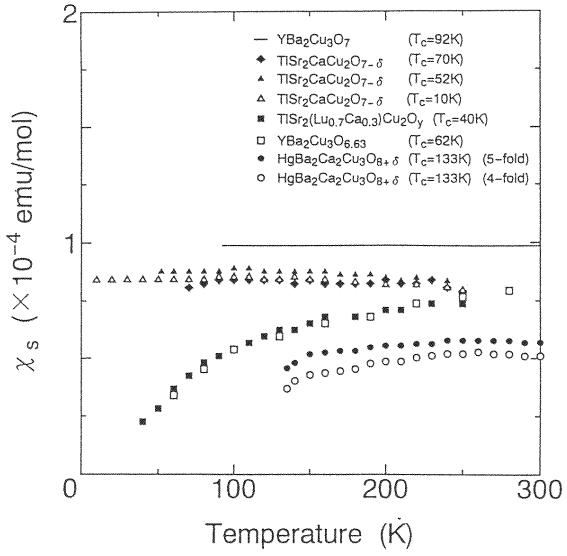

Figure 6.4: Temperature dependence of spin susceptibility deduced from ^{63}Cu Knight shift for various high-T_c compounds [12].

spin fluctuations since they are filtered away by the form factor. The form factors $F_\perp(\boldsymbol{q})$ and $F_\parallel(\boldsymbol{q})$ for respective direction of the magnetic field are written in terms of the hyperfine couplings as

$$\begin{aligned} F_\perp(\boldsymbol{q}) &= A_\perp + 2B[\cos(q_x a) + \cos(q_y a)] \qquad (6.5)\\ F_\parallel(\boldsymbol{q}) &= A_\parallel + 2B[\cos(q_x a) + \cos(q_y a)] \\ G(\boldsymbol{q}) &= 2C\cos(\frac{1}{2}q_x a) \qquad (6.6)\end{aligned}$$

where a is the distance between Cu sites. Then with the use of the dynamical susceptibility, $\chi(\boldsymbol{q},\omega)$, $^{63}(1/T_1)$ and $^{17}(1/T_1)$ are given by

$$^{63}\left(\frac{1}{T_1}\right)_\parallel = \frac{3k_BT}{2}\frac{1}{\mu_B^2\hbar^2}\sum_{\boldsymbol{q}} F_\perp(\boldsymbol{q})^2\frac{\mathrm{Im}\chi(\boldsymbol{q},\omega_n)}{\omega_n} \qquad (6.7)$$

$$^{63}\left(\frac{1}{T_1}\right)_\perp = \frac{3k_BT}{4}\frac{1}{\mu_B^2\hbar^2}\sum_{\boldsymbol{q}} (F_\perp(\boldsymbol{q})^2 + F_\parallel(\boldsymbol{q})^2)\frac{\mathrm{Im}\chi(\boldsymbol{q},\omega_n)}{\omega_n} \qquad (6.8)$$

$$^{17}\left(\frac{1}{T_1}\right) = \frac{3k_BT}{4}\frac{1}{\mu_B^2\hbar^2}\sum_{\boldsymbol{q}} G(\boldsymbol{q})^2\frac{\mathrm{Im}\chi(\boldsymbol{q},\omega_n)}{\omega_n} \qquad (6.9)$$

where ω_n is the NMR frequency.

In the case of AF spin fluctuations, the $\boldsymbol{q}$-sums in eqs.(6.7) and (6.8) are dominated by contributions around $\boldsymbol{q} = \boldsymbol{Q} = (\pi/a, \pi/a)$. However, the sum around $\boldsymbol{q} = 0$ is dominant in eq.(6.9) because of the property $G(\boldsymbol{Q}) = 0$ at $\boldsymbol{Q} = (\pi/a, \pi/a)$. Then we have

$$^{63}\left(\frac{1}{T_1T}\right) = ^{63}\Delta(A-4B)^2\frac{\mathrm{Im}\chi(\boldsymbol{Q},\omega_n)}{\omega_n} \qquad (6.10)$$

,

$$^{17}\left(\frac{1}{T_1T}\right) = ^{17}\Delta C^2\frac{\mathrm{Im}\chi(0,\omega_n)}{\omega_n} \qquad (6.11)$$

, with $^{63}\Delta$ and $^{17}\Delta$ describing the respective width in the $\boldsymbol{q}$-space.

Figures.6.5(a) and (b) indicate the contrasting T dependence of $1/T_1T$ in ^{63}Cu and ^{17}O in the CuO_2 plane for both $YBa_2Cu_3O_7$ ($YBCO_7$) with T_c=90 K and $YBCO_{6.65}$ with T_c= 60 K. Namely $^{17}(1/T_1T)$ is

found to be proportional to the static spin susceptibility $\chi_s(T)$, as indicated by solid lines in Fig.6.5(a). Comparison with Fig.6.5 (b) shows that the dynamical susceptibility is significantly peaked around $\boldsymbol{Q} = (\pi/a, \pi/a)$ [13].

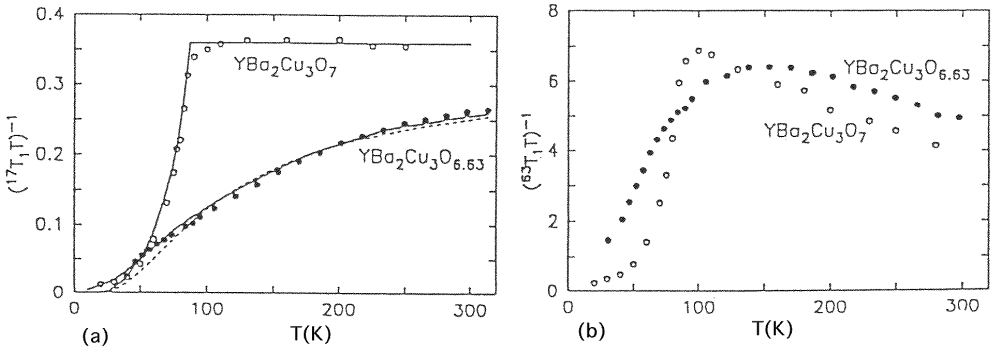

Figure 6.5: Temperature dependence of (a) $^{17}(T_1T)^{-1}$ and (b) $^{63}(T_1T)^{-1}$ in $YBa_2Cu_3O_7$ with T_c=92K and $YBa_2Cu_3O_{6.65}$ with T_c=60 K [13].

If we assume that $\mathrm{Im}\chi(\boldsymbol{Q}+q,\omega)$ obeys the double Lorentzian form in momentum ($\boldsymbol{q}$) and energy (ω) distributions, Eqs.(1.84) $-$ (1.89) lead to $^{63}(1/T_1T)$ in the form

$$^{63}\left(\frac{1}{T_1T}\right) \propto (A-4B)^2\frac{\chi_{\boldsymbol{Q}}(T)}{\Gamma_0}. \tag{6.12}$$

Figures 6.6 (a) and (b) show the T dependences of $^{63}(1/T_1T)$ and $^{63}(T_1T)$ in $La_{2-x}Sr_xCuO_4$ with various Sr content, x [14, 15]. This demonstrates that $\chi_{\boldsymbol{Q}}(T)$ follows the Curie-Weiss law due to the substantial spin fluctuations around $\boldsymbol{Q}$. We remark that in the uniform susceptibility the Curie-Weiss law is not seen in contrast to heavy-electron systems.

Since we have $\Gamma_{\boldsymbol{Q}}(T)\chi_{\boldsymbol{Q}}(T)$ =constant according to eq.(1.87), the ensuing relation

$$^{63}(T_1T) = \alpha\Gamma_{\boldsymbol{Q}}(T) \tag{6.13}$$

provides a direct measurement of the damping rate $\Gamma_{\boldsymbol{Q}}$ of AF spin fluctuations around $\boldsymbol{Q}$. Since T_1T in $La_{2-x}Sr_xCuO_4$ varies linearly with temperature as displayed in Fig.6.6 (b), we obtain

$$\Gamma_{\boldsymbol{Q}}(T) = \beta[T + T^*(x)]. \tag{6.14}$$

From an experimental relation: $T^*(x) \propto (x-0.05)$, $\Gamma_{\boldsymbol{Q}}(T)$ for x=0.05 approaches zero towards T=0. This is consistent with the fact that x=0.05 is just the phase boundary between the superconducting and the magnetic phases.

On the other hand, the nuclear spin-spin Gaussian decay rate, $1/T_{2G}$ provides a measure of the magnetic correlation length $\xi(T)$ [16, 17, 18]. In two-dimensional system, the integration in eq.(1.146) leads to the relation $1/T_{2G} \propto \xi(T)$. In underdoped high-T_c compounds such as $YBCO_{6.65}$[17] and $YBa_2Cu_4O_8$[19], the temperature dependence of T_{2G} follows a Curie-Weiss law. Hence we have the relation $1/\xi(T) = a + bT$. From the experimental relation of $(T_1T)/T_{2G}$=constant, as shown in Fig.6.7, a remarkable relation

$$\Gamma_{\boldsymbol{Q}}(T) = \frac{c}{\xi(T)} \tag{6.15}$$

follows for spin fluctuations in underdoped high-T_c cuprates. A scaling argument for quantum critical fluctuations has been put forth [20, 21] in describing the above relation between $\Gamma_{\boldsymbol{Q}}(T)$ and $\xi(T)$ in the normal state for underdoped high-T_c cuprates.

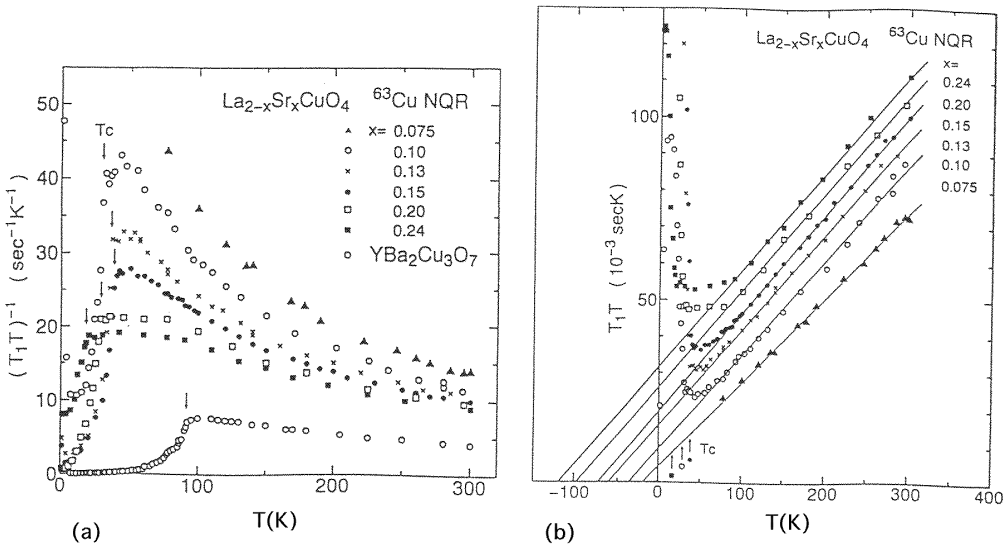

Figure 6.6: Temperature dependence of $^{63}(T_1T)^{-1}$ (a) and $^{63}(T_1T)$ (b) in $La_{2-x}Sr_xCuO_4$ with various x. [14, 15].

In the underdoped region the high-T_c cuprates deviate most strongly from conventional materials. As seen in Fig.6.5(b), $^{63}(1/T_1T)$ for the underdoped $YBCO_{6.65}$ has a shallow peak around 150 K followed by the significant decrease down to T_c=60 K[22, 13]. This behavior suggests the presence of a pseudo spin gap in spin excitations, and has been confirmed by subsequent neutron experiments as well [23]. In addition to these anomalies in magnetic excitations, the pseudo gap of the same size and $\boldsymbol{q}$ dependence as the d-wave superconducting gap has been revealed by the photoemission experiments[24]. The persistence of the gap above T_c leads to an argument that phase fluctuation may be the determining factor of T_c. At present, it is controversial whether the pseudo gap is interpreted as some superconducting fluctuations [25] or the spin excitation gap from some resonating-valence-bond (RVB)-type singlet state[26, 27].

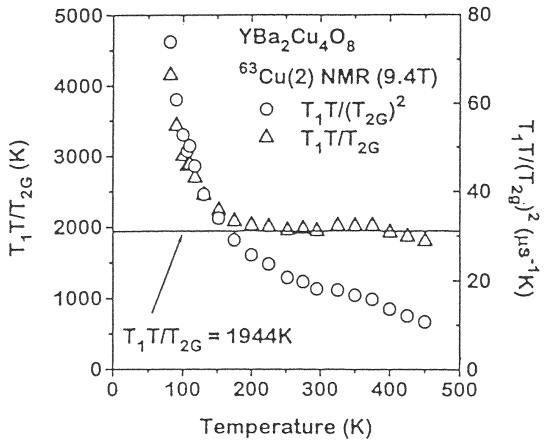

Figure 6.7: T dependence of the $(T_1T)/T_{2G}$ for the underdoped $YBa_2Cu_4O_8$[19]

By contrast, in optimum and overdoped high-T_c compounds such as $YBCO_7$[28], Hg(1223) [29] and $TlSr_2CaCu_2O_{8+\delta}$ (Tl1212) [30], the experimental relation $(T_1T)/(T_{2G})^2$= constant holds as shown in

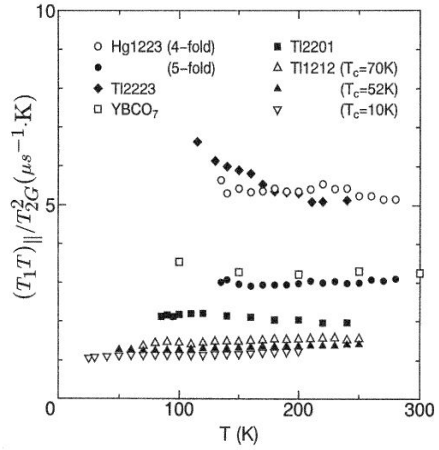

Figure 6.8: Temperature dependence of $(T_1T_{\parallel})/(T_{2G})^2$ for the optimum and overdoped high-T_c cuprates [29, 30]. Differences in the hyperfine coupling constant have been corrected.

Fig.6.8. This leads to the relation

$$\Gamma_{\boldsymbol{Q}}(T) = \frac{c'}{\xi^2(T)}, \tag{6.16}$$

which is consistent with phenomenological RPA-type approaches [31, 32].

By combining both NMR and neutron experimental results, it is suggested that the quantum critical aspect of spin correlations in underdoped systems is relevant to the onset of the high-T_c superconductivity. Increasing the number of holes causes spin correlations to be overdamped and leads to enhancement of T_c. With further increase of the hole content, a dramatic change in the spin dynamics occurs as shown

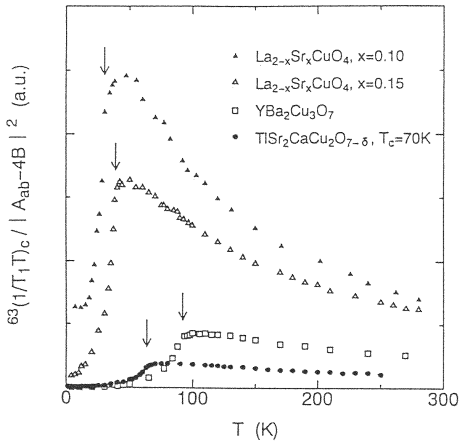

Figure 6.9: Change of the quantity $^{63}(T_1T)_c^{-1}/(A_{ab}-4B)^2 = (\alpha\Gamma_{\boldsymbol{Q}})^{-1}$ with increasing hole content [29, 30].

in Fig.6.9 [33]. Namely $\mathrm{Im}\chi(\boldsymbol{Q},\omega)$ is suppressed in the low temperature region, suggesting that $\Gamma_{\boldsymbol{Q}}$ increases. As a result $(1/T_1T)$ stays constant in a wide range of T. Doping of holes above an optimum value makes the AF correlation length shorter and decreases the T_c. This change was extracted from

the anisotropy of $R = (T_1T)_\perp/(T_1T)_\parallel$. For the case where $\chi(\boldsymbol{q})$ is strongly peaked at $\boldsymbol{q} = \boldsymbol{Q}$, we obtain

$$^{63}R_{AF} = \frac{(A_\perp - 4B)^2 + (A_\parallel - 4B)^2}{2(A_\perp - 4B)^2}, \tag{6.17}$$

whereas if $\chi(\boldsymbol{q})$ is $\boldsymbol{q}$-independent,

$$^{63}R_r = \frac{(A_\perp^2 + 4B^2) + (A_\parallel^2 + 4B^2)}{2(A_\perp^2 + 4B^2)}, \tag{6.18}$$

follows. ^{63}R's in various high-T_c cuprates are collected in Fig.6.10. ^{63}R decreases progressively from $^{63}R_{AF}$ to $^{63}R_r$ with increasing B or holes. The AF spin correlation in Tl1212 with T_c=10 K are considerably weaker, and that in Tl2201 with T_c=0 is almost absent. Both cases are close to the limit $^{63}R_r$. This shows that the presence of the AF spin fluctuation is correlated with the occurrence of superconductivity.

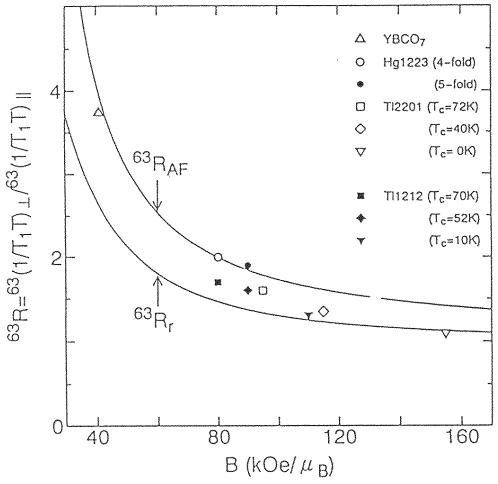

Figure 6.10: The anisotropy ratio $^{63}R_{ex} = ^{63}(1/T_1T)_{ab}/^{63}(1/T_1T)_c$ in high-T_c cuprates with various T_c's and hole contents. Lines indicated by $^{63}R_{AF}$ and $^{63}R_r$ describe the limiting cases for strongly $\boldsymbol{q}$-dependent AF spin correlations and $\boldsymbol{q}$-independent ones, respectively [30].

We note that the spin fluctuation spectrum becomes broader in the q-space as the characteristic energy $\Gamma_{\boldsymbol{Q}}$ increases with increasing hole content. This variation of q dependence of spin dynamics suggests that T_c has a maximum at an optimum characteristic energy $\Gamma_{\boldsymbol{Q}}$ in the range of 20-40 meV. The q dependence of spin fluctuations is a necessary condition for the occurrence of superconductivity [30, 34]. These properties are consistent with some phenomenological models [32, 35, 36] for spin-fluctuation-induced superconductivity. They also provide explanation for the d-wave superconductivity established experimentally. However, any microscopic theory is not yet presented.

It is noteworthy that the nature of low energy spin fluctuations in high-T_c cuprates is **non-local**, dominated by the superexchange interaction $J_{ex} \sim 1500K$ which is clearly present in the parent AF insulator. On the other hand the spin fluctuation in heavy-electron systems is nearly **local** due to the weak hybridization between f- and conduction electrons. In the latter systems, the q dependent magnetic response emerges only well below the effective Fermi temperature in a range of 10-100 K.

6.3 The p-d Hybridization Model

As the simplest model to investigate the quasi two-dimensional cuprates, we consider a square lattice where each copper site at a lattice point $\boldsymbol{R}_j = (n, m)$ has the $3d_{x^2-y^2}$ orbital. The model is shown schematically in Fig.6.11. The annihilation operator of the corresponding hole is represented by $d_{j\sigma}$

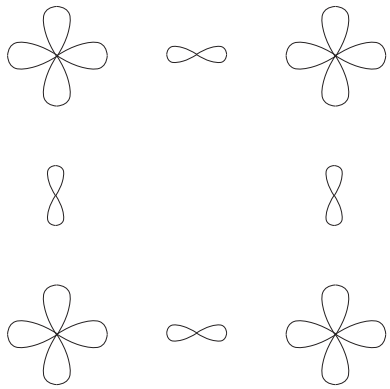

Figure 6.11: The geometry of the p-d hybridization model. Each Cu site with the $3d_{x^2-y^2}$ orbital is surrounded by four O sites with anti-bonding $2p_x$ or $2p_y$ orbitals.

with spin σ. The d-hole has Coulomb repulsion U_d. For each oxygen at $\boldsymbol{r}_i = (n + 1/2, m)$, we take the $2p_x$ anti-bonding orbital which interacts most strongly with the $3d$ hole. The annihilation operator of the hole is written as $c_{i\sigma}$. Similarly for each oxygen site at $\boldsymbol{r}_l = (n, m + 1/2)$, we take the $2p_y$ orbital with the annihilation operator written as $c_{l\sigma}$. The Hamiltonian is given by

$$H = H_1 + H_2, \tag{6.19}$$

$$H_1 = \sum_{ij}\sum_{\sigma} t_{ij} c^{\dagger}_{i\sigma} c_{j\sigma} + \sum_{i}\sum_{\sigma} \epsilon_d d^{\dagger}_{i\sigma} d_{i\sigma} + V \sum_{<ij>}\sum_{\sigma} (c^{\dagger}_{i\sigma} d_{j\sigma} + d^{\dagger}_{j\sigma} c_{i\sigma}), \tag{6.20}$$

$$H_2 = U_d \sum_{j} n_{d\uparrow} n_{d\downarrow}, \tag{6.21}$$

where $t_{ii} = \epsilon_p$ is the level of a 2p hole and the nearest neighbor 2p-2p transfer is given by $t_{ij} = -t_p$. The strong covalency between 2p and $3d$ holes is taken into account by V. The sum is over nearest neighbors of Cu and O sites.

In order to simplify the notation we have chosen the phase of the operator $d_{j\sigma}$ at $\boldsymbol{R}_j = (n, m)$ so that the odd parity of the p state is compensated. Namely, if $n + m$ is odd the phase is chosen opposite to that at a site with $n + m$ even. Then V is taken to be a constant. The change of phase corresponds to the shift $(\pi/a, \pi/a)$ of the Brillouin zone. This p-d hybridization model has an obvious similarity to the Anderson lattice. However, relative magnitudes of parameters are much different from those for heavy electrons. The typical values are:

$$U_d = 10.5, t = 1.3, \epsilon_p - \epsilon_d \equiv \Delta = 3.6,$$

in units of eV [37].

Since U_d is much larger than any other parameters in the model, it is reasonable to work with another effective Hamiltonian which eliminates the double occupation of a $3d$ orbital which corresponds to a $3d^8$ configuration. One can also assume that ϵ_d is deep enough below the Fermi level and can neglect the $3d^{10}$ configuration. Then the spin operator $\boldsymbol{S}_j$ is sufficient to describe the dynamics of the $3d$ hole. For 2p holes we introduce the notation:

$$x_{i\sigma} = \frac{1}{\sqrt{2}}(c_{i-\hat{x}/2,\sigma} + c_{i+\hat{x}/2,\sigma}), \tag{6.22}$$

$$y_{i\sigma} = \frac{1}{\sqrt{2}}(c_{i-\hat{y}/2,\sigma} + c_{i+\hat{y}/2,\sigma}), \tag{6.23}$$

$$a_{i\sigma} = \frac{1}{\sqrt{2}}(x_{i\sigma} + y_{i\sigma}), \tag{6.24}$$

where $\hat{x}$ and $\hat{y}$ denote unit vectors along each axis. Note that these operators use a non-orthogonal basis so that the fermion anti-commutator $\{x_{i\sigma}, y^{\dagger}_{j\sigma}\}$ does not vanish if $x_{i\sigma}$ and $y^{\dagger}_{j\sigma}$ have a common oxygen

orbital. The effective Hamiltonian is given by

$$H_{eff} = \sum_i H_i + J \sum_{<ij>} \boldsymbol{S}_i \cdot \boldsymbol{S}_j - \frac{4NV^2}{\Delta}, \tag{6.25}$$

$$H_i = -2t_p \sum_\sigma (x^\dagger_{i\sigma} y_{i\sigma} + y^\dagger_{i\sigma} x_{i\sigma}) + 2t_s \sum_\sigma a^\dagger_{i\sigma} a_{i\sigma} + 4J_s \sum_{\alpha\beta} \boldsymbol{S}_i \cdot a^\dagger_{i\alpha} \boldsymbol{\sigma}_{\alpha\beta} a_{i\beta}, \tag{6.26}$$

where the origin of energy is taken to be the 2p hole level ϵ_p. Here the new parameters J, J_s and t_s are given by

$$J = \frac{4V^4}{\Delta^2}\left(\frac{1}{U_d} + \frac{1}{\Delta}\right),\ J_s = V^2\left(\frac{1}{\Delta} + \frac{1}{U_d - \Delta}\right),\ t_s = V^2\left(\frac{1}{\Delta} - \frac{1}{U_d - \Delta}\right). \tag{6.27}$$

The parameter t_s describes the effective transfer between 2p orbitals induced by p-d hybridization. The transfer occurs not only between $2p_x$ and $2p_y$, but also between $2p_x$ and $2p_x$ sandwiching the copper site. The spectra of the 2p bands without account of J_s is given by

$$E(\boldsymbol{k}) = t_s(\cos k_x + \cos k_y) \pm \sqrt{t_s(\cos k_x - \cos k_y)^2 + 16(t_p - t_s)^2 \cos^2 \frac{1}{2}k_x \cos^2 \frac{1}{2}k_y}. \tag{6.28}$$

It is instructive to compare eq.(6.25) to the Kondo lattice model discussed in Chapter 3. The two models are essentially the same except for the difference in relative magnitudes of parameters, and the filling of the conduction band. The large J_s is favorable to formation of a singlet which is composed of $3d$ and 2p holes sitting at nearest neighbors. This state is often called the Zhang-Rice singlet [38]. The Zhang-Rice singlet in the p-d hybridization model evolves continuously into the Kondo singlet as the ratio J_s/t_s becomes smaller, as long as there are enough 2p holes to screen the $3d$ spin. Accordingly the extension of the singlet wave function grows as the singlet energy scale decreases. Let us consider the case where there is precisely one 2p hole per unit cell of the lattice. In the limit of large J_s, all 2p holes form the Zhang-Rice singlet, and there are no mobile carriers. Then the system should become an insulator. This state corresponds to the Kondo insulator in the opposite limit of small J_s. The important feature common to both insulating states is that the ground state connects continuously to the band insulator. We recall that for description of the hydrogen molecule, both the Heitler-London picture and the molecular orbital picture are useful. The Zhang-Rice singlet is close to the Heitler-London picture.

In contrast to heavy electron metals, however, the 2p holes are absent unless the material is doped. Without 2p holes the effect of J_s does not appear explicitly in physical properties, and the effective model to describe the dynamics of the $3d$ holes reduces to the Heisenberg model. Actually from numerical work [39], the presence of some important corrections to the Heisenberg model are suggested. Namely taking a small cluster Cu_4O_8 with a free boundary condition, one computes low-lying levels by exact numerical diagonalization of the Hamiltonian given by eq.(6.25). Then fitting of these levels by an effective model requires not only the Cu-Cu nearest-neighbor exchange but a large 4-spin interaction. However it is not clear whether this result remains the same as the system size increases.

Let us consider a situation where a single 2p hole is doped in the insulating state. Because of the large coupling J_s, the 2p hole forms a singlet with any of $3d$ hole, and the entity can move due to the non-orthogonality of 2p orbitals. The resultant moving unit can alternatively be viewed as a defect in $3d$ spins. The mathematical expression of the latter view is called the t-J model as discussed in the next section.

6.4 Separation of Spin and Charge in Dynamics

The characteristic energy of spin fluctuations in heavy electron systems is much smaller than of the f-charge excitation which is $|\epsilon_f|$ or U. This is seen in the dynamical susceptibilities of spin and charge as discussed in Chapter 3. In this sense the spin and charge have different dynamical scales. The velocity of the excitations, however, is the same in the low-energy limit. This is because the Fermi liquid ground state has the single Fermi velocity which sets the energy of quasi-particles in the metallic state. Having the same velocity does not depend on strength of the correlation. A similar situation holds in the insulating case called the Kondo insulator (except in one-dimension to be discussed below). Namely, the energy gap is common for both spin and charge excitations, as in usual semiconductors. The appearance of strong correlation is in the spectral intensity which is much smaller for the charge excitation near the

threshold. If a bound state is present such as excitons, the spin excitation has a lower threshold than the charge excitation because of the exchange interaction between the excited pair. This difference of the threshold, however, is also seen in semiconductors.

In one dimension, on the other hand, the spin and charge excitations can really have different velocities. This is in strong contrast with the Fermi liquid state, and is called spin-charge separation. We take the t-J model as the simplest model to display the characteristics in one dimension. The model under finite magnetic field h is given by

$$\mathcal{H} = \mathcal{P}\sum_{i\neq j}[-t_{ij}\sum_{\sigma} c^{\dagger}_{i\sigma}c_{j\sigma} + \frac{1}{2}J_{ij}(\boldsymbol{S}_i\cdot\boldsymbol{S}_j - \frac{1}{4}n_in_j)]\mathcal{P} - 2h\sum_i S_{iz}, \tag{6.29}$$

where $\mathcal{P}$ is the projection operator to exclude double occupation of each site. The t-J model can be derived from the Hubbard model as an effective model in the limit of large U. It can also be obtained from the p-d hybridization model in the limit of large binding energy of the Zhang-Rice singlet. Here we regard instead the transfer $-t_{ij}$ and the exchange J_{ij} between the sites i, j as free parameters in the model. In some special cases the model can be solved exactly. The first case is that the parameters satisfy $t_{ij} = J_{ij}/2 = J/2$ for nearest neighbors and zero otherwise. In this case the model can be solved analytically by use of the Bethe ansatz [40, 41]. Another solvable case is when the parameters take a long-range form

$$J_{ij} = 2t_{ij} = JD(x_i - x_j)^{-2},\ D(x_i - x_j) = (N/\pi)\sin[\pi(x_i - x_j)/N]. \tag{6.30}$$

The quantity $D(x_i - x_j)$ corresponds to the chord distance between the two sites in the ring-shaped system. In the second case it has been shown [42] that the ground state can be obtained explicitly. Let us take the completely up-polarized state as the reference state, and x_α denotes the site occupied by a down spin, and y_ℓ does a vacant (hole) site. Then the eigenfunction of the ground state at $h = 0$ takes the following form:

$$\Psi_{\rm G}(\{x\},\{y\}) = \exp[-i\pi(\sum_{\alpha=1}^{M} x_\alpha + \sum_{\ell=1}^{Q} y_\ell)]\prod_{\alpha>\beta} D(x_\alpha - x_\beta)^2 \prod_{\ell>m} D(y_\ell - y_m)\prod_{\alpha,\ell} D(x_\alpha - y_\ell). \tag{6.31}$$

This wave function has the same form as the Gutzwiller wave function if the reference state is taken to be the vacant state instead of the fully polarized one.

One can also derive low-lying excited states starting from this wave function. The procedure of derivation is rather involved, and we give here only the results [43]. The spin susceptibility χ_s at zero temperature is given by

$$\chi_s = \frac{\partial(n_\uparrow - n_\downarrow)}{\partial h} = \frac{4}{\pi^2 J(1-|m|)} \equiv \frac{2}{\pi v_s}, \tag{6.32}$$

which depends only on magnetization $m = \langle n_{i\uparrow} - n_{i\downarrow}\rangle$ per site and is independent of the filling $n = \langle n_{i\uparrow} + n_{i\downarrow}\rangle$. This is a manifestation of the spin-charge separation. The spin velocity v_s is defined by analogy with the Fermi velocity which would have entered in the absence of interaction. Similarly we introduce the charge velocity v_c by the charge susceptibility χ_c at $T = 0$ which is given by

$$\chi_c = \frac{\partial(n_\uparrow + n_\downarrow)}{\partial \mu} = \frac{4}{\pi^2 J(1-n)} \equiv \frac{2}{\pi v_c}. \tag{6.33}$$

This is now independent of the magnetization m. It is remarkable that spin and charge susceptibilities have exactly the same form as functions of m and n, respectively.

The specific heat is linear in temperature as in the case of the Fermi liquid. The coefficient γ is given by

$$\gamma = \chi_s + \chi_c, \tag{6.34}$$

which shows that both spin and charge excitations contribute to the linear specific heat. It is clear that the charge velocity vanishes in the high-density limit. As a result the specific heat diverges due to the soft charge excitation. On the other hand, the spin velocity remains finite for all densities without magnetization, but diverges in the limit $m \to 1$. Figure 6.12 shows χ_s at finite temperatures and with $m = 0$ [44]. It is seen that χ_s increases linearly from zero temperature, which is to be contrasted

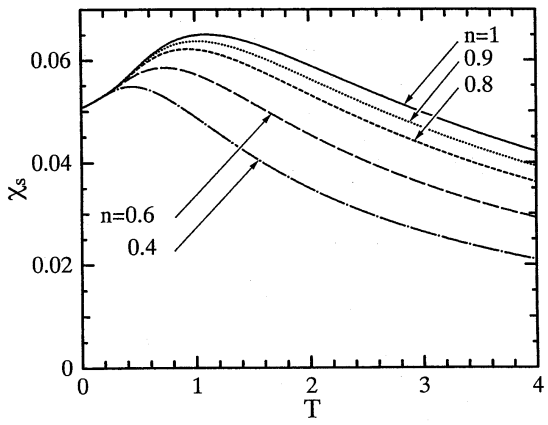

Figure 6.12: The spin susceptibility of the supersymmetric t-J model with the long-range interaction.

with the T^2 dependence in the Fermi liquid. The slope is independent of the filling and is given by $\partial\chi_s/\partial T = 16/(\pi J)^2$. However, in the presence of magnetization χ_s has the T^2 dependence as given by

$$\chi_s = \frac{4}{\pi^2(1-m)J}\left[1 + \frac{8T^2}{3\pi^2(1-m)^4J^2}\right] + O(T^3). \tag{6.35}$$

Remarkably, the charge susceptibility has again the same form as given by eq.(6.35) with m replaced by n. This nice symmetry is specific to the present supersymmetric model. In other one-dimensional fermion systems, the spin-charge separation appears as the different spin and charge velocities only. The spin susceptibility of the Heisenberg chain is given by the same formula as eq.(6.32) with $m = 0$ at $T = 0$, but the temperature dependence involves $\ln T$ [45]. This complication can be understood by perturbation theory from the high-density (spin-chain) limit of the present t-J model which is called the Haldane-Shastry model [46, 47].

Numerical studies in one dimension have also been made for the Anderson lattice model or the Kondo lattice model. This includes the Monte Carlo calculation and the numerical diagonalization of the Hamiltonian. At present it is still not possible for these numerical studies to deal with the Kondo energy T_K if it is much smaller than the bare parameters in the model. Only the numerical renormalization group for the single impurity has achieved the treatment of the minute scale. Recently, a new numerical method called the density matrix renormalization group has been introduced [48] and is becoming an area of very active investigation.

6.5 Epilogue — to Be or Not to Be a Fermi Liquid

The strong correlation among electrons appears in two qualitatively different ways: perturbative and non-perturbative. This distinction persists even though we restrict the discussion to the paramagnetic state. In the case of the Fermi liquid, the ground and low-lying excited states are adiabatically connected to corresponding states in the noninteracting Fermi gas. On the other hand, the electronic states in one dimension are not accessible by perturbation theory with respect to the interaction among electrons. In this sense the distinction between the Fermi liquid and the non-Fermi liquid is clear at zero temperature. However at finite temperature the distinction is not always possible; even in the Fermi liquid the sharp discontinuity of the momentum distribution at the Fermi surface is absent. This ambiguity causes a lot of dispute about the nature of electronic states in high temperature superconductors in the normal state.

The terminology of "spin-charge separation" is popular in the area of high-T_c superconductivity. As we have discussed, the phenomenon is well established in one-dimensional electron systems. Since there are no ideal one-dimensional system in the real world, the problem is how important is the three-dimensional perturbation. In two dimensions, on the other hand, there is still no established answer about the relevance of the non-Fermi liquid state. The importance of forward scattering is emphasized which

might break the Fermi liquid nature of excitations [49]. If one uses the renormalization group to decide the relevance or irrelevance of the Coulomb interaction, the critical dimension turns out to be one [50]. Hence the two-dimensional system belongs to the universality class of higher dimensions. However, if the fixed-point behavior is limited only to very narrow region, this behavior is less relevant experimentally. Instead, some different behavior in the crossover region may dominate the most interesting parameter regions. For example, in the quasi-one-dimensional system where the interchain coupling is very weak, the one-dimensional behavior will dominate although the system is driven eventually to the three-dimensional fixed point.

As explained in the present chapter, superconducting oxides probed by the NMR [13, 22] and neutron-scattering [23] show an apparent gap for spin excitations. The charge excitation as observed by optical absorption is gapless. In connection with the problem of Fermi liquid or not, it is very important whether the spin and charge excitations have really different thresholds of excitations, or they have simply different scales for dynamics. In a spectroscopic experiment it is obviously impossible to distinguish between zero spectral intensity and small but finite one. In fact, even in three-dimensional systems the optical experiment sometimes claims an energy gap apparently larger than the one measured by a magnetic probe such as neutron scattering and NMR. We have seen in many places in this book that the strong correlation brings about very different spectral weights between the spin and charge excitations even in the Fermi liquid state. Thus in order to decide Fermi liquid or not, one must examine more detailed dependence of the spectrum upon temperature and frequency. It seems that the experimental results so far are not sufficient by themselves to resolve the issue.

In heavy electron systems, the non-Fermi liquid ground state has other occasions to appear without the spin-charge separation. The first case is realized near the critical boundary between the paramagnetic ground state and a magnetic one. An example is an alloy system $CeCu_{6-x}Au_x$ [51]. With increasing x, there appears a region where the magnetic susceptibility and the specific heat shows logarithmic dependence on temperature. In this case the characteristic energies on both sides of the phase boundary are reduced near the critical region. As a result even a "low temperature" in the usual experimental sense can already be above the characteristic energy.

The second instance for the non-Fermi liquid is closely related to the electronic structure of U ions. For example the quadrupolar Kondo effect discussed in Chapter 2 is a candidate to realize the non-Fermi liquid in impurity systems. In the dilute alloy $U_{1-x}Th_xRu_2Si_2$ the non-Fermi liquid seems to be realized as a consequence of an isolated U impurity [52]. Another example where the interplay between the strong correlation and the disorder effect is also important is $U_{1-x}Y_xPd_3$ [53, 54]. In the latter case the local Fermi liquid is resumed in the dilute limit of U ions [55]. Deviation from the Fermi-liquid behavior is also seen near the quantum critical point where the ground state of the system changes from paramagnetic to antiferromagnetic or to spin-glass [56]. Distinction between these cases should be made possible by varying external parameters and seeing the dependence of physical quantities on these parameters.

Although the present book focused mostly on heavy electrons in rare-earth and actinide compounds, comparative study together with $3d$ electron systems should be rewarding [57]. The recent interest common in f- and d-electron systems is the coupling between spin and orbital degrees of freedom. This appears in f-electron systems as the quadrupole ordering in CeB_6 as discussed in Chapter 4 and TmTe [58]. Essentially the same ordering is called orbital order in $3d$ electron systems such as $La_{1-x}Sr_xMnO_3$. In the latter system, a hole is doped by addition of Sr [59] and the magnetic anisotropy changes drastically [60].

Another interesting phenomenon to be clarified in the near future is the occurrence of heavy electrons in systems with very small number of carriers. Typical examples such as CeP and Yb_4As_3 are discussed in Chapter 4. The antiferromagnetic correlation between localized pair of electrons tend to form a singlet. If there are many fluctuating singlets around each spin, the correlation looks similar to the Kondo screening. Namely instead of mobile conduction electrons, surrounding spins may also provide singlet cloud by slow fluctuation of spins. If the spin fluctuations are gapless, they lead to large T-linear specific heat. In the Fermi liquid, the slow spin fluctuation appears as an enhanced effective mass. Even though the number of carriers is small the slow spin fluctuation can appear as a large specific heat. Because of these new developments, the field of strongly correlated electrons including heavy electrons will still remain one of the most challenging fields in condensed-matter physics for both theory and experiment.

Bibliography

[1] J.G. Bednorz and K.A. Müller, Z. Phys. **B 64**, 189 (1986).

[2] For review, see for example, Proc. Int. Conf. Material and Mechanism of Superconductivity High-Temperature Superconductivity V, Physica **C 282-287** (1997).

[3] B. Keimer, N. Belk, R. J. Birgeneau, A. Cassanho, C.Y. Chen, M. Greven, M.A. Kastner, A. Aharony, Y. Endoh, R.W. Erwin, and G. Shirane, Phys. Rev. B **46**, 14034 (1992).

[4] Y. Kubo, Y. Shimakawa, T. Manako and H. Igarashi, Phys. Rev. **B43**, 7875 (1991).

[5] Y. Kitaoka, et al, Physica **C153-155**, 83 (1988).

[6] T. Imai, T. Shimizu, H. Yasuoka, Y. Ueda and K. Kosuge, J. Phys. Soc. Jpn. **57**, 2280 (1988).

[7] K. Ishida et al, Physica **C179**, 29 (1991).

[8] K. Ishida et al, J. Phys. Soc. Jpn. **63**, 2803 (1993).

[9] K. Ishida, Y. Kitaoka, K. Asayama, K. Kadowaki and T. Mochiku, J. Phys. Soc. Jpn. **63**, 1104 (1994).

[10] Y. Kitaoka, K. Ishida and K. Asayama, J. Phys. Soc. Jpn. **63**, 2052 (1994).

[11] F. Mila and T.M. Rice, Phys. Rev. **B40**, 11382 (1989).

[12] Y. Kitaoka et al, J. Phys. Chem. Solid. **56**, 1931 (1995).

[13] M. Takigawa, Electronic Properties and Mechanism of High-T_c Superconductors, edited by T. Oguchi et al (North-Holland, 1992) 123.

[14] Y. Kitaoka, S. Ohsugi, K. Ishida and K. Asayama, Physica **C170**, 189 (1990).

[15] S. Ohsugi, Y. Kitaoka, K. Ishida and K. Asayama, J. Phys. Soc. Jpn. **60**, 2351 (1991).

[16] C.H. Pennington and C.P. Slichter, Phys. Rev. Lett. 66, 381 (1991).

[17] M. Takigawa, Phys. Rev. **B 49**, 4158 (1994).

[18] D. Thelen and D. Pines, Phys. Rev. **B49**, 3528 (1994).

[19] R.L. Corey, N.J. Curro, K. O'Hara, T. Imai and C.P. Slichter, Phys. Rev. **53**, 5907 (1996).

[20] A.V. Chubukov, S. Sachdev, and J. Ye, Phys. Rev. **B49**, 11919 (1994).

[21] V. Barzykin and D. Pines, Phys. Rev. **B52**, 13585 (1995).

[22] H. Yasuoka, T. Imai and T. Shimizu, Springer Series in Solid State Science 89, Strong Correlation and Superconductivity, eds. by H. Fukuyama et al, (Springer-Verlag, New York, 1989) p.254.

[23] J. Rossat-Mignod at al, Physica **B169**, 58 (1991).

[24] A.G. Loeser et al, Science **273**, 325 (1996); H. Ding et al, Nature (London) **382**, 511 (1996).

[25] V. Emery and S. Kivelson, Nature (London) **374**, 434 (1995).

[26] P.W. Anderson, Science **235**, 1196 (1987).

[27] H. Fukuyama, Prog. Theor. Phys. Suppl. **108**, 287 (1992).

[28] T. Imai, C.P. Slichter, A.P. Paulikas, and B. Veal, Phys. Rev. **B 47**, 9158 (1993).

[29] K. Magishi et al, J. Phys. Soc. Jpn. **64**, 4561 (1995).

[30] K. Magishi et al, Phys. Rev. **B54**, 10131 (1996).

[31] A. Millis, H. Monien and D. Pines, Phys. Rev. **B42**, 167 (1990).

[32] T. Moriya, Y. Takahashi and K. Ueda, J. Phys. Soc. Jpn. **59**, 2905 (1990).

[33] Y. Kitaoka, K. Ishida, G.-q. Zheng, S. Ohsugi and K. Asayama, J. Phys. Chem. Solid. **54**, 1358 (1993).

[34] Y. Kitaoka, K. Fujiwara, K. Ishida, K. Asayama, Y. Shimakawa, T. Manako and Y. Kubo, Physica **C179**, 107 (1991).

[35] K. Ueda, T. Moriya, Y. Takahashi, J. Phys. Chem. Solids, **53**, 1515 (1992).

[36] P. Monthoux and D. Pines, Phys. Rev. **B50**, 16015 (1994).

[37] M.S. Hybertsen, M. Schlüter and N.E. Chrestensen, Phys. Rev. **B39**, 9028 (1989).

[38] F.C. Zhang and T.M. Rice, Phys. Rev. **B37**, 3759 (1988).

[39] H.-J. Schmidt and Y. Kuramoto, Physica **C167**, 263 (1990).

[40] B. Sutherland, Phys. Rev. **B12**, 3795 (1975).

[41] P.-A. Bares, G. Blatter and M. Ogata, Phys. Rev. **B44**, 130 (1991).

[42] Y. Kuramoto and H. Yokoyama, Phys. Rev. Lett. **67**, 1338 (1991).

[43] Y. Kuramoto and Y. Kato, J. Phys. Soc. Jpn. **64**, 4518 (1995).

[44] Y. Kato and Y. Kuramoto J. Phys. Soc. Jpn. **65**, 1622 (1996).

[45] S. Eggert, I. Affleck and M. Takahashi, Phys. Rev. Lett. **73**, 332 (1994).

[46] F.D.M. Haldane, Phys. Rev. Lett. **90**, 635 (1988)

[47] S. Shastry, Phys. Rev. Lett. **90**, 639 (1988)

[48] S.R. White, Phys. Rev. B**48**, 10345 (1993).

[49] P.W. Anderson Phys. Rev. Lett. **64**, 1839 (1990).

[50] W. Metzner, Physica **B197**, 457 (1994).

[51] H.v. Lohneysen, J. Phys. Condens. Matter **8**, 9689 (1996).

[52] H. Amitsuka and T. Sakakibara, J. Phys. Soc. Jpn. **63**, 736 (1994).

[53] C.L. Seaman et al, Phys. Rev. Lett. **67**, 2882 (1991).

[54] B. Andraka and A.M. Tsvelick, Phys. Rev. Lett. **67**, 2886 (1991).

[55] Y. Aoki et al, Physica **B206& 207**, 451 (1995).

[56] P. Gegenwart et al, Phys. Rev. Lett. **81**, 1501 (1998).

[57] M. Imada, A. Fujimori and Y. Tokura: Rev. Mod. Phys. **70**, 1039 (1998).

[58] T. Matsumura, S. Nakamura, T. Goto, H. Shida and T. Suzuki , Physica **B223&224**, 385 (1996).

[59] Y. Tokura, A. Urushibara, Y. Moritomo, T. Arima, A. Asamitsu and G. Kido, J. Phys. Soc. Jpn. **63**, 3931 (1994).

[60] K. Hirota, N. Kaneko, A. Nishizawa and Y. Endoh, J. Phys. Soc. Jpn. **65**, 3736 (1996).

Appendix A

Linear Response Theory

The linear response theory is based upon two basic assumptions [1]:
(a) the system is in thermal equilibrium before the external perturbation $H_{ex}(t)$ such as magnetic field is switched on;
(b) the system develops adiabatically in the course of infinitesimally slow increase of $H_{ex}(t)$;
On these assumptions let us first consider the expectation value of an operator A for the ground state $|\Psi_g\rangle$. In the Schrödinger picture the time dependence of the expectation value comes from that of the state vector $|\Psi_g(t)\rangle$. The latter is given by

$$i\frac{\partial}{\partial t}|\Psi_g(t)\rangle = [H + H_{ex}(t)]|\Psi_g(t)\rangle. \tag{A.1}$$

In order to deal with the external field perturbationally we introduce a unitary operator $U(t)$ such that

$$|\Psi_g(t)\rangle = \exp(-iHt)U(t)|\Psi_g(-\infty)\rangle, \tag{A.2}$$

where $|\Psi_g(-\infty)\rangle$ is the ground state without H_{ex}. Substituting this into the Schrödinger equation we obtain

$$i\frac{\partial}{\partial t}U(t) = \exp(iHt)H_{ex}(t)\exp(-iHt)U(t) \equiv H^H_{ex}(t)U(t), \tag{A.3}$$

where the Heisenberg representation $H^H_{ex}(t)$ has been introduced. In solving eq.(A.3) we use the assumption (a) as the boundary condition $U(-\infty) = 1$. Iterative solution starts with replacing $U(t)$ on the right hand side by 1 and integrating with respect to t, giving

$$U(t) = 1 - i\int_{-\infty}^{t} dt' H^H_{ex}(t') + O(H^2_{ex}). \tag{A.4}$$

Then we get

$$\langle\Psi_g(t)|A|\Psi_g(t)\rangle = \langle\Psi_g(-\infty)|U(t)^\dagger A^H(t)U(t)|\Psi_g(-\infty)\rangle \tag{A.5}$$

$$= \langle\Psi_g(-\infty)|A^H(t)|\Psi_g(-\infty)\rangle - i\int_{-\infty}^{t} dt'\langle\Psi_g(-\infty)|[A^H(t), H^H_{ex}(t')]|\Psi_g(-\infty)\rangle + O(H^2_{ex}). \tag{A.6}$$

At finite temperature $T = \beta^{-1}$ the system is in the thermal equilibrium at $t = -\infty$ characterized by the density operator $\exp(-\beta H)/Z$. By the assumption (b) the distribution function at any later time is given by the same density operator. Then the quantity $\delta\langle A^H(t)\rangle$ which describes deviation of $\langle A^H(t)\rangle$ from equilibrium is given by

$$\delta\langle A^H(t)\rangle = -i\int_{-\infty}^{t} dt'\langle[A^H(t), H^H_{ex}(t')]\rangle, \tag{A.7}$$

within linear order in H_{ex}. Equation (A.7) is called the Kubo formula of the linear response theory.

Let us write $H^H_{ex}(t')$ in terms of an external field $\phi\exp(-i\omega t')$ coupled with an operator $B(t')$ as $H^H_{ex}(t') = -B(t')\phi\exp(-i\omega t')$. Then eq.(A.7) gives

$$\delta\langle A^H(t)\rangle = \chi_{AB}(\omega)\exp(-i\omega t)\phi, \tag{A.8}$$

where the dynamical susceptibility $\chi_{AB}(\omega)$ is given by

$$\chi_{AB}(\omega) = i\int_{-\infty}^{t} dt' \langle [A^H(t), B(t')] \rangle \exp[i\omega(t-t')]. \tag{A.9}$$

In the special case of the magnetic response against the external magnetic field with frequency ω and wave number $\boldsymbol{q}$, we obtain eq.(1.43). The superscript H has been omitted there.

If the external field is static the susceptibility is obtained simply by putting $\omega = 0$. The resultant static response corresponds to the adiabatic susceptibility as is clear by the derivation. If the system is always in contact with the heat bath, on the other hand, the static response should be isothermal. In order to obtain the isothermal susceptibility we write

$$\exp[-\beta(H + H_{ex})] = \exp(-\beta H) U_T(\beta) \tag{A.10}$$

and derive $U_T(\beta)$ up to first order in the static perturbation H_{ex}. This is analogous to eq.(A.3) except the boundary condition $U_T(0) = 1$ and use of the imaginary time $i\lambda$ with $0 < \lambda < \beta$ in the integral. The result for the magnetic susceptibility is given by eq.(1.57) in Chapter I.

Appendix B

Spectral Representation and Fluctuation-Dissipation Theorem

The retarded Green function with two physical observables A and B is defined as follows:

$$\langle [A,B]\rangle(z) \equiv -i\int_0^\infty dt\langle [A(t),B]\rangle e^{izt}, \tag{B.1}$$

where z lies in the upper half plane. As a special case one obtains the dynamical susceptibility as

$$\chi_{\mu\nu}(\boldsymbol{q},\omega) = -\langle [M_\mu(\boldsymbol{q}), M_\nu(-\boldsymbol{q})]\rangle(\omega+i\delta). \tag{B.2}$$

It is clear that $\langle [A,B]\rangle(z)$ is analytic in the upper half plane of z since it is finite and is derivable any number of times. This analyticity comes from the positive integration range and means the causality that the response cannot precede the external perturbation. In terms of many-body eigenstates $|n\rangle$ and $|m\rangle$ with energies E_n and E_m, one can evaluate eq.(B.1) as

$$\langle [A,B]\rangle(z) = \underset{n}{\mathrm{Av}}\sum_m \frac{A_{nm}B_{mn}}{z-\omega_{mn}}[1-\exp(-\beta\omega_{mn})] \tag{B.3}$$

where Av_n is the thermal average over n and $\omega_{mn} \equiv E_m - E_n$. Note that $\langle [A,B]\rangle(z)$ can be extended also to the lower half plane as an analytic function of z by eq.(B.3). This piece is in fact the advanced Green function defined by

$$\langle [A,B]\rangle(z) \equiv i\int_{-\infty}^0 dt\langle [A(t),B]\rangle e^{izt}. \tag{B.4}$$

the integral of which converges for z in the lower half plane. After all we see that singularities of $\langle [A,B]\rangle(z)$ as defined by eq.(B.3) lie only on the real axis.

We introduce the spectral function $I_{AB}(\omega)$ by

$$I_{AB}(\omega) = \underset{n}{\mathrm{Av}}\sum_m A_{nm}B_{mn}[1-\exp(-\beta\omega)]\delta(\omega-\omega_{mn}) = \int_{-\infty}^\infty \frac{dt}{2\pi}e^{i\omega t}\langle [A(t),B]\rangle. \tag{B.5}$$

In terms of $I_{AB}(\omega)$ the retarded Green function is expressed as

$$\langle [A,B]\rangle(z) = \int_{-\infty}^\infty d\omega \frac{I_{AB}(\omega)}{z-\omega}, \tag{B.6}$$

which is called the spectral representation or the Lehmann representation.

One then introduces the relaxation function (or the canonical correlation function) by

$$\langle A(t);B\rangle \equiv \frac{1}{\beta}\int_0^\beta d\lambda\langle A(t-i\lambda)B\rangle, \tag{B.7}$$

and its Laplace transform

$$\langle A;B\rangle(z) \equiv \int_0^\infty dt\langle A(t);B\rangle e^{izt}. \tag{B.8}$$

This quantity gives the time development $\langle A(t)\rangle_{ex}$ when a constant external field coupled with B is suddenly switched off at $t = 0$. Hence the name of relaxation function. Note that $\langle A(t = 0); B\rangle$ is the static susceptibility, and that the statistical operator $\exp[-\beta(H + H_{ex})]/Z$ as appeared in eq.(A.10) remains the same for $\langle A(t > 0)\rangle_{ex}$. In terms of the spectral function, the relaxation function is given by

$$\langle A(t); B\rangle = \int_{-\infty}^{\infty} d\omega \frac{I_{AB}(\omega)}{\beta\omega} e^{-i\omega t}. \tag{B.9}$$

as can be checked by taking matrix elements with respect to eigenstates. Hence we obtain a relation to the Green function:

$$\langle A; B\rangle(z) = (iz\beta)^{-1}\{\langle [A, B]\rangle(z) - \langle [A, B]\rangle(0)\}. \tag{B.10}$$

Let $\dot{B}$ denote the time derivative of the operator B. The spectral function $I_{A\dot{B}}(\omega)$ is related to $I_{AB}(\omega)$ by $I_{A\dot{B}}(\omega) = i\omega I_{AB}(\omega)$ which is easily checked with use of eq.(B.5). Then the following identities can be proved.

$$\beta\langle A; \dot{B}\rangle(z) = -\langle [A, B]\rangle(z), \tag{B.11}$$

$$\beta\langle A(t); \dot{B}\rangle = i\langle [A(t), B]\rangle. \tag{B.12}$$

Finally one introduces the symmetrized correlation function by

$$\langle \{A(t), B\}\rangle \equiv \langle A(t)B + BA(t)\rangle. \tag{B.13}$$

By taking matrix elements as in eq.(B.1) we obtain

$$\langle \{A(t), B\}\rangle = \int_{-\infty}^{\infty} d\omega \coth\left(\frac{\beta\omega}{2}\right) I_{AB}(\omega) \exp(-i\omega t), \tag{B.14}$$

where eq.(B.5) has been used. Of most physical interest is the case $B = A^\dagger$. The spectral function is then a real positive quantity for positive ω and satisfies

$$I_{AA^\dagger}(\omega) = -I_{AA^\dagger}(-\omega) = -\frac{1}{\pi}\mathrm{Im}\langle [A, A^\dagger]\rangle(\omega + i\delta). \tag{B.15}$$

In the case of $t = 0$ and $B = A^\dagger$, the left-hand side of eq.(B.14) describes the fluctuation of the quantity A, while $I_{AA^\dagger}$ in the right-hand side describes the dissipation of energy by the linear response. Hence eq.(B.14) is called the fluctuation-dissipation theorem.

Appendix C

Rayleigh-Schrödinger Perturbation Theory and Higher-Order Renormalization

C.1 Expansion of the Effective Hamiltonian

As discussed in Chapter 1, the effective Hamiltonian H_{eff} in the Brillouin-Wigner perturbation theory depends on the eigenenergy to be derived. This dependence becomes inconvenient if one wants to do direct perturbation theory in higher order. The alternative scheme, called the Rayleigh-Schrödinger (RS) perturbation theory, is designed to give Ω and hence H_{eff} in a form which involves only eigenenergies of H_0. Thus the RS perturbation theory is free from the unknown energy E_i. In order to derive H_{eff} in the RS perturbation theory we write the Schrödinger equation in the form

$$(E - H_0)\psi = E\psi - H_0\Omega P\psi = V\Omega P\psi, \tag{C.1}$$

where the index i to specify an eigenstate is omitted, and we used the property $\Omega P\psi = \psi$ for an eigenstate of $H_0 + V$. Applying the projection operator P on both sides of eq.(C.1), and further applying Ω, we obtain the alternative form:

$$\Omega(E - H_0)P\psi = E\psi - \Omega H_0 P\psi = \Omega PV\Omega P\psi, \tag{C.2}$$

where we used the property $PH_0 = H_0P$. Subtracting eq.(C.2) from eq.(C.1), we obtain

$$[\Omega, H_0]P\psi = (1 - \Omega P)V\Omega P\psi. \tag{C.3}$$

We make the power series expansion:

$$\Omega = \Omega_0 + \Omega_1 + \Omega_2 + \ldots, \tag{C.4}$$

where Ω_n denotes the $O(V^n)$ contribution with $\Omega_0 = 1$. Comparing terms with the same order of magnitudes on both sides of eq.(C.3), we obtain

$$[\Omega_n, H_0] = QV\Omega_{n-1} - \sum_{j=1}^{n-1} \Omega_j PV\Omega_{n-j-1} \tag{C.5}$$

Then the effective Hamiltonian is also expanded as

$$H_{eff} = P(H_0 + V)P + H_2 + H_3 + \ldots, \tag{C.6}$$

with $H_n = PV\Omega_{n-1}P$ for $n \geq 2$. Matrix elements of some lower-order parts are explicitly given by

$$\langle a|H_2|b\rangle = \langle a|V(\epsilon_b - H_0)^{-1}QV|b\rangle, \tag{C.7}$$

and

$$\langle a|H_3|b\rangle = \langle a|V\frac{1}{\epsilon_b - H_0}QV\frac{1}{\epsilon_b - H_0}QV|b\rangle - \sum_c \langle a|V\frac{1}{\epsilon_b - H_0}\frac{1}{\epsilon_c - H_0}QV|c\rangle\langle c|V|b\rangle. \tag{C.8}$$

where $Q = 1 - P$ and all states represented by $|a\rangle, |b\rangle$ and $|c\rangle$ belong to the model space.

In the Rayleigh-Schrödinger perturbation theory, there are two kinds of terms in H_n with $n \geq 3$; the first one is of the same form as the one in the Brillouin-Wigner perturbation theory (except for the eigenenergy in the denominator), and the second constitutes the correction terms which originate from the second term in eq.(C.5) or in eq.(C.8). The latter terms play an important role to accomplish the linked-cluster expansion. Namely by removing the restriction that the number of local electron is unity at any stage of intermediate states, one can apply a variant of Wick's theorem to prove the cancellation of unlinked parts in the Rayleigh-Schrödinger perturbation theory [2]. The final form of the effective Hamiltonian conserves the number of local electrons in each order of perturbation. Hence in the model space with one and only one local electron which obeys either the Fermi or Bose statistics, one can reproduce the actual situation in the Kondo-like impurity model with the local number constraint.

In order to deal with the energy denominator in the second term of eq.(C.8), the concept of the "folded diagram" is useful. Namely one draws a local electron line propagating from left to right to represent the presence of P in the intermediate state. An example is shown in Fig.C.2. Then the energy denominator is associated with difference of left-going energies and the right-going ones just as in the other diagrams such as Fig.C.1. By comparing the energy denominators given by eq.(C.8), and those given by the rule mentioned above, one can confirm that both give identical results.

C.2 Renormalization of the Kondo Model

In Chapter 2 we described the lowest-order renormalization of the Kondo model where the fixed point of the model corresponds to infinity of the exchange coupling. Because of the infinite coupling constant, all higher-order terms become large and there is no analytical way to control the renormalization. However, in the multi-channel Kondo model given by eq.(2.102) with a large number n of the orbitals, the third-order renormalization describes the non-trivial fixed point correctly [3]. The reason for this is explained below.

In order to perform renormalization explicitly we first introduce the approximation to set $\epsilon_b = 0$ in eq.(C.8). This approximation is equivalent to neglect the energy dependence of the effective interaction. Then in the third-order we deal with effective Hamiltonian given by

$$H_3^L = V(H_0^{-1}QV)^2 + \sum_c VH_0^{-1}(\epsilon_c - H_0)^{-1}QVPV. \tag{C.9}$$

Let us assume the constant density of states for n conduction bands each of which per spin is given by

$$\rho_c(\epsilon) = (2D)^{-1}$$

for $|\epsilon| < D$ and zero otherwise. The model space consists of the local spin and such conduction electrons whose energy ϵ is within the range $[-D + |dD|, D - |dD|]$ where $dD(< 0)$ is the infinitesimal change of the cut-off energy. In order to minimize the number of electrons to deal with, the Fermi sea is chosen as the vacuum for conduction electrons, and excitations are described as particles and holes generated from the vacuum.

In the third-order effective Hamiltonian, we have to consider only two diagrams shown in Figs.C.1 and C.2. It can be shown by the use of eq.(C.9) that other diagrams without loop of conduction electrons describe shift of the ground-state energy, and do not contribute to renormalization [4]. In Fig.C.1, the energy denominators are obtained by associating the excitation energy D with one of two lines in the electron loop. The result of energy integration is given by

$$\int_{-D}^{0} d\epsilon' \frac{1}{(-D + \epsilon')^2} + \int_0^D d\epsilon \frac{1}{(-D - \epsilon)^2} = \frac{1}{D}. \tag{C.10}$$

On the other hand the product of the spin operators take the form $S^\alpha S^\beta S^\gamma \mathrm{Tr}(s^\alpha s^\gamma) s^\beta$, where the trace is over the spin states of conduction-electrons. The folded diagram has the same energy denominators

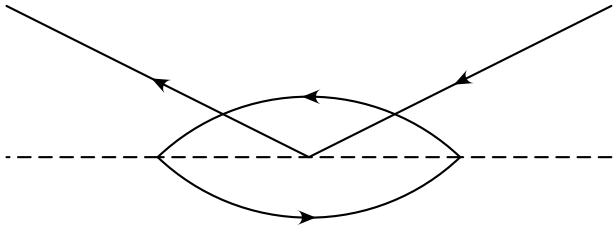

Figure C.1: An exchange scattering diagram in the third order. The solid line shows a conduction-electron state, while the dashed line the local electron state making up the impurity spin. The projection operator Q requires one of two conduction-electron states making a loop to have energies near the band edges.

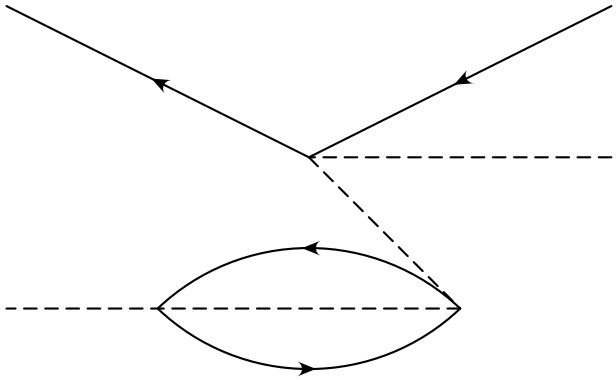

Figure C.2: The third-order folded diagram. The assignment of energy denominators are explained in the text.

as given by eq.(C.10), and its spin part is given by $S^\alpha S^\gamma S^\beta \mathrm{Tr}(s^\alpha s^\gamma) s^\beta$. Then contributions from the two diagrams combine to give

$$S^\alpha [S^\beta, S^\gamma] \mathrm{Tr}(s^\alpha s^\gamma) s^\beta = -\frac{1}{2} \boldsymbol{S} \cdot \boldsymbol{s}. \tag{C.11}$$

where we use the identity $[S^\alpha, S^\beta] = i\epsilon_{\alpha\beta\gamma} S^\gamma$.

Adding the second-order contribution derived in Chapter 2, we obtain the scaling equation:

$$\frac{dg}{dl} = -g^2 + \frac{1}{2} g^3. \tag{C.12}$$

where $l = \ln D$ and the dimensionless coupling constant $g = J\rho_c$ has been introduced. Note that the present scheme of renormalization extends the the poor man's scaling [5] with a different idea. In the poor man's scaling one considers the t-matrix of the exchange scattering which involves infinite number of perturbation terms. To the contrary, the effective interaction in the present scheme does not have intermediate states belonging to the model space. In the case of n-fold degenerate conduction band, each loop of conduction electron lines acquires the factor n by summing over degenerate orbitals. This loop appears from the third-order diagrams as shown in Figs.C.1 and C.2. We then obtain instead of eq.(C.12)

$$\frac{dg}{dl} = -g^2 + \frac{n}{2} g^3, \tag{C.13}$$

The fixed point of the renormalization group is given by $g = g_c = 2/n$ which is small in the case of large n. Thus the fixed point is within the reach of the perturbative renormalization. If one considers still higher order diagrams, one would have the expansion [6, 7]:

$$\frac{dg}{dl} = -g^2 + \frac{n}{2} g^3 + (an + b) g^4 + (cn^2 + dn + e) g^5 + ... \tag{C.14}$$

where a to e are numerical constants independent of n. Since the total contribution from the third and higher-order terms in the right-hand side is of $O(1/n^3)$ with $g = O(1/n)$, the first two terms of $O(1/n^2)$ are sufficient in deriving the fixed point in the leading order of $1/n$.

Appendix D

Spectral Shape and Relaxation Rate

We introduce an inner product $\langle A|B\rangle$ between the two operators A and B by

$$\langle A|B\rangle = \int_0^\beta d\tau \langle \exp(\tau H) A \exp(-\tau H) B\rangle \equiv \beta \langle A; B\rangle, \tag{D.1}$$

where the canonical correlation function $\langle A; B\rangle$ has been defined by eq.(B.7). The inner product corresponds to the static susceptibility χ_{AB}. By introducing the Liouville operator $\mathcal{L}$ as $\mathcal{L}A \equiv [H, A]$, simple calculation shows that

$$\langle A|\mathcal{L}|B\rangle \equiv \langle A|\mathcal{L}B\rangle = \langle \mathcal{L}A|B\rangle. \tag{D.2}$$

Hence $\mathcal{L}$ is hermite with respect to this inner product. The dynamical susceptibility which is defined by eq.(A.9) is written as

$$\chi_{AB}(z) = \langle A|\frac{\mathcal{L}}{\mathcal{L}-z}|B\rangle. \tag{D.3}$$

The relaxation function defined by eq.(B.8) is represented by

$$\langle A; B\rangle(z) = \langle A|\frac{i}{z-\mathcal{L}}|B\rangle \equiv C_{AB}(z). \tag{D.4}$$

We now consider the dynamical magnetic susceptibility $\chi_M(z)$ by setting $A = B = M$ in eq.(D.3) with M being the z-component of magnetic moment. The projection operator $\mathcal{P}$ is defined by

$$\mathcal{P} \equiv |M\rangle \chi_M^{-1} \langle M|, \tag{D.5}$$

where χ_M is the static susceptibility given by $\chi_M = \langle M|M\rangle$. It is obvious that $\mathcal{P}^2 = \mathcal{P} = \mathcal{P}^\dagger$ which is a necessary condition for a projection operator. We also introduce a projection operator $\mathcal{Q}$ complementary to $\mathcal{P}$ by $\mathcal{Q} = 1 - \mathcal{P}$. In order to obtain the relaxation function $C_M(z)$ we have to invert the operator $z - \mathcal{L}$. We note the following identity for the 2×2 matrix:

$$\left[\begin{pmatrix} a & b^* \\ b & c \end{pmatrix}^{-1}\right]_{11} = \frac{1}{a - b^* c^{-1} b}, \tag{D.6}$$

which can be generalized to the case where the entries c and b are a matrix and a column vector, respectively. Namely we identify

$$a = \mathcal{P}(z - \mathcal{L})\mathcal{P},\ b = -\mathcal{Q}\mathcal{L}\mathcal{P},\ c = \mathcal{Q}(z - \mathcal{L})\mathcal{Q}. \tag{D.7}$$

Then we obtain the following result [8]:

$$C_M(z) = i\chi_M[z - \Omega + i\Gamma(z)]^{-1} \tag{D.8}$$

where

$$\Omega = \chi_M^{-1} \langle M|\mathcal{L}|M\rangle, \tag{D.9}$$

describes the systematic motion corresponding to precession. The effect of random force is described by $\Gamma(z)$ which is given by

$$\Gamma(z) = \chi_M^{-1} \langle \mathcal{Q}\dot{M} | \frac{i}{z - \mathcal{Q}\mathcal{L}\mathcal{Q}} | \mathcal{Q}\dot{M} \rangle, \tag{D.10}$$

where $\dot{M} = i\mathcal{L}M$.

This exact expression is very useful to evaluate relaxation rates in the lowest-order perturbation theory. Let us assume that the zeroth-order Hamiltonian H_0 of the total system $H = H_0 + H_1$ conserves M. Then up to $O(H_1^2)$ we can approximate

$$\Gamma(z) = \chi_M^{-1} \langle [H_1, M] | i(z - \mathcal{L}_0)^{-1} | [H_1, M] \rangle + o(H_1^2), \tag{D.11}$$

where $\mathcal{L}_0$ is the Liouville operator corresponding to H_0. This result can be derived by noting $\langle M | \dot{M} \rangle = \langle [M, M] \rangle = 0$ and $\mathcal{Q}\dot{M} = \dot{M}$. As a physical relaxation function we put $z = \omega + i\delta$. The imaginary part of $\Gamma(\omega)$ describes a shift in the resonance frequency. The real part, on the other hand, corresponds to the magnetic relaxation rate. The lowest-order result for it is given by

$$\Gamma(\omega) = \pi \chi_M^{-1} \langle [H_1, M] | \delta(\omega - \mathcal{L}_0) | [H_1, M] \rangle. \tag{D.12}$$

Usually we have $\mathcal{L}_0 \dot{M} \neq 0$. In this case $\Gamma(z)$ is a smooth function of $z = \omega + i\delta$ around $\omega = 0$ in the upper half plane. As long as ω is much smaller than the characteristic frequency of $\mathcal{L}_0\dot{M}$, we may put $\omega = 0$ and neglect $\mathrm{Im}\Gamma$. In this case the spectral shape takes the Lorentzian form:

$$\frac{1}{\omega} \mathrm{Im}\chi_M(\omega) = \frac{\chi_M \Gamma}{\omega^2 + \Gamma^2}. \tag{D.13}$$

It is straightforward to generalize the above formalism to the case where a set of operators A_i ($i = 1, 2, \ldots$) constitute slow variables. The projection operator to this set is defined by

$$\mathcal{P} \equiv \sum_{ij} |A_i\rangle \chi^{-1} \langle A_j|, \tag{D.14}$$

where χ is the susceptibility matrix an element of which is given by $\chi_{ij} = \langle A_i | A_j \rangle$. Then we obtain the following identity for the relaxation function matrix $C(z)$:

$$C(z) = i\chi[z - \Omega + i\Gamma(z)]^{-1}, \tag{D.15}$$

where elements of the matrix Ω is given by

$$\Omega_{ij} = \sum_l (\chi^{-1})_{il} \langle A_l | \mathcal{L} | A_j \rangle, \tag{D.16}$$

and those of $\Gamma(z)$ by

$$\Gamma_{ij}(z) = \sum_l (\chi^{-1})_{il} \langle \mathcal{Q}\dot{A}_l | \frac{i}{z - \mathcal{Q}\mathcal{L}\mathcal{Q}} | \mathcal{Q}\dot{A}_j \rangle. \tag{D.17}$$

We now turn to a general spectral shape of $\chi_M(z)$ including non-Lorentzian cases. The relaxation function in the real time domain is written as

$$\langle M(t) | M \rangle = \langle M | \exp(-i\mathcal{L}t) | M \rangle \equiv \langle\langle \exp(-i\mathcal{L}t) \rangle\rangle \langle M | M \rangle, \tag{D.18}$$

where we have introduced the average $\langle\langle \cdots \rangle\rangle$. The spectral moments $\langle \omega^n \rangle$ ($n = 0, 1, 2 \ldots$) are given by

$$\langle \omega^n \rangle \equiv \int_{-\infty}^{\infty} \frac{d\omega}{\pi} \omega^{n-1} \mathrm{Im} \frac{\chi_M(\omega)}{\chi_M} = \langle\langle \mathcal{L}^n \rangle\rangle. \tag{D.19}$$

Thus the full set of moments completely determine the spectrum. Corresponding to the average $\langle\langle \cdots \rangle\rangle$ we can define the cumulant average $\langle\langle \cdots \rangle\rangle_c$ [9]. Namely,

$$\langle\langle \exp(-i\mathcal{L}t) \rangle\rangle = \exp[\langle\langle \exp(-i\mathcal{L}t) \rangle\rangle_c - 1] \equiv \exp[-i\langle\omega\rangle t + X(t)]. \tag{D.20}$$

The $X(t)$ is determined by the set of cumulants $\langle\omega^n\rangle_c \equiv \langle\langle\mathcal{L}^n\rangle\rangle_c$ as

$$X(t) = \sum_{n=2}^{\infty} \frac{(-it)^n}{n!} \langle\omega^n\rangle_c. \tag{D.21}$$

Thus the full set of cumulants also determine the spectrum completely. The particularly important quantity is the second order cumulant

$$\langle\omega^2\rangle_c = \langle\langle\mathcal{L}^2\rangle\rangle - \langle\langle\mathcal{L}\rangle\rangle^2. \tag{D.22}$$

The function $X(t)$ starts from zero at $t = 0$ and should decrease with increasing t. We introduce a characteristic time τ_R in $X(t)$ such that $\mathrm{Re}X(\tau_R) \sim -1$. Then the relaxation function becomes negligible for $t \gg \tau_R$. For large enough t, on the other hand, $X(t)$ should behave as

$$X(t) \to -i(\delta\omega - i\Gamma)t, \tag{D.23}$$

with $\delta\omega$ being the shift of the resonance frequency. The long-time behavior is non-analytic in t because of the dissipation in the system. Hence this behavior does not follow from the first order term in eq.(D.21). A characteristic time τ_C is defined as the one after which the short time behavior crosses over to the long time one given by eq.(D.23).

We consider the extreme cases: (i) $\tau_C \gg \tau_R$, and (ii) $\tau_C \ll \tau_R$ assuming for simplicity $\langle\omega\rangle = \delta\omega = 0$. In the case (i) the short time behavior of $X(t)$ determines the spectrum. Then we can rely on the expansion given by eq.(D.21). The resultant spectrum is of the Gaussian shape given by

$$\mathrm{Im}\frac{\chi_M(\omega)}{\omega} = \sqrt{\frac{\pi}{2}}\frac{\chi_M}{D}\exp[-\frac{1}{2}\left(\frac{\omega}{D}\right)^2], \tag{D.24}$$

where

$$D^2 = \chi_M^{-1}\langle\dot{M}|\dot{M}\rangle, \tag{D.25}$$

and we have $D \sim \tau_R^{-1}$. It is possible to apply the perturbation theory to derive D. The lowest-order result is used in estimating T_{2G} in Chapter 1. In the case (ii), on the contrary, the long-time behavior dominates the spectrum. This gives rise to the Lorentzian shape. The relaxation rate in the lowest order perturbation theory is given by eq.(D.12) with $\omega = 0$, which is roughly given by $\Gamma \sim D^2\tau_C \sim \tau_C/\tau_R^2$. The relaxation rate is smaller than the case (i) with the same magnitude of D. According to specific mechanism which controls τ_C, this reduction of the relaxation rate is called motional narrowing or exchange narrowing.

Appendix E

Green Function in the Imaginary Time

We introduce the Matsubara representation by

$$e^{\tau H} A e^{-\tau H} \equiv A^{(M)}(\tau) \tag{E.1}$$

with $-\beta < \tau < \beta$. This corresponds to the Heisenberg representation in the imaginary time τ. Then the Matsubara Green function $D_{AB}[\tau]$ is defined by

$$D_{AB}[\tau] = -\langle T_\tau A^{(M)}(\tau) B\rangle = \begin{cases} -\langle A^{(M)}(\tau) B\rangle, & (\tau > 0) \\ -\langle B A^{(M)}(\tau)\rangle, & (\tau < 0) \end{cases} \tag{E.2}$$

where T_τ is the time-ordering symbol. If A and B are generalized to fermion operators, the Green function becomes $+\langle B A^{(M)}(\tau)\rangle$ for $\tau < 0$ as discussed later.

By taking matrix elements one can show that the Green function is periodic in τ with period β, i.e.

$$D_{AB}[\tau] = -\int_{-\infty}^{\infty} d\omega I_{AB}(\omega) \frac{e^{-(\beta+\tau)\omega}}{1 - e^{\beta\omega}} = D_{AB}[\tau + \beta]. \tag{E.3}$$

with $-\beta < \tau < 0$. Therefore one can make a Fourier transform

$$D_{AB}[\tau] = T \sum_n D_{AB}(i\nu_n) \exp(-i\nu_n \tau) \tag{E.4}$$

where $i\nu_n = 2\pi i n T$ with n integer is called (even) Matsubara frequency. The Fourier component $D_{AB}(i\nu_n)$ is calculated as

$$D_{AB}(i\nu_n) = \int_0^\beta d\tau D_{AB}[\tau] \exp(i\nu_n \tau) = \int_{-\infty}^{\infty} d\omega \frac{I_{AB}(\omega)}{i\nu_n - \omega}. \tag{E.5}$$

Thus we obtain a remarkable relation

$$D_{AB}(i\nu_n) = \langle [A, B]\rangle(i\nu_n). \tag{E.6}$$

Namely the Matsubara Green function with $\nu_n > 0$ is continued analytically to the retarded Green function, and with $\nu_n < 0$ to the advanced Green function [10].

In the case of fermionic operators ψ_A and $\psi_B^\dagger$, we define the Matsubara Green function $G_{AB}[\tau]$ as follows:

$$G_{AB}[\tau] = -\langle T_\tau \psi_A^{(M)}(\tau) \psi_B^\dagger\rangle = \begin{cases} -\langle \psi_A^{(M)}(\tau) \psi_B^\dagger\rangle & (\tau > 0) \\ \langle \psi_B^\dagger \psi_A^{(M)}(\tau)\rangle & (\tau < 0). \end{cases} \tag{E.7}$$

The Green function now has the anti-periodic property with $-\beta < \tau < 0$

$$G_{AB}[\tau] = -\int_{-\infty}^{\infty} d\epsilon \rho_{AB}(\epsilon) \frac{e^{-(\beta+\tau)\omega}}{1 + e^{\beta\omega}} = -G_{AB}[\tau + \beta], \tag{E.8}$$

where the spectral function $\rho_{AB}(\epsilon)$ is defined by

$$\rho_{AB}(\epsilon) = \underset{n}{\mathrm{Av}} \sum_m (\psi_A)_{nm}(\psi_B^\dagger)_{mn}[1+\exp(-\beta\epsilon)]\delta(\epsilon-\epsilon_{mn}). \tag{E.9}$$

The Fourier transform $G_{AB}(i\epsilon_n)$ is now with odd Matsubara frequency $i\epsilon_n = \pi i(2n+1)T$ with n integer and has the spectral representation

$$G_{AB}(i\epsilon_n) = \int_0^\beta G_{AB}[\tau]\exp(i\epsilon_n\tau) = \int_{-\infty}^{\infty} d\epsilon \frac{\rho_{AB}(\epsilon)}{i\epsilon_n - \epsilon}. \tag{E.10}$$

The analytic continuation $G_{AB}(z)$ with z in the upper half-plane corresponds to the retarded Green function, i.e.

$$G_{AB}(z) = -i\int_0^\infty dt e^{izt}\langle\{\psi_A(t),\psi_B^\dagger\}\rangle \tag{E.11}$$

with the anticommutator. If z is in the lower half-plane $G_{AB}(z)$ gives the advanced Green function

$$G_{AB}(z) = +i\int_{-\infty}^0 dt e^{izt}\langle\{\psi_A(t),\psi_B^\dagger\}\rangle. \tag{E.12}$$

The spectral intensity $\rho_{AB}(\epsilon)$ can be given also in terms of the integral

$$\rho_{AB}(\epsilon) = \int_{-\infty}^{\infty} dt e^{i\epsilon t}\langle\{\psi_A(t),\psi_B^\dagger\}\rangle. \tag{E.13}$$

Appendix F

Path Integral Representation of the Partition Function

F.1 Grassmann Numbers and Coherent States

The basic property of the Grassmann numbers is that they anticommute in contrast to the c-number. Let η_1 and η_2 be Grassmann numbers. Then we require

$$\eta_1\eta_2 = -\eta_2\eta_1. \tag{F.1}$$

We also require that the Grassmann numbers commute with any c-number and anticommute with fermion creation and annihilation operators. The complex conjugate has the following property:

$$(\eta_1\eta_2)^* = \eta_2^*\eta_1^* = -\eta_1^*\eta_2^*, \tag{F.2}$$

which may look curious if Grassmann numbers are real, but assures the reality condition $(\eta_1^*\eta_1)^* = \eta_1^*\eta_1$.

The derivative of Grassmann numbers is defined by

$$\frac{\partial}{\partial\eta_i}\eta_j = \delta_{ij}, \tag{F.3}$$

which is analogous to the usual derivative. We note, however, that the differential $d\eta_i$ is also a Grassmann number. Then we introduce the definite integrals $\int d\eta 1$ and $\int d\eta\eta$ which are sufficient for the single variable because higher powers of η vanish. The first integral is the Grassmann number, while the second commutes with all other Grassmann numbers and hence is a c-number. In order to make the two integrals invariant against the linear shift $\eta \to \eta + \xi$ with ξ a constant Grassmann number, we require

$$\int d\eta\eta = 1, \quad \int d\eta 1 = 0. \tag{F.4}$$

The first equality sets the normalization of the integral. The second one, where 0 is a Grassmann number, follows from the invariance

Let us take a fermionic single-particle state $|1\rangle = f^\dagger|0\rangle$ where $f^\dagger$ denotes the creation operator. The coherent state $|\eta\rangle$ associated with a complex Grassmann number η is constructed by

$$|\eta\rangle = \exp(f^\dagger\eta)|0\rangle = (1 + f^\dagger\eta)|0\rangle = |0\rangle - \eta|1\rangle. \tag{F.5}$$

The coherent state is a superposition of zero- and single-particle states. It is the eigenstate of the annihilation operator f. In fact the action of f upon $|\eta\rangle$ gives

$$f|\eta\rangle = \eta|\eta\rangle. \tag{F.6}$$

The hermitian conjugate of this equation is $\langle\eta| = \langle\eta|f^\dagger$. Furthermore the inner product of the coherent states is given by

$$\langle\eta_1|\eta_2\rangle = \exp(\eta_1^*\eta_2) \tag{F.7}$$

Thus we obtain for an operator function $F(f^\dagger, f)$ which is any of f or $f^\dagger$ or $f^\dagger f$

$$\langle \eta_1 | F(f^\dagger, f) | \eta_2 \rangle = F(\eta_1^*, \eta_2) \exp(\eta_1^* \eta_2). \tag{F.8}$$

Of most importance is the relation

$$\int d\eta^* d\eta |\eta\rangle\langle\eta| \exp(-\eta^*\eta) = |0\rangle\langle 0| + |1\rangle\langle 1| = \mathbf{1}, \tag{F.9}$$

which is the identity operator. This relation is used in the next section to set up the path integral representation of the partition function. It is clear that the coherent states span the overcomplete set for $|0\rangle$ and $|1\rangle$.

F.2 Partition Function

For illustrative purpose of using the Grassmann integration technique, we begin with a trivial Hamiltonian $H(f^\dagger, f) = \epsilon f^\dagger f$ for which the (grand) partition function Z is given by $Z = 1 + \exp(-\beta\epsilon)$. Here the chemical potential is chosen as the origin of energy.

We consider the partition function for a Hamiltonian H and represent the trace by the integral over coherent states

$$Z = \int d\eta_1^* d\eta_1 \langle \eta_1 | \mathrm{e}^{-\beta H} | -\eta_1 \rangle \exp(-\eta_1^* \eta_1), \tag{F.10}$$

where we have used eq.(F.9) and $\langle n|\eta\rangle\langle\eta|e^{-\beta H}|n\rangle = \langle\eta|e^{-\beta H}|n\rangle\langle n|-\eta\rangle$ with $n = 0$ or 1. We decompose $\exp(-\beta H) \sim (1 - \delta\tau H/M)^M$, with $\delta\tau = \beta/M$ for a large integer M ($\gg 1$) and insert the identity given by eq.(F.9) $(M-1)$ times between each decomposed factor. This is often called the Suzuki-Trotter decomposition. Then we obtain with use of eq.(F.8)

$$Z = \int \prod_{i=1}^{M} d\eta_i^* d\eta_i R(\eta_1^*, \eta_2) \exp[-\eta_1^*(\eta_1 - \eta_2)] R(\eta_2^*, \eta_3) \times \cdots \exp[-\eta_M^*(\eta_M - \eta_{M+1})] R(\eta_M^*, \eta_{M+1}), \tag{F.11}$$

where $R(\eta_1^*, \eta_2) = 1 - \delta\tau H(\eta_1^*, \eta_2) \sim \exp[-\delta\tau H(\eta_1^*, \eta_2)]$ and $\eta_{M+1} \equiv -\eta_1$. In the limit of large M, one may write η_i as $\eta(\tau)$ for the range $0 < \tau < \beta$ with the boundary condition $\eta(\beta) = -\eta(0)$. Then one can make a Fourier expansion of $\eta(\tau)$ using the odd Matsubara frequency. Provided the highest frequency appearing in the summation is much smaller than $(\delta\tau)^{-1}$, one may replace the difference $\eta(\tau_i) - \eta(\tau_{i+1})$ by $\delta\tau\partial\eta(\tau)/\partial\tau$.

It is also possible to represent the partition function with many degrees of freedom and with interparticle interactions as an integral over Grassmann numbers. Instead of single $\eta(\tau)$, we have to introduce for each single-particle state α the corresponding Grassmann variable η_α. The multiple integrals over Grassmann numbers is called the functional integral or the path integral and is written as $\mathcal{D}\eta^*\mathcal{D}\eta$. The latter name comes from the analogy to the path integral in single-particle quantum mechanics.

As is clear in the derivation, the Hamiltonian must have the normal ordered form where the creation operators stand to the left of annihilation operators. Then one may extend eq.(F.8) to many variables as

$$\langle \{\eta_\alpha\} | F(\{f_\alpha^\dagger\}, \{f_\alpha\}) | \{\eta'_\alpha\} \rangle = F(\{\eta_\alpha^*\}, \{\eta'_\alpha\}) \exp(\sum_\alpha \eta_\alpha^* \eta'_\alpha). \tag{F.12}$$

The final formula for a general normal ordered Hamiltonian turns out to be

$$Z = \int \mathcal{D}\eta^* \mathcal{D}\eta \exp(-S), \tag{F.13}$$

$$S = \int_0^\beta d\tau [\sum_\alpha \eta_\alpha^* \frac{\partial}{\partial\tau} \eta_\alpha + H(\tau)] \tag{F.14}$$

The quantity S is often called the action and the integrand in S the Lagrangian in analogy to the real time formulation of the path integral.

Appendix G

Many-Body Perturbation Theory

G.1 Gaussian Integral over Grassmann Numbers

By noting the identity $\exp(-\eta^* A\eta) = 1 - \eta^* A\eta$ with A a c-number, we obtain the simplest Gaussian integral over the Grassmann numbers η and η^* as

$$\int d\eta^* d\eta \exp(-\eta^* A\eta) = A. \tag{G.1}$$

Similarly with ξ a Grassmann number one can prove

$$\int d\eta^* d\eta \exp(-\eta^* A\eta + \xi^*\eta + \eta^*\xi) = A\exp(\xi^* A^{-1}\xi), \tag{G.2}$$

either by expanding the exponential or by the change $\eta \to \eta - A^{-1}\xi,\ \eta^* \to \eta - \xi^* A^{-1}$ of integration variables. These results can be extended to the case of many variables. Namely for an hermitian c-number matrix A we obtain

$$\int \prod_i d\eta_i^* d\eta_i \exp(-\sum_{ij} \eta_i^* A_{ij}\eta_j) = \det A, \tag{G.3}$$

which can be checked by diagonalizing the matrix A by a unitary transformation and recognizing that $\det A$ is the product of eigenvalues. Equation (G.3) should be compared with the usual Gaussian integration over N c-numbers. The latter gives $\pi^N \det A^{-1}$. Similarly as the multi-variable extension of eq.(G.2) we get

$$\int \prod_i d\eta_i^* d\eta_i \exp\Big[-\sum_{ij} \eta_i^* A_{ij}\eta_j + \sum_i (\xi_i^*\eta_i + \eta_i^*\xi_i)\Big] = \det A\ \exp(-\sum_{ij} \xi_i^* G_{ij}\xi_j) \equiv Z(\xi^*, \xi) \tag{G.4}$$

with $G = -A^{-1}$.

We introduce the average of Grassmann numbers by the relation

$$\langle \eta_i^*\eta_j\rangle_0 \equiv \int \prod_m d\eta_m^* d\eta_m\ \eta_i^*\eta_j \exp(-\sum_{ij} \eta_i^* A_{ij}\eta_j)/\det A. \tag{G.5}$$

This average is easily evaluated by taking derivative of $Z(\xi^*, \xi)$. Namely we have

$$\langle \eta_i^*\eta_j\rangle_0 \equiv -\lim_{\xi^*,\xi\to 0} \frac{1}{Z}\frac{\partial^2}{\partial\xi_i\partial\xi_j^*} Z(\xi^*, \xi) = G_{ji}. \tag{G.6}$$

Thus there is a correspondence $\eta_j \to \partial/\partial\xi_j^*, \eta_i^* \to -\partial/\partial\xi_i$ in taking the average. We can generalize this result to averages involving $2n$ Grassmann variables as follows:

$$\langle \eta_1^*\eta_{n+1}\eta_2^*\eta_{n+2}^* \ldots \eta_n^*\eta_{2n}\rangle_0 = \sum_P \mathrm{sgn}P\ G_{n+1,P(1)} G_{n+2,P(2)} G_{2n,P(n)}, \tag{G.7}$$

where P denotes a permutation of n variables, and the sign factor sgn$P$ accounts for the anticommuting property. This relation is equivalent to Wick's theorem as will be explained shortly.

We interpret the set variables η_i as representing not only the set of N single particle states but the set of M imaginary times between 0 and β generated by the Suzuki-Trotter decomposition . For example we consider the trivial case of $H = \epsilon f^\dagger f$ with $N = 1$. Then the integral for Z is evaluated as

$$Z = \det_\tau \left(\frac{\partial}{\partial \tau} + \epsilon \right), \tag{G.8}$$

where the determinant is for the $M \times M$ matrix with M going to infinity. The meaning of the derivative becomes clear if we first rewrite

$$Z = \exp \left[\mathrm{tr}_\tau \ln \beta \left(\frac{\partial}{\partial \tau} + \epsilon \right) \right], \tag{G.9}$$

and use the complete set of anti-periodic functions $\exp(-i\epsilon_n \tau)/\sqrt{\beta}$ in taking the trace. Multiplication of β for the argument of the logarithm is only to make the argument dimensionless. The exponent corresponds to $\ln Z = -\beta\Omega$ which becomes

$$-\beta\Omega = \sum_n \ln \beta(-i\epsilon_n + \epsilon). \tag{G.10}$$

This sum is actually divergent and does not reproduce the correct answer ln[1+exp$(-\beta\epsilon)$]. The divergence originates from the replacement of the difference in eq.(F.11) by the differential. In practical application to be explained below, this difficulty is not serious because one can use a reference state for which the thermodynamic potential is derived without using the path integral. Then the deviation $\Delta\Omega$ from this reference state is convergent. Alternatively one can absorb the divergence by requiring that both Ω and $\partial\Omega/\partial\epsilon = \langle f^\dagger f \rangle$ go to zero as $\epsilon \to \infty$. Then using

$$\sum_n (i\epsilon_n - \epsilon)^{-2} = \beta^2 e^{\beta\epsilon}/(e^{\beta\epsilon} + 1)^2, \tag{G.11}$$

and integrating twice with respect to ϵ we obtain the correct result.

G.2 Wick's Theorem

The path integral representation applies also to Green functions. By using the Heisenberg representation $f_\alpha(\tau) = \exp(\tau H) f \exp(-\tau H)$ in the imaginary time (Matsubara representation) with a general normal ordered Hamiltonian H, one can show the equivalence of averages:

$$\langle T_\tau f_\alpha^\dagger(\tau_1) f_\beta(\tau_2) \rangle = \int \mathcal{D}\eta^* \mathcal{D}\eta \; \eta_\alpha^*(\tau_1)\eta_\beta(\tau_2) \exp(-S)/Z \equiv \langle \eta_\alpha^*(\tau_1)\eta_\beta(\tau_2) \rangle, \tag{G.12}$$

the left-hand side of which is the Green function. This equivalence can be proved for the case of $\tau_1 > \tau_2$ by the Trotter decomposition of

$$\exp[-(\beta - \tau_1)H] f_\alpha^\dagger \exp[-(\tau_1 - \tau_2)H] f_\beta \exp[-\tau_2 H]. \tag{G.13}$$

The other case of $\tau_1 < \tau_2$ can be done similarly. Note that T_τ does not appear in the average of η variables.

It is convenient to introduce the partition function $Z(\xi^*, \xi)$ in the presence of the Grassmann external fields $\xi_\alpha(\tau)^*, \xi_\alpha(\tau)$. They appear in the Lagrangian as $\xi^\dagger\eta + \eta^\dagger\xi$ where the variables are regarded as vectors with state and time indices. In a particular case of a noninteracting Hamiltonian $H = \sum_{\alpha\beta} h_{\alpha\beta} f_\alpha^\dagger f_\beta$, the matrix element of $-A$ is given by $i\epsilon_n \delta_{\alpha\beta} - h_{\alpha\beta}$ where we have made the Fourier transform to Matsubara frequencies. Then we can use the result of Gaussian integration explained above. For example the inverse matrix $-A^{-1} = G$ is nothing but the Green function matrix. In analogy to eq.(G.6) one can show

$$\langle \eta_\alpha^*(\tau_1)\eta_\beta(\tau_2) \rangle = -\lim_{\xi^*, \xi \to 0} \frac{1}{Z} \frac{\delta^2}{\delta\xi_\alpha(\tau_1)\delta\xi_\beta^*(\tau_2)} Z(\xi^*, \xi) = G_{\beta\alpha}(\tau_2 - \tau_1), \tag{G.14}$$

where the last quantity denotes the Green function.

There is now a correspondence

$$\eta_\alpha(\tau) \to \delta/\delta\xi^*_\alpha(\tau),\ \eta^*_\alpha(\tau) \to -\delta/\delta\xi_\alpha(\tau) \tag{G.15}$$

in taking the average. By using this relation and eq.(G.4) for $Z(\xi^*, \xi)$, one can derive the Wick's theorem as follows:

$$\langle T_\tau f^\dagger(\tau_1) f(\tau_{n+1}) \dots f^\dagger(\tau_n) f(\tau_{2n})\rangle = \sum_P \mathrm{sgn}P\, G(\tau_{n+1} - \tau_{P(1)}) \dots G(\tau_{2n} - \tau_{P(n)}), \tag{G.16}$$

where the index α for single-particle states has been omitted for notational simplicity. The result at finite temperature is also called the Bloch-de Dominicis theorem. Use of the correspondence given by eq.(G.15) for the Hamiltonian with two-body interaction $V(f^\dagger, f)$ leads to formal representation of the partition function Z in terms of the one $Z_0(\xi^*, \xi)$ without V but with external fields as [11]

$$Z = -\lim_{\xi^*,\xi\to 0} \exp\left[-\int_0^\beta d\tau V(\frac{\delta}{\delta\xi}, -\frac{\delta}{\delta\xi^*})\right] Z_0(\xi^*, \xi). \tag{G.17}$$

By expanding this expression in terms of V and using Wick's theorem, one can derive the perturbation theory in terms of Feynman diagrams.

Alternatively we consider the partition function without external fields writing the action $S_0 + S_1$ where $S_1 = \int_0^\beta d\tau V(\tau)$. The partition function are written as

$$Z = Z_0\langle \exp(-S_1)\rangle_0, \tag{G.18}$$

where Z_0 comes from S_0, and $\langle\cdots\rangle_0$ denotes the average in term of the unperturbed action. Taking the logarithm of eq.(G.18) we obtain the shift Ω_1 of the thermodynamic potential as

$$\Omega_1 = -T[\langle \exp(-S_1)\rangle_c - 1], \tag{G.19}$$

where $\langle\cdots\rangle_c$ is the unperturbed cumulant average as explained in Appendix D. In terms of Feynman diagrams, the cumulant average eliminates all unlinked parts in each order of S_1. Hence eq.(G.19) gives the linked-cluster expansion.

G.3 Variational Property and the Luttinger-Friedel Sum Rule

We consider a situation where a coupling

$$\int_0^\beta d\tau \int_0^\beta d\tau' f^\dagger_\alpha(\tau) U_{\alpha\beta}(\tau - \tau') f_\beta(\tau'), \tag{G.20}$$

to the fictitious external field $U_{\alpha\beta}(\tau - \tau')$ is present in the system. $U_{\alpha\beta}(\tau - \tau')$ may be viewed as a Gaussian average of product of two external fields. In the following we use a simplified notation where tr means the trace over both spatial and imaginary-time degrees of freedom.

With slight change δU in U, the thermodynamic potential Ω varies by the amount

$$\beta\delta\Omega(U) = \mathrm{tr}(G\delta U), \tag{G.21}$$

where G is the Green function which is a matrix in space and time indices. We now eliminate δU in favor of the changes δG of the Green function and $\delta\Sigma$ of the self-energy matrix Σ. With use of the Dyson equation $G^{-1} = g^{-1} - U - \Sigma$ where g is the bare green function, we obtain

$$G\delta U = -G\delta(G^{-1} + \Sigma) = -\delta(\ln G^{-1} + G\Sigma) + (\delta G)\Sigma. \tag{G.22}$$

The trace of the last term in the right hand side is given as the change $\delta\Phi$ of certain quantity Φ. In the diagrammatic language, Φ is given by the sum of skeleton diagrams for Ω. A skeleton diagram is defined as such that does not include any self-energy parts as subdiagrams. This identification makes it possible to integrate the differential relation (G.21). We obtain

$$\beta(\Omega\{G\} - \Omega_0) = \Phi\{G\} - \mathrm{tr}(\Sigma G) - \mathrm{tr}\ln(G^{-1}g), \tag{G.23}$$

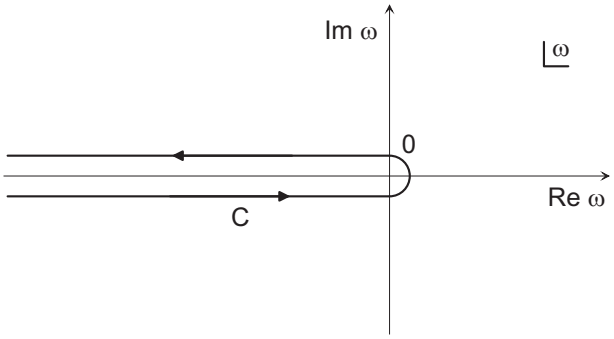

Figure G.1: Deformation of the integration contour from along the imaginary axis to the one encircling the negative real axis.

where Ω_0 is the thermodynamic potential for the noninteracting system. Note that there is no explicit appearance of U in eq.(G.23). The Ω as a functional of G is stationary against the change of G, as can be checked easily [12, 13]. This variational property is very analogous to that in the Helmholtz free energy F against the change in the chemical potential, or the Gibbs energy G against the change in the number of particles [14]. In all cases, the Legendre transformation of natural variables is involved behind the variational property.

Let us consider the zero-temperature limit of eq.(G.23) in the imaginary frequency domain. The contribution of a given diagram to Φ remains the same if the internal frequency $i\epsilon$ of a Green function is increased. In other words we have for this change

$$\delta\Phi = \delta\epsilon \mathrm{tr}(\Sigma\frac{\partial G}{\partial\epsilon}) = 0. \tag{G.24}$$

By partial integration the above equality leads to

$$\mathrm{tr}(G\frac{\partial\Sigma}{\partial\epsilon}) = 0. \tag{G.25}$$

With this setup we represent the total number N of electrons in the system as

$$N = \mathrm{tr}\exp(i\epsilon 0_+)G = -\mathrm{tr}\exp(i\epsilon 0_+)\frac{\partial \ln G}{i\partial\epsilon}. \tag{G.26}$$

where we have used eq.(G.25) in the second equality. For definiteness we first consider the homogeneous system and replace the trace by

$$\mathrm{tr} \to \sum_{\boldsymbol{k}}\int_{-\infty}^{\infty}\frac{d\epsilon}{2\pi} = \sum_{\boldsymbol{k}}\int_C\frac{d\omega}{2\pi i}, \tag{G.27}$$

with $i\epsilon = \omega$ and the integration contour C is shown in Fig.G.1. Here we have utilized the convergence factor $\exp(i\epsilon 0_+)$ in deforming the integration contour.

Then we obtain

$$N = \sum_{\boldsymbol{k}}\int_{-\infty}^{0}\frac{d\omega}{\pi}\mathrm{Im}\frac{\partial \ln G(\boldsymbol{k},\omega+i\delta)}{\partial\omega} = \frac{1}{\pi}\mathrm{Im}\sum_{\boldsymbol{k}}\ln[-G(\boldsymbol{k},i0_+)], \tag{G.28}$$

The minus sign with $G(\boldsymbol{k},i0_+)$ comes from the contribution at $\omega\to-\infty$. In the Fermi liquid, the self-energy $\Sigma(\boldsymbol{k},i0_+)$ becomes real because of the restriction in the available damping processes. Hence $G(\boldsymbol{k},i0_+)$ is also real. If $G(\boldsymbol{k},i0_+)$ is positive, which is the case for small $|\boldsymbol{k}|$, the phase $\mathrm{Im}\ln[-G(\boldsymbol{k},i0_+)]$ of the Green function is π. On the other hand $G(\boldsymbol{k},i0_+)$ becomes negative as $|\boldsymbol{k}|$ goes to infinity. The surface of $\boldsymbol{k}$ where $G(\boldsymbol{k},i0_+)$ changes sign is nothing but the Fermi surface. Thus eq.(G.28) tells us that the volume inside the Fermi surface of the interacting system remains the same as that of the noninteracting one with the same number N of particles [12]. This property is called the Luttinger sum

rule which distinguishes the itinerant f electrons from the localized ones with no participation in the Fermi volume.

We remark that the sum rule can in fact be applied to systems with finite magnetization or without translational symmetry. By shifting the internal energy for up-spin Green functions only, we obtain eq.(G.24) for the up spin. This is because the Coulomb interaction does not mix different spin components. Then we obtain eq.(G.25) for each spin component. In terms of the Green function $G_\sigma(\boldsymbol{k}, \omega + i\delta)$ with z-component $\sigma/2$ of spin, the total magnetization $M = N_\uparrow - N_\downarrow$ is given by

$$M = \frac{1}{\pi}\mathrm{Im}\sum_{\boldsymbol{k}\sigma} \sigma \ln[-G_\sigma(\boldsymbol{k}, i0_+)]. \tag{G.29}$$

For systems without the translational invariance, the most successful application is the proof of the Friedel sum rule for the Anderson model [15]. If the perturbation theory converges in the latter case we have the relation

$$n_f = \frac{2}{\pi}\mathrm{Im}\ln[-G_f(i0_+)], \tag{G.30}$$

where n_f is the number of f electrons and $G_f(i0_+)$ is the f-electron Green function at the Fermi surface. The above relation is called the Friedel sum rule. The number n_f is not necessarily an integer in this case.

G.4 Path Integral over Auxiliary Fields

Instead of dealing with the electron-electron interaction as it stands, it is often useful to introduce auxiliary fields so that the electrons interact via these fields. Consider the operator

$$\exp(-\delta\tau U n_\uparrow n_\downarrow), \tag{G.31}$$

which appears in eq.(F.11) for the partition function. We here concentrate on a particular site and have discarded the site index for simplicity. The operator $n_\uparrow n_\downarrow$ can be written in alternative forms as:

$$n_\uparrow n_\downarrow = \frac{1}{2}n - 2(S^z)^2 = \frac{1}{2}n - \frac{2}{3}\boldsymbol{S}\cdot\boldsymbol{S}. \tag{G.32}$$

The density term with $n = n_\uparrow + n_\downarrow$ becomes a constant by the site summation and we concentrate first on the spin term $2(S^z)^2$. We use the following identity:

$$\exp[Ay^2] = \int_{-\infty}^{\infty} \frac{dx}{\sqrt{2\pi A}} \exp[-\frac{x^2}{A} - 2xy], \tag{G.33}$$

with $A > 0$. In the case of negative A, the integration over x runs from $-i\infty$ to $i\infty$. This identity is applied to each factor in eq.(F.11) for the partition function with

$$A = 2U, \quad y = \sqrt{\delta\tau}S^z, \quad x = \sqrt{\delta\tau}\phi. \tag{G.34}$$

We then obtain the following expression for the Hubbard model:

$$Z = \int \mathcal{D}\eta^*\mathcal{D}\eta\mathcal{D}\phi \exp[-\int_0^\beta d\tau\mathcal{L}(\tau)], \tag{G.35}$$

$$\mathcal{L}(\tau) = \mathcal{L}_0(\tau) + \frac{1}{2U}\sum_i \phi_i(\tau)^2 + 2\sum_i \phi_i(\tau)S_i^z(\tau) = \mathcal{L}_0(\tau) + \mathcal{L}_\phi(\tau), \tag{G.36}$$

where $\mathcal{L}_0$ is the Lagrangian without interaction, and we have discarded the constant term in the Lagrangian. The procedure of introducing the auxiliary fields ϕ_i is called the Hubbard-Stratonovich transformation.

One can perform the integration over Grassmann numbers exactly because the action is bilinear with respect to them. The result is given by

$$Z = \int \mathcal{D}\phi \exp\left[-\int_0^\beta d\tau \sum_i \frac{1}{2U}\phi_i(\tau)^2 + \mathrm{tr}\ln(g^{-1} - \phi\sigma_z)\right], \tag{G.37}$$

where tr is the trace over imaginary time and space, and g in the logarithm is the unperturbed green function matrix. Thus the original Fermion problem is reduced to another one with fluctuating magnetic field ϕ.

The spin-spin correlation function in the imaginary time is given by

$$\langle T_\tau S^z(\tau)S^z(\tau')\rangle = Z^{-1}\int \mathcal{D}\eta^*\mathcal{D}\eta\mathcal{D}\phi \exp[-\int_0^\beta d\tau\mathcal{L}_0(\tau)]\frac{\partial^2}{4\partial\phi_i(\tau)\partial\phi_j(\tau')}\exp[-\int_0^\beta d\tau\mathcal{L}_\phi(\tau)] \quad \text{(G.38)}$$

Thus $\partial/\partial\phi_i$ acts like the spin operator, which is natural since ϕ_i has a meaning of a fluctuating magnetic field conjugate to S_i^z. In the present case of the Gaussian distribution of ϕ_i, one can make partial integration in eq.(G.38) and obtain for the magnetic susceptibility

$$\chi(\boldsymbol{q}, i\nu) = \frac{1}{U}\left[\frac{1}{U}\langle|\phi(\boldsymbol{q}, i\nu)|^2\rangle - 1\right], \quad \text{(G.39)}$$

where we have introduced the Fourier transform $\phi(\boldsymbol{q}, i\nu)$ of $\phi_i(\tau)$ and $\langle\ldots\rangle$ means the statistical average. This equation shows that the field $\phi_i(\tau)$ also has the meaning of fluctuating magnetization upon proper scaling and subtraction. The subtraction removes the part of $\langle|\phi(\boldsymbol{q}, i\nu)|^2$ which remains in the high frequency limit.

As the simplest application of the above formalism, we derive the RPA susceptibility. We expand the logarithm in eq.(G.37) up to second order in ϕ. Then after Fourier transform we obtain

$$\chi(\boldsymbol{q}, i\nu) = \frac{1}{U}\left(\frac{1}{1 - U\chi_0(\boldsymbol{q}, i\nu)/2} - 1\right) = \frac{\chi_0(\boldsymbol{q}, i\nu)}{1 - U\chi_0(\boldsymbol{q}, i\nu)/2}, \quad \text{(G.40)}$$

which corresponds to the RPA discussed in Chapter 1.

We note that the result obtained above in fact depends on the particular choice among those in eq.(G.32). If we chose the second decomposition, we would have obtained the susceptibility where U in eq.(G.40) replaced by $U/3$. It is evident that the lowest order expansion of the logarithm caused the difference. In order to obtain the correct result to $O(U)$ for $\chi(\boldsymbol{q}, i\nu)$, one has to make expansion of the logarithm up to $O(\phi^4)$ which gives correct result for $\langle|\phi(\boldsymbol{q}, i\nu)|^2\rangle$ to $O(U^2)$. The first factor $1/U$ in eq.(G.39) reduces the order of U by one, so that the lowest order expansion of the logarithm is not sufficient to obtain the $O(U)$ result for the susceptibility. Thus the RPA result obtained above is fortuitous as the lowest order theory.

It is more convenient for numerical calculation such as the Monte Carlo simulation to use the Ising-type discrete auxiliary field $\sigma = \pm 1$ instead of using the continuous one [16]. The identity we use now is the following:

$$\exp[A(S^z)^2] = \frac{1}{2}\sum_\sigma \exp(-B\sigma S^z), \quad \text{(G.41)}$$

where B satisfies the relation $\exp(A/4) = \cosh(B/2)$ with $A, B > 0$. This relation is easily confirmed by applying both sides of eq.(G.41) to each eigenstate of S_z. We can solve for B as

$$B = 2\ln[\exp(A/4) + \sqrt{\exp(A/2) - 1}]. \quad \text{(G.42)}$$

Thus the partition function is written, after introducing the Ising variable σ_i to each site and discretizing τ, as

$$Z = \prod_{i,j}\int d\eta_i(\tau_j)^* d\eta_i(\tau_j)\sum_{\sigma_i(\tau_j)}\exp[-\delta\tau\sum_j \mathcal{L}(\tau_j)], \quad \text{(G.43)}$$

$$\mathcal{L}(\tau_j) = \mathcal{L}_0(\tau_j) + I\sum_i S_i^z(\tau_j)\sigma_i(\tau_j), \quad \text{(G.44)}$$

where $\cosh(\delta\tau I/2) = \exp(\delta\tau U/2)$ with $\delta\tau = \tau_j - \tau_{j-1}$. Note that one has $I \gg U$ as $\delta\tau$ approaches 0. The path integral over fermions can be done exactly as before. Thus one is left with the partition function of a fictitious Ising model with interactions dependent on space and time difference. The summation over Ising variables is conveniently dealt with by the Monte Carlo sampling.

Bibliography

[1] R. Kubo, J. Phys. Soc. Jpn. **12**, 570 (1957).

[2] I. Lindgren and J. Morrison, *Atomic Many-Body Theory*, (Springer Verlag, Berlin, 1986).

[3] P. Nozieres and A. Blandin, J. Physique **41**, 193 (1980).

[4] Y. Kuramoto, European J. Phys. B **5**, 457 (1998).

[5] P.W. Anderson, J. Phys. C**3**, 2439 (1970).

[6] A.A. Abrikosov and A.A. Migdal, J. Low Temp. Phys. **3**, 519 (1970).

[7] J. Gan, N. Andrei and P. Coleman, Phys. Rev. Lett. **70**, 686 (1993).

[8] H. Mori, Prog. Theor. Phys. **34**, 399 (1965).

[9] R. Kubo, J. Phys. Soc. Jpn. **17**, 206 (1962).

[10] A.A. Abrikosov, L.P. Gorkov, I.E. Dzyaloshinskii, *Methods of Quantum Field Theory in Statistical Physics*, (Dover, New York, 1975).

[11] J. Zinn-Justin, *Quantum Field Theory and Critical Phenomena* (Oxford University Press, Oxford, 1993).

[12] J. Luttinger and J. Ward, Phys. Rev. **118**, 1417 (1960);

[13] G. Baym, Phys.Rev. **127**, 835 (1962).

[14] C. De Dominicis and P.C. Martin, J. Math. Phys. **5**, 14 (1964).

[15] D.C. Langreth, Phys.Rev. **150**, 516 (1966).

[16] J.E. Hirsch, Phys. Rev. B**28**, 4059 (1983).

æ

Index